ABSTRACT

Title of Dissertation:	EPITAXIAL GROWTH AND CHARACTERIZATION OF ^{28}Si AND ALUMINUM DELTA LAYERS FOR HYBRID QUANTUM COMPUTING
	Ke Tang Doctor of Philosophy, 2021
Dissertation directed by:	Professor Raymond J. Phaneuf Department of Material Science and Engineering Dr. Joshua M. Pomeroy National Institute of Standards and Technology

Novel isotopically enriched and aluminum (Al) delta-doped silicon crystals with exceptional material properties are proposed and developed, in an effort to bridge superconducting quantum information with silicon-based quantum devices for a new generation of solid-state quantum computing. Quantum computing platforms based on semiconducting and superconducting qubits are two powerful candidates. For semiconductor spin qubits, long coherence times can be achieved when using isotopically enriched ^{28}Si as a host material. However, qubit coupling in semiconductor qubits is difficult to achieve due to the nanometer scale of the devices. For superconductor qubit devices, millimeter scale with long spatial coherence length makes them relatively easy to couple multiple qubits, but losses at the material interface are limiting the device performance. Our ultimate objective is to create a

hybrid system where both Si spin qubits and superconductor qubits are coupled in a nuclear spin-free and interface-free material. To achieve this, a superconducting semiconductor with monocrystalline structure is proposed. One possible candidate is through Al delta-doped ^{28}Si, as highly Al doped Si is expected to have a 10× higher critical temperature (T_c) than highly boron (B) doped Si ($T_c \approx 0.6$ K). The focus of this thesis is to attack two materials limitations for realizing a monocrystalline, super-semiconducting hybrid architecture: 1) substantially reducing ^{29}Si that limits coherence of semiconducting spin qubits and 2) exploring supersaturated, Al-doped silicon as a system for localized superconductivity within silicon with a potential Tc > 1K.

In the first part of this thesis, we demonstrate the advancements in isotopically enriched ^{28}Si in terms of chemical purity, enrichment, and electrical properties. In this work, a new, compact UHV version of the hyperthermal Penning ion source was designed and built. An improvement in the chemical purity from 98.47 % to 99.97 %, while maintaining a ^{28}Si enrichment of > 99.999987 % (0.832 ppm ^{29}Si) has been achieved. We broaden the material variety of ^{28}Si at different levels in the quantum information community by demonstrating the ability to grow isotopically enriched ^{28}Si epitaxial films with precisely controlled (≈ 90 % accuracy) enrichment levels, ranging from natural abundance to < 1 ppm ^{29}Si. In addition, to better assess the quality of our ^{28}Si material, we have successfully fabricated and measured ^{28}Si MOSFET devices, and compared to those from natural abundance Si on the same substrate. The charge carrier mobility on isotopically enriched ^{28}Si is found to be

approximately a factor of 3 lower compared to the natural abundance Si, a result of the short-range scattering (impurity scattering).

In the second part of this thesis, we report on the material growth and characterization of super-saturated Al delta layers in Si and explore the possibility for superconductivity. To reach a critical density needed for superconducting transition, the first step is to study the saturation density of this dopant and a way to confine it in 3D. Using a combination of different characterization tools, the maximum 2D atom density of one atomic layer of Al on Si(100) surface before cluster formation is found to be 3.4×10^{14} cm^{-2}. We also studied the effects of different material growth methods on electrical conduction and the possibility of reaching higher 3D density of Al in this Si-Al-Si heterostructure. We found that Al delta doping in Si behaves differently compared to other dopants: the incorporation anneal does not change the dopant activation efficiency. Standard molecular beam epitaxy (MBE) and locking layer (LL) growth on Al layer is not successful and Al dopant activation is found to be < 50 %, most likely due to the tendency of Al atoms to move toward the surface and the cluster states been developed from the thermal anneals. The electrical conduction of this delta layer at low temperature is also studied and modeled using a temperature dependent two-carrier type model, which is the first reported conducting Al delta layer in Si. We believe that reaching the superconducting transition using an Al delta layer as a dopant in Si is possible, but this requires further studies both experimentally and theoretically to minimize the Al segregation in order to achieve a high enough 3D dopant density.

EPITAXIAL GROWTH AND CHARACTERIZATION OF ^{28}Si AND ALUMINUM DELTA LAYERS FOR HYBRID QUANTUM COMPUTING

by

Ke Tang

Dissertation submitted to the Faculty of the Graduate School of the
University of Maryland, College Park, in partial fulfillment
of the requirements for the degree of
Doctor of Philosophy
2021

Advisory Committee:
Professor Raymond J. Phaneuf, Chair/Advisor
Dr. Joshua M. Pomeroy, Co-Advisor
Professor John Cumings
Professor Lourdes G. Salamanca-Riba
Professor Martin Peckerar

Foreword

Chapter 3 is partially reproduced from Review of Scientific Instruments 90, 083308 (2019); https://doi.org/10.1063/1.5097937, with the permission of AIP publishing. (I am the first author of this paper).

Chapter 4 is partially reproduced from Journal of physics communications, 4(3), 035006 (2020); https://doi.org/10.1088/2399-6528/ab7b33, under a Creative Commons Attribution (CC BY) license. (I am the first author of this paper).

Chapter 5 is partially reproduced from AIP Advances 9, 125153 (2019); https://doi.org/10.1063/1.5128098, under a Creative Commons Attribution (CC BY) license. (I am the second author of this paper).

Permission to Reuse Content

REUSING AIP PUBLISHING CONTENT

Permission from AIP Publishing is required to:

- republish content (e.g., excerpts, figures, tables) if you are not the author
- modify, adapt, or redraw materials for another publication
- systematically reproduce content
- store or distribute content electronically
- copy content for promotional purposes

To request permission to reuse AIP Publishing content, use RightsLink® for the fastest response or contact AIP Publishing directly at rights@aip.org and we will respond within one week:

For RightsLink, use Scitation to access the article you wish to license, and click on the Reprints and Permissions link under the TOOLS tab. (For assistance click the "Help" button in the top right corner of the RightsLink page.)

To send a permission request to rights@aip.org, please include the following:

- Citation information for the article containing the material you wish to reuse
- A description of the material you wish to reuse, including figure and/or table numbers
- The title, authors, name of the publisher, and expected publication date of the new work
- The format(s) the new work will appear in (e.g., print, electronic, CD-ROM)
- How the new work will be distributed and whether it will be offered for sale

Authors do not need permission from AIP Publishing to:

- quote from a publication (please include the material in quotation marks and provide the customary acknowledgment of the source)
- reuse any materials that are licensed under a Creative Commons CC BY license (please format your credit line: "Author names, Journal Titles, Vol.#, Article ID#, Year of Publication; licensed under a Creative Commons Attribution (CC BY) license.")
- reuse your own AIP Publishing article in your thesis or dissertation (please format your credit line: "Reproduced from [FULL CITATION], with the permission of AIP Publishing")
- reuse content that appears in an AIP Publishing journal for republication in another AIP Publishing journal (please format your credit line: "Reproduced from [FULL CITATION], with the permission of AIP Publishing")
- make multiple copies of articles–although you must contact the Copyright Clearance Center (CCC) at www.copyright.com to do this

REUSING CONTENT PUBLISHED BY OTHERS

To request another publisher's permission to reuse material in AIP Publishing articles, please use our Reuse of Previously Published Material form. (We require documented permission for all reused content.)

Reuse of Previously Published Material Form (pdf)

Unless the publisher requires a specific credit line, please format yours like this:

Reproduced with permission from J. Org. Chem. 63, 99 (1998). Copyright 1998, American Chemical Society.

You do not need permission to reuse material in the public domain, but you should still include an appropriate credit line which cites the original source.

https://publishing.aip.org/resources/researchers/rights-and-permissions/permissions/

Reusing IOP Published Content

In order to reuse content published by IOP or its partners, you will need to request express permission. The way you will need to obtain this permission depends on what material you wish to reuse, and how you wish to reuse it

When permission is not needed:
There are a few instances you don't need permission to reuse IOP published content:

- If the new work in which you are reusing the content is also being published by IOP or one of its partners. IOP already has the permission to use this content, so you do not need to request it again
- If the content was published on an open-access basis that allows the type of reuse you need. For details of open access licences, please see Creative Commons Licences.
- If you are the original author of the content you wish to reuse, and your reuse falls within the allowances of our Author Rights policy

Reusing content from IOP- or ECS- owned Journals:
To reuse content from any journal owned by IOP or ECS, we have partnered with the Copyright Clearance Centre (CCC) to use their Republication Service. You can find further details on how to use this service here: CCC Republication Service
This applies to any journals listed under IOP Publishing or The Electrochemical Society in the Publishing partners tab

Acknowledgements

I would first like to express my sincere gratitude to Dr. Josh Pomeroy, my co-advisor at NIST, for supporting and guiding me through the years that I worked with him. I am grateful for his patience and concern. Josh's way of critical thinking and problem-solving will always serve me well when moving forward. I also want to thank Professor Ray Phaneuf, my advisor at UMD, for his practical advices and kindness that helped me achieving the academic milestones in my Ph.D. study.

I want to thank Dr. Kevin Dwyer, Josh's previous student, for providing warm welcome and detailed guidance after I joined this group. Kevin was probably another "professor" to me in my point of view, where he taught me how to manipulate all those complicated experimental apparatus in our lab. I want to thank our former group members, Dr. Aruna Ramanayaka and Dr. Hyun Soo Kim for fruitful collaborations and helpful discussions. This project cannot go anywhere further without their help. I also want to thank our group members and the PIs at NIST including Yanxue Hong, Zac Barcikowski, Ryan Stein, Dr. David Simons, Dr. Roy Murray, Dr. Binhui Hu, Dr. Michael Stewart, Dr. Neil Zimmerman and Dr. Garnett Bryant for helpful consultations and supports. I appreciate Dr. Karen A. DeRocher and Dr. Frederick Meisenkothen at NIST for the atom probe tomography (APT) measurements in Chapter 6. Thank you and great respect to other collaborators at NIST, including Terry Moore, Dr. Xiqiao Wang and Dr. Pradeep Namboodiri.

I want to thank most to my family members who consistently supported me throughout my life. I want to thank my mom and dad for everything they have done

for me. My dog Zena for the emotional support and especially my dear wife Sophia for the endless love and accompany throughout the years of this long journey. The work presented here would be impossible without them.

Finally, I want to thank all the committee members: Professor John Cumings, Professor Lourdes G. Salamanca-Riba and Professor Martin Peckerar and their precious times for reviewing this thesis.

Table of Contents

List of Figures

Chapter 1: Introduction

Progress in the semiconductor industry has been greatly advanced and expanded in the past decades largely in an attempt to follow Moore's law. Originated from Gordon Moore in 1965, this predicted that the number of transistors in an integrated circuit (IC) should double every two years. Progressing from the first metal-oxide-semiconductor field-effect transistors (MOSFET), which have critical dimensions that are micron in size, IC's now have billions of transistors. Recently, the mass production of devices at the 3 nm node using fin field-effect transistor (FinFET) and extreme ultraviolet lithography (EUVL) has been made commercially available [1]. The race continues as IBM announced their new 2 nm process using nanosheet or gate-all-around transistors recently. Although the "2 nm" described here is not the actual dimension of the transistors, the shrinking in size will eventually lead to a fundamental limit where quantum effects dominate the device performance [2]. Even with these great advancements, classical computers that use classical bits 0 and 1 are still limited when solving certain types of problems.

The quantum computer, in analogy to its classical counterpart, is made up of quantum bits or "qubits". A qubit is a two-level system (e.g. an electron spin that has spin up and spin down or a photon that has vertical and horizontal polarization, etc.) that exhibits unique quantum properties including superposition and entanglement. Superposition is the ability of a quantum system to be in multiple states simultaneously, at least until it is measured. It allows a qubit to not only be in the states labeled $|0\rangle$ or $|1\rangle$, but also in the state :

$$|\psi\rangle = \cos(\theta/2)\,|0\rangle + e^{i\varphi}\sin(\theta/2)|1\rangle \quad (1.1)$$

, where θ and φ are real phase angles defined on the Bloch sphere, as shown in Fig. 1.1. On the Bloch sphere, the basis states $|0\rangle$ and $|1\rangle$ are the north and south poles, respectively and the superposition states are on the equator. An arbitrary qubit state can be expressed as a point on the surface. The entanglement of the qubits describes the correlation between qubit states. A two-qubit state $\frac{1}{\sqrt{2}}(|01\rangle + |10\rangle)$ can be used to express entanglement, where one qubit depends on the other. By combining superposition and entanglement with quantum algorithms, an exponential increase in the computing power can be achieved when solving certain types of problems, such as prime factorization [3], numerical optimization [4], machine learning [5], complex simulations [6], data searching [7], etc.

Quantum algorithms are based on quantum computing models. One of the most commonly used is the quantum circuit model [8]. In this model, it has been proved that arbitrary single-qubit rotations with two-qubit controlled NOT gates are universal and can provide a set of gates to implement any quantum algorithms [9]. Besides, one qubit state can be controlled by another using a two-qubit controlled NOT (CNOT) gate, where a π rotation is applied around the x-axis if the control is in $|1\rangle$ [10]. The core of building a quantum computer is to have a qubit with high-fidelity single and two-qubit gates. The control fidelity (a measure of how "close" the two quantum states are) depends mainly on the manipulation time and the coherence time. The manipulation time refers to the time required for a single manipulation, characterized by a rotation angle of π or 2π. The coherence time (T_2) is also called the dephasing

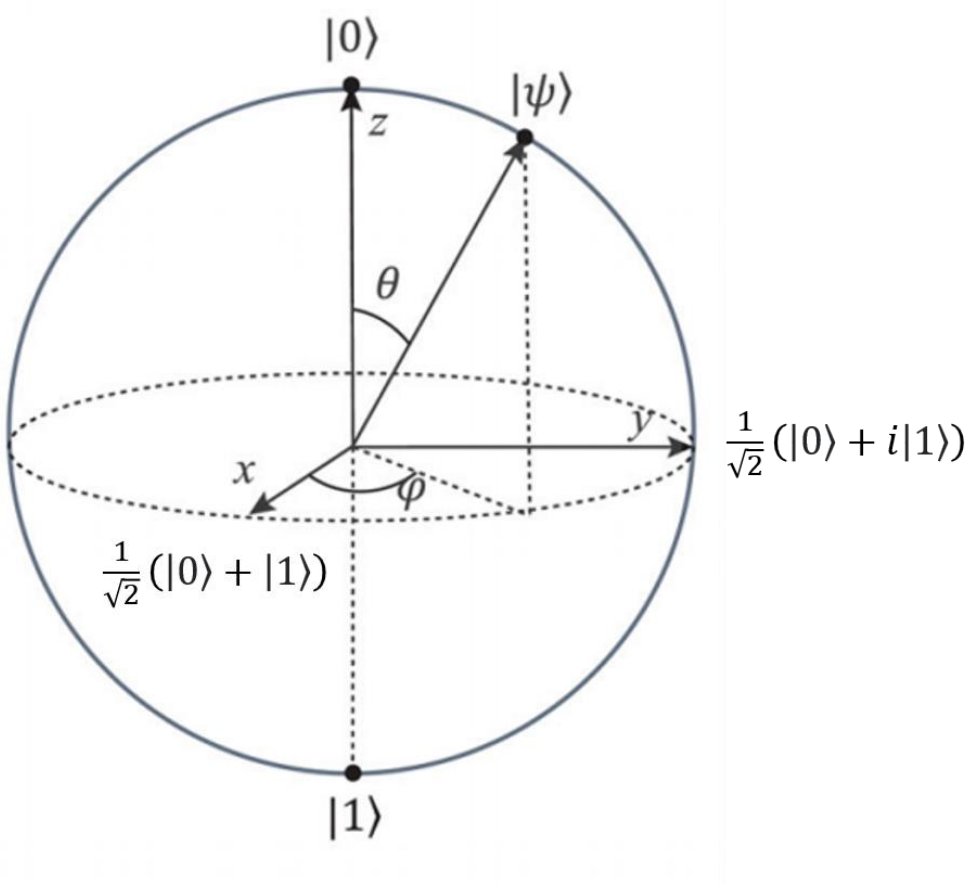

Figure 1.1: A schematic diagram of a Bloch sphere representing the qubit states. The north pole and south pole represent the basis states |0⟩ and |1⟩, respectively. Any point on this sphere represents a linear combination of the basis states. A π/2 pulse rotation changes the qubit from the |0⟩ to a superposition state. (Modified from [10], an Open Access article distributed under the terms of the Creative Commons Attribution License.)

time, defined as the time that a qubit can keep its quantum coherence properties. In coherent measurements, T_2 can be obtained by measuring the decay time of Larmor precession and Ramsey fringes [11]. Those decay times are usually denoted by T_2^* as they are smaller than T_2 due to experimental or environmental imperfections. Dynamical decoupling pulses [12] can be used to convert T_2^* to T_2.

1.1 Semiconductor and Superconductor Quantum Information

There are many possible candidate approaches toward building a quantum computer, such as ion traps [13, 14], superconducting circuits [15, 16], spins or quantum dots in semiconductors [17, 18], nitrogen vacancy centers [19, 20], nuclear magnetic resonance techniques [11], etc. Among those, semiconductor quantum information is a powerful candidate due to its compatibility to the modern semiconductor industry. In 1998, Loss and DiVincenzo first proposed to use semiconductor quantum dots as qubits and demonstrated single spin manipulations [21]. For a gate defined quantum dot device, the electrodes can be biased to form potential well to trap electrons, and the electron spins can be manipulated via an external magnetic field. Such quantum dots can also be formed in other material systems, such as GaAs [22], Si MOS and silicon-on-insulator (SOI) [23], nanowires [24], graphene [25], self-assembled crystals [26], etc. As an alternative to Si MOS quantum dots that utilize electron spins, Bruce Kane proposed to use the nuclear spin of a single ^{31}P donor in silicon as a qubit [27]. STM lithography with atomic scale precision and ion implantation are the two common ways to fabricate this kind of qubit devices. For the STM lithography approach, a single phosphorus (P) donor and a donor molecule are placed on the Si surface using STM lithography to selectively lift off hydrogen from a H-passivated surface [28]. A single-electron transistor (SET) for charge sensing is formed beneath it. The qubit is again surrounded by metallic gates and an aluminum microwave antenna generates an oscillating magnetic field over the device. The quantum information stored in each ^{31}P nuclear spin is read out

by measuring the tunneling current between the target qubit and the adjacent neutral donor. For the ion implantation approach, donor ions are implanted in a small region in the silicon and the spins of both the electron bound to the donor and the donor nucleus can be used as qubits [29].

In silicon spin qubits, one of the greatest advantages is the potential for extremely long coherence times. Silicon is a promising candidate due to its intrinsic material properties and the existence of techniques for fabrication of devices at increasingly smaller length scales. It has been widely accepted in this community that silicon can be an excellent host material for quantum devices that utilize charges and/or spins. Silicon can provide a nearly ideal environment for spins which results in a very long coherence time, due to its weak spin-orbit coupling and the existence of a nuclear spin-free isotope, ^{28}Si. In Si spin qubits, the major source of decoherence comes from the random strain field and the inhomogeneous magnetic field noise (or the Overhauser field) generated by nuclear and impurity spins. Natural abundance Si is composed of three isotopes: ^{28}Si (92.2 %), ^{29}Si (4.7 %) and ^{30}Si (3.1 %). The ^{29}Si isotope has a non-zero nuclear spin (I = 1/2) that causes random fluctuations and inhomogeneities in the background magnetic field, while ^{28}Si and ^{30}Si have no net nuclear spin. By eliminating the presence of ^{29}Si isotopes, both nuclear and electron spins in isotopically enriched ^{28}Si interact much less with their environment, resulting in a great enhancement in coherence time T_2 [30, 31]. Theoretical studies have predicted that the increase in coherence time is proportional to the reduction in ^{29}Si isotope concentration [32, 33]. Bulk electron spin resonance (ESR) and NMR

experiments of ^{31}P spins in ^{28}Si have been carried out by numerous research groups, where coherence times exceeding seconds have been achieved [30, 31, 34, 35].

Despite the advantages, there are also challenges associated with silicon-based quantum information. The semiconductor qubits have been expected to have good scalability and coupling considering the success in semiconductor industry, however, the largest number of qubits that can be controlled in the same device to date is still less than ten [36]. With isotopically purified ^{28}Si, the complicated valley degeneracy and resulting necessary elaborate control of the small electronic wave function still remain as challenges [10, 23]. There are six degenerate minima of the conduction band in Si and these subbands form valleys. For donors in Si, the valley degeneracy is not a concern since the dopant atom (such as ^{31}P) has a strong confinement potential that can lift the valley states degeneracy easily. However, for Si quantum dots, there are four in-plane valleys and two out-of-plane valleys and the two lower valleys greatly affect the qubit control and manipulation [23]. As a consequence, the valley state degeneracy can cause a significant decrease in spin lifetime [37], renormalize the g-factor [38], deteriorate spin initialization and may limit the dephasing time [39].

On the material standpoint, the supply of the isotopically enriched ^{28}Si within this community is very limited. Perhaps the most highly enriched single crystal bulk ^{28}Si is from the International Avogadro Project [40], which was produced using centrifuge enriched gaseous silane and a long process chain resulting in zone refined, single crystal silicon with a residual ^{29}Si isotope fraction of about 10^{-5} mol/mol [41]. The end goal in that case was to produce a macroscopic artifact (≈1 kg) of enriched silicon for metrological purposes. Quantum information applications do not require macroscopic

quantities of ^{28}Si for each device, so an alternative, less expensive strategy has been to grow epitaxial ^{28}Si layers on natural silicon substrates using isotopically enriched silane gas, e.g., chemical vapor deposition (CVD) grown ^{28}Si epilayers on 300 mm^2 substrates that is enriched to 99.992 % [42] . Remnants from other sources [43] of ^{28}Si also exist, providing access for research efforts, typically with enrichments ≤ 99.9 % ^{28}Si, including the float-zone grown samples from Keio University[44], CVD grown thin films at Princeton University [45], solid-source molecular beam epitaxy (MBE) grown thin films at Technical University of Munich (TUM) [46], ion beam method from Penning source based ion implanter [47], etc.

As an alternative, superconductor-based qubit is another promising candidate for quantum information due to its macroscopic nature. Unlike semiconductor qubits where coupling is challenging (mainly due to the nanometer scale), a degree of scalability has already been demonstrated for superconductor qubits: a 53 superconducting qubit computer was demonstrated by Google in 2019 and a 65-qubit computer was announced by IBM in 2020. In 1999, Nakamura et al. developed the first qubit for superconducting quantum computing [48]: a Josephson junction (JJ) based Cooper-pair Box (CPB) in the charge regime. Since then, superconducting qubit has been developed rapidly. A high fidelity two-qubit gate using 5 qubits [49] was demonstrated in 2014 and this provided an important step towards surface code schemes [50, 51]. Depending on different degrees of freedom, superconducting qubits can be divided into different categories: charge qubits [48, 52], phase qubits [53], flux qubits [54, 55], transmission line shunted plasmon oscillation or “transmon” qubits

[56], etc. An important step is to embed the qubits in a superconductor micro-resonator to introduce circuit quantum electrodynamics (cQED) [16, 57-59].

Compared to other quantum computation systems, superconductor qubits have the following advantages. The first is the high design capability that is associated with different types of qubits (charge, phase, flux, etc.). Secondly, different parameters such as energy level and coupling strength can be adjusted by changing the capacitance, energy, and inductance of the JJ. In addition, superconductor qubit has good scalability and is easy to couple using capacitance or inductance due to its circuit nature.

One limitation for this type of qubit is the relatively short coherence time. Originally, the coherence time for charge qubit was only a few nanoseconds. In 2007, a transmon CPB has been demonstrated with a longer coherence time [56]. By embedding a transmon device in a 3D cavity, the coherence time has been further extended to 100 μs [60], but this is still orders of magnitude lower than that achievable with semiconductor spin qubits that is in the range of seconds to even minutes [30, 34]. This limit in the coherence time for the heterogeneous devices used in superconducting qubits usually comes from the losses in or at the material interfaces, such as the oxides on the superconductor, insulator and interlayer dielectrics [61].

Both semiconductor and superconductor qubits have their own strengths and weaknesses, largely based on the nature of the material platforms that have been used. Recently, an approach [61] trying to combine the superconducting and semiconducting materials into a single crystalline lattice with no interface has been

proposed, where the strength of both types might be achieved simultaneously. This proposed hybrid quantum device would consist of superconducting wires and Josephson junctions in a single crystalline isotopically enriched ^{28}Si to reduce the coherence loss at the dielectric interface. Qubits with enhanced coherence time and cQED coupling might be expected. In order to fabricate this new hybrid quantum device, a two-dimensionally (2D) confined superconducting semiconductor material with single crystalline properties would be beneficial.

1.2 Superconducting Semiconductors

A semiconductor with superconducting properties was first reported in a heavily boron doped diamond grown by microwave plasma CVD with high temperature and pressure. The highest reported critical temperature of this kind of superconductor is 11.4 K [62]. Superconducting semiconductors have also been demonstrated in other semiconductor material systems, such as GeTe, $SrTiO_3$, In_2O_3, PbTe [63-66], etc. For a semiconductor, the band gap is usually larger than the superconducting energy gap, so that an intrinsic semiconductor is not superconducting [67]. In order to reach superconductivity, doping of impurity atoms in the semiconductor above the metal-insulator-transition (MIT) is required. This is because impurity atoms that substitute into the semiconductor lattice create energy states (donor or acceptor states) located within the band gap. For a degenerately donor-doped semiconductor that has high enough concentration, the electrons remain in the conduction band even at a temperature of 0 K. Those electrons contribute to the electrical conduction and works as unpaired electrons in the normal state of a superconductor [67]. However, such a

high density of dopants usually corresponds to a concentration higher than the equilibrium solid solubility limit. And this non-equilibrium doping causes inhomogeneous material properties such as dopant segregation, cluster formation and polycrystalline materials [68-70].

Non-equilibrium doping techniques have been used to produce doping density above the solid solubility limit. These includes chemical vapor deposition, gas immersion laser doping, high fluence ion implantation with high temperature annealing [68, 71-74], etc. For example, single-crystalline Al and Ga in Ge made by ion implantation and rear-side flash lamp annealing showed superconductivity at 0.15 K and 0.45 K, respectively, with a doping density of 6 at. % [74]. Heavily doped boron (B) in silicon above the solubility limit (1.2 at. %) using gas immersion laser doping has also been demonstrated [71]. A superconducting transition at 0.35 K has been observed, with a doping density of 6.5 at. % (or 3.2×10^{21} cm^{-3}) [71]. The value of T_c is expected to increase as the dopant concentration increases based on a phonon-mediated BCS type mechanism [75]. Since this early work, exploring other dopants with potentially higher T_c has become of great interest, especially for STM lithography based nanodevices. Aluminum (Al) as a dopant in Si is one of the possible candidates. A highly doped Al in Si structure is predicted to have a T_c ten times higher than the case for B under the same doping concentration [75]. However, superconducting Al in Si has not been demonstrated yet, mostly due to the extremely low solid solubility limit of Al in Si (0.04 – 0.06 at. %) and the tendency of segregation at high doping density [76].

Delta doping with low temperature molecular beam epitaxy (MBE) is an alternative method that can be used to fabricate 2D dopant layers with high enough atom density and low thermal budget. With this growth method, sharp dopant profiles with atomically abrupt junctions might be made in Si. Those delta-doped layers have a sharp spike in their dopant profiles that resembles a delta function in the growth direction. Several groups have reported the growth of various delta-doped layers in Si, such as B, P and Sb [77-80]. A dopant density higher than the solubility limit has been demonstrated in Sb delta-doped layers [81, 82] and a density as high as 1×10^{22} cm^{-3} has been reached in MBE-grown B delta layers [83]. Delta-doped 2D systems might also be a precursor for many low-dimensional devices, such as nanowires, SETs, etc.

1.3 Objectives and Project Goals

Given the advantages and limitations of the superconducting-based and semiconducting-based quantum computation systems, the strength of the two might be combined. It may be possible to merge the two approaches and make a single-crystal superconducting device out of a semiconductor. In this case, qubits with extremely long coherence times, good coupling and scalability might be realized.

^{28}Si with sufficiently high refinement nearly eliminates unwanted nuclear spins and provides an excellent environment to host spin qubits. On the other hand, Al delta layers in Si is a new material system that has the potential to have a much higher T_c compared to that for B doping. By combining the two, a nanometer scale spin qubit can be coupled together with a millimeter scale superconducting qubit. Our ultimate

objective is to create a hybrid system where both Si spin qubits and superconductor qubits are coupled in a nuclear spin-free and interface-free material. The focus of this thesis is to attack two materials limitations for realizing a monocrystalline, super-semiconducting hybrid architecture: 1) substantially reducing ^{29}Si that limits coherence of semiconducting spin qubits and 2) exploring supersaturated, Al-doped silicon as a system for localized superconductivity within silicon with a potential Tc > 1K.

There are challenges associated with each of the material systems that we want to pursue. In this work, we will break down those challenges in smaller parts. For isotopically enriched ^{28}Si, one of the difficulties is the material supply. As we briefly described in the previous section, the ^{28}Si materials within this community are of very limited quantity or are not being replenished. A material source that can provide high isotopic enrichment and chemical purity simultaneously, while keeping the growth process simple and flexible is needed. Another difficulty for enriched silicon is the determination of metrics for quantum information, in terms of enrichment, crystallinity, and purity. Unlike classical specifications like electronic-grade and metallurgical-grade Si (EGS and MSG), a quantum metric for "how good is good enough" is still unclear. Achieving superconductivity with Al delta layers in silicon is quite an ambitious goal. Hole-based dopant systems have drawn a lot of attentions recently, as a longer coherence time due to the suppression of hyperfine interaction between the hole and nuclear spins can be achieved [84, 85]. But they are generally not as well studied as electron-based systems. Al delta layer has only been successfully fabricated recently by our group [86]. However, the material properties

of the Al delta-doped layers in silicon are largely unknown, such as Al dopant configuration at various growth temperatures, dopant incorporation and activation in silicon lattice, low temperature electrical conduction, etc.

To overcome the challenges listed above and provide insights on this field for further studies, we have developed the follow specific goals for those two material systems:

Isotopically enriched ^{28}Si:

1. Produce ^{28}Si material with high enrichment (< 1 ppm ^{29}Si) and chemical purity (< 10^{16} cm^{-3}) simultaneously.

2. Demonstrate precise control (< 50 % deviation) of the ^{28}Si enrichment levels in a wide range to support the correlation study of ^{29}Si concentrations and coherence times.

3. Fabricate a ^{28}Si MOSFET as part of an effort to underpin the material standards needed for quantum grade silicon and establish a standard approach for the inter-comparison of these materials.

Al delta layers:

1. Study the 2D configuration of Al on Si(100) and the maximum atom density for one atomic layer.

2. Explore possible improvements in material growth methods for dopant activation and reaching the critical 3D density (2 at.%) for superconductivity.

3. Study the low temperature electrical conduction mechanism of the Al delta layer in Si.

1.4 Outline

- **Chapter 2:** The experimental apparatus and methods used to grow and characterize the ^{28}Si thin film, Al delta layer and natural MBE Si are introduced. This includes the description of the hyperthermal energy ion beam system, the ultra-high vacuum (UHV) preparation and deposition chamber and the *in-situ* characterization STM chamber. The basic principles for ion beam deposition, STM scanning and the Hall measurements used for device characterization are also presented.
- **Chapter 3:** Design and characterization of a new UHV ion source to produce ^{28}Si with improved chemical purity while maintaining the same level of isotopic enrichment. The vacuum has been improved by a factor of ≈ 100, result in an improve in chemical purity from 98.47 % to 99.97%, measured by SIMS. The enrichment capability is preserved, with a ^{28}Si isotope fraction of 99.99987 %.
- **Chapter 4:** Targeted enrichment: the ability to grow isotopically enriched ^{28}Si epitaxial films with precisely controlled enrichment levels over a wide range. A model is developed to predict and control the ^{29}Si concentration and the targeted enrichment is achieved by periodically switching the mass analyzer magnetic field to the appropriate ion species ($^{28}Si^{+}$ and $^{29}Si^{+}$). An accuracy of ≈ 90 % is achieved between the targeted enrichment value and the deposited enrichment value.

- **Chapter 5:** ^{28}Si MOSFET is fabricated and characterized compared to commercial silicon. A maximum mobility of ≈ (1740 ± 2) cm^2/Vs and an electron density of (2.7 × 10^{12} ± 3 × 10^8) cm^{-2} and ≈ (6040 ± 3) cm^2/Vs at an electron density of (1.2 × 10^{12} ± 5 × 10^8) cm^{-2} at T = 1.9 K for devices fabricated on ^{28}Si and ^{nat}Si have been measured, respectively, a result of the short-range scattering (impurity scattering).
- **Chapter 6:** For Al delta layers in Si, the 2D configuration and the maximum 2D density of Al as a dopant on Si(100) surface is studied using STM, SIMS and APT. The result is compared to the theoretical studies from the literature. The maximum density of one atomic layer of Al that can be deposited on Si(100) is found to be most likely 3.4 × 10^{14} cm^{-2}, in accord with the literature prediction. The 3D density of the Al delta layer peak is also found to be 6.2 × 10^{20} cm^{-3} (1.2 at. %).
- **Chapter 7:** A systematic study of the growth methods for Al delta layers in Si and the materials characterization using STM and low temperature magnetotransport measurements are presented. Possible ways to improve 3D dopant confinement and dopant activation are explored. The conduction mechanism of this delta layer at low temperature is also measured using Hall devices and a two-carrier type conduction model is used to explain the observed behavior: carriers from the delta layer dominated at low T and thermally excited carriers dominated at higher T.

- **Chapter 8:** A summary of the technical and scientific results is presented. Future research directions and possible experiments enabled by this work are discussed.

Chapter 2: Experimental Apparatus and Methods

In this chapter, the experimental apparatus and methods for ^{28}Si and Al delta layer materials synthesis will be introduced. Most of the experiments involving the preparation, fabrication and characterization of the materials are conducted in the ultra-high vacuum (UHV) chambers. First, I will introduce the UHV vacuum condition and chamber configuration, which consists of a ^{28}Si ion source deposition chamber, a UHV deposition and analysis chamber, and a scanning tunneling microscopy (STM) chamber. Then I will talk about the sample preparation for both *ex situ* and *in situ* cleaning of Si (100) substrates. Followed by an introduction on the UHV deposition of the hyperthermal ion beam system, the electron beam evaporated natural Si system and the thermal evaporated elemental Al deposition system. Finally, the STM used for materials characterization will also be introduced.

2.1 UHV Chamber Configuration

To achieve high cleanliness for material growth and to suppress various contaminations from the background, all the chambers are designed and built to be UHV compatible. The schematic of the experimental apparatus is shown in Fig. 2.1. The hyperthermal ion beam chamber is located at the left with green dashed lines. Ion source, electromagnetic lenses and apertures are in this chamber. The deposition and analysis chamber is in the middle with blue lines. Sample manipulation and heating stage, natural Si and elemental Al deposition sources, reflection high energy electron

diffraction (RHEED) and Auger spectrometer are in this chamber. A portion of the magnetic transfer rod is shown on the top, which was used to transfer sample from the deposition chamber to the STM chamber. The deposition chamber is also connected to a separate load lock system on the right, where sample loading and unloading take place. The bottom is the STM chamber surrounded by orange lines. The four vacuum chambers (including the load lock) are all maintained at UHV condition and separated by gate valves.

All chambers are kept at UHV conditions. The deposition chamber has two turbopumps (Pfeiffer and Edward Vacuum, with pumping speed of 685 L/s and 300 L/s, respectively), an ion pump and a titanium sublimation pump with a liquid nitrogen cryoshroud. To reach an acceptably low base pressure, a bake out of the chamber is necessary. The procedure includes wrapping the chamber with Al foils and heating up the chamber with heat tapes to above 150 °C for a few days for better thermal conductivity and stability. During the process, water and other impurity gases are slowly desorbed from the chamber interiors and are pumped out. The typical pressure after bake out is about 5×10^{-11} Torr (6.67×10^{-9} Pa). We use a residual gas analyzer (RGA) to monitor the partial pressure of the vacuum components in our chamber. As shown in Fig. 2.2, the partial pressures of the main contributors, such as H_2, H_2O, O_2, CO_2 and N_2 are shown.

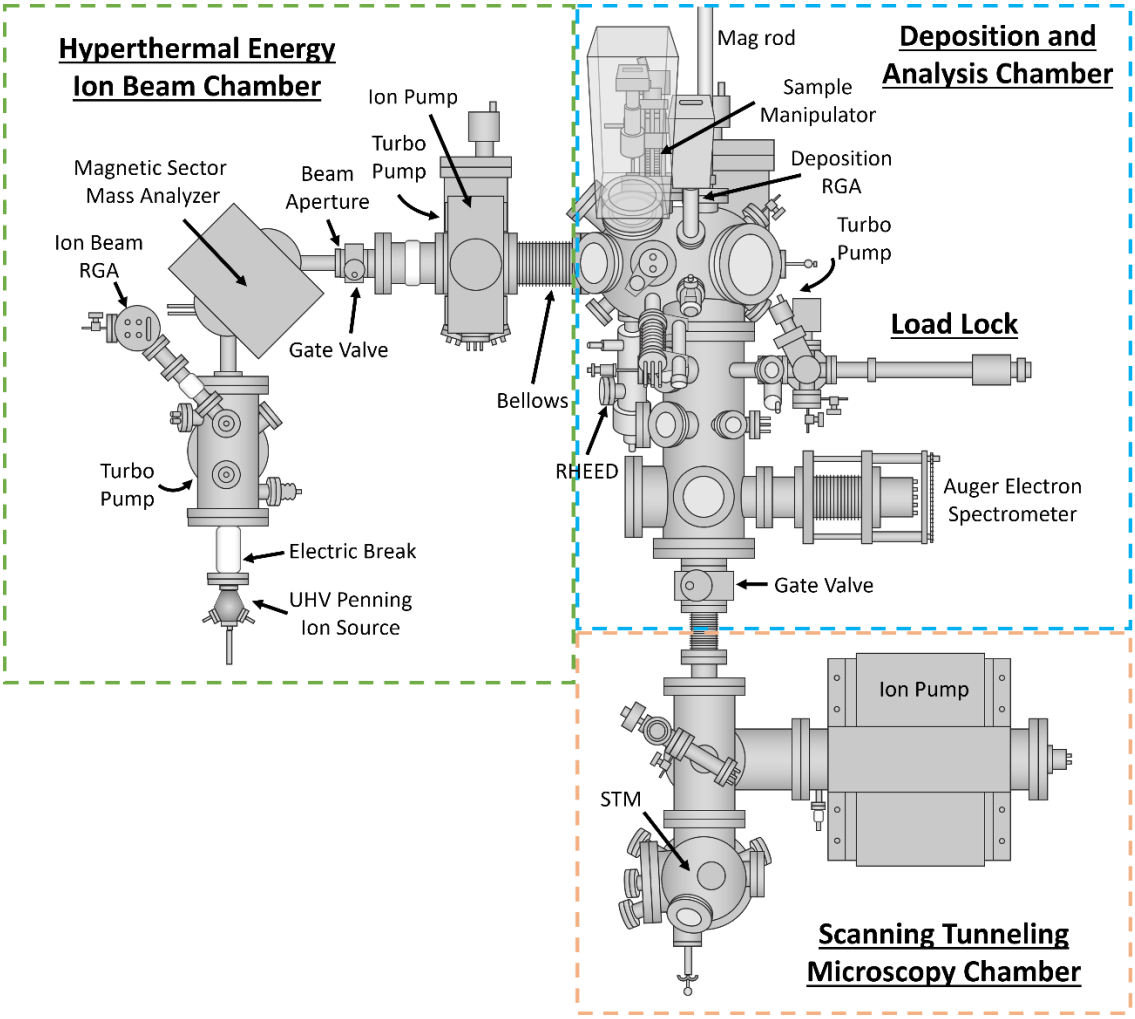

Figure 2.1: Top-down schematic of the experimental apparatus. This includes the ion beam chamber (green), deposition and analysis chamber (blue), STM chamber (orange) and the load lock used for sample loading into the deposition chamber. All four sections of the chambers are separated by UHV compatible gate valves. (Modified from Ref. [87] with permission)

A 5-axis sample manipulator is located in the middle of deposition chamber to position samples, surrounded by the ^{28}Si ion beamline, RHEED, RGA, e-beam evaporator (natural Si) and quartz crystal microbalance (QCM). This allows quick access for multiple processes, such as substrate preparation, material growth and *in situ* characterizations.

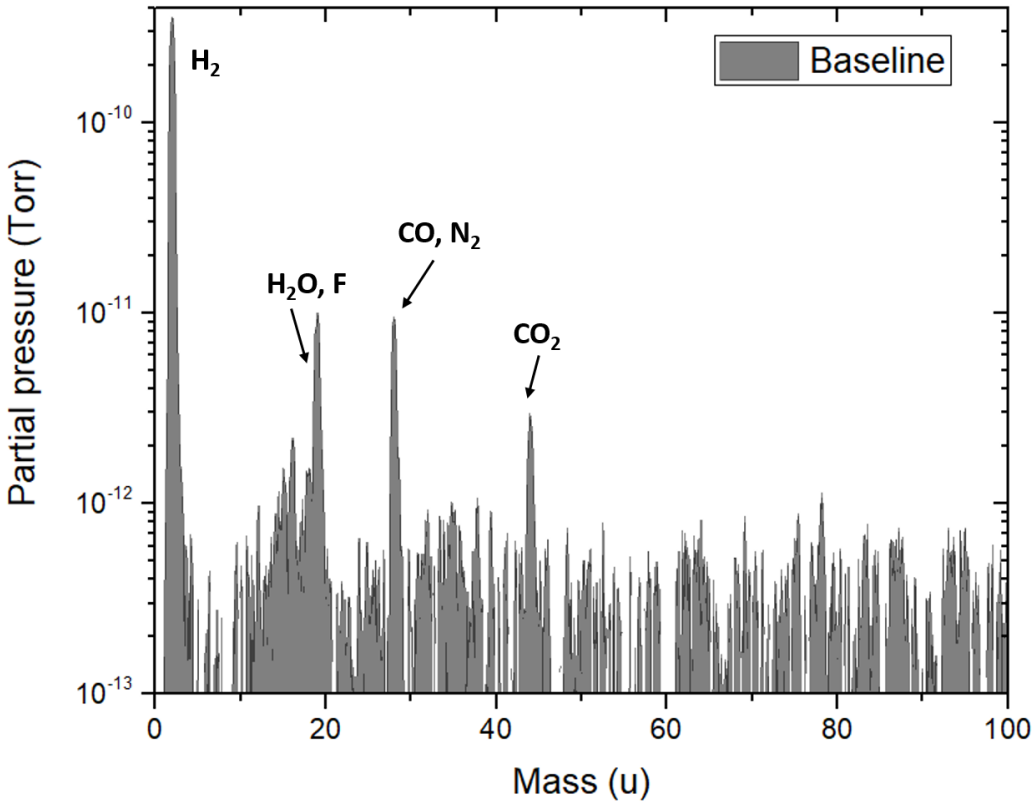

Figure 2.2: RGA spectrum of the deposition chamber baseline.
The pressure is at pressure 6×10^{-11} Torr. The partial pressure peaks of the typical components: H_2, H_2O, O_2, CO_2 and N_2 can be seen.

2.2 Sample Preparation

2.2.1 *Ex situ* Preparation

To prepare a clean substrate for further deposition and fabrication with low contamination and high crystallinity, we divide our sample preparation into two steps: *ex situ* and *in situ*. *Ex situ* preparation is introduced to the sample before entering the vacuum chamber. In this work, most of the samples used are intrinsic float-zone refined Si(100) wafers with resistivity > 10 kΩcm. The wafer is first spin coated with

S1813 photo-resist to protect the surface from scratches and diced into pieces (chips) with dimensions 4 mm × 10 mm. Then the chips are taken into the cleanroom and cleaned with complementary-metal-oxide semiconductor (CMOS) procedures. This is to remove the organic and metal contaminations from the surface. The cleaning recipe is as followed:

1. Remove photo-resist in PG remover 80 °C, 20 mins
2. Isopropanol (IPA) 1 min, RT; rinse with DI water
3. Downstream asher or RIE photo-resist Descum 60 s
4. 50:1 H_2O:HF dip, 10s; DI rinse
5. SC-1 clean 10:1:1 H_2O:NH_4OH:H_2O_2 at 80 °C, 12 mins; DI rinse
6. Piranha clean 3:1 H_2SO_4:H_2O 12 mins; DI rinse
7. 50:1 H_2O:HF dip, 10s; DI rinse
8. SC-2 clean 5:1:1 H_2O:HCl:H_2O_2 at 80 °C, 12 mins; DI rinse
9. Blow dry with N_2

The sample is then loaded into the load lock chamber within 1 hour to reduce surface contamination. Note that during the transfer, the sample will have a thin chemical oxide layer with a few nm grown naturally on the surface. This will act as a protecting layer and will be thermally removed during *in situ* preparation.

2.2.2 *In situ* Preparation

Once the samples are loaded into the vacuum chamber, two methods of heating are performed for *in situ* cleaning of the substrate. One method is called “RH”, which consists of a back heater utilizing the radiative heating from a tungsten wire, typically

444 with current and voltage < 10A and 15V, respectively. Another method is called
445 “DH”, or Joule heating, which uses resistive heating by passing current through the
446 sample. Fig. 2.3 shows a glowing Si substrate at 1000 °C, the sample stage and the
447 wiring diagram of the RH and DH. RH is located at the back of the sample and a
448 finger is connecting from DH^+ through the sample to DH^-. Usually for intrinsic
449 silicon samples, since the resistance is too high at room temperature, RH is needed to
450 pre-heat the sample to about 300 °C to reduce the resistance and thus allow
451 conduction through DH. The loaded sample will first be heated with both RH and DH
452 to a temperature of about 600 °C. This is process is called “degas”, which slowly
453 removes water molecules sticking to the sample surface. After degassing, the sample
454 will be flash annealed using DH from 600 °C to 1200 °C in a few seconds. This
455 process will be repeated for 5-6 times, each with a duration of 10 s at 1200 °C. This is
456 to remove the thin native oxide layer of SiO_2 grown on the surface by a sublimation
457 process at high temperature, without the formation of SiC and step bunching at the
458 surface [88, 89]. Each heating cycle is kept short so as to prevent outgassing of the
459 manipulator parts. After flash anneal process, the substrate will be cooled down
460 rapidly to 600 °C and then ramped down to RT, with a rate of 1 °C/s. The sample
461 substrate is then either examined using RHEED or transferred to the STM chamber
462 for surface characterization. Typically, a flat, clean surface of Si (100) with (2 × 1)
463 reconstructed dimer rows and adjacent Si terraces perpendicular to each other

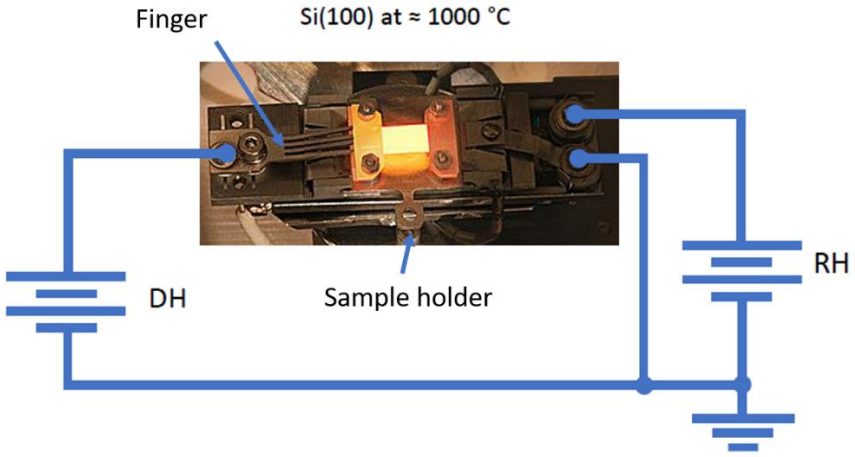

Figure 2.3: Sample stage on the manipulator and the wiring diagram. The glowing Si (100) substrate is heated to 1000 °C by running current through the sample using DH. Typical current and voltage for flash anneal is ≈ 10 A and 5 V, respectively. (Modified from Ref. [87] with permission)

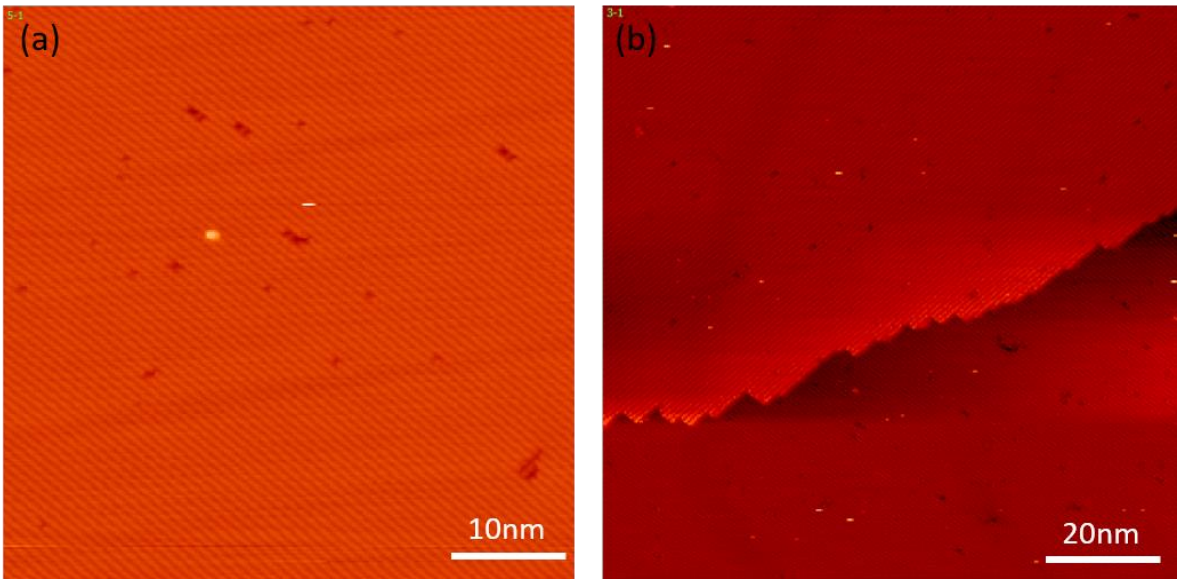

Figure 2.4: STM images of a Si (100) substrate after 1200 °C flash anneal. (a) 2 × 1 reconstructed dimer rows are clearly observed. (b) A larger scale image: Si dimer rows and terraces perpendicular to each other can be seen. Images are acquired with a tip bias of -2 V and a current setpoint of 110 pA. Some dark spots are also visible in this image, those are the vacancy defects or missing Si atoms on the surface.

can be seen, as shown in Fig. 2.3. Some dark spots are also visible in Fig. 2.4, which are most likely vacancy defects or missing Si atoms on the surface.

Since we need to rapidly change and accurately control the temperature of our sample for both sample preparation, deposition and post-anneal processes, an accurate way for temperature measurement is very important. In this work, we use a Process Sensor pyrometer with temperature range 300 °C to 1300 °C and spectral range of 1.45 to 1.8 μm to measure temperatures. The temperature reading of the pyrometer depends on the emissivity e and it changes rapidly according to the temperature. For example, e changes from < 0.1 to > 0.7 when T changes from 100 °C to above 1000 °C, respectively [90, 91]. Although the emissivity values are well studied, and reported in the literature, deviations due to difference in experimental equipment can be introduced to the "true" emissivity values, such as the aging and covering of the deposition materials on the view window. People use both Au-Si and Al-Si eutectic samples to calibrate the emissivity. A eutectic is a homogenous mixture of two materials that has a lower melting point than any of the constituents. The eutectic temperature for Al-Si is about 577 °C [92] and for Au-Si is about 363 °C [93]. The Au-Si eutectic is produced by an Au wire on the edge of Si substrate and the Al-Si eutectic is produced by depositing 500 nm of Al onto the center of a Si substrate. As we increase the current from DH across the sample, the substrate temperature increases until a phase transition is visible at the eutectic point. After stabilizing at the eutectic point, the pyrometer emissivity is adjusted so that it matches the eutectic temperatures of the alloy. 3 calibrated emissivity has been obtained with different

temperature range: e ≈ 0.25 with T < 475 °C; e ≈ 0.42 with T < 625 °C and e ≈ 0.68 with T > 800 °C, which is very close to the values reported in the literature [94].

2.3 UHV Deposition Systems

2.3.1 Hyperthermal Ion Beamline

This section relies heavily on the previous works done within our group, mainly contributed from my NIST supervisor Dr. Josh Pomeroy and his previous group member Dr. Kevin Dwyer. During my PhD, I was responsible for the modifications and upgrades of the beamline, such as the new UHV ion source, ion beam sweeper, new gas system, etc. Those changes will be introduced in section 3. Here I will present the important features of this ion beamline in terms of basic functioning and characterization.

2.3.1.1 Experimental Setup

The hyperthermal ion beamline system consists of four main parts: the gas manifold, the ion source, the transport system and the magnetic sector mass analyzer. In the initial setup, the ion source is a traditional Penning-type ion source, also known as Penning Ionization Gauge (PIG), built by a partnership of Physicon Corporation and Dr. Barbara Cooper. The transport system (including electromagnetic lenses) and magnetic sector mass analyzer are a result of creative partnership between Cornell University and Dr. Pomeroy's group. The basic principle of this type of gas discharge was firstly demonstrated by Phillips [95]. Later on, Baumann and Bethge have

extensively studied and optimized the PIG ion source, which included the dependence of ion current on gas flow, magnetic field and anode/cathode voltages [96-99]. The schematic of the ion beamline system is shown in Fig. 2.5. The insert shows the design of this gas mode Penning ion source with gas inlet, source magnet, anode, cathode and extraction cusp. During operation, a plasma is generated between the cathode and anode of the PIG ion source with a radially confined magnetic field. The anode is typically at 50 V and the cathode varies from -1 kV to -3.5 kV. The plasma ionizes and breaks down the working gas molecules (mostly SiH_4 in this work) to mostly singly charged ions [87]. Those ions are then extracted by a high voltage extraction cusp, accelerated by a transport voltage of about -4 kV and focused by an Einzel lens onto the focal point of the mass analyzer. This transport voltage is applied to the whole ion beam chamber with other voltage components floating on top of it. The purpose of this high voltage transport is to suppress the effect from space charge (continuum of electrical charges distributed over a three-dimensional region) [100] repulsion of the positively charged ions.

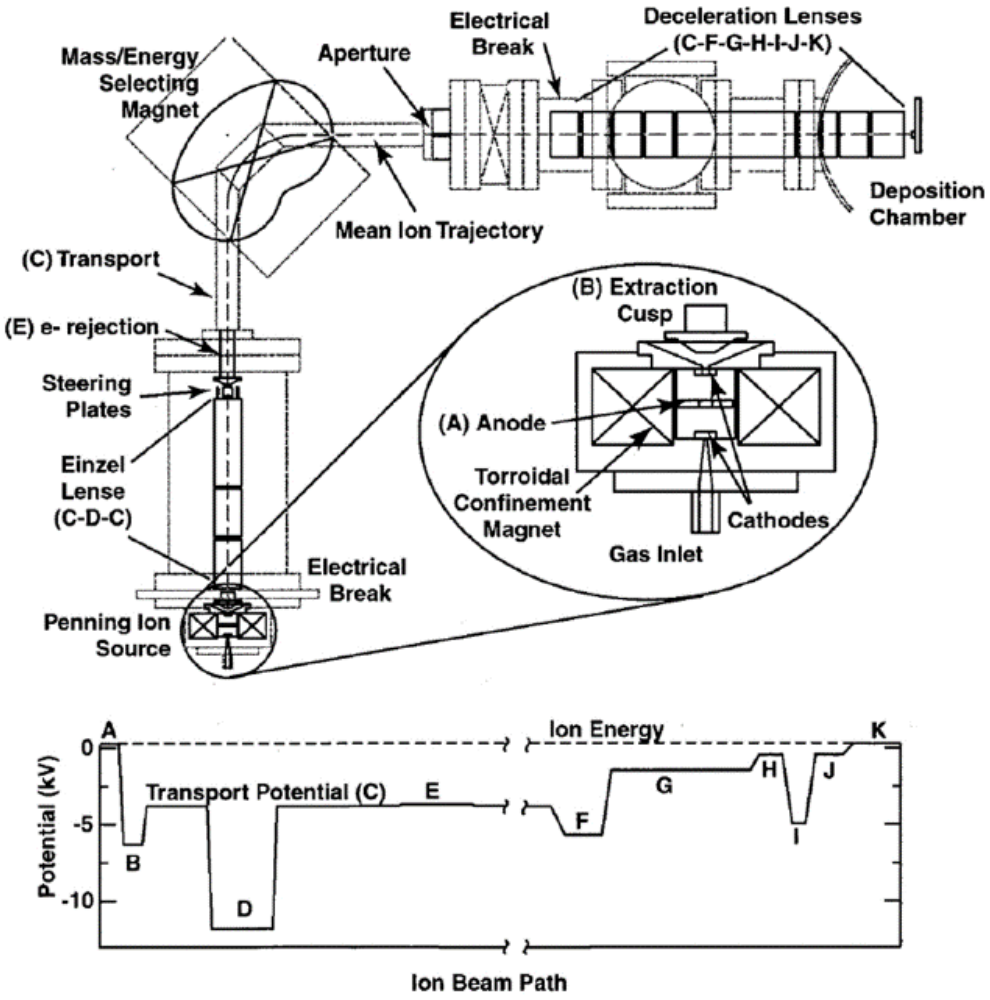

544

545 Figure 2.5: Hyperthermal ion beamline schematics.
546 The details of the gas mode Penning ion source including the gas inlet, source
547 magnet, anode, cathode and extraction cusp are shown in the inset. A potential
548 landscape is shown from anode (A) all the way to the end of deceleration lenses (K)
549 in the bottom figure. Ions from the ion source are first accelerated to the transport
550 voltage (-4 keV) and then decelerated back to ≈ 40 eV before hitting the target sample
551 at ground potential in the deposition chamber. (Taken from Ref. [101] with
552 permission of the Journal)
553

554 After being focused and accelerated, positively charged ions are transported into a
555 magnetic sector mass analyzer (bending magnet). Due to the Lorentz force, ions of
556 the same kinetic energy but with different mass-to-charge ratio will have different
557 trajectories at the exit location where an aperture is tuned at a particular value of m/Z

(where Z is the ionic charge in units of the proton charge e). In the case of ^{28}Si, the mass-to-charge ratio is tuned to be 28 amu/e and all other ions like $^{29}Si^{+}$ and $^{30}Si^{+}$ will be blocked by the aperture. The mass resolution of the current aperture is changing as a function of mass in units of amu, and the value of $m/\Delta m$ at 28 amu is ≈ 74 [101]. At the bottom of Fig. 2.5, the potential changes of the ions in the ion beam as they pass through each component (with label A to K) is shown. After passing through the aperture, the ions will pass through a series of deceleration lenses (labeled F to K) that refocus and decelerate them to a desired energy before reaching the final stage in the deposition chamber.

The operation procedures of the hyperthermal ion beam deposition of ^{28}Si are described below:

1. Inject working gas (SiH_4 in this work) from the gas line into the ion source using a high precision leak valve.
2. Turn on and set the voltages for anode and cathode. For SiH_4 operation, a typical anode voltage is ≈ 50 V and cathode voltage is in the range of ≈ -1.5 kV to -3.2 kV.
3. Set the voltage V_T for transport to be -4 kV.
4. Turn on voltages V_E and V_F for extraction cusp and focus, those are floating on top of the transport.
5. Turn on the ion source magnet to ignite a plasma in the ion source.
6. Set the magnetic sector mass analyzer to the target ion mass (28 amu).
7. Turn on the deceleration lenses A2, B1-B4 and X. Collect and monitor the ion current at the deposition position using an aperture.

8. Starting from the anode voltage, fine tuning the voltages along the beamline all the way to the final lens to maximize the ion current detected at the deposition location.

9. Prepare sample to target temperature and open gate valve to start deposition.

2.3.1.2 Ion Beam Characterization

Here we introduce the methods to characterize the ion beam for isotopically enriched ^{28}Si deposition. The first important aspect is the ion beam mass spectrum collected from the magnetic sector mass analyzer. The ion current is measured using a home-made aperture located at the deposition position with a picoammeter (with a typical background noise of 10 pA) while sweeping the magnetic field of the mass analyzer, which corresponds to sweeping the mass/charge ratio, m/Z of the ions. Measuring and analyzing the mass spectrum of the ion beam is a critical step for both assessing the mass separation of the ion species, which limits the enrichment level of ^{28}Si, and detecting the contamination levels in the ion source, such as gas molecules contributed from background C, O and N. The mass spectra for SiH_4 gas and other background gas species are shown in Fig. 2.6. Panel (a) shows an example of the mass spectrum using SiH_4 gas during ^{28}Si deposition. The y-axis is the ion current in log scale collected at the sample location, the x-axis is the magnetic current of the mass analyzer, which also corresponds to the mass of the ions. Ion current peaks are marked according to the ion species, such as the $^{28}Si^+$ and various Si hydride ions due to incomplete cracking of the SiH_4 molecules. For example, the ions at 28 amu are from $^{28}Si^+$, the ions at 29 amu consists of both $^{29}Si^+$ and $^{28}SiH^+$, and the ions at 30 amu are from a combination of $^{30}Si^+$, $^{29}SiH^+$ and $^{28}SiH_2^+$, etc. Those ion species are

distinguishable with a higher mass separation, for example, during the SIMS measurement of the isotope fractions [102]. The typical ion current obtained for $^{28}Si^{+}$ is a few hundred nA, which is about 10% of the total current of SiH_4. To obtain the mass separation ability of the system, a phenomenological Gaussian fit of the following form is used to fit the spectrum:

$$I = I_0 + \frac{B}{\sigma\sqrt{2\pi}} \exp\left(-\frac{1}{2}\left(\frac{m-m_c}{\sigma}\right)^2\right) \quad (2.1)$$

where I is the ion current measured, I_0 is the current offset from the background noise, B is the area of the Gaussian, m is the mass, m_c is the center of the mass peak and σ is the standard deviation of the fit. The factors that affect the mass resolution include the width of the aperture, energy spread of the ion beam, angular distribution due to lensing effects, etc... The fluctuation of the current from the detector is < 100 pA. As shown in panel (a), the Gaussian peak fits well with the collected data with symmetrical shape, indicating that the beam is experiencing very small perturbation from scattering effects, which usually can be seen with the presence of a non-symmetrical shoulder peak that is ≈ 10 % of the primary peak height. From the fitting, the separation between 28 amu and 29 amu peak centers is about 11 σ, which corresponds to a lower bound on the ^{29}Si concentration of about 10^{-26} isotope fraction in the ^{28}Si film, assuming negligible gas scattering and side wall scattering [103]. In some occasions, there might be a small shoulder peak observed in addition to the main peaks. This is likely due to non-ideal beam tuning, resulting from the ion scattering off the mass analyzer aperture.

Ion beam mass spectra of the possible background contaminations that are presented in the ion beam along with the SiH_4 gas are also shown. Panel (b) shows a

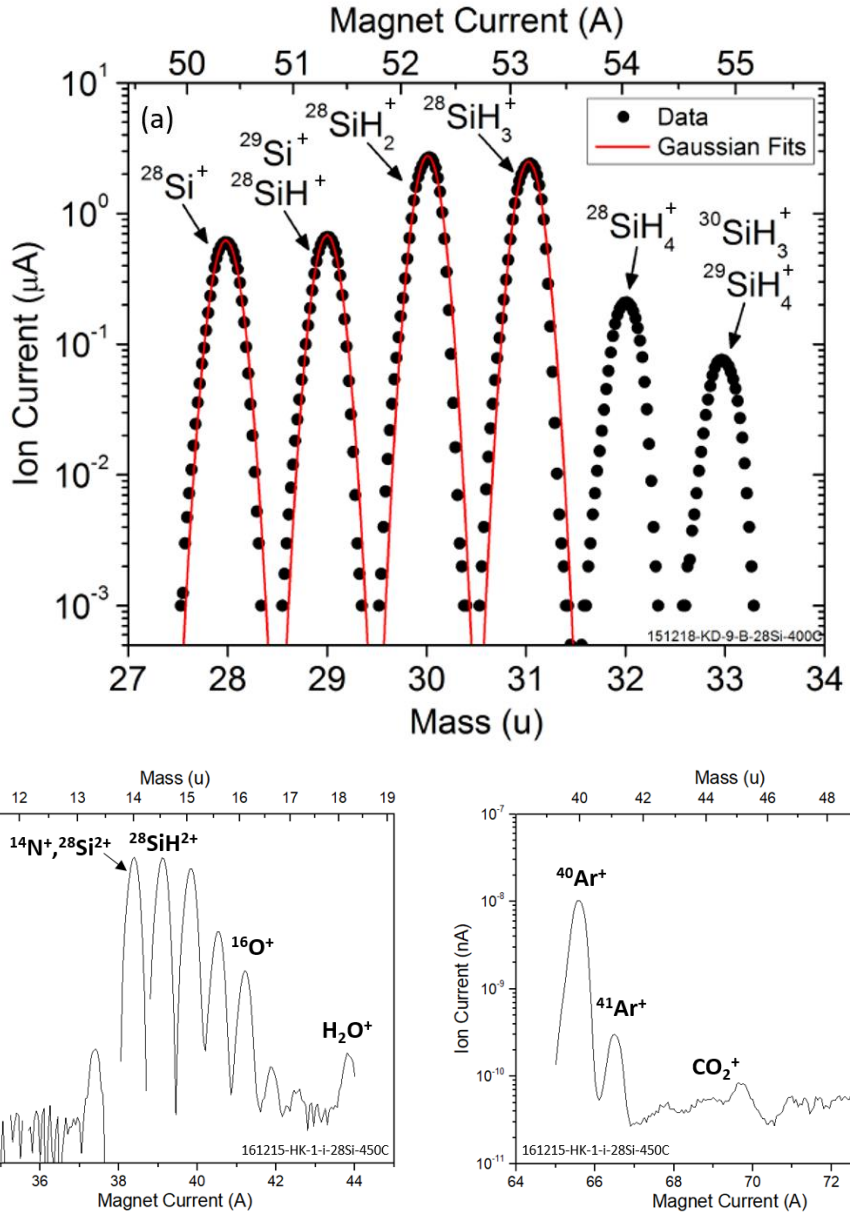

Figure 2.6: Ion beam mass spectra of working gas SiH_4.
Panel (a) shows the ion current collected at the sample deposition location using a 4.9 mm^2 aperture. ^{28}Si ions and Si hydride ions can be seen from 28 amu to 33 amu. Gaussian fits using equation (2.1) are presented as red solid lines, showing a good fit. Panel (b) and (c) are taken using the new UHV ion source. They show the related background gas contaminations and doubly charged Si hydride ions ranging from 12 amu to 50 amu. Possible contaminants include: CO_2, N, O and H_2O. Ar is present in the ion beam since we are using Ar gas as a dilution gas and some residual gas may be remained in the gasline. (Panel (a) is modified from Ref. [87] with permission)

spectrum in the range of 11 amu to 20 amu. Possible candidates for those peaks are: $^{12}C^+$ (12 amu), $^{14}N^+$ (14 amu), $^{16}O^+$ (16 amu) and H_2O^+ (18 amu). The presence of ^{12}C, ^{14}N and ^{16}O can be a source of chemical impurities in the ^{28}Si film since they can pass through the mass-selective aperture in the form of CO^+ and N_2^+ (28 amu). Contributions from the doubly charged silane molecules and Si ions are also possible, such as $^{28}Si^{2+}$ (14 amu),$^{28}SiH^{2+}$ (14.5 amu), $^{28}SiH_2^{2+}$ (15 amu), etc. Panel (c) shows the possible contributions from higher mass peaks, such as $^{40}Ar^+$ (40 amu) and CO_2^+ (44 amu).

Another important aspect of the ion beam characterization is the energy. The energy distribution of the ion beams can be measured by a "roll off" curve (Fig. 2.7) by reverse biasing the aperture in front of the current collector. As the aperture voltage is increased, the current initially decreases as a power law, approximately linearly, corresponding to an increasing collection of secondary electrons produced by ions colliding on the metal surfaces. As the bias voltage exceeds the energy of the slower ions, those ions are repelled and result in a further, sharper decrease in current until only secondary electrons are being collected, producing a negative current at high bias voltages [101]. The total current as a function of bias voltage can be modelled as:

$$I(V) = I_0 - I_b \mathrm{erf}\left(\frac{V-E_b}{\sqrt{2}\sigma_b}\right) - I_e V^{\gamma} \qquad (2.2)$$

where I_0 is the zero bias current, the second term is the integrated Gaussian of the total ion beam current with E_b the mean ion energy, the third term is a phenomenological power law accounting for the increase in secondary electron current [104]. An example of the energy distribution curve is shown in Fig. 2.7.

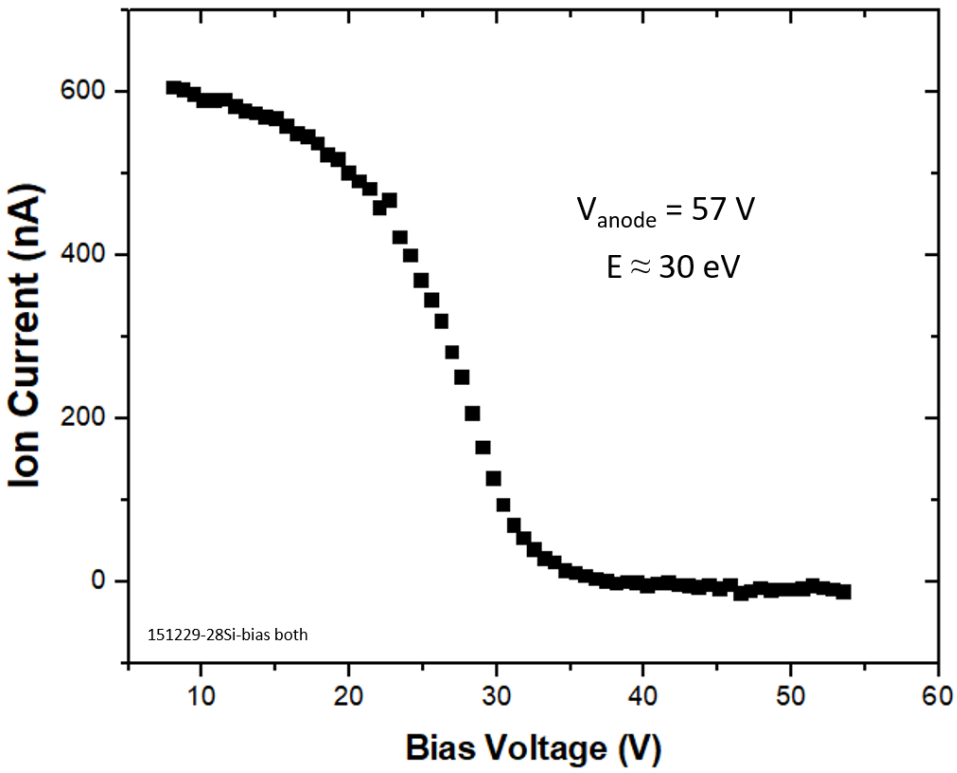

Figure 2.7: Beam energy roll off curve for $^{28}Si^{+}$.
As the bias voltage increases, the ion current first decreases linearly as the positively charged are repelled. At the bias voltage, the ion current decreases more rapidly until a negative current is reached. The anode voltage is set at 57V, the extracted mean ion energy is about 30 eV.

The spatial distribution of the beam spot of our ^{28}Si deposition is measured by using the same aperture for collecting the ion current while scanning in two dimensions. The aperture hole is about 3mm in diameter and it is attached to a collector plate behind it. As a result, ion current passing through the aperture can be collected and used to estimate the flux of the ion beam. Fig.2.8 is an example of the collected 2D map of the ion current using Ar gas [87]. The typical maximum current at the center is about 550 nA, where the adjacent contour line represents a 10 % drop in the measured ion current respect to the center. The spatial distribution is 4 mm in

z-direction and 8 mm in y-direction. However, the size of the actual ion beam with relatively large thickness (since the current density at the edges are too small) is smaller, usually ≈ 4π mm^2. A beam spot with similar size is used for ^{28}Si deposition.

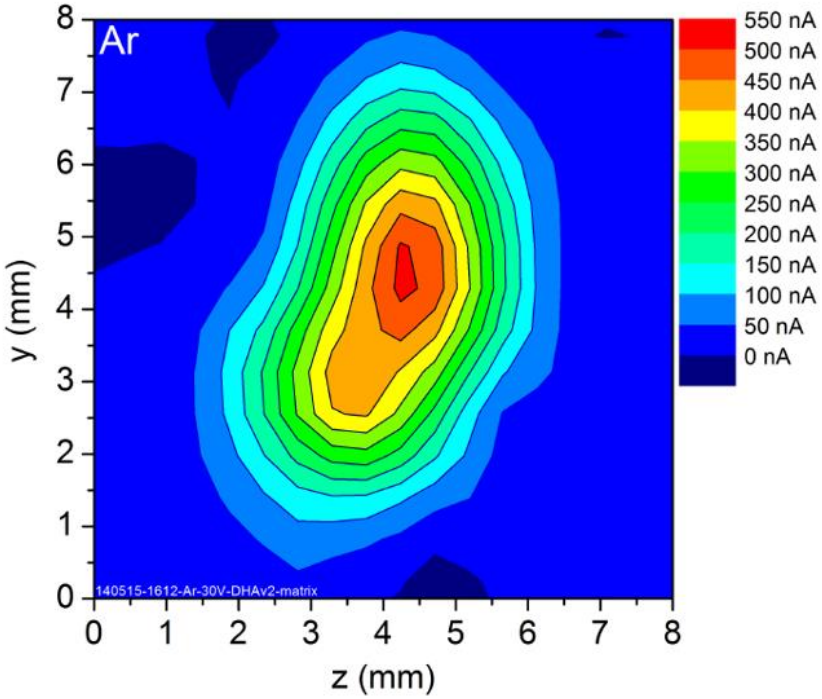

Figure 2.8: 2D mapping of the ion beam spot with Ar.
The detector aperture is moving in y and z direction during the scan. The center maximum current is about 550 nA, with 10% drop to the adjacent contour lines. The real beam spot size with relatively large thickness is estimated to be about 4π mm^2. (Taken from Ref. [87] with permission)

2.3.2 Electron Beam Evaporation of Natural Si

The natural Si deposition source is located at the bottom of the UHV deposition chamber. It is an electron beam evaporator from Thermionics Lab, Inc. The schematic of the design of this electron gun is shown in Fig. 2.9. Panel (a) is the CAD drawing of the electron gun from Thermionics, where the source material is put in the middle

of a copper pocket. One advantage of this design compared to the previously used Si source is that the electrons from the filament are generated at the side of the pocket and re-focused onto the source material by a magnetic field. This prevents the source material and evaporated flux to be exposed from the filament, both reducing the source of contamination to the deposited samples and increasing the lifetime of the filament. Cooling water lines are used to prevent the overheating of the electron gun, with a typical water flow of 1.0 GPM at a source power < 3000W. Panel (b) shows the assembly of the system on the deposition chamber, where the e-gun is at the bottom of the housing. A liquid nitrogen cryoshroud is located on top of the e-gun with a hole aligned to the source center. A float zone (FZ) refined, intrinsic silicon source with volume of 1 cm^3 is used in this work, the chemical purity of this Si is 99.999%.

A QCM is mounted on top of the deposition chamber with a linear translator so that it can be moved to the same deposition location as the substrate. The deposition rate varies depending on the power that we put into the e-gun. Fig. 2.10 shows the deposition rate measured at the deposition location as a function of source power, which is approximately 30 cm away from the Si source. Note that this rate is measured with newly loaded source material, a gradual decrease in deposition rate is expected as the Si source is consumed after hours of deposition. The typical pressure during deposition is about 1×10^{-9} Torr (1.35×10^{-7} Pa).

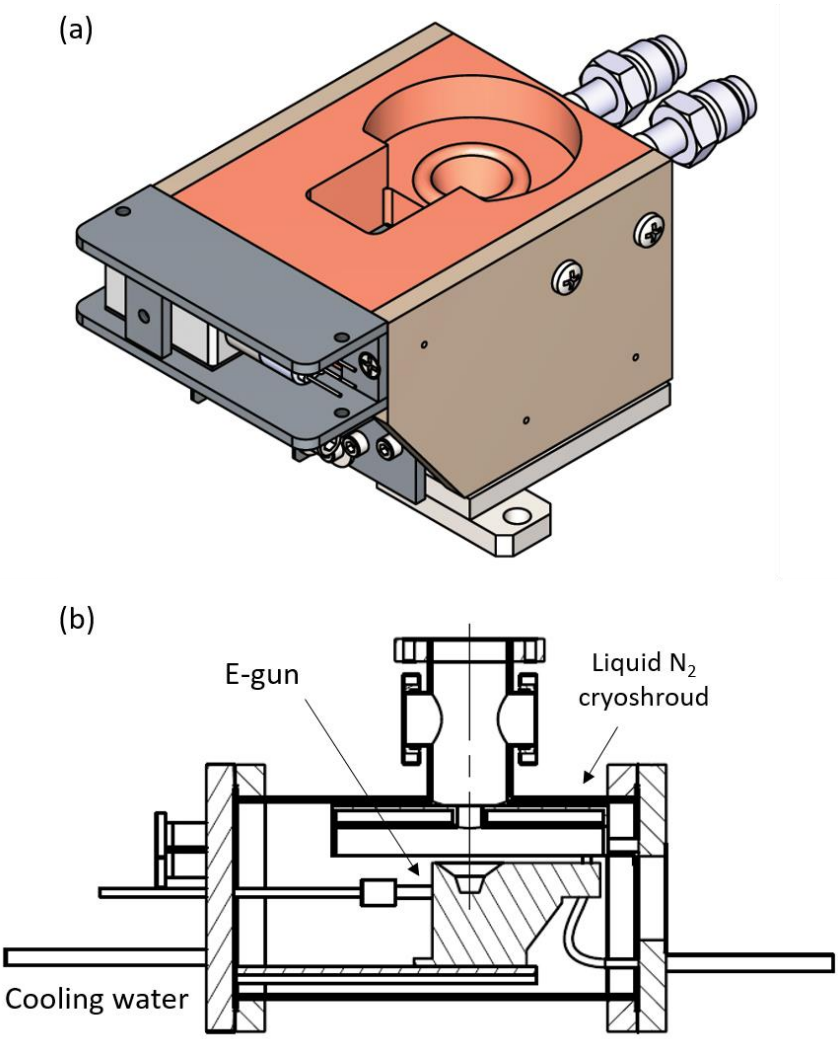

Figure 2 9: The schematics of the Si e-gun.
(a) the electron beam evaporation source, with copper pocket for source material. The filament is located at the side of this e-gun so that the evaporated flux will not be in contact with the filament. This will increase both the lifetime of the filament and the chemical purity of the deposited film. (b) a side view assembly of the electron gun with cryoshroud. The e-gun system is located at the bottom of the deposition chamber (see Fig. 2.1), where the manipulator can rotate the sample to allow normal incidence of the evaporated flux. (Panel a is taken from Thermionics).

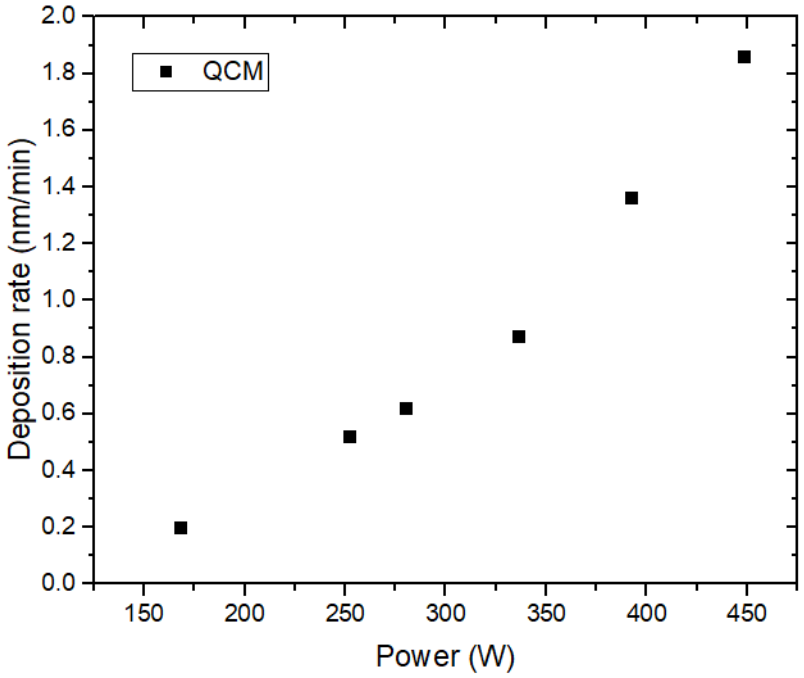

Figure 2.10: E-gun Si deposition rate vs power, measured by QCM.
The deposition rate is controlled by the power of the Si source. Note that this rate is measured with newly loaded source material, a gradual decrease in deposition rate is expected as the Si is consumed after hours of deposition.

2.3.3 Thermal Evaporation of Al

The Al delta layers are deposited using a thermal evaporation furnace similar to a Knudson cell in UHV deposition chamber. It is a commercial Radak furnace from Luxel. The Al source is located at the end of the deposition chamber near the STM, which has a shutter controlled by a pneumatic valve. Ultra-high purity Al pellets (99.999%) are used as source materials and are loaded in a pyrolytic boron nitride (PBN) liner. The liner is then mounted inside an alumina crucible, with a thermocouple at the bottom, as shown in Fig. 2.11. Since the liner and the crucible are made of two different materials, the difference in thermal expansion coefficient may

cause the cracking of the crucible during cool down where Al will contract more strongly than the PBN liner, putting it in a mixture of tensile and shear stress. To prevent this from happening, we have to be extra cautious during the cool down process, usually with less than 0.5 °C/s around the melting point. We normally keep the Al furnace at a temperature (≈ 770 °C) above the melting point of the Al (660 °C) while maintaining a low rate of evaporation to ensure longer lifetime.

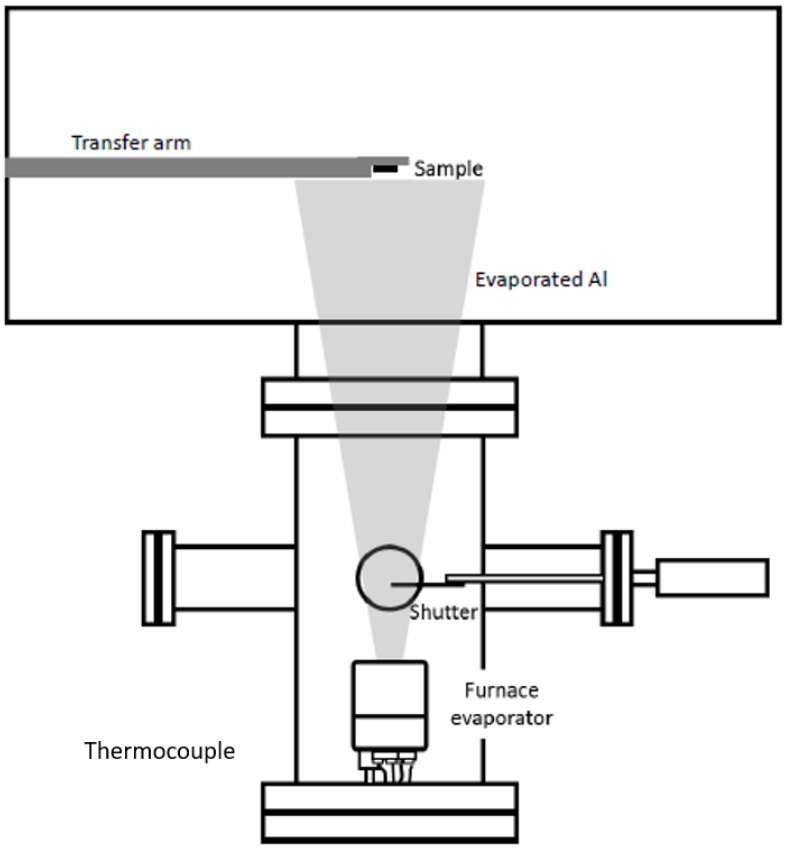

Figure 2.11: A schematic of the thermal evaporation source of Al.
The furnace is located at the bottom of the deposition chamber (as shown in Fig. 2.1) near the STM. A shutter is installed with a pneumatic valve control. A transfer arm (mag rod) is used to move samples to target location for Al deposition and to STM chamber for characterization. (Modified from Ref. [76] with permission)

2.4 Scanning Tunneling Microscope (STM)

The samples grown from the ion beamline and deposition chamber can be transferred to the STM chamber for *in situ* characterization. This prevents contamination to the surface during transport out of vacuum and provide flexibility for surface inspection during the deposition and annealing steps. STM is a non-destructive tool for imaging surfaces at the atomic level. It can be used to distinguish features smaller than 0.1 nm with a 0.01 nm depth resolution [105]. The STM is based on quantum tunneling and piezoelectric effect, where the first allows us to image the surface and the second allows us to control the tip position with angstrom-level precision. As shown in Fig. 2.12, a typical setup includes a sharp metallic tip that is brought within several angstroms to the sample surface using a piezoelectric tube with electrodes. This 3D piezoelectric tube rasters the tip position in the lateral x and y directions and the axial z direction is controlled by a feedback loop which compares the tunneling current with the set value. When voltage is applied between the tip and the sample, electrons can tunnel through and the current can be calculated using the time-dependent perturbation theory. The tunneling current I_T is exponentially dependent to the distance between the tip and the sample d. It can be expressed as [106]:

$$I_T \propto \int_{-\infty}^{\infty} \rho_t(E - eV_T)\rho_s(E)(f_t(E - eV_T) - f_s(E))\,|M(E - eV_T, E)|^2 dE \qquad (2.3)$$

where ρ_t and ρ_s are the density of state of the tip and sample, respectively, $f(E)$ is the Fermi-Dirac distribution for the electrons and $|M|^2$ is the tunneling matrix element,

781 which is a function of the bias voltage V_T, electron mass and wavefunctions of the

782 tunneling electron before and after tunneling.

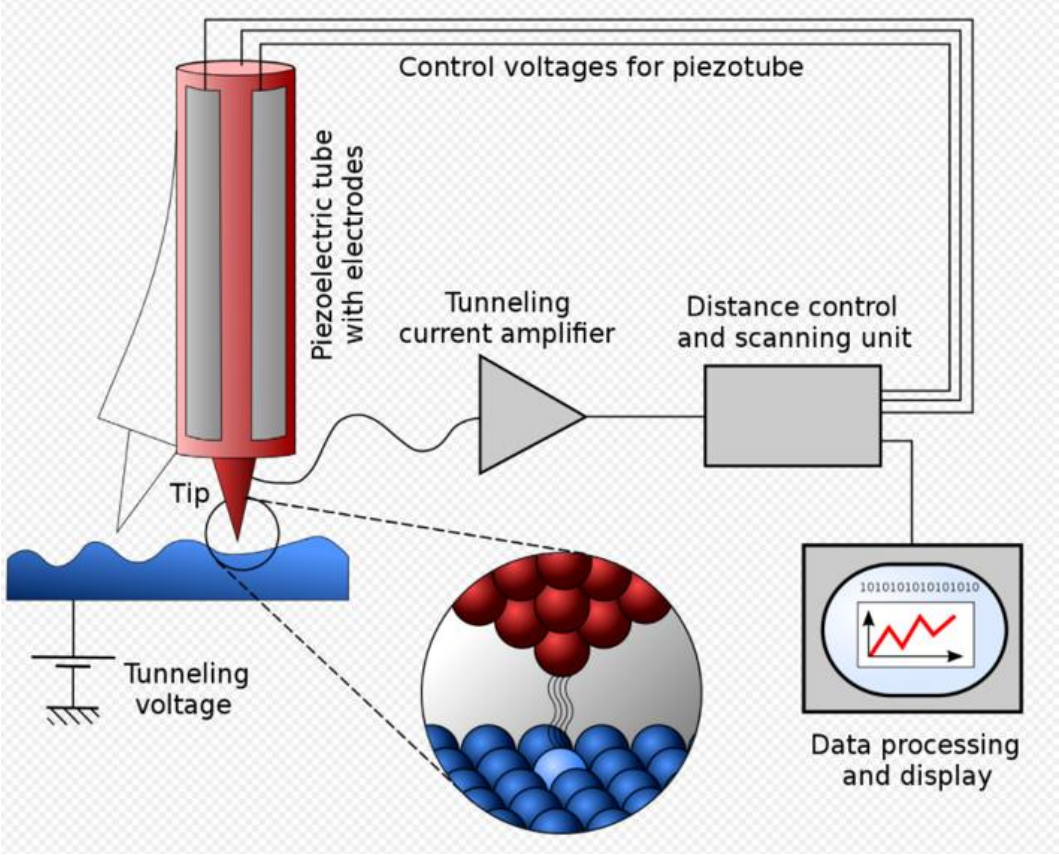

783

784 Figure 2.12: A schematic drawing of a STM.
785 When the tip is brought within a few nm to the surface with a bias voltage applied
786 between the two, electrons can tunnel from the apex of the tip to the sample, or vice
787 versa. A constant current mode is used in this work. The tunneling current is
788 maintained at the setpoint by a 3D piezoelectric feedback loop, which provides the
789 topography of the sample surface. (Taken from Ref. [107])
790

791 In this work, STM is frequently used to determine the surface quality of the

792 sample between each processing steps. For example, after substrate flashing,

793 isotopically enriched ^{28}Si and natural abundance Si deposition, Al delta layer

794 deposition and thermal annealing. It is also used to estimate the 2D areal density of Al

795 being deposited on the substrate, as will be discussed in Chapter 6. For a Si substrate,

796 the typical scanning parameters are -2 V, 100 pA with a pixel resolution of 300 × 300.

For deposited Si epitaxial thin films and Al delta layers, positive tip bias of +2 V, 100 pA are used. From time to time, the tip becomes “dirty”, meaning that contaminant molecules accumulate on the tip end, resulting in a degradation in image quality. When this happens, the tip either needs to be replaced or re-conditioned using a tip preparation tool. The tip preparation tool is located at the bottom of the deposition and analysis chamber near the load lock (see Fig. 2.1). A thoriated tungsten filament is used to emit electrons (emission current < 3 mA). The tip is moved to a short distance (1 mm or less) right opposite the filament and is biased up to 1 kV. In this high electric field, the emitted electrons are accelerated and bombard the apex of the tip. This will clean the deposits from the tip and extend the lifetime of that tip for STM imaging.

2.4 Hall Devices and Measurements

Hall bar devices have been made on the Al delta layer samples in order to characterize the electrical properties (carrier type, density and mobility) of this heterostructure at low temperature. Fig. 2.13 shows a microscope image of a Hall bar and a Van der Pauw devices after fabrication. The device was fabricated on top of a Si-Al-Si heterostructure with ≈ 50nm Si capping layer. This mesa-etched Hall bar device was patterned using photolithography and RIE etching. The dimension of one Hall bar is 50 μm × 1000 μm. The bright yellow pads are the Al contact pads for wire bonds and electrical conduction.

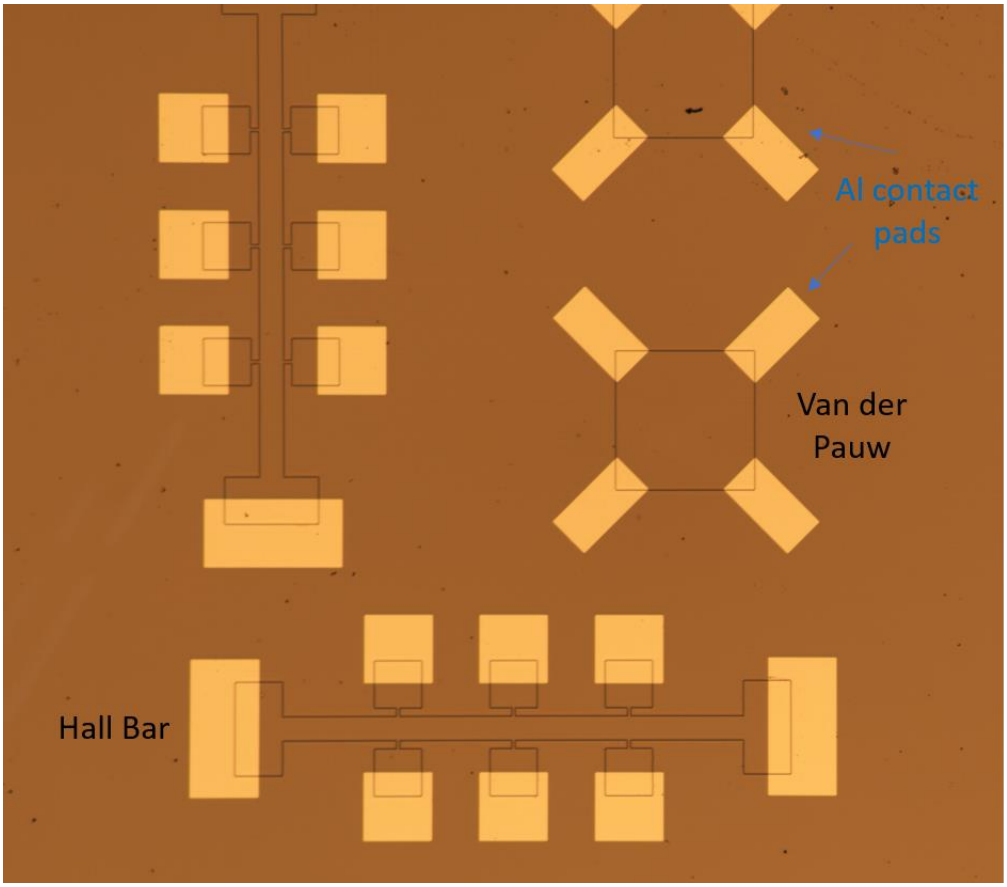

Figure 2.13: Microscope image of Hall bar and Vander Pauw devices.
Mesa-etched Hall bar devices after fabrication. The bright yellow pads are the Al contact pads for electrical conduction. The rectangular device is the Van der Pauw and the bottom device is the Hall bar.

The Hall effect measurement was originated from Edwin H. Hall, where a voltage difference is produced across an electrical conductor with a transverse current and perpendicular magnetic field (to the current) [108]. From the Hall measurement, the carrier type, carrier density and mobility of the dopant can be obtained. The basic principle of Hall measurement is based on the Lorentz force, which is a combination of both electric and magnetic forces. A total force of $-q(\mathbf{E} + \mathbf{v} \times \mathbf{B})$ will be experienced by a charge when moving along the electric field direction perpendicular to an applied magnetic field. A schematic of the Hall measurement setup is shown in

Fig. 2.14, assume a constant current is applied from top to the bottom of the Hall bar in the presence of a perpendicular magnetic field. Due to the Lorentz force, electrons will drift away from the current direction toward the left, resulting in an excess negative charge on this side of the device. This will result in a potential difference between the two sides of the device, called Hall voltage V_H (or V_{xy} as marked in Fig.2.14). The magnitude of this voltage is equal to *IB*/*qnd*, where *q* is the elementary charge, *n* is the bulk density and *d* is the thickness of the sample. It can be converted to a 2D sheet density $n_s = nd$. The relationship between the Hall voltage and the carrier density and mobility is described as:

$$n_s = IB/q|V_H| \tag{2.4}$$

$$\mu = |V_H|/R_{sq}IB = 1/qn_sR_{sq} \tag{2.5}$$

,where R_{sq} is the sheet resistance.

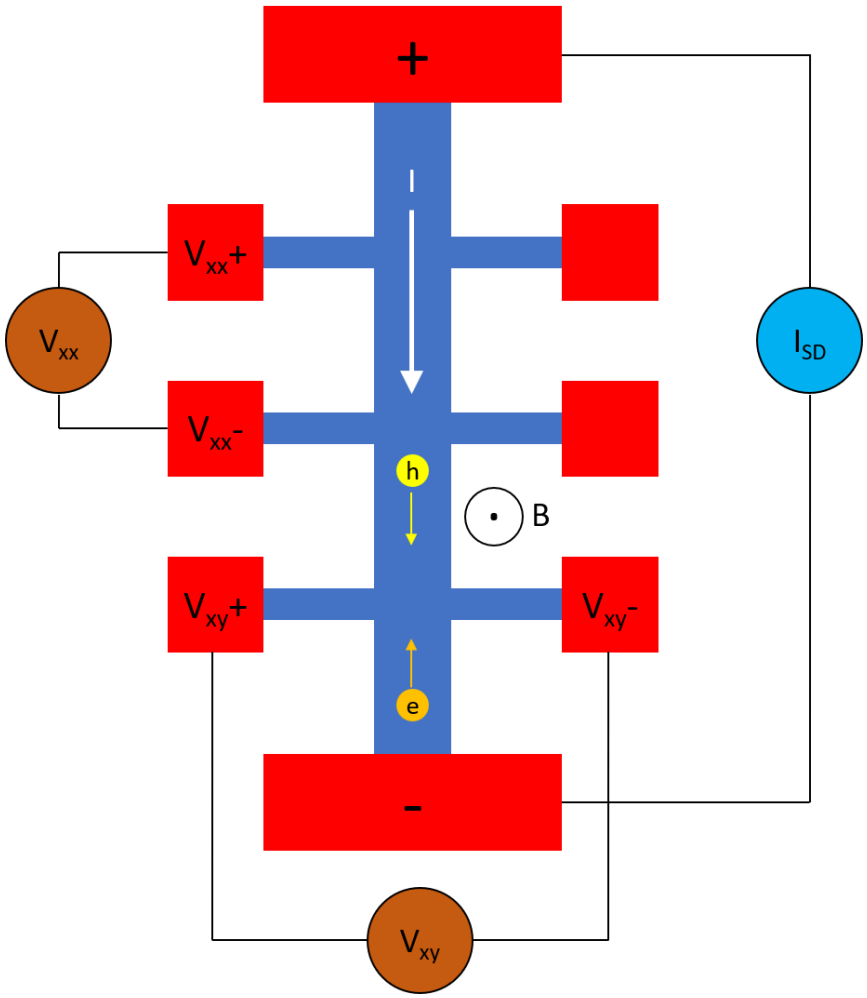

Figure 2.14: Schematic of Hall effect measurement.
Hall effect caused by the Lorentz force applied on moving charges. A voltage difference is produced across an electrical conductor/semiconductor with a transverse current and perpendicular magnetic field (to the current).

Chapter 3: Ultra-high Vacuum Ion Source for ^{28}Si Deposition

In this chapter, an ultra-high vacuum (UHV) compatible Penning ion source is presented as an upgrade to our prior ion source. The main goal of this new design is to improve chemical purity of our ^{28}Si thin films while preserving the same enrichment capability (< 1 ppm ^{29}Si). Enriched ^{28}Si is a critical material for quantum information due to the absence of nuclear spins. In some cases, the material must be grown by low temperature molecular beam epitaxy (MBE), followed by scanning tunneling microscopy (STM) hydrogen lithography to produce qubit devices. Traditional high-purity physical vapor methods typically deliver a very small fraction of source material onto the target substrate, making the cost for use with highly enriched source materials very high. Thus, directed beam sources provide an efficient alternative. This UHV Penning source uses all metal or ceramic parts and a removable electromagnet to allow bake-out. The source gas is commercial (natural isotope abundance) silane gas (SiH_4), an inexpensive source material. High enrichment levels up to 99.99987 % (corresponding to 8.32×10^{-7} mol/mol ^{29}Si) and a high chemical purity of 99.965 % are obtained without post-processing. I will discuss the design concept and the capabilities of this new UHV ion source, including its discharge properties with SiH_4, the ion mass spectrum, STM surface topography of a deposited film, and the chemical purity improvements measured by secondary ion mass spectroscopy (SIMS). Further upgrades including the ion beam sweeper and UHV gas line system with purifier will also be presented.

3.1 Introduction

Isotopically enriched silicon-based qubits that utilize electron and/or nuclear spins in quantum dots and/or donors are competitive candidates for quantum computation (or memory) due to very long coherence times [109], [29] and high gate fidelities [110],[111]. Compared to natural abundance silicon, the coherence times increase orders of magnitude when using isotopically enriched ^{28}Si as host material. Natural silicon contains ≈ 4.7 % ^{29}Si (nuclear I = ½), which causes random fluctuations and inhomogeneities in the background magnetic field and dramatically reduces the qubit coherence time. By reducing the ^{29}Si nuclear spin density to < 0.005 %, ^{31}P nuclear spin coherence times (T_{2n}) approaching an hour [30] and electron spin coherence times (T_{2e}) exceeding a second [31] have been reported in ^{28}Si. However, as was introduced in Chapter 1, the supply of isotopically enriched ^{28}Si is scarce and limited. The isotopically enriched ^{28}Si materials within this community are either not extremely enriched (≈ 99.9 % ^{28}Si), are of very limited quantity, or are not being replenished.

We have previously reported on our ability to make very highly enriched ^{28}Si, where we used a Penning ion source to ionize natural abundance SiH_4 gas, mass filtered the ions, decelerated them to hyperthermal energies, and thus deposited isotopically enriched ^{28}Si *in situ* [103],[101],[112]. Using this method, enrichment of ^{28}Si > 99.99983 % (< 10^{-6} mol/mol ^{29}Si) was achieved. This is the highest ^{28}Si enrichment known to be reported so far. However, the chemical purity of the silicon films using this ion source was relatively poor (98.47 %). SIMS was used to determine the dominant chemical impurities of carbon (C), oxygen (O) and nitrogen (N). Our prior

system analysis assumed only background impurities in the growth chamber could be incorporated, however, mass 28 amu impurities mixed into the silane source gas in the inferior vacuum region of the ion source were also transported ballistically (not just diffusively) along with the silicon ion beam, due to their similar molecular mass. For example, N_2^+, CO^+ and other mass 28 amu ionized compounds such as $C_2H_4^+$ and CNH_2^+ can pass through our mass selector to the sample since our mass resolution does not discriminate at that level (< 0.03 amu).

Therefore, here we target the vacuum condition of the ion source chamber for improving the chemical purity of our films. Our prior Penning source was not ultra-high vacuum (UHV) compatible. It used rubber O-rings for vacuum seal and plastics for high voltage isolation with a base pressure of $\approx 2.7 \times 10^{-6}$ Pa ($\approx 2 \times 10^{-8}$ Torr). Consequently, the ^{28}Si films grown using that ion source had C concentrations in the range of 10^{20} cm^{-3}, and O and N concentrations in the range of 10^{19} cm^{-3}, respectively. This impurity level is a problem for device fabrication (e.g., high quality oxide growth) and can potentially act as a source of decoherence for qubits in silicon [113, 114]. Fig. 3.1 (a) shows an ellipsometry measurement on a 4mm × 10mm sample after thermal oxide growth on ^{28}Si thin film using the prior ion source. The ^{28}Si beam spot (mountain shape) is marked with red arrow. The color scale on the right represents the thickness of the oxide. As we can see, oxide growth on top of ^{28}Si is limited, with an average oxide thickness of < 20nm, compared to > 80nm on the area without ^{28}Si. Fig. 3.1 (b) is a summary plot of the oxide thickness vs oxidation time on a natural Si substrate and deposited ^{28}Si. The oxide grows smoothly on natural Si vs time but is largely limited on ^{28}Si sample. Further analysis has been done with SEM and

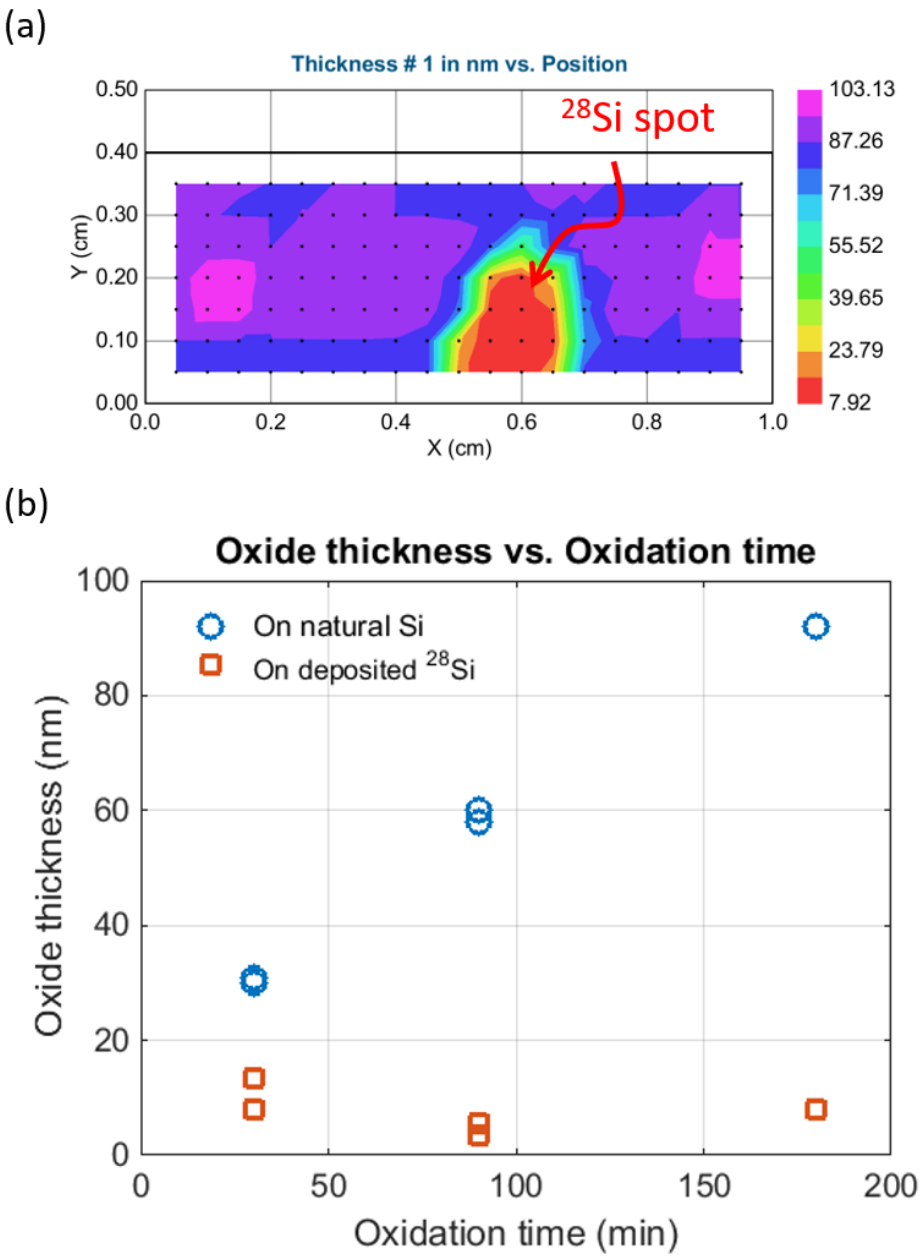

Figure 3.1: Oxide growth with ^{28}Si thin film deposited by the prior ion source. Panel (a) shows an ellipsometry measurement of the oxide thickness on a 4 mm × 10 mm sample with ^{28}Si deposited. The middle area marked with red arrow is the ^{28}Si spot. Oxide growth is largely limited at that area. Panel (b) is a summary of the oxide thickness vs oxidation time for two samples: natural Si substrate and ^{28}Si thin film. Oxide was grown successfully on the natural Si but not ^{28}Si. (Taken from Dr. A. N. Ramanayaka with permission)

energy-dispersive X-ray spectroscopy (EDS), but none of them showed evidence of a surface impurity layer that is present before going into furnace. Nonetheless, it is

most likely that the chemical impurity concentration presents in the ^{28}Si is too high, and that suppresses the oxidation process. Therefore, a new UHV ion source is needed to eliminate residual gases in the ion source and the chemical impurities in the ^{28}Si film.

As described above, the system with the newly designed UHV ion source must produce highly enriched ^{28}Si (< 10^{-6} mol/mol ^{29}Si) and improved chemical purity (< 10^{18} cm^{-3} impurities) at the same time. The specific goals are: 1) to reduce ionization source base pressure to < 3×10^{-8} Pa (≈ 2×10^{-10} Torr) to increase the film chemical purity; 2) to identify the source's optimum operating conditions for epitaxial thin film deposition; and 3) to enrich epitaxial ^{28}Si thin films to < 10^{-6} mol/mol ^{29}Si. In this chapter, we present the details of our new ion source able to achieve these goals, present the data and discuss these performance metrics.

3.2 Experimental Setup

The design of the UHV ion source is described below in Fig. 3.2. In addition to achieving ultra-high vacuum, this UHV ion source must also be compatible with the existing ion transport, mass filter and deposition system. The details of the associated system are introduced in Chapter 2 and can be found elsewhere [87, 101], however, a brief description is presented here to assist understanding. To recap, the enriched silicon system consists of five subsystems: the gas line, the ionization source, ion transport, the deposition chamber and a scanning tunneling microscope (STM) chamber. The ion source is a Penning-type ion source [115], which has a cylindrical anode and cathodes at each end that creates an axial confining potential well. The

ion's radial confinement is provided by an axial magnetic field from an electromagnet, which also helps focus ions for extraction. During the discharge, a plasma is formed by accelerating electrons from the cathodes that ionize the gas molecules. SiH_4 is used in this case, although Ar and Ne have also been used for diagnostics. Ions are extracted using an extraction cusp adjacent to one end of the source and transmitted into a system of electrostatic lenses. Since we are using hyperthermal energy ions (< 50 eV kinetic energy) that are susceptible to Coulomb repulsion (space charge) effects [100], the transport system is typically operated at -4 kV (i.e., ions are accelerated to > 4 keV while transiting the lenses and mass filter) and decelerated before deposition. As a result, high voltage isolation between the ion source and the rest of the systems (transport and gas inlet) is required. In the prior ion source, a plastic transition plate between the ion source and transport chamber was used as electric isolation and was one of the major causes of poor vacuum. In the new design, we use an 8" CF reducer nipple with ceramic neck to mate the ion source to the transport system and use ceramic standoffs for the gas inlet, as shown in Fig. 3.2.

Apart from the compatibility with the existing system, several other factors constrain the design of this UHV ion source. First, all components need to be UHV (< 1.33×10^{-7} Pa or 10^{-9} Torr) compatible and bakeable (> 150 ºC), including the gas injection. Therefore, all tubes from the SiH_4 gas bottle to the ion source feedthrough use vacuum coupling radiation (VCR) fittings to prevent air (C, O, N rich) from leaking into the gas line. Second, all plastics components such as polytetrafluoroethylene (PTFE) and nylon are replaced with ceramics. Plastics can contribute fluorine and chlorine compounds, as well as lighter gases, and present

problems when the ion source becomes hot during baking. Third, the prior ion source's electromagnet was buried inside the housing without efficient cooling. Heating of the electromagnet caused outgassing and source instability, the wire insulation commonly failed, and baking was not possible. In the new design, the magnet is a separate component outside the vacuum system, water-cooled and removable for baking. The central field at 50 A, 12.5 V is 0.11 T. Furthermore, to ease replacement of the anode and cathodes, the core of the ion source can be easily taken in and out without disturbing the magnet or other elements. Finally, the new ion source is designed to be compact and easy to maintain, using mostly simple or commercial parts.

A schematic of the UHV Penning ion source is shown in Fig. 3.2 and discussed in detail below. Our design goal was to keep the ion source dimensions as compact as possible and fully supported by the 70 mm CF base flange, while also having > 5 kV electrical isolation between the anode and the cathodes. The ion source is shown in Fig. 3.2 with dimensions and geometry correct according to the scale bar. The ion source's plasma region has three main consumable components shown as dark red: the anode, cathode and anti-cathode inserts. The distance between the cathodes and the anode is based on Ref. [96], where the performance of the gas discharge has been optimized. The anode, cathode and anti-cathode supports are 304 stainless steel (SS). The cathode inserts are constantly eroded by ions during plasma discharge and this design allows the anode and cathode inserts to be replaced easily, minimizing the maintenance steps and time. The lifetime of the cathodes depends on material type, gas source and energy of the impact, but typical insert lifetimes are about 20 - 30 h.

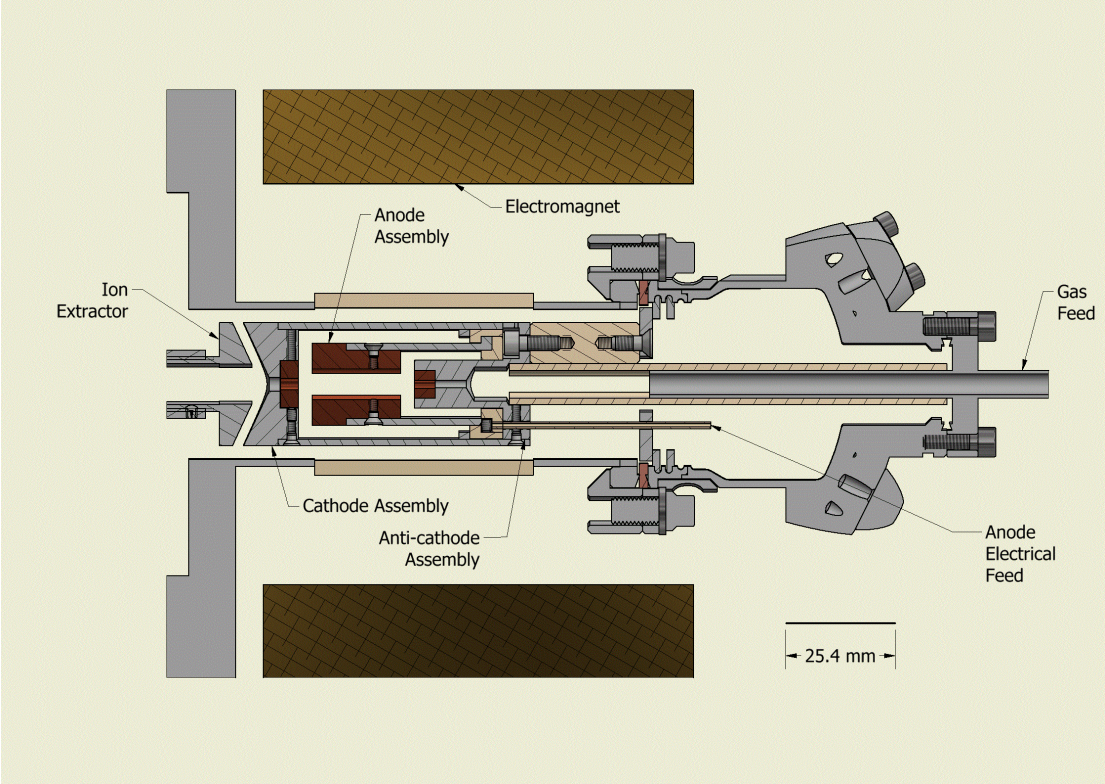

Figure 3.2: Simplified, cross sectional schematic diagram of the UHV ion source. Sliced along the axis – most parts are cylindrically symmetric. Insulating parts are shown in off-white. Consumable parts are in dark red. The vacuum housing is unhatched with the stainless-steel components shown in gray. The electromagnet solenoid is shown shaded brown and cross-hatched above and below the ion source insert. Source gas enters from the right, and ions are extracted to the left, where a system of electrostatic optics transports them downstream (not shown).

For the purpose of hyperthermal (5 eV to 100 eV) ^{28}Si epitaxial thin film growth, the plasma potential and the final energy of the ions are approximately set by the anode voltage [101], which is typically at around 40 - 50 V. The hyperthermal energy range allows atoms to land relatively softly onto the substrate during deposition, improving the ^{28}Si island density and crystalline quality without introducing large number of point defects [101].

The high voltage feedthroughs and the gas inlet are also shown on the base flange at right. The anode and cathode supports are connected by small copper wires that pass through thin insulating tubes to the feedthroughs and are fixed with vented screws (to prevent virtual leaks). Ceramic rings and top hat washers are inserted to provide electrical isolation between cathodes and anode, which typically have a 3 kV potential difference, and to maintain good geometric alignment. The main body (vacuum wall) is designed to be at the cathode potential (copper standoffs) or at a different potential, e.g., earth ground (ceramic standoffs—shown). For example, using ceramic standoffs allows the ion source body to be grounded so that a mass flow controller can be installed to provide precise control of the gas flow. Under some circumstances, the plasma power can substantially heat the central components leading to high voltage breakdown, which can be better mitigated with the copper standoffs that conduct heat away efficiently.

3.3 Ion Source Discharge Properties

The discharge properties of this UHV ion source using SiH_4 gas are studied to determine the optimum operation conditions. The arc (plasma) current and the total ion beam current extracted from the ion source are affected by the ion density and the electron temperature of the discharge, and those quantities are influenced by the arc voltage, flow rate and source magnetic field [96]. In Fig. 3.3, the total $^{28}Si^{+}$ ion current and arc current are shown as functions of these three parameters. The measurements were done by first maximizing the ion current while changing source magnetic field and flow rate at -2.7 kV arc voltage. These values of magnetic field and flow rate are

then marked as optimum values H_{opt} and F_{opt} in Fig. 3.3. Then, each of the three parameters is uniaxially varied while the other two are kept constant at their optimum values.

The ion and arc current dependence on arc voltage is shown in Fig. 3.3 (a). The discharge begins at around -1.7 kV and the ion current increases monotonically with the arc voltage up to a first maximum at -2.7 kV, and then shows weak structure suggestive of higher order plasma modes at -3.4 kV and -3.8 kV. The arc current shows a similar trend but reaches a maximum at -2.4 kV and has weaker mode structure. In Fig. 3.3 (b), the ion current versus source magnetic field is shown while keeping the arc voltage at -2.7 kV and the gas flow at -0.02 sccm. The plasma ignites at about 0.06 T and the total ion current increases rapidly reaching a maximum at 0.067 T. Here the mode structure is more pronounced with two other ion current maxima appearing at 0.077 T and 0.086 T. The arc current again shows a similar trend to the ion current, where three somewhat weaker, corresponding maxima are observed. The variation of the ion current vs. the flow rate while keeping the arc voltage at -2.7 kV and the magnetic field at 0.077 T (the ion current at 0.067 T is slighter higher, but less stable during the beam operation) is shown in Fig. 3.3 (c). Unlike in arc voltage and source magnetic field, the ion current vs. flow rate shows a large peak at 0.02 sccm and a softer, broader peak at 0.11 sccm. The arc currents increase monotonically after ignition over the entire range studied. The optimum operating condition for ^{28}Si deposition using SiH_4 gas is therefore at -2.7 kV arc voltage, 0.077 T source magnetic field and 0.02 sccm (1.87×10^{-4} Pa or 1.4×10^{-6} Torr) flow rate.

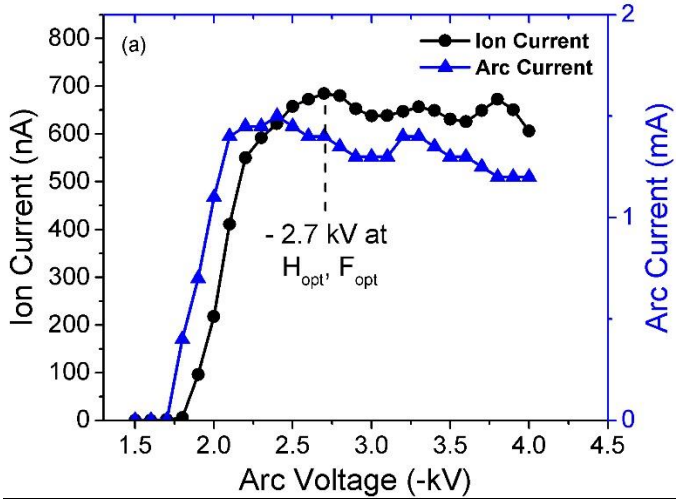

1072

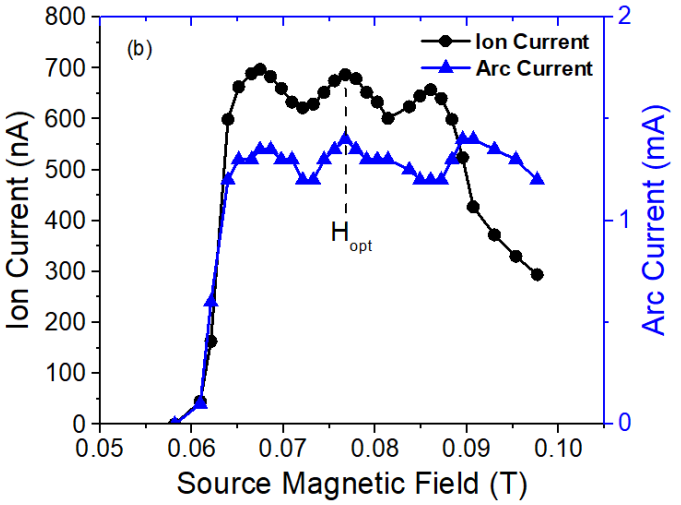

1073

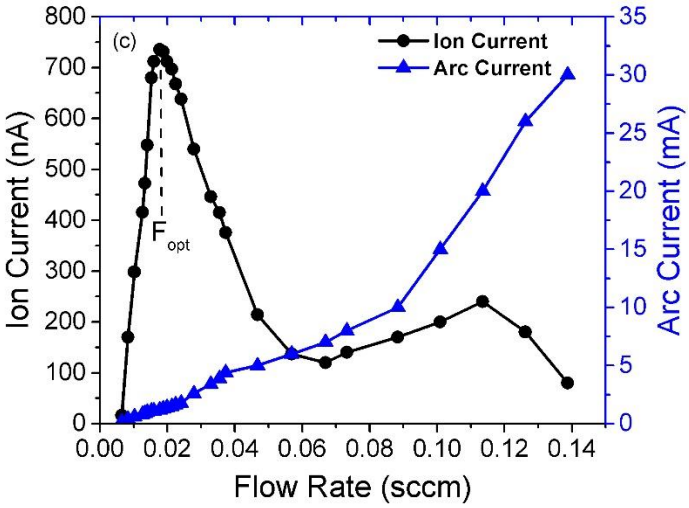

1074
1075

1076 Figure 3.3: ^{28}Si ion current (black) and discharge current (blue) characteristics.

(a) as a function of arc voltage; (b) as a function of source magnetic field, and (c) as a function of SiH_4 flow rate. The measurement uncertainties are ± 1 nA for ion current and ± 0.2 mA for arc current, respectively. Optimum conditions at: -2.7 kV arc voltage, 0.077 T source magnetic field and 0.02 sccm (1.87×10^{-4} Pa or 1.4×10^{-6} Torr) flow rate.

These values closely match those of the previous ion source on which this source was based [96].

3.4 Vacuum and Chemical Purity Improvements

Having discussed the plasma performance of the ion source, we now move on to evaluating the improvements in gas cleanliness and efficacy for silicon enrichment that motivate this effort. To enrich the silicon effectively, once the ion source is coupled to the beamline [101], the transmitted silicon ions must have trajectories well separated from each other when sweeping the magnetic field of the ion mass separator in the beamline. This allows one mass to be selected by the separator aperture while rejecting other masses. The mass spectra of the silicon ion beam taken with the prior and UHV ions sources are compared and shown in Fig. 3.4 (a). The ion mass spectrum is collected using a second, custom aperture plate on the sample stage to monitor the ion current while scanning the magnetic field of the mass analyzer. Six singly charged SiH_4 related peaks are shown. The first peak at mass 28 amu corresponds to $^{28}Si^+$ ions, while the rest of the peaks result from a combination of isotopes and hydrides due to the incomplete cracking of SiH_4 gas molecules. In an ion beam deposition, there are a lot of factors that can affect the enrichment of the deposited film, such as the substrate temperature, background silane partial pressures,

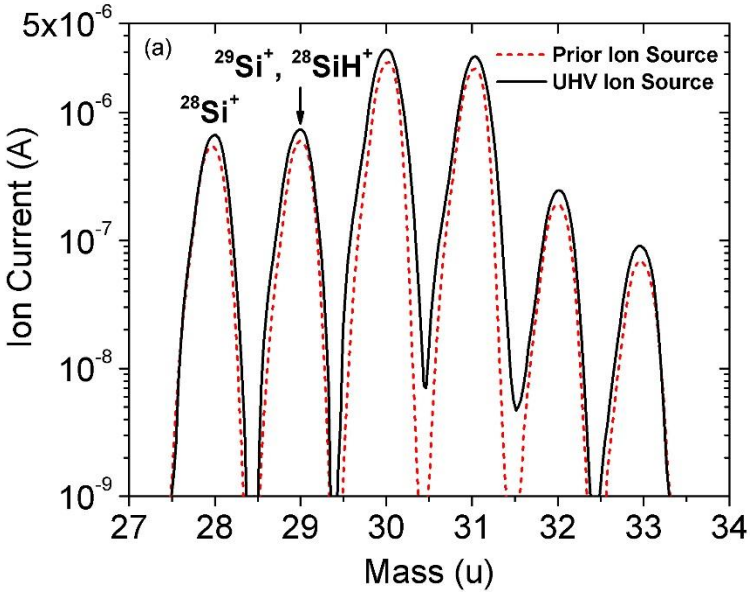

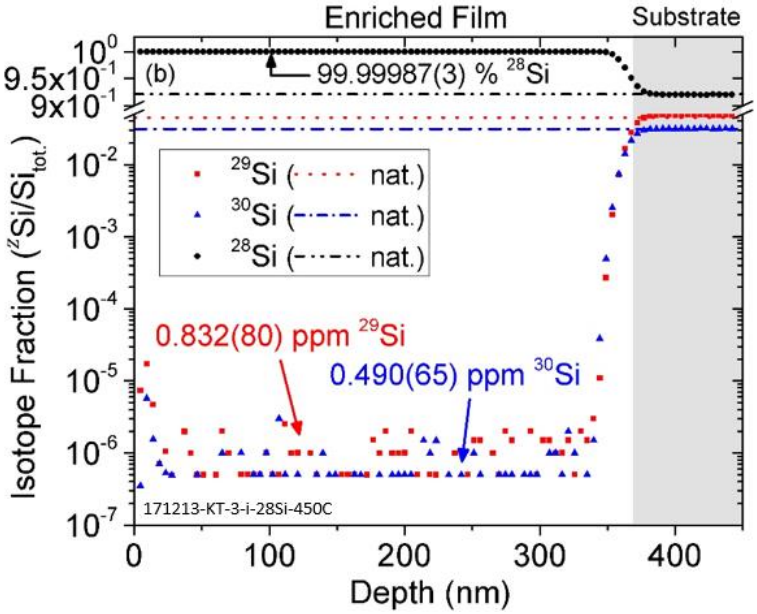

Figure 3.4: Comparison of the two mass spectra and the enrichment SIMS. (a) The ion beam mass spectra of the prior (red dashed) and new (solid black) UHV ion source are shown for comparison. The ion current after passing through the mass selecting magnet shows six peaks, which consist mostly of $^{28}Si^+$ ions at 28 amu and other isotopes combined with hydrides at higher masses. The peak shapes and isotope separation between 28 amu and 29 amu indicate similar enrichment capability. (b) A SIMS depth profile of ^{28}Si thin film shows the isotope fractions of ^{28}Si, ^{29}Si and ^{30}Si using the UHV ion source, confirming excellent enrichment with an average of 99.99987(3) %.

etc. Among them, one of the most important factors is the mass separation between mass 28 amu and 29 amu peaks (See ref. [103] for detailed analysis of mass selectivity). An overlap of the two peaks means that part of $^{29}Si^{+}$ also passes through the aperture and will be introduced into the deposited film. The UHV ion source's similar peak shape and separation compared to the prior source indicate good mass selectivity (> 5 σ from center to center) for enrichment, and similar current suggests a similar growth efficiency with this ion source. Note that there is some degradation in separation at higher mass peaks (> 30 u), but for ^{28}Si thin film, the primary peaks to be considered are 28 amu and 29 amu. Typically, we use a deposition rate of 1 nm/min and the ion source is stable throughout the deposition (usually 6 h to 8 h). Higher growth rate might be achieved by using different plasma modes (e.g. higher flow rate), but generally results in shorter cathode lifetime and larger surface roughness of the deposited film (see Ref. [87] for details in higher pressure plasma mode).

The enrichment of a typical ^{28}Si film is shown in Fig. 3.4 (b). SIMS was used to profile the isotopic fraction of ^{28}Si, ^{29}Si and ^{30}Si of the deposited ^{28}Si film grown using this UHV ion source. The SIMS measurement was taken near the center part of the enriched silicon film, which is usually the thickest. The residual isotope fraction of ^{29}Si is shown as squares with an average value of $8.32(80) \times 10^{-7}$ mol/mol in the film and ^{30}Si is shown as triangles with an average value of $4.91(65) \times 10^{-7}$ mol/mol. The ^{28}Si total enrichment for this sample is 99.99987(3) %. The enrichment level can vary some from run to run, but comparing several samples deposited using the prior

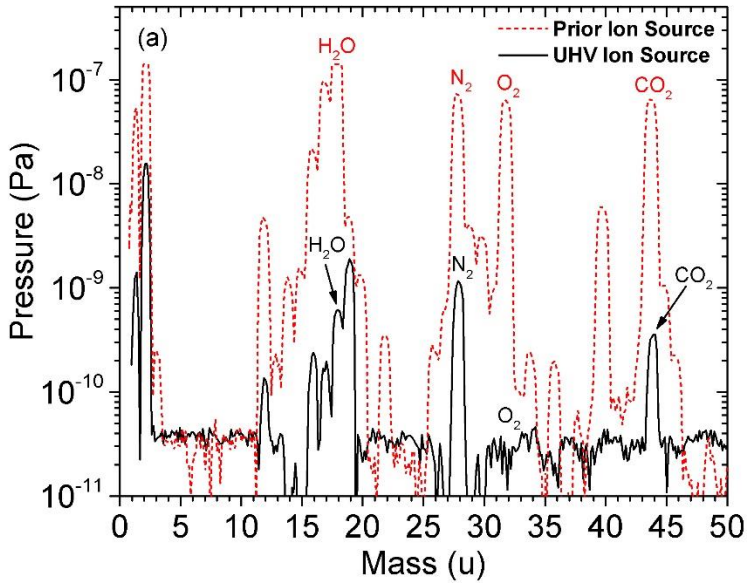

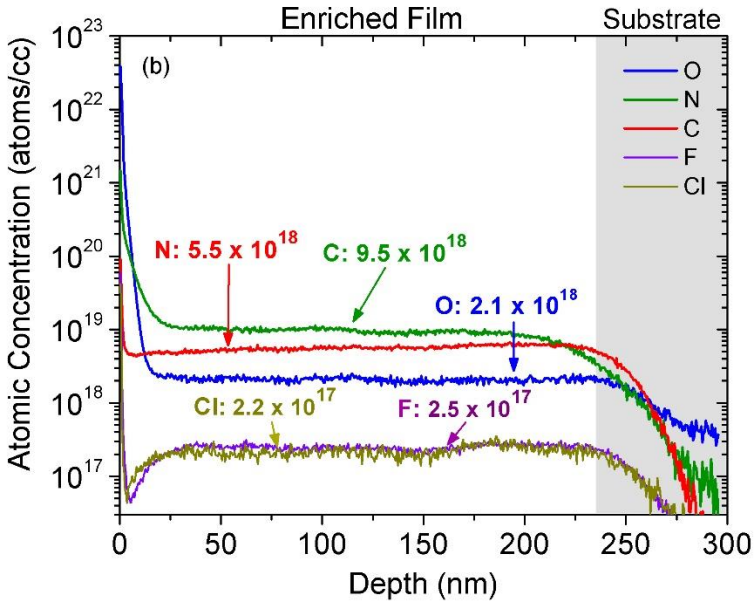

Figure 3.5: Comparison of the RGA and chemical SIMS.
(a) Residual gas analysis (RGA) demonstrating the comparison in background gas density between the two ion sources. The red curve in (a) is the prior ion source with base pressure 2.7×10^{-6} Pa (2×10^{-8} Torr) and the black curve is the UHV ion source with base pressure 2.7×10^{-8} Pa (2×10^{-10} Torr). Major peaks are labeled with the dominant gases. (b) A SIMS depth profile of the residual chemical impurities in a ^{28}Si thin film deposited using the UHV ion source. The estimated chemical purity of this sample is 99.965(2) %.

ion source with samples from this ion source, we conclude that the ^{28}Si enrichment is maintained (<1 ppm ^{29}Si) with this UHV ion source.

Since the growth chamber pressure is typically maintained at 6.7×10^{-9} Pa (5×10^{-11} Torr), the background gas composition in the ion source was estimated to be the leading contributor to film contamination in the prior source and the primary motivation for building a UHV ion source. The baseline pressure as measured with an ion gauge (uncertainty of 10 % to 20 %) has been improved by a factor of a hundred in this UHV ion source compared to the prior ion source, now reaching 2.7×10^{-8} Pa (2×10^{-10} Torr). The partial pressures of various gas components as measured by a residual gas analysis (RGA) in the prior and UHV ion sources are shown in Fig. 3.5 (a) and Table I. These show the qualitative improvement in vacuum conditions and chemical compositions and confirm that the impurities contributed from the ion source vacuum have been reduced by a factor of 100.

TABLE I. Partial pressure peaks of the key gas contaminants relevant to silicon thin film purity as measured by residual gas analysis (RGA). The estimated uncertainty is in the range of 10 % to 20 %.

Impurity	*Mass (u)*	*Pressure in prior ion source (Pa)*	*Pressure in UHV ion source (Pa)*
H_2O	18	$> 1.4 \times 10^{-7}$	6.1×10^{-10}
N_2	28	7.3×10^{-8}	1.1×10^{-9}
O_2	32	6.3×10^{-8}	2.8×10^{-11}
CO_2	44	6.5×10^{-8}	3.5×10^{-10}

A SIMS depth profile showing the chemical impurity concentrations for C, N, O, F and Cl in a ^{28}Si thin film deposited using this UHV ion source is shown in Fig. 3.5 (b). The average concentration level for carbon is $9.5(8) \times 10^{18}$ cm^{-3}; nitrogen is

5.5(5) × 10^{18} cm^{-3} and oxygen is 2.1(2) × 10^{18} cm^{-3} between 30 nm and 235 nm. As a comparison, the total chemical purity of the ^{28}Si film has been improved from ≈ 98.5 % (first chemical SIMS using the prior ion source) to 99.965(2) %. From previous SIMS measurement (not shown), we found that the ^{12}C concentration in the film is roughly 400 times higher than ^{13}C. This means that the ^{12}C is also enriched (> 98.9 %) in the ion beam process and the ^{13}C concentration is approximately 3 × 10^{16} cm^{-3}. Similarly, the ^{15}N concentration is < 2 × 10^{16} cm^{-3}. Therefore, at this contamination level, the largest factor for the nuclear spin bath is still expected to be ^{29}Si (≈ 0.83 ppm), plus some contributions from ^{13}C (< 0.6 ppm) and ^{15}N (< 0.4 ppm) as well. Further improvement in chemical purity is needed to reduce the effects from ^{13}C and ^{15}N.

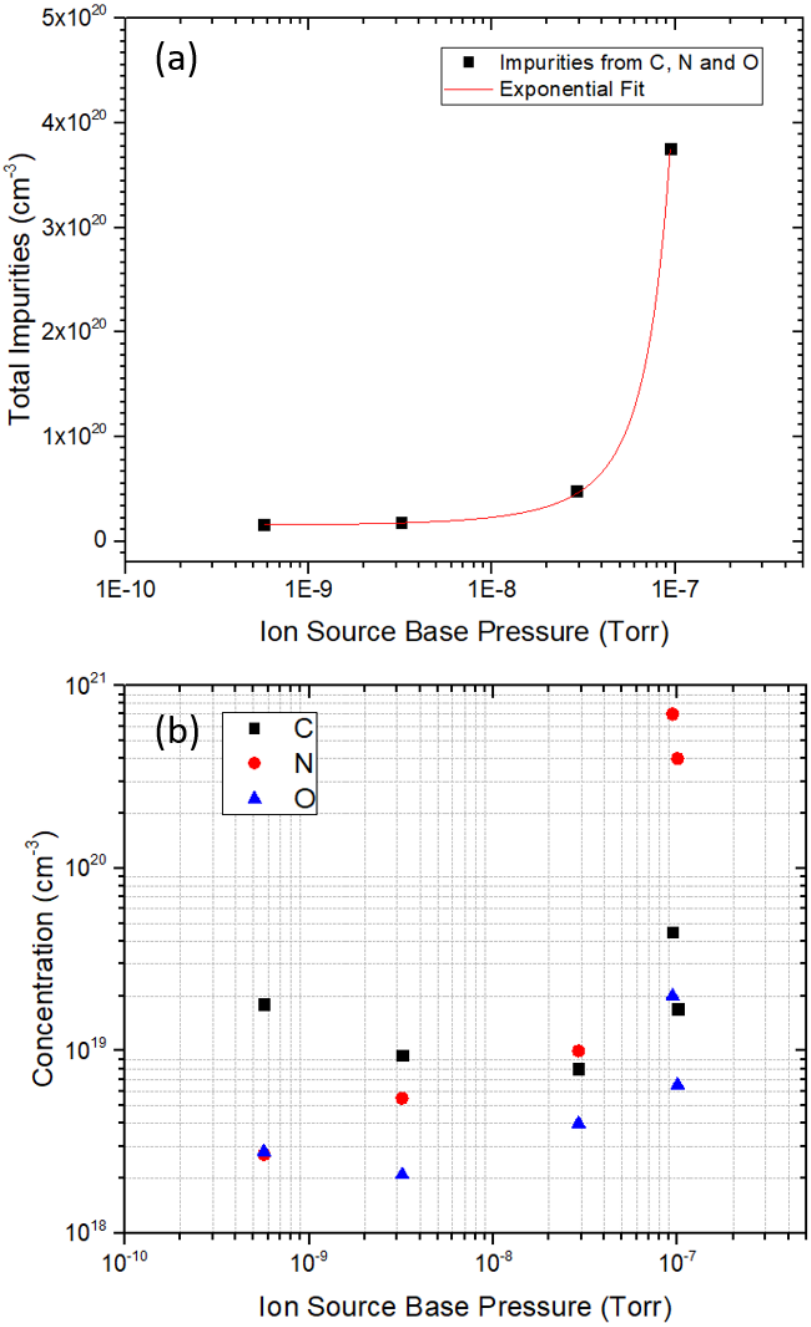

Figure 3.6: Chemical purities (C, N and O) of the ^{28}Si thin film vs ion source base pressure.
The higher-pressure data are from the prior ion source. Panel (a) shows the total chemical impurity increases exponentially vs base pressure. The improvements in purity seem to become negligible at pressure < 10^{-9} Torr. Panel (b) shows the impurity concentrations of the main contributors: C, N and O. N showed the largest improvement (260×) with ion source vacuum while C (5×) and O (10×) showed less improvements.

The correlation between the chemical purities vs ion source base pressure is studied in Fig. 3.6. Panel (a) shows a summary of the total chemical purity in our ^{28}Si film vs the source base pressure. The data is taken from both the prior and the new UHV ion source. An exponential decay in total impurity level is observed in terms of base pressure. Panel (b) shows the impurity concentrations of the main contributors: C, N and O. Despite the substantial improvement in total chemical purity (43 ×) compared to the prior ion source, we found the improvement was not fully correlated to the vacuum improvement (100 ×). This indicates that at this concentration level, the vacuum condition of the ion source is not the only limiting factor that affects the chemical purity of the ^{28}Si film. For example, N showed the largest improvement (≈ 260 times) with the base pressure, varying from $7 \times 10^{20}\,cm^{-3}$ to $2.7 \times 10^{18}\,cm^{-3}$. C and O showed smaller improvements, varying from $4.5 \times 10^{19}\,cm^{-3}$ to $9.5 \times 10^{18}\,cm^{-3}$ (≈ 5 times) and $2 \times 10^{19}\,cm^{-3}$ to $2.1 \times 10^{18}\,cm^{-3}$ (≈ 10 times), respectively. It is likely that for N, the ion source base pressure is the dominating factor as it showed the strongest correlation. Note that in Fig. 3.6 (b), the chemical impurities of C, N and O increased a little at the lowest base pressure. We believe that this is due to the degradation and contamination presented in the silane gas system over time, again indicating that the ion source base pressure is not the only dominating factor for chemical purity.

We also found that the impurity concentrations are not correlated to the growth rate and background partial pressures, where the background impurities should be much less than $10^{18}\,cm^{-3}$, indicating the origin of the impurities is from the ion source chamber instead of the growth chamber. Therefore, the cleanliness of the silane gas

system, impurity ions sputtering from the cathodes and anode materials and chemical compounds formed in the ion source plasma may also be contributing factors. Further study is needed to fully explore the origin of the contaminations in the film and to seek additional purity improvements. Possible solutions may include post-annealing at 950 °C in UHV (preliminary work shows that the N concentration can be reduced to low 10^{17} cm^{-3} after annealing), installation of silane gas purifier to purify the gas line, etc.

3.5 Epitaxial Quality of ^{28}Si Thin Film

Molecular beam epitaxy (MBE) growth of Si has been extensively studied and characterized in the past decades [116]. In 1990, Eaglesham and his coworkers reported the existence of a critical thickness h_{epi} for epitaxy at a given temperature [117], where the epitaxial film breaks down and becomes amorphous. The critical thickness increases exponentially as the deposition temperature increases (also dependent on deposition rate). For example, for a deposition rate of 0.4 nm/min, the critical thickness is 25 nm at 200 °C on Si (100) surface and increases to 120 nm at 300 °C. In general, h_{epi} is limited to a deposition rate of a few nm/min at low temperatures. When T > 500 °C, solid phase epitaxy (SPE) dominates because the recrystallization process becomes faster than the deposition rate, resulting in a very large value of h_{epi} [87]. Further studies have pointed out that for low temperature MBE of Si, a highly defective region is formed in the epitaxial film before the development of amorphous phase [118-122]. Most of the defects observed are stacking faults and microtwins [119]. Several hypotheses have been raised to explain

the transition from epitaxy to amorphous. One possible explanation is the incorporation of H during deposition, where H could segregate and accumulate onto the surface and disturb the surface bonding of the lattice [123]. Another possibility is the accumulation of defects during growth process until epitaxial breakdown of the film [124]. However, very large defect density (10^{14} cm^{-2}) is required to support this assumption. Eaglesham also raised the hypothesis that the roughening of the growth surface itself can cause breakdown of the epitaxial layer at low temperature [125].

In this work, we use ion beam deposition to grow epitaxial ^{28}Si. Ion beam deposition has been demonstrated to have similar results to MBE in terms of h_{epi} and defect density. However, it has also been shown that the use of hyperthermal energy ions helps to extend h_{epi} to be thicker values at given temperature and deposition rate [119, 126-130]. Low energies in the range of 10 – 50 eV also provide other benefits to the deposited surface. For example, energy can be transferred to the film through neutralization of the ions (approximately the ionization potential of 8.15 eV) and this energy can enhance the mobility of the nearby atoms [131]. In addition, hyperthermal energy ions help to suppress the formation of 3D islands and step pinning from impurities [127, 128] and they can also create vacancies that facilitate adatom

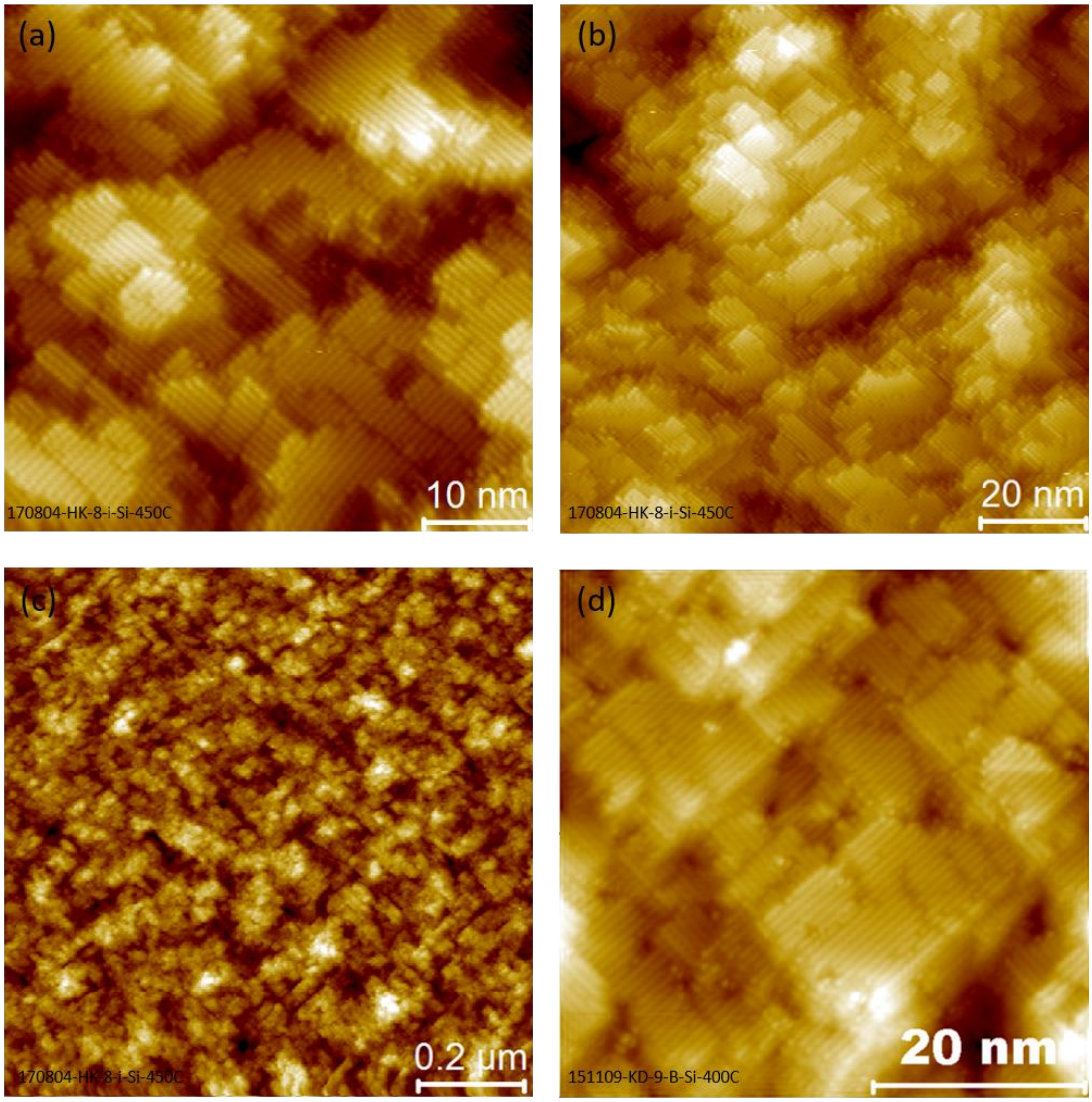

Figure 3.7: STM surface topography of two ^{28}Si films using both ion sources. (a) through (c) are from the new UHV ion source. The images are taken using a bias voltage of +2 V and tunneling current of 100 pA. Panel (a) is a 50 nm × 50 nm scan of the ^{28}Si surface with 2 × 1 reconstructed Si dimer rows, steps and terraces, indicating the epitaxial alignment of the ^{28}Si atoms with the Si (100) substrate. Panel (b) and (c) shows a larger area scan of the sample, where relatively smooth, epitaxial 3D islands are observed. This film is deposited at 450 °C with a thickness of 191 nm measured by SIMS depth profiling. Panel (d) shows another sample deposited using prior ion source. The film is deposited at 400 °C with a thickness of 120 nm also measured by SIMS. Similar structures and surface roughness are seen in this image, indicating a similar epitaxial quality of the deposited film. (The STM images shown in this figure is taken by Dr. Hyun-soo Kim).

incorporation [132]. As a result, the energy of the deposited ^{28}Si we use is usually in the range of 30 - 50 eV. The growth temperature is chosen to be ≈ 450 °C to ensure a high enough h_{epi} but the lowest contribution of ^{29}Si from the background SiH_4 gas since higher T results in thermally activated incorporation of the silane molecules [133].

STM was used to characterize the surface topography of the deposited ^{28}Si thin films. Fig. 3.7 shows the 3D island growth of the epitaxial surface of the deposited ^{28}Si films using both prior and our improved UHV ion sources. Images were taken with a tip bias of +2 V and tunneling current of about 100 pA. Panel (a) through (c) are from the same sample deposited at 450 °C with thickness of about 191 nm using the UHV ion source. The film thickness was determined by the SIMS depth profiling. Panel (a) is a small area scan of the sample showing multiple islands with clear 2 × 1 reconstructed Si dimer rows, steps and terraces, indicating the epitaxial alignment of the ^{28}Si atoms with the Si (100) substrate. The relatively smooth epitaxial surface has a root mean squared (RMS) roughness value of 0.32 nm in the 50 nm × 50 nm image range. Very few defects are observed in this image. Panel (b) and (c) are the larger scale images, where multiple 3D islands are visible. As a comparison, panel (d) shows a ^{28}Si film deposited under similar condition by the prior ion source where the sample is deposited at 400 °C with a thickness of 120 nm. Similar structures and surface roughness are observed, indicating similar quality of the deposited film. In general, the deposited ^{28}Si thin films are epitaxial with relatively good surface qualities. It also means that the crystal quality of the deposited film is relatively insensitive to its chemical purity, at least at this level.

3.6 Further Improvements

3.6.1 Lens Upgrade and Ion Beam Sweeper

To further improve the cleanliness and deposition capabilities of this ion source, we have upgraded the deceleration lens system and designed a new ion beam sweeper. In the previous set up of the transport and deceleration lens system, plastics including Teflon were used for high voltage isolations. Those polymers contribute to outgassing and may act as sources of contamination to the vacuum chamber, especially when closer to the higher temperature regions. To avoid this, all plastics and Teflon parts were removed and the new design for mechanical support and high voltage isolation is demonstrated in Fig. 3.8. Plastic rods and screws were used to connect and separate each lens elements from A2 to B2 and X. They are now replaced by a mounting tray made of high purity stainless-steel with metal screws and ceramic washers. Ceramic saddles are also used between the mounting tray and the lens elements for high voltage isolation. Two insulating rods with cylindrical stainless-steel frames are used to support the weight of the lens while providing alignment for the lens elements.

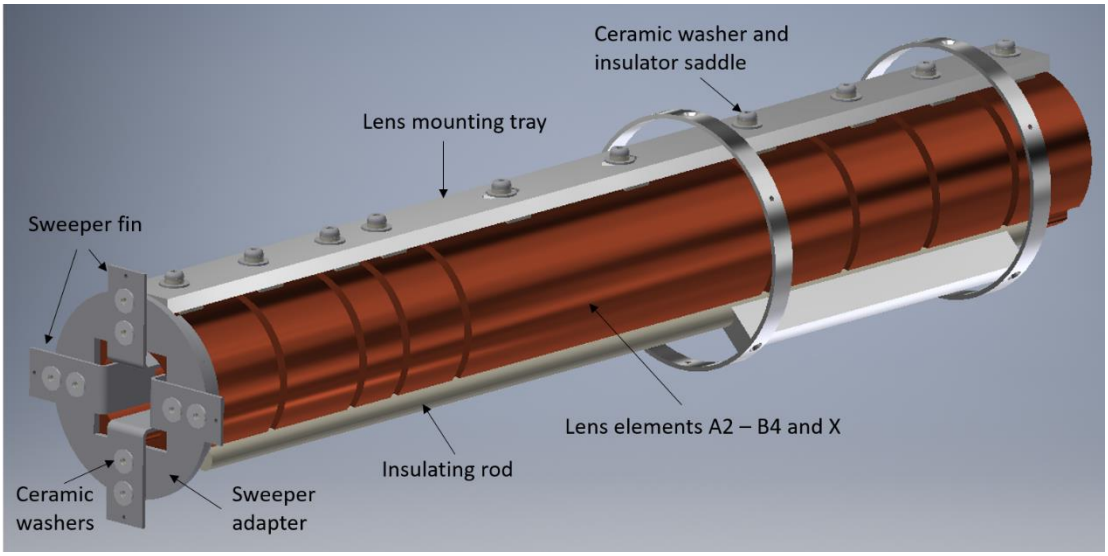

Figure 3.8: A schematic of the upgraded ion beam lens system and new sweeper. All plastics and Teflon parts are removed from the lens system. Alumina insulating rods, ceramic washers and mounting saddles are used to provide high voltage isolation and mechanical support of the lens elements. The sweeper is located at the end of the deceleration lens X right before the deposition sample stage. The sweeper is made of copper and is connected to lens X by an adapter. Sweeper fins are fixed on the adapter using metal screws and ceramic washers for isolation. Electrical feedthroughs are connected to the fin with kapton coated copper wires. To deflect the ion beam (≈ 40 eV energy) for 2 mm in one direction, a voltage of ≈ 10 V is used on the sweeper fin.

An ion beam sweeper was designed and installed at the end of the deceleration lenses. The reason for the ion beam sweeper is to smooth out the topography of the ^{28}Si film. As mentioned in Chapter 2, the deposited ^{28}Si film is a few mm in size and has a mountain shape with the thickest area in the middle of the beam spot. This can cause problems for further device fabrication due to the uneven thickness of the film. By using parallel plate electrodes, the ion beam can be deflected and controlled in two dimensions using a function generator. The schematic of this sweeper is also shown in Fig. 3.8. An adapter is mounted at the end of the deceleration lens element X. Four sweeper fins are attached but electrically isolated from the adapter by metal screws and ceramic washers. Electrical feedthroughs are connected to those fins with

kapton coated copper wires. To produce a relatively smooth film on our 4 mm × 10 mm sample, we would need to sweep the ion beam periodically with a spatial range of ± 2 mm in the horizontal direction while keeping the other direction constant. The final beam spot will be in the dimension of about 3 mm × 6 mm (this is largely because 3 - 4 mm in the horizontal direction of the sample is covered by the clamps of the sample holder). To deflect an ion beam with energy ≈ 40 eV, a voltage difference of ≈ 10 V and ≈ 8 V is needed between the left/right and top/bottom electrodes, respectively. Only preliminary tests have been done using this sweeper; further experiments are needed to better tune the sweeper with the deceleration lenses and SIMS would be used to measure the thickness of the deposited film at various locations on the sample.

3.6.2 UHV Gas Line with Purifier

Another possible improvement for chemical purity is the upgrade of the silane gas line system. In the past, VCR tubings and UHV leak valves were used for gas manipulation. However, silane gas is highly reactive and can slowly react with the interior of the metal tubing overtime. To address this problem, a UHV gas line with a silane purifier was designed and a routine replacement of the metal parts was needed. The silane purifier is a micro gas purification and filtration system purchased from Matheson. It is made of some porous materials that can absorb H_2O, CO_2 and O_2 molecules to < 0.1 parts per billion (ppb) and CO to < 1 ppb. It can also adsorb other contaminants such as NO_x, SO_x and H_2S from the gas line. Future effort is needed to install and deposit ^{28}Si using this purifier. SIMS will be performed to measure the

improvements in chemical purity and a reasonable guess for the improved level of C, N and O will be in the ≈ 10^{17} – 10^{18} cm^{-3} level.

3.7 Conclusion

In this chapter, an upgraded version of the UHV hyperthermal ion beam system has been introduced. We demonstrated the design, experimental implementation and performance of this UHV ion source system. The discharge properties based on arc voltage, source magnetic field and flow rate have been studied and optimized for ^{28}Si. The performance of the UHV ion source for enriched silicon deposition is demonstrated through the ion mass spectrum and SIMS measurements of an enriched film. As a result, the vacuum has been improved from 2.7 × 10^{-6} Pa (≈ 2 × 10^{-8} Torr) to 2.7 × 10^{-8} Pa (≈ 2 × 10^{-10} Torr), with a factor of 100×. A total purity of 99.965 % is obtained, with a factor of 43× improvement. We found that for N concentration, it is largely correlated to the ion source base vacuum; while for C and O, less improvements were seen. This means that below the 10^{19} cm^{-3} concentration region, ion source vacuum might not be the only dominating factor that affects the chemical purity of the ^{28}Si film. Other factors such as cleanliness of the gas line, background contamination, ion sputtering might be limiting. In addition, we showed that the isotopically enriched ^{28}Si thin film deposited is epitaxial with good surface quality and crystallinity using STM. The deposited film also has high enrichment level of 99.99987(3) %, indicating that the ability for highest enrichment among all methods reported is maintained. With possible future improvements, such as the ion beam

sweeper and UHV gas line with purifier, we believe we can further improve the chemical purity of the film to have C, O and N contents < $10^{17} – 10^{18}$ cm^{-3}. This will be an important step forward to produce high quality ^{28}Si that is suitable for quantum information studies.

This chapter is reproduced from Ref. [134] with permissions from all the co-authors.

Chapter 4: Targeted Enrichment of ^{28}Si thin films

In this chapter, we report on the growth of isotopically enriched ^{28}Si epitaxial films with precisely controlled enrichment levels, ranging from natural abundance ratio of 92.2 % all the way to 99.99987 % (0.832×10^{-6} mol/mol or 0.832 ppm ^{29}Si). Isotopically enriched ^{28}Si is regarded as a nearly ideal host material for semiconducting quantum computing due to the lack of ^{29}Si nuclear spins. However, the detailed mechanisms for quantum decoherence and the exact level of enrichment needed for quantum computing remain uncertain. In the previous chapters, we introduced the use of hyperthermal energy ion beam for ^{28}Si deposition with certain mass-to-charge ratio (28 amu/e). Here we switch the mass selective magnetic field periodically to control the ^{29}Si concentration. We develop a model to predict the residual ^{29}Si isotope fraction based on the deposition parameters and measure the deposited film using secondary ion mass spectrometry (SIMS). The first generation of the targeted enrichment film had a value which agreed with the predicted value within a factor of 2. With the improvements in current measurement and ion source stability, the second generation of targeted enrichment showed improved, excellent agreement with the prediction, deviating on average by only 10 %.

4.1 Introduction

As interest grows in using isotopically enriched ^{28}Si to achieve longer coherence times in quantum information processing, better understanding of the mechanisms

behind decoherence in electron spin becomes important. In 1958, Gordon and Bowers first measured the coherence time T_2 of electrons bound to lithium and phosphorus donors in isotopically enriched Si with $T_2 = 0.5$ ms [135], [136], which was much longer than the coherence time in natural Si. This demonstrated that, in those donor electron spin systems, residual ^{29}Si contributes significantly to the electron spin decoherence. Recently, theoretical studies using cluster expansion techniques [137], [32], [33] by Witzel *et al.* predicted that every order of magnitude increase in isotopic enrichment results in approximately the same order of magnitude increase in the coherence time, until limited by non-Si spins. Excellent agreement between the theory and experiment has been shown with bulk ESR measurements, with one measurement done at 0.0005 % ^{29}Si [138] and others from 0.08 % to 99.2 % ^{29}Si [32]. However, emerging single ^{31}P spin measurements in ^{28}Si have indicated performance better than predicted [35], [139], motivating additional studies. The discrepancy found between the experiments and theory indicates that the phase space of coherence versus enrichment, especially in the limit of few spins and high isotopic enrichment regimes, remain largely unknown.

As a result, a specific need exists for enriched ^{28}Si to have different, targeted values of enrichment to study the dependence of quantum coherence time on residual ^{29}Si concentration. Although various research groups have been able to make isotopically enriched ^{28}Si [140], [141], [44], [45], [102] (explained in detail in Ref. [43]), the ability to predict and control the residual ^{29}Si isotope fraction within ^{28}Si precisely has not yet been demonstrated. The discreteness and the limited number of the enrichment levels available within this community make a detailed determination of the optimal enrichment difficult to accomplish.

In this chapter, we present a method that allows us to produce ^{28}Si with precisely controlled isotopic enrichments. We develop a model that allows us to choose and predict the level of enrichment for our ^{28}Si. We deposit ^{28}Si thin films with ^{29}Si concentrations ranging from our baseline ($< 1 \times 10^{-6}$ mol/mol) to natural abundance (4.7 %) and measure the isotope fractions of the residual ^{29}Si and ^{30}Si using secondary ion mass spectroscopy (SIMS). The measured enrichments are then compared to the model prediction and show excellent agreement, deviating on average by only 10 %.

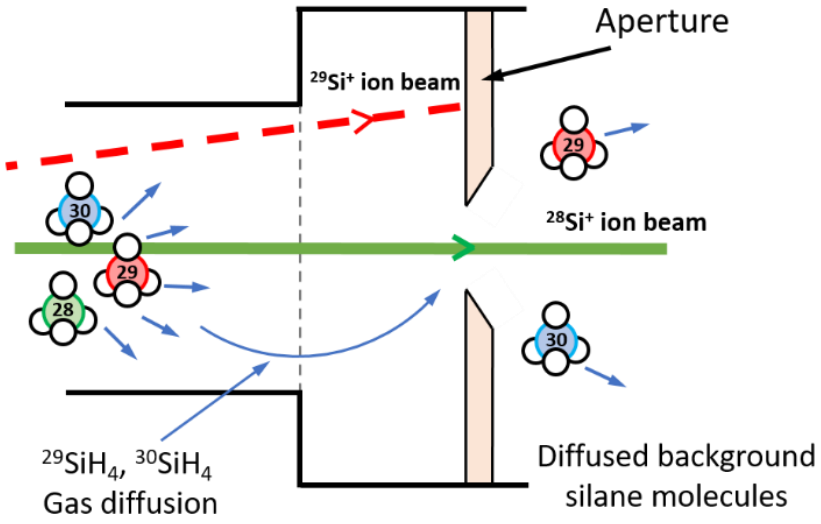

Figure 4.1: A schematic illustration of the origin of ^{28}Si and ^{29}Si. The solid green and red lines represent $^{28}Si^+$ and $^{29}Si^+$ ion beam respectively. During ^{28}Si deposition, mass selective magnetic field is tuned such that only $^{28}Si^+$ ions can pass through and $^{29}Si^+$ ions are blocked by the aperture. Apart from the Si ions, SiH_4 gas molecules can also pass through the aperture and adhere to the substrate. The background silane gas contribution to the film is approximately 10^{-6} mol/mol.

4.2 Experimental Methods

To achieve a targeted enrichment, sources of ^{29}Si that can enter the film are studied, as shown in Fig. 4.1. Even with the magnetic field tuned at a certain mass-to-

charge ratio, for example 28 amu/e, $^{29}Si^{+}$ ions might still pass through the mass selective aperture if the mass resolution (determined by the width of the ion beam exiting the ion source, the aperture width and the spread in ion energy) is poor. Here we use a mass spectrum to characterize the Si ions. It is generated by monitoring the ion current at the deposition location while scanning the mass analyzer magnetic field. A mass spectrum is shown in Fig. 4.2 (a) for targeted enrichment, where peaks for $^{28}Si^{+}$ ions (mass 28 amu), $^{29}Si^{+}$ ions (mass 29 amu) and the corresponding ionized hydrides (mass 29 amu to 32 amu) due to incomplete cracking, can be seen. It is very similar to the previously shown mass spectra (Fig. 3.4), the values in height of the 28 amu and 29 amu peaks are extracted to estimate the deposition parameters. The mass separation is obtained by fitting the mass peaks with Gaussians. The center of the mass 28 amu peak is about 7.4 σ (standard deviation) away from the center of 29 amu peak, indicating a lower bound of ^{29}Si isotope fraction of 10^{-13} at the 28 amu mass position. Another source of ^{29}Si comes from the residual background SiH_4 molecules as they can diffuse through the aperture hole and adhere to the sample substrate. In addition, mass 29 amu ions might lose energy and fall into the 28 amu trajectory in the mass analyzer. However, this effect would be asymmetric, and since there is no observed scattering tail effect, we assume that all the current at mass 28 amu peak is from $^{28}Si^{+}$. Therefore, the main active contributors of ^{29}Si considered in this chapter are from ion beam itself and the diffused background silane gas from the ion source to the deposition chamber.

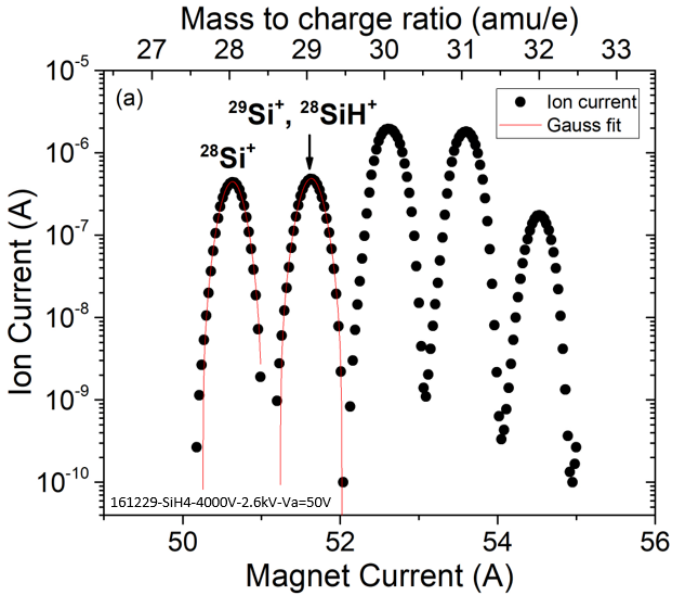

1483

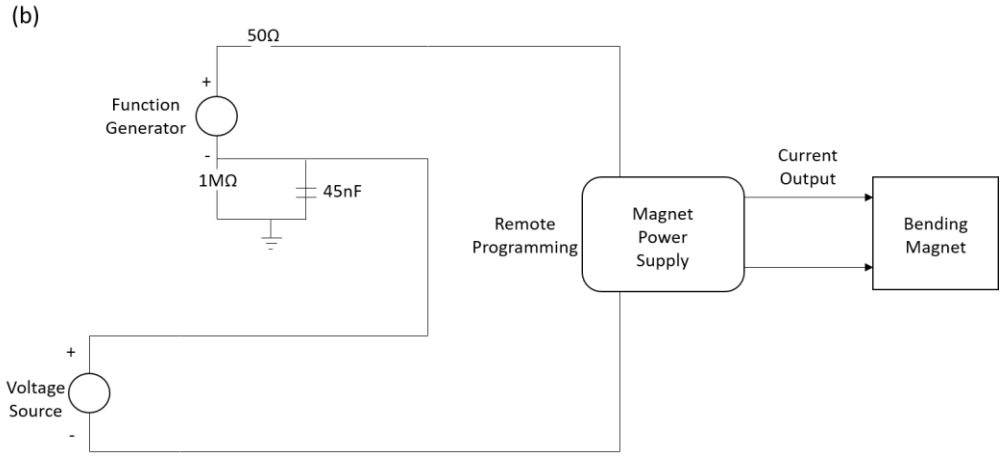

1484

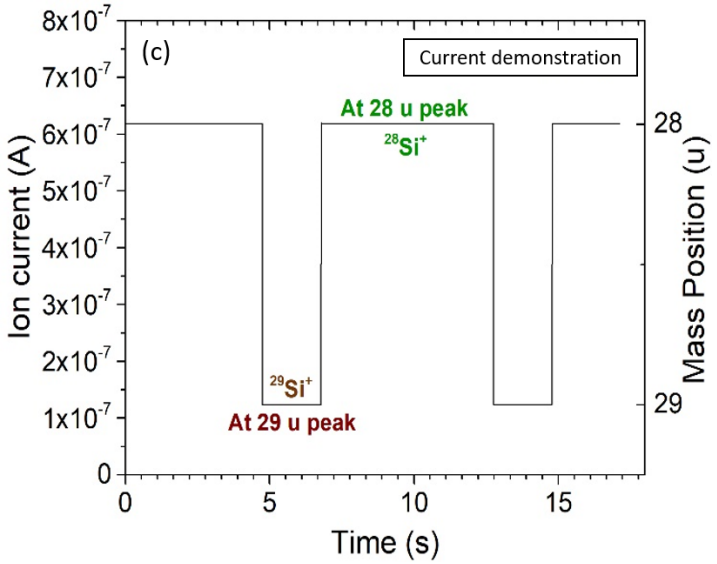

1485

Figure 4.2: Demonstration of the targeted enrichment.
(a) An ion beam mass spectrum used for checking mass resolution and calculating the deposition parameters described in equation 1 and 2. Gaussian fits for both mass 28 amu and mass 29 amu are shown in red, with a mass separation of 7.4 σ. (b) The block diagram of the targeted enrichment control. A DAQ function generator is used to trigger a periodic asymmetric square wave to control the output of the mass analyzer. (c) An example of an ion current for targeted enrichment, plotted as the current collected at the sample stage versus time. The corresponding mass positions at 28 amu and 29 amu peaks are also shown on the right. The duty cycle is selected such that the dwelling time at mass 28 amu is 75 % and the dwelling time at mass 29 amu is 25 %.

The experimental concept for targeted enrichment is described in detail here. In previous work, we produced isotopically pure ^{28}Si that has a ^{29}Si isotope fraction < 1 × 10^{-6} mol/mol by tuning the mass selective magnetic field to be centered on the mass 28 amu peak only. However, if we tune the magnetic field to the value at mass 29 amu peak for a certain fraction of the cycle, we can mix ^{29}Si into our ^{28}Si film. By controlling the dwelling times Δt_{28} (time spent on the mass 28 amu peak) and Δt_{29} (time spent on the mass 29 amu peak), we can control the amount of $^{29}Si^{+}$ deposited onto the sample. This periodic switching is achieved by using a pulse generator (DAQ with LABVIEW) to trigger an asymmetric square wave to control the output of the mass analyzer. The block diagram for the control is shown in Fig. 4.2 (b). The output of the mass analyzer, which contains both the magnet current and the switching periods, determines the mass positions and the dwelling times of the ion beam. Fig. 4.2 (a) and (c) demonstrate an example of the control parameters. The peak of the square wave (green) corresponds to the mass 28 amu peak ($^{28}Si^{+}$ only), at a magnet current of 50.6 A, with an ion current of 620 nA and Δt_{28} of 6 s. The valley of the square wave (red) corresponds to the mass 29 amu peak ($^{29}Si^{+}$ and $^{28}SiH^{+}$, where the ratio of ^{29}Si at this mass peak is approximately equal to the natural abundance ratio),

at a magnet current of 51.6 A, with an ion current of 124 nA and Δt_{29} of 2 s. These parameters would correspond to a ^{29}Si isotope fraction of 3000 ppm (3×10^{-3} mol/mol), with roughly 1 monolayer of Si deposited per cycle.

In this way, by tuning the dwelling times Δt_{28} and Δt_{29}, we are able to produce any desired enrichment level, ranging from natural abundance (4.7 % ^{29}Si) to our baseline (< 1×10^{-6} mol/mol ^{29}Si).The dwelling time Δt_{28} at mass 28 amu, and Δt_{29} at 29 amu can be any combination as long as it is within the response time of the analyzer power supply and the magnet, which is about 2 ms and 50 ms in the range of our interests, respectively. However, to ensure the epitaxial quality and homogeneity of the deposited ^{28}Si material, $\Delta t_{28} + \Delta t_{29}$ should be a short cycle, generally corresponding to less than a monolayer of material growth.

During deposition, the ion beam is tuned to its optimum fluence condition, where a SiH_4 flow rate of 0.02 sccm (corresponds to a chamber pressure of 1.87×10^{-4} Pa or 1.4×10^{-6} Torr) and a growth rate of about 1.0 to 1.5 nm/min [134] is used, as discussed in Chapter 3. Higher growth rate is also achievable using high pressure plasma mode of the ion source, but generally results in a higher surface roughness of the deposited film. The substrate temperature is chosen to be 450 °C, which produces the lowest baseline ^{29}Si isotope concentration and highest epitaxial film quality [133] for this experimental setup.

A model (assuming transport limited kinetics) is developed to calculate the isotope fractions of the deposited ^{28}Si layer, including the contributions from the background silane gas:

$$f^{29} = \frac{\Delta t_{29} \times D_{29} \times A + {}^{29}C_z \times (\Delta t_{29} \times D_{29} + \Delta t_{28} \times D_{28})}{(\Delta t_{29} \times D_{29} + \Delta t_{28} \times D_{28}) \times (1 + {}^{28}C_z + {}^{29}C_z + {}^{30}C_z)} \quad (4.1)$$

$$L = (\Delta t_{29} \times D_{29} + \Delta t_{28} \times D_{28}) \times \left(1 + {}^{28}C_z + {}^{29}C_z + {}^{30}C_z\right) \quad (4.2)$$

where f^{29} is the isotope fraction of ^{29}Si, L is the number of monolayers per cycle, D_{28} is the deposition rate of ^{28}Si at mass 28 amu peak current, D_{29} is the deposition rate at 29 amu peak current, A is the atomic percentage of ^{29}Si at 29 amu peak, which consists both $^{29}Si^+$ and $^{28}SiH^+$ ions. ${}^{28,29,30}C_z$ are the flux ratios from the background silane diffusion, which can be calculated using the equation derived from Ref. [23]:

$$^{x}C_z = \frac{F_g \times a_x \times s}{F_g \times s + F_i}, \quad (4.3)$$

where F_g is the silane gas flux and F_i is the ^{28}Si ion flux, s is the effective incorporation fraction and a_x is the natural abundance ratio of the corresponding silicon isotopes in SiH_4. In this experimental setup, since we are using a low SiH_4 pressure mode for ^{28}Si deposition, the background gas contribution is typically < 1 ppm (10^{-6} mol/mol) ^{29}Si, which has negligible impact on most of the enrichment levels but is still included in the calculation.

4.3 Targeted Enrichment Results

4.3.1 First-Generation of Targeted Enrichment

In each deposition, typically two or three layers of ^{28}Si with different enrichments are grown on one substrate based on the model described above, each with a layer thickness of about 100 nm. The experimental sequence is to choose a target value first, then estimate the value after deposition based on the actual experimental parameters and finally compare to the measured value using SIMS. It is worth

noticing that the ion beam growth condition might change a little during deposition due to ion source instability. Therefore, the estimated values calculated after deposition may deviate from the targeted values before deposition, but generally the deviation is small (5.7 % on average for the 2^{nd} generation). The comparison between the estimated values and the measured values are shown in Table III and V.

The isotope fractions of ^{28}Si, ^{29}Si and ^{30}Si as a function of layer thickness in the film and the substrate are measured using SIMS. Isotopic measurements of silicon were made in a CAMECA IMS-1270E7 large geometry secondary ion mass spectrometer. The samples were bombarded with a primary ion beam of O_2^+ ions at an impact energy of 8 keV and a current of 1 nA (for most of the samples). The beam was focused to a probe size of a few micrometers in diameter and it was raster-scanned over a 50 μm x 50 μm area. Positive secondary ions were accepted for detection from the central 20 μm x 20 μm portion of the rastered area as defined by a field aperture in a focal plane of the mass spectrometer. The entrance and exit slits of the spectrometer were selected to produce a mass resolving power of about 6000 ($M/\Delta M$ at 10 % of peak maximum). This resolving power is necessary to separate cleanly the ^{29}Si peak from the ^{28}SiH peak that is produced during the SIMS process. Under these conditions we estimate that less than 10^{-5} of the ^{28}SiH signal contributes to the ^{29}Si measurement. Depth profiles of the silicon isotopes ^{28}Si, ^{29}Si and ^{30}Si through a deposited film were acquired by monitoring ^{28}Si for 1 s, ^{29}Si for 10 s, ^{28}SiH for 1 s and ^{30}Si for 10 s in each data cycle and collecting a sufficient number of data cycles until the profile penetrated into the silicon substrate. The sputter rate as determined by measuring the final crater depths with a stylus profilometer was

approximately 0.16 nm/s under these conditions. The depths of only a few craters were measured, and the determined sputter rate was used to determine the depth scales for all profiles. In a few profiles the ion current was reduced to 0.5 nA to acquire a higher data density and the sputter rate was taken as half of the value for 1 nA. In those cases, the entrance slit was widened slightly to regain the same signal levels as with a 1 nA beam. Isotope ratios of $^{29}Si/^{28}Si$ and $^{30}Si/^{28}Si$ were calculated on a cycle-by-cycle basis. Average isotopic ratios for a film or a layer of a multilayer film were calculated by averaging the cycle-by-cycle ratio measurements in the portion of a profile where the ratios were at a relatively constant value. These values were then corrected for instrumental mass fractionation based on the differences between the measured ratios from a natural silicon wafer and the accepted natural values. Uncertainties were determined from the standard deviation of the mean of the measurements and were usually similar to Poisson estimations based on the total number of detected counts of the minor isotopes. In some cases, the minor isotope signals were not constant, and the standard deviations were larger than the Poisson estimates.

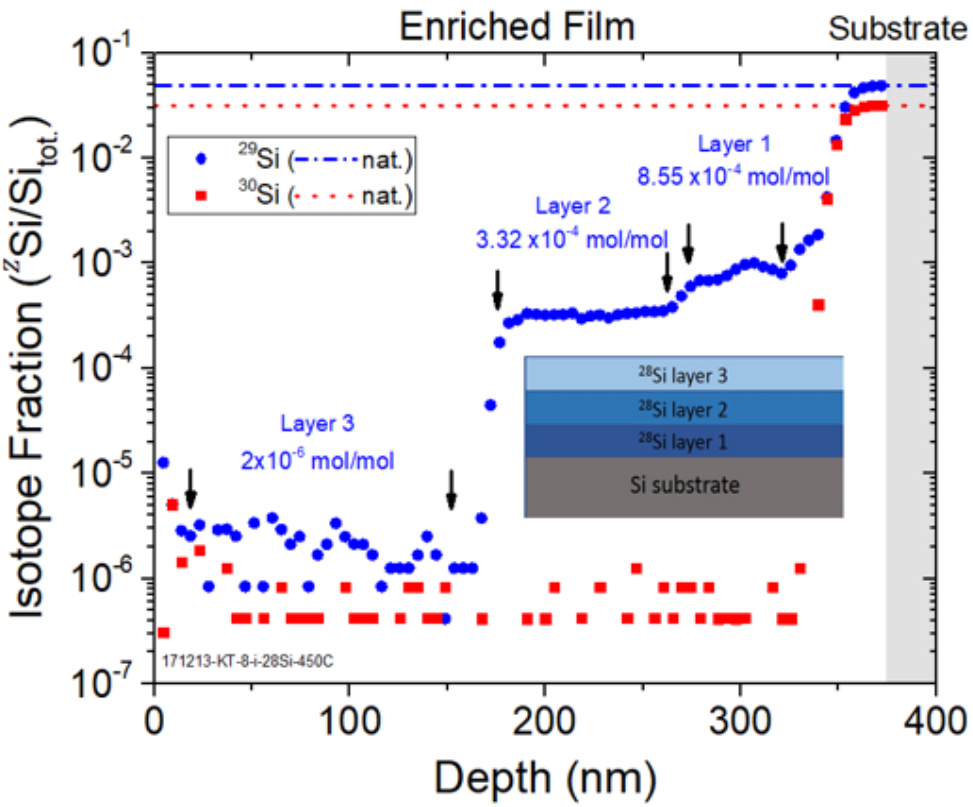

Figure 4.3: A SIMS depth profile of a first-generation targeted enrichment sample. The inset shows a schematic diagram of the targeted enrichment sample layer structures. Usually a few layers with different ^{29}Si isotope fractions are deposited on a float-zone silicon substrate and then capped with pure ^{28}Si layer. The ^{29}Si and ^{30}Si isotope fractions are shown in blue dots and red squares, respectively. Natural abundance ratios of ^{29}Si and ^{30}Si are shown in dashed lines.

Fig. 4.3 shows an example of the SIMS depth profile of the first-generation targeted enrichment samples, where three different enrichment levels can be distinguished. The SIMS measurements were taken near the center of the ^{28}Si deposit, which is usually the thickest, to match the parameters used in the model. The average isotope fraction of ^{29}Si in the surface layer (baseline) is measured to be (2.05 ± 0.46) × 10^{-6} mol/mol, from the range of 20 nm to 170 nm depth. From 0 nm to 20 nm, the higher values of ^{29}Si and ^{30}Si are due to the artifacts from the surface tail effect. This surface tail is formed because the sample has been exposed to air and contamination

during the transport from UHV chamber to the SIMS measurement. Those impurity atoms from surface contamination were pushed into the material by the primary ion beam of SIMS [142]. Two subsequent layers are also shown from 170 nm to 270 nm and 270 nm to 340nm, with an average ^{29}Si isotope fraction of $(332 \pm 5) \times 10^{-6}$ mol/mol and $(885 \pm 38) \times 10^{-6}$ mol/mol, respectively. The estimated values are 215×10^{-6} mol/mol and 460×10^{-6} mol/mol. The deviation is approximately within a factor of 2. Note that some fluctuations can be seen in layer 1, this is not due to the measurement error of SIMS since there is enough number of counts for measuring ^{29}Si (this is in contrast with < 1 ppm region where the fluctuation is largely due to insufficient atom counts). The reason for this fluctuation might be due to the instability of the ion source during deposition and it will be discussed in detail in the next section.

Four samples with different layers of enrichment are measured. The comparison between the targeted and measured ^{29}Si isotope fractions is shown in detail in Table. III and a correlation plot of the estimated versus the measured ^{29}Si isotope fraction is shown in Fig. 4.4. The range is shown from the baseline values (around 1 ppm of ^{29}Si) up to 10000 ppm. The data points generally follow the line of the linear fit, but the deviation between the estimated and measured values is still quite high, with an average of 57.77%. Improvements are needed to achieve a better control of the deposited samples.

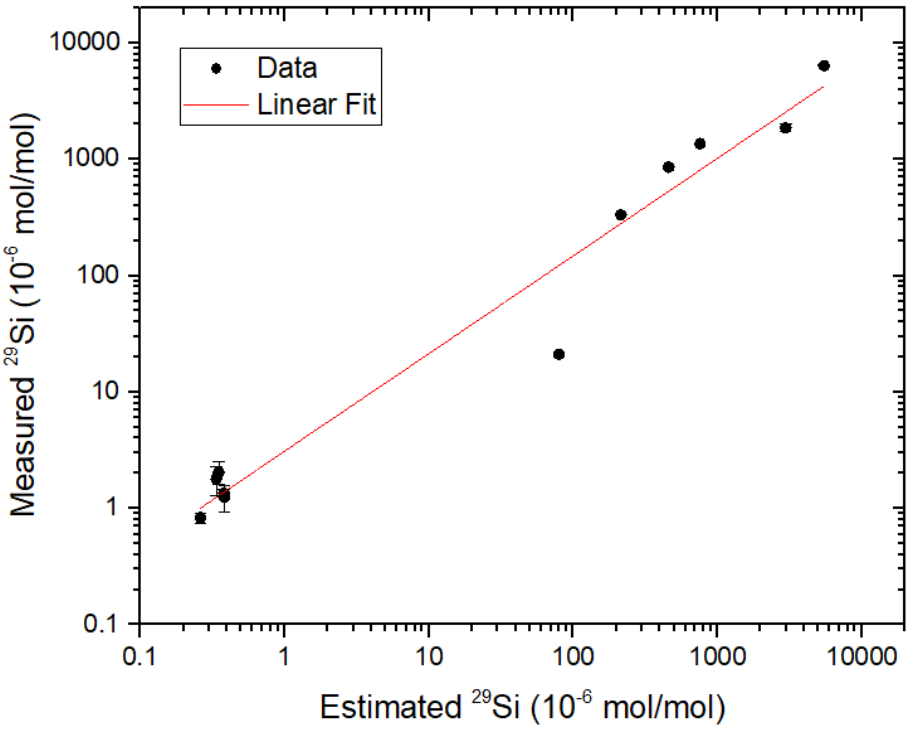

Figure 4.4: A correlation plot showing the measured ^{29}Si isotope fractions as a function of targeted ^{29}Si isotope fractions for the first-generation samples. The average total deviation from the estimated values is 57.8%.

Table III. A comparison between the estimated and measured ^{29}Si isotope fractions of the first-generation samples. The deviations shown here are between the estimated and the measured values. The total deviation on average is (57.8 ± 11.1) %.

Targeted (10^{-6} mol/mol)	Estimated from deposition (10^{-6} mol/mol)	Measured by SIMS (10^{-6} mol/mol)	Deviation
100	80	21	73.8%
200	215	332	54.4%
400	460	855	85.9%
800	760	1361	79.1%
3000	2988	1858	37.8%
6000	5500	6361	15.7%

4.3.2 Methods of Improvements

From the SIMS depth profile, we observed fluctuations in some of the deposited layers of ^{28}Si. We believe the main reason for this deviation is the instability of the ion source during deposition process. For example, the estimated values of enrichment depend largely on the deposition rate of the peak current D_{28} and D_{29}. Any changes in the ion current will result in a deviation from the estimated value. During deposition in the first-generation samples, we observed both gradual and abrupt changes in the total ion current ratio between mass 28 amu and 29 amu peaks. A gradual decrease of the ion current is likely due to the erosion of cathodes from the ion sputtering and precipitation of solids on the anodes inside the UHV Penning ion source. The cathode and anode material used was copper (Cu), which has a sputter yield of 5.41 atoms/ion using $^{28}Si^{+}$ with energy of 3 keV. This number is calculated using the simulation software "The Stopping and Range of Ions in Matter" (SRIM). Fig. 4.5 shows the pictures of the eroded anodes and cathodes. As the erosion happens, the shape of the anode and cathode changes during beam run. This will affect the geometry of the plasma formed and the efficiency of ions been extracted into the transport system, as observed as a gradual decrease in the ion current during deposition. As the service time gets longer, Si will be deposited and forms flakes at the surface of the Cu anodes and cathodes, as shown in the black materials in Fig. 4.5. Those flakes will alter the potential inside the ion source and will cause either an arc during beam run or even a short between the cathode and anode. Usually when a short happens, maintenance has to be done by breaking the vacuum and reassembling the ion source to replace anode and cathodes.

To improve the stability and lifetime of the ion source, different cathode materials are investigated. As compared to Cu, titanium (Ti), tungsten (W), iron (Fe), stainless-steel (SS) and molybdenum (Mo) all have smaller sputter yields when bombarded by Si ions. However, other properties also need to be considered when depositing ^{28}Si thin films, such as the price of the material, ease of machining, chemical purity, alloying, etc. Table IV. shows a summary of the SRIM simulation result with three candidate materials. Ti is chosen to be the new anode and cathode material because it has the lowest sputter yield and highest purity (99.999%), with relatively low cost. High purity Ti rods with 3 cm in diameter and 5 cm in length are purchased from American Elements and are machined into cylindrical anodes and cathodes.

Table IV. Summary of the SRIM results on different anode and cathode materials. The ion energy of the Si^+ used in the simulation is 3 keV, with 10000 ions in total.

Material type	Atomic mass (u)	Density (g/cm^3)	Sputter yield (atoms/ion)
Cu	63.54	8.92	5.41
W	183.8	19.35	2.09
Ti	47.9	4.52	1.42

Fig.4.5 shows a comparison between the anodes and cathodes using Cu and Ti after hours of service. Panel (a) and (b) are the Cu cathodes and anti-cathodes used in the ion source after 26 hours of service. Due to ion bombardment, the center of the cathode rings was eroded. Si flakes (shown as dark deposit on Cu) adhered on the cathode surfaces were also observed after long hours of service. The average lifetime of a Cu anode/cathode before maintenance is ≈ 21 hours. Either a low ion current or a

short between anode and cathode was experienced, indicating the need for maintenance.

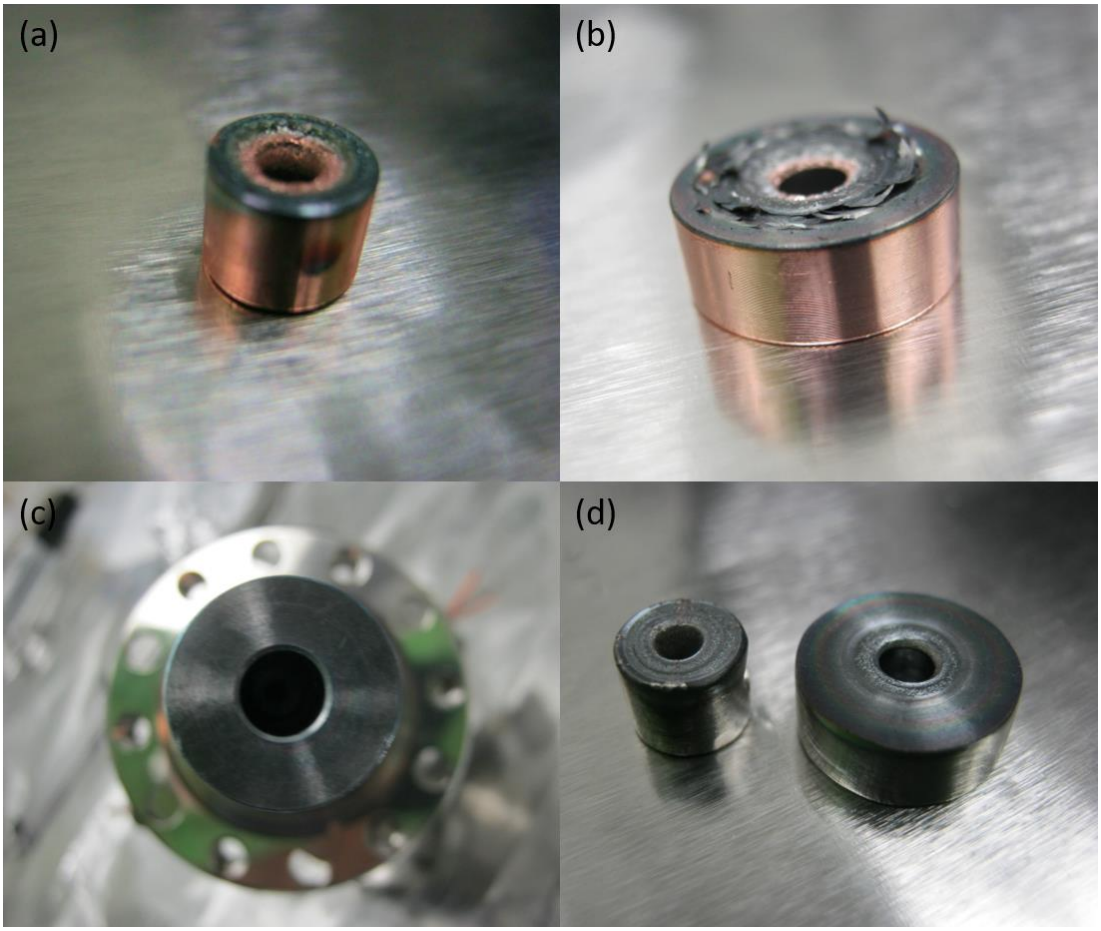

Figure 4.5: Ion source anodes and cathodes after hours of beam runs.
(a) and (b) are the copper cathodes after 26 hours of service. Erosion from the ion bombardment at the center of the cathode rings can be seen, with some silicon flakes adhered on the surface. (c) and (d) are the titanium anode and cathodes, respectively, after 37 hours of service. Less erosion is observed on titanium, with less Si flakes adhered on the surface. Titanium anodes and cathodes in general have a longer (2×) lifetime and better stability.

Panel (c) and (d) showed the anode and cathodes made of high purity Ti, respectively, after 37 hours of service. Less erosion and less Si flakes were observed. The average lifetime using Ti is ≈ 38 hours, roughly 2× longer than using Cu. This also means

better stability in terms of ion current. A smoother ion current with less fluctuation and slower decrease rate is obtained with Ti anodes and cathodes.

Another factor that affects the accuracy of the prediction for targeted enrichment is the ion current measurement. In the first-generation samples, the ion current was measured using a large aperture of 4.9 mm^2. This introduces uncertainty because the SIMS crater is measuring at the center of the beam spot (<< 1 mm^2) while using a larger aperture is estimating the average over a larger area. And as we introduced in Chapter 2, the contour map of the ion beam shape shows a higher ion density closer to the center compared to the edges. To solve this problem, a smaller aperture with 0.785 mm^2 is used to estimate the ion current in the second-generation samples. This allows better estimation because the area of the ion current density used to calculate the enrichment is closer to the area measured by SIMS. In addition, the ion current is measured both at the beginning and at the end of the deposition to account for any changes in the ion current (28 amu and 29 amu) peak shapes due to long deposition times.

4.3.3 Second-Generation of Targeted Enrichment

With the improvements in both ion source stability after replacing the cathode materials and ion current measurement, better accuracy between target and measured enrichment values has been achieved in the second-generation targeted enrichment samples. Fig. 4.6 is an example of the SIMS depth profile of a second-generation targeted enrichment sample. The average isotope fraction of ^{29}Si in the surface layer (baseline) is measured to be $(0.83 \pm 0.09) \times 10^{-6}$ mol/mol, from the range of 30 nm to

170 nm depth. Two subsequent layers are also shown from 170 nm to 310 nm and 310 nm to 417 nm, with an average ^{29}Si isotope fraction of (1599 ± 7) × 10^{-6} mol/mol and (3583 ± 20) × 10^{-6} mol/mol, respectively. The targeted values are 1600 × 10^{-6} mol/mol, with a deviation (compared to the measured value) of 0.06 % and 3500 × 10^{-6} mol/mol, with a deviation of 2.4 %.

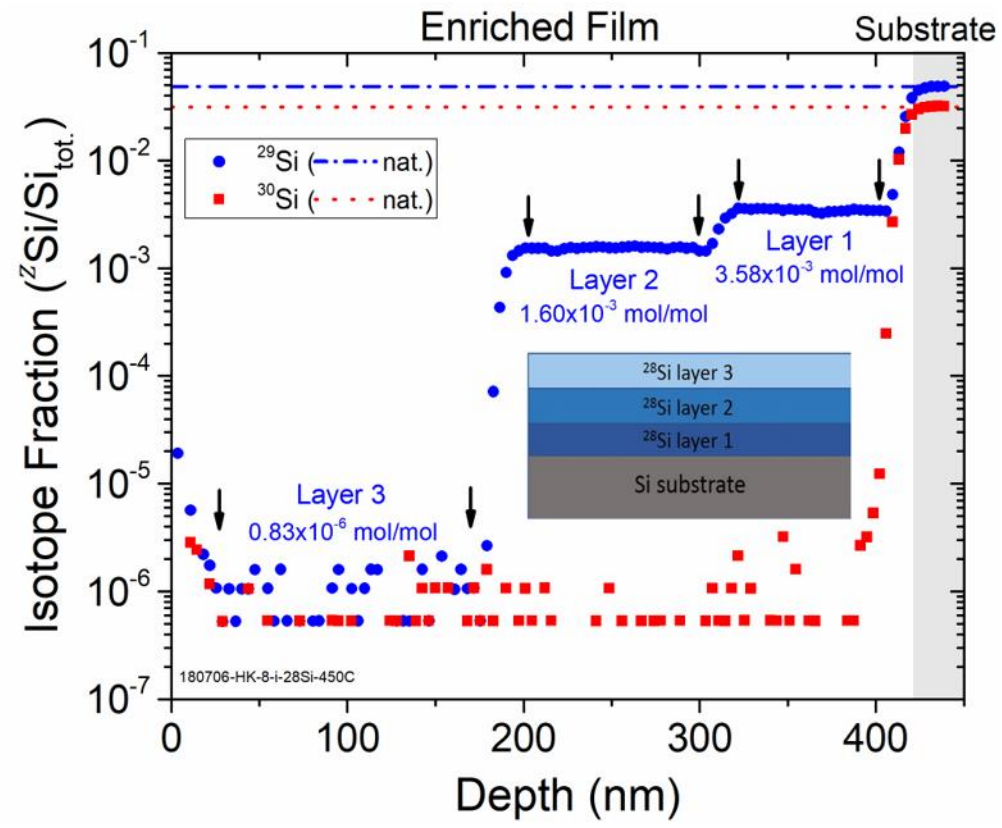

Figure 4.6: A SIMS depth profile of a second-generation targeted enrichment sample. The inset shows a schematic diagram of the targeted enrichment sample layer structures. Two layers with different ^{29}Si isotope fractions are deposited on a float-zone silicon substrate and then capped with pure ^{28}Si layer. The ^{29}Si and ^{30}Si isotope fractions are shown in blue dots and red squares, respectively. Natural abundance ratios of ^{29}Si and ^{30}Si are shown in dashed lines. Better stability is seen in each layer with a flatter ^{29}Si concentration profile.

Table V. A comparison between the target, estimated and measured ^{29}Si isotope fractions. The deviation shown here are between the target and the measured values. The total deviation on average is (10.4 ± 5.0) %.

Target (10^{-6} mol/mol)	Estimated from deposition (10^{-6} mol/mol)	Measured by SIMS (10^{-6} mol/mol)	Deviation
1	0.7	0.83	17.0%
10	9.9	10.5	5.0%
30	34.1	30	0.0%
40	40.7	20.5	48.8%
60	62.1	81	35.0%
75	77	74	1.3%
90	88.1	87	3.3%
300	316	300	0.0%
800	797	784	2.0%
1600	1630	1599	0.1%
3500	3530	3583	2.4%

As a comparison, the estimated values from the model after deposition are calculated to be (1630 ± 15) × 10^{-6} mol/mol, with a deviation of 1.9 % and (3530 ± 30) × 10^{-6} mol/mol, with a deviation of 1.5 %.

The comparison between the target and measured ^{29}Si isotope fractions is shown in detail in Table. V and a correlation plot of the targeted versus the measured ^{29}Si isotope fraction is shown in Fig. 4.7. In total, 11 targeted enrichment levels have been plotted on a log scale, ranging from 0.83 × 10^{-6} mol/mol to 3583 × 10^{-6} mol/mol of ^{29}Si. Both a linear fit and a confidence band in log-log scale are included to show the accuracy of the prediction. As shown in the figure, all data points are within 95 % confidence band. The average deviation between the targeted and measured enrichments across the entire range of measurements is found to be 10 %. The one data point measured at 20 × 10^{-6} mol/mol has the largest deviation from the targeted value and the largest relative uncertainty. This deviation was caused by the ion

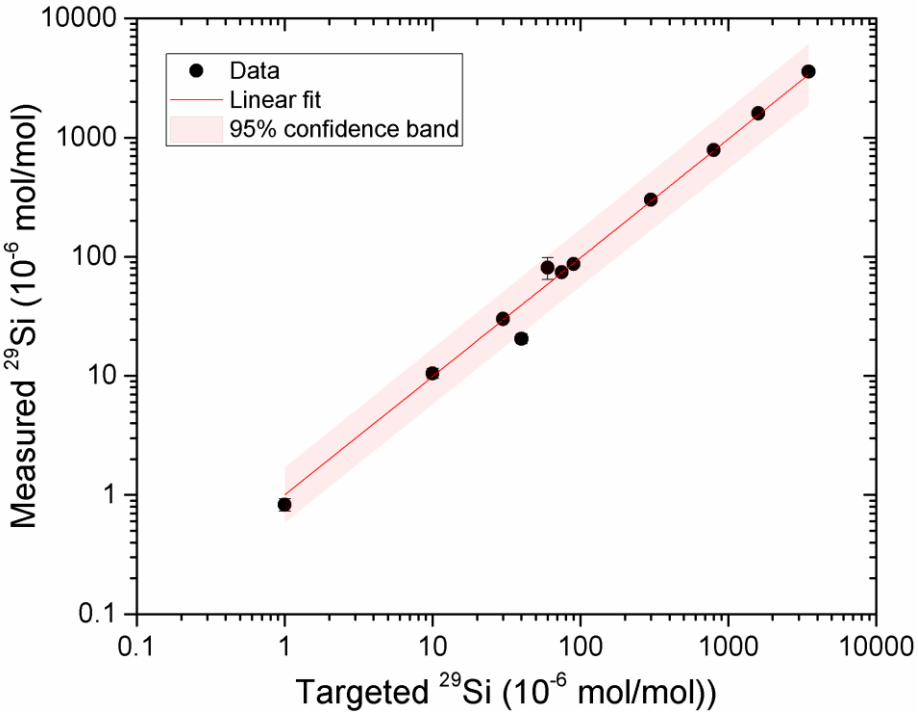

Figure 4.7: A correlation plot showing the measured ^{29}Si isotope fractions as a function of targeted ^{29}Si isotope fractions.
A linear fit and 95 % confidence band are included to assist comparison. An average deviation of 10 % has been obtained over a wide range, from 0.83×10^{-6} mol/mol to 3.58×10^{-3} mol/mol of ^{29}Si.

source, where the ion beam condition was unstable during this deposition compared to others. To further improve the stability of the ion source, cleaning of the ion source using argon plasma between each run may be helpful. This will remove excess silicon flakes that slowly aggregated on the interior of the ion source, which causes fluctuation in the plasma region. Another source of uncertainty may come from the location of the ^{28}Si spot. Since our ^{28}Si deposit is in the shape of a hill instead of flat surface, the measured location might still be different from where it has been estimated, even with a smaller aperture. For example, if the measured spot is closer to the edge, the ion current density will be smaller compared to the center of the beam spot. This usually results in a higher ^{29}Si concentration, partially from the background

silane gas (since the background pressure is constant) and partially from the slight changes in the 28 amu and 29 amu peak shapes. The installation of an ion beam sweeper to smooth out the deposited film may help. Furthermore, the SIMS measurement uncertainty also acts as a factor, mainly limited by counting statistics, especially at lower ^{29}Si concentrations, where the number of counts is dramatically lower compared to higher ^{29}Si concentrations.

4.4 Conclusion

In this chapter, we have reported on a method that allows us to achieve targeted enrichment of the ^{28}Si epitaxial thin films. We have developed a model to predict and control the residual isotope fraction of the ^{29}Si in the film precisely and compare its results to the values measured using SIMS. The first-generation of targeted enrichment showed a relatively good accuracy, within a factor of 2 compared to the targeted values. With the improvements in ion source stability and ion current measurement, we have achieved an excellent agreement between the targeted and the measured values over a wide range of enrichments in the second-generation samples, with small deviation of only 10 % on average. This deviation can be improved by further increasing the stability of our ion source and possibly by using an ion beam sweeper. We believe this is an important step forward to enrich the material supply of ^{28}Si at different levels within this community and to explore the qualifying metric for "quantum grade" silicon in terms of enrichments.

This chapter is reproduced from Ref. [143] with permissions from all the co-authors.

Chapter 5: Potential Qualifying Metrics for "Quantum Grade" Silicon - ^{28}Si MOSFET

Across solid state quantum information, material deficiencies limit performance through enhanced relaxation, charge defect motion, or isotopic spin noise. While classical measurements of device performance provide cursory guidance, specific qualifying metrics and measurements applicable to quantum devices are needed. For quantum applications, new material metrics, e.g., enrichment, are needed, while existing classical metrics such as mobility might be relaxed compared to conventional electronics. In this chapter, we examine locally grown silicon that is superior in enrichment, but inferior in chemical purity compared to commercial-silicon, as part of an effort to underpin the material standards needed for quantum grade silicon and establish a standard approach for the inter-comparison of these materials. We use a custom, mass-selected ion beam deposition technique, which has produced isotopic enrichment levels up to 99.999 98 % ^{28}Si, to isotopically enrich ^{28}Si, but with chemical purity of only > 99.97% due to the molecular beam epitaxy techniques used. From this epitaxial silicon, we fabricate top-gated Hall bar devices simultaneously on ^{28}Si and on the adjacent natural abundance Si substrate for inter-comparison. Using standard-methods, we measure maximum mobilities of ≈ (1740 ± 2) cm^2/Vs at an electron density of ($2.7 \times 10^{12} \pm 3 \times 10^8$) cm^{-2} and ≈ (6040 ± 3) cm^2/Vs at an electron density of ($1.2 \times 10^{12} \pm 5 \times 10^8$) cm^{-2} at T = 1.9 K for devices fabricated on ^{28}Si and ^{nat}Si, respectively. For magnetic fields B > 2 T, both devices demonstrate well developed Shubnikov-de Haas oscillations in the longitudinal

magnetoresistance. This provides the transport characteristics of isotopically enriched ^{28}Si and will serve as a benchmark for the classical transport of ^{28}Si at its current state and low temperature, epitaxially grown Si for quantum devices more generally.

5.1 Introduction

Conventional electronics have been industrialized for decades; consequently, precise metrics based on macroscopic properties, such as chemical purity, charge carrier mobility, and defect density, are established for qualifying a material, e.g., silicon, for conventional electronics. While silicon has long been the workhorse of conventional electronics, it is also becoming a promising host for spin based quantum information processing devices [21, 136].

Even though silicon has improved tremendously over the decades to meet demands of today's state-of-the-art transistors, this excellent material is still not sufficient to support quantum information. For example, in spin-based quantum information systems, the presence of the ^{29}Si isotope in natural abundance silicon reduces coherence times due to its nonzero nuclear spin of $I = 1/2$. Nuclei with nonzero spin in the host lattice act as a source of decoherence for spin based qubits [135], as they interact with the electron spin through hyperfine interactions [144, 145]. However, by placing a spin qubit in an isotopically enriched 99.995% ^{28}Si environment [40], the development of silicon based quantum devices has gained considerable momentum, with reports of exceptionally long quantum coherence times [30, 34].

The need for some level of enrichment provides an example of how "semiconductor grade" silicon quality may be necessary but is not sufficient to meet the needs of quantum information processing (QIP). Furthermore, the metrics for conventional silicon may not always be relevant for QIP, e.g., the ease of carrier motion as quantified by mobility may not be directly relevant to quantum device performance where confinement and coherence in the absence of motion are critical. Additionally, as we establish properties and their numerical thresholds that are sufficient for QIP, relatively simple qualifying metrics that act as general proxies for properties more challenging to measure are invaluable. However, it may be noted that mobility in and of itself is not important, but it could be a good proxy for estimating spin-qubit relaxation or coherence [146].

As part of a larger program to identify and quantify "quantum grade" silicon, we are identifying (1) properties beyond those considered for semiconductor grade silicon critical to QIP; (2) the relevance and priority of properties currently considered critical for semiconductors; and (3) standard methods that may be used for QIP properties or provide a general indicator for challenging properties, e.g., coherence time, as three main goals that are paramount for the development of metrics for "quantum grade" silicon. This work is part of a broader effort to find ways besides making and measuring qubits to provide diagnostics that will indicate the likely performance of qubits early in a fabrication stream.

This chapter presents devices, methods, and results for a comparative study of magnetotransport properties between (1) high isotopic enrichment, low chemical purity and (2) high chemical purity, natural abundance (low isotopic enrichment)

silicon. This characterization sets the stage for determining whether coherence properties in quantum dot devices correlate with the trends in simpler, traditional measurements since the benefit of enrichment on coherence may outpace the liability of some additional contaminants. In a detailed theoretical study, Witzel et al. [147] illustrated that the coherence of a spin qubit can, in principle, be increased by an order of magnitude for every order of magnitude increase in the isotopic enrichment of ^{28}Si in the qubit's Si environment. A comprehensive experimental investigation of this prediction, however, is hindered due to the discreteness of the available isotopic enrichment levels. Among the four different enrichment levels that have been reported [40, 148-150] only 99.98% ^{28}Si and 99.995% ^{28}Si have been utilized for quantum electronic device fabrication [29, 30, 139]. Moreover, contemporary methods for producing isotopically enriched ^{28}Si materials are based on chemical vapor deposition (CVD) techniques and are not compatible with qubit architectures requiring low temperature processing, e.g., STM fabricated single dopant atom qubits [151]. In contrast, the method used for producing ^{28}Si reported here is compatible with all the contemporary qubit architectures and represents molecular beam epitaxy (MBE) grown Si more generally. While the coherence of a spin qubit is predicted to improve at higher isotopic enrichment levels [147], how other material properties will limit the expected enhancement of qubit coherence is unclear. To the best of our knowledge, no study yet has attempted to correlate macroscopic electrical characteristics with the performance of quantum devices. Yet, such a study will be an essential component for defining metrics for "quantum grade" silicon within the three main goals identified earlier.

5.2 ^{28}Si MOSFET Devices

The ^{28}Si materials are produced using the ion beam deposition method introduced in Chapter 2 and 3. Gated Hall bar devices are fabricated on isotopically enriched ^{28}Si epilayers in order to electrically characterize the material. Typically, the isotopically purified ^{28}Si spot is ≈ 4 mm^2 – 8 mm^2 in area and covers only a small fraction of the starting float-zone grown, natural abundance, intrinsic Si substrate with dimensions of 4 mm × 10 mm; see Fig. 5.1 (a). Due to the reduced coverage of the ^{28}Si spot, devices on isotopically enriched and natural abundance Si can be fabricated on the same Si chip at the same time. This eliminates the effect of certain imperfections on the fabrication process (e.g., oxide growth) when comparing the electrical properties of the devices. A schematic cross section of a device fabricated on a ^{28}Si spot is shown in Fig. 5.1 (b). The structure of the devices fabricated on ^{nat}Si, i.e., outside the ^{28}Si spot, is identical (went through sample vacuum, thermal and fabrication processes) except without the ^{28}Si layer. An optical micrograph of the gated multiterminal Hall bar device is shown in Fig. 5.1 (c).

The isotope fraction of the ^{28}Si epilayers is measured by SIMS. In Fig. 5.1 (d), the SIMS-derived isotopic ratio of ^{29}Si/^{28}Si is shown as a function of depth at several locations near the fabricated Hall bar device. For the device reported here, the level of isotopic enrichment measured at locations 1, 2, and 3 corresponds to ≈ 99.976 %, ≈ 99.980 %, and ≈ 99.993 % ^{28}Si, respectively. This confirms that the Hall bar device is located on top of the deposited ^{28}Si spot as we expected. Figure 5.1 (d) also reveals

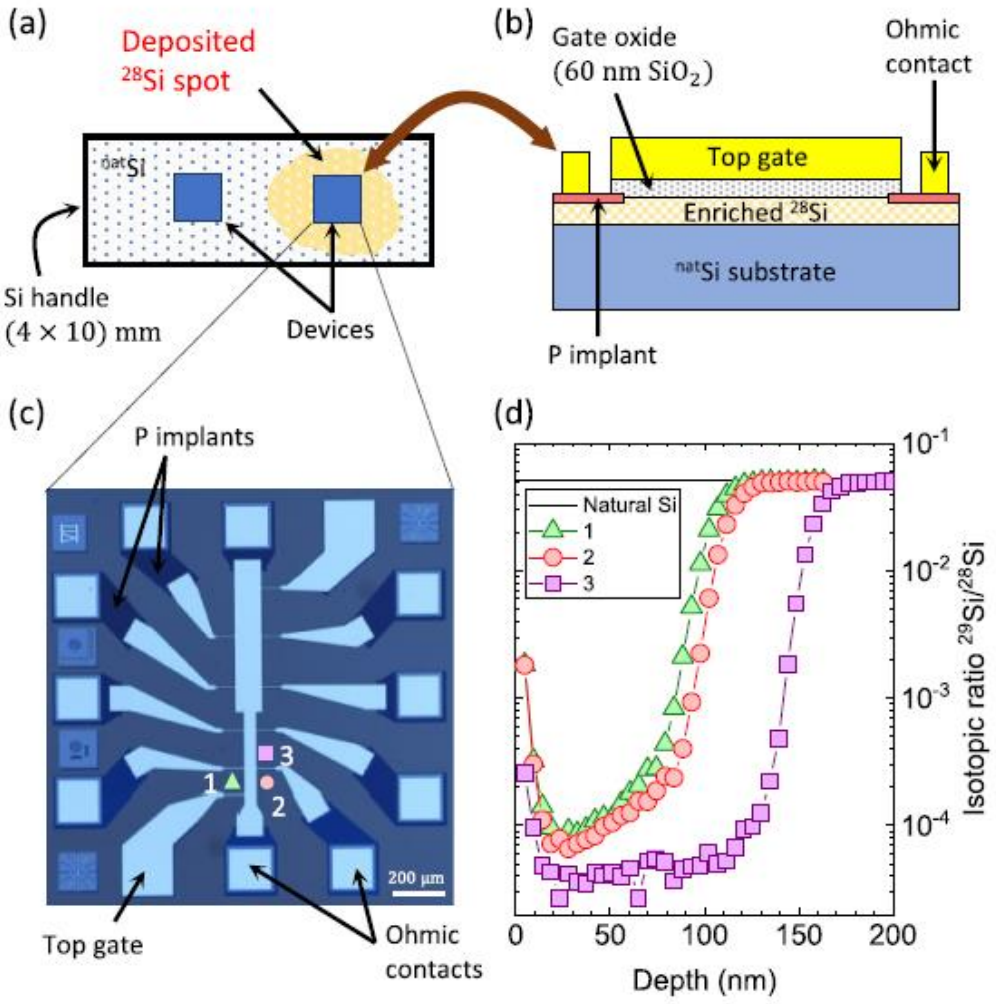

Figure 5.1: ^{28}Si MOSFET device and measurements.
(a) A schematic illustrating the device layout of a given sample. Reduced coverage of the ^{28}Si spot allows us to fabricate devices on ^{28}Si and ^{nat}Si simultaneously. (b) Schematic representation of the gated Hall bar device fabricated on ^{28}Si is shown. (c) An optical micrograph of a gated multiterminal Hall bar device fabricated on ^{28}Si is shown. (d) The isotopic ratios of ^{29}Si/^{28}Si at positions 1 (△), 2 (○), and 3 (□) in (c) are shown. The shift in the rising edge at different positions corresponds to the thickness variation in the deposited ^{28}Si film. Measured ^{29}Si isotopic ratios at locations 1, 2, and 3 are $(149 \pm 18) \times 10^{-6}$ mol/mol, $(128 \pm 14) \times 10^{-6}$ mol/mol, and $(45 \pm 2) \times 10^{-6}$ mol/mol, respectively.

the thickness nonuniformity of the deposited ^{28}Si epilayer, i.e., the thickness of the ^{28}Si epilayer at location 3 is greater than those of locations 1 and 2. Moreover, separate SIMS measurements on these isotopically enriched ^{28}Si epilayers reveal that

the films contain adventitious chemical impurities, namely, C, N, and O, with approximate atomic concentrations of 2×10^{19} cm^{-3}, 3×10^{17} cm^{-3}, and 3×10^{18} cm^{-3}. However, the atomic concentrations of these chemical impurities on the handle wafer were below the SIMS detection limit ($\leq 10^{16}$ cm^{-3}). We believe that these chemical impurities were being introduced by the ion beam.

5.3 Magnetotransport Measurements

The low field magnetotransport data of ^{28}Si and ^{nat}Si on the same sample are shown in Fig. 5.2. Panel (a) shows the drain current (top and bot end of the Hall bar as shown in Fig. 5.1(c)) vs gate voltage at T = 4K. The drain current is proportional to inversion charge and the velocity that the charge travels from source to drain and the gate voltage controls the amount of inversion charge that carriers the current. Three curves with different symbols (square, circle and triangle) show the corresponding source drain voltage and a threshold voltage (V_G needed to turn on the device) is obtained at around 2 V. Panel (b) shows the extracted charge carrier mobility as a function of carrier density for both ^{nat}Si (red square) and ^{28}Si (blue circle) at T = 1.9 K. We find that maximum mobilities at T = 1.9 K for ^{28}Si and ^{nat}Si are: μ_{28Si} = (1740 ± 2) cm^2/V·s at an electron density n of ($2.7 \times 10^{12} \pm 3 \times 10^8$) cm^{-2} and μ_{natSi} = (6040 ± 3) cm^2/V·s at an electron density of ($1.2 \times 10^{12} \pm 5 \times 10^8$) cm^{-2}. Charge carrier mobilities for these devices are within the typical range of mobilities for Si-MOS (Metal Oxide Semiconductor) devices fabricated using non-MBE (e.g., CVD) growth techniques [23, 152], the maximum mobility for a Si-MOS device to date being > 4×10^4 cm^2/V·s [153]. In contrast, mobilities reported for Si-MOS devices fabricated on

MBE grown Si range from 900 $cm^2/V{\cdot}s$ to 1250 $cm^2/V{\cdot}s$ [116, 154], likely due to the excess chemical impurities presented in the MBE film.

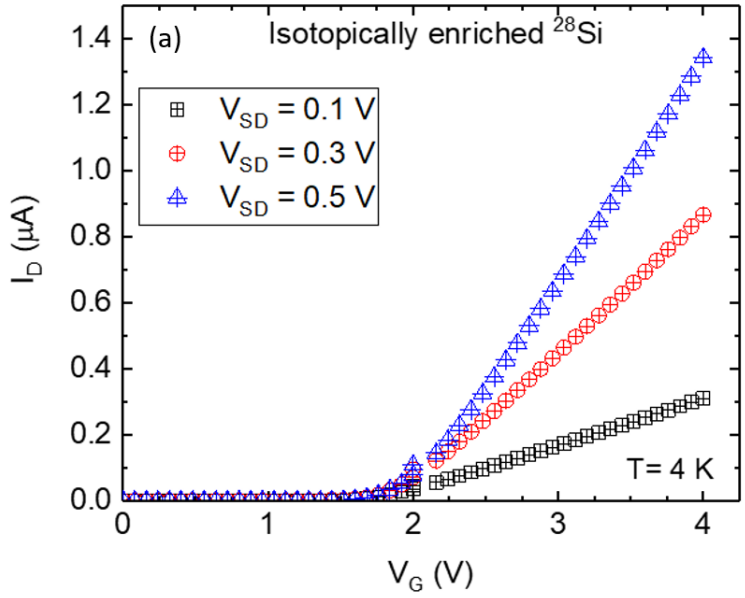

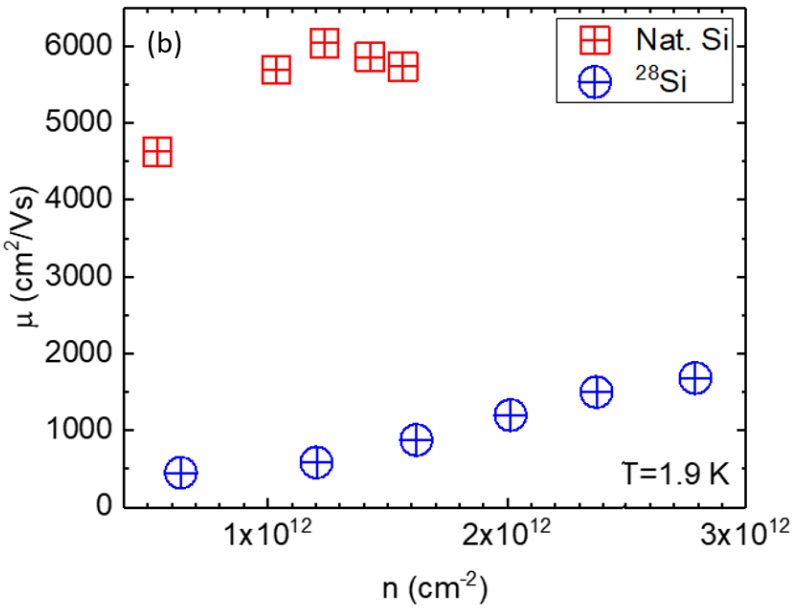

Figure 5.2: Magnetotranport data of the ^{28}Si MOSFET.
(a) the drain current vs gate voltage at T = 4 K. Three curves with different symbols shows the corresponding source drain voltage. (b) Charge carrier mobility as a function of carrier density for both ^{nat}Si (red square) and ^{28}Si (blue circle) at T = 1.9 K.

Table VI. Macroscopic materials and electrical properties of natural abundance ^{nat}Si, and isotopically enriched ^{28}Si.

Property		Material: ^{nat}Si	Material: ^{28}Si
Avg. ^{28}Si concentration		92.23%	99.983%
Impurities (cm^{-3})	C	$\leq 10^{16}$	2×10^{19}
	N		3×10^{17}
	O		3×10^{18}
Max. mobility μ ($cm^2/(V\,s)$)		(6040 ± 3)	(1740 ± 2)
Percolation density n_p (10^{11} cm^{-2})		(2.3 ± 2)	(4.2 ± 2)

In order to estimate the percolation electron density n_p which refers to the critical density for conduction, we extrapolate the electron density as a function of gate voltage (as determined from Hall measurements) back to the threshold voltage (as determined from the channel current I_{sd} vs V_g), i.e., $n_p = n_e(V_{th})$. Using this method, we find percolation densities of $(2.3 \pm 2) \times 10^{11}$ cm^{-2} for ^{nat}Si and $(4.2 \pm 2) \times 10^{11}$ cm^{-2} for ^{28}Si. Since the percolation density is a measure of the disordering of a system, the two times larger density in ^{28}Si supports the fact that there are more impurity scatterings in the film than in ^{nat}Si. A summary of these macroscopic materials and electrical properties for the on-chip ^{nat}Si and ^{28}Si is provided in Table VI.

The magnetoresistance (R_{xx}) and the Hall resistance (R_{xy}) at 1.9 K for isotopically enriched ^{28}Si and natural abundance Si are shown in Fig. 5.3 (a) and Fig. 5.3 (b), respectively. Both devices show well developed SdH oscillations in R_{xx} with accompanying plateaus in R_{xy}. SdH oscillations are oscillations of the resistivity

parallel to the current flow in the edge states of a 2D electron gas when an external magnetic field is applied. They are related to the quantum-Hall effect and have a periodicity of $1/B$. When a magnetic field is applied to the 2D electron gas, the electrons in the bulk perform circular motions. In the border region, the electrons circular motion is suppressed due to the scattering events occurred at the interface. These scattering events give those electrons a higher energy and the magnetic field causes the quantization of the energy band (Landau-level). With a higher magnetic field, the energy gap between the Landau-levels becomes larger. As the field increases, the highest Landau-level gets nearer to the Fermi energy and there will be states available for scattering in the bulk region. This is the cause of the peaks in the SdH oscillations. The slight asymmetry in R_{xx} in Fig. 5.3 (a) could be due to several reasons, e.g., magnetic impurities in the grown ^{28}Si film or inhomogeneity of the magnetic field which might be a cause of the non-planar 2D electron gas [155, 156]. The Hall resistance shows nonidealities particularly in the ^{nat}Si device [Fig. 5.3 (b)] where R_{xy} is nonmonotonic. These nonidealities could be due to scattering between discrete degenerate states at the tails due to level broadening [157, 158]. However, a detailed discussion of the asymmetry of R_{xx} and the flatness of the Hall plateaus is outside the scope of this article. We also see a lifting of the four-fold degeneracy at $B > 5$ T for ^{nat}Si, which is likely due to the spin degree of freedom, but, at this time, we are unable to determine whether this is due to the spin or valley degree of freedom, due to the limitations in the experimental setup.

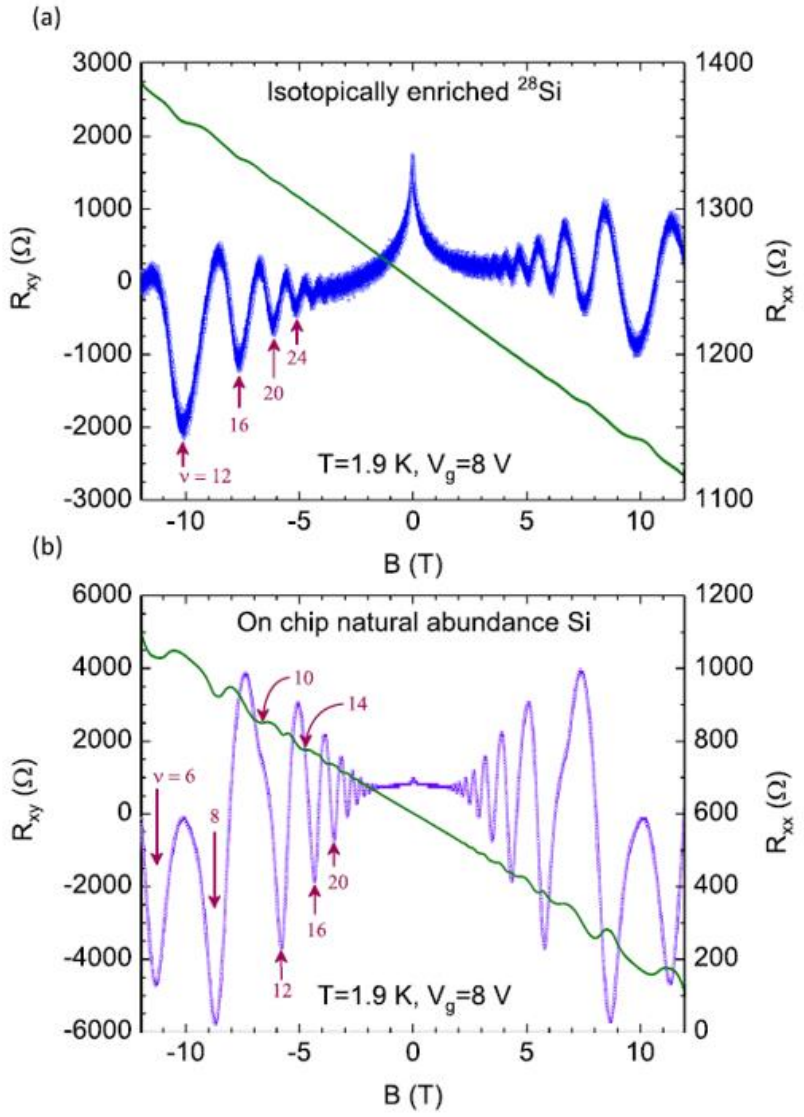

Figure 5.3: The magnetoresistance R_{xx} and the Hall resistance R_{xy} vs B field. The resistances measured for the devices fabricated on (a) isotopically enriched ^{28}Si epi-layer and (b) natural Si substrate are shown. For both devices, the corresponding filling factors (ν) are shown at the minima of Shubnikov-de Hass oscillations. In contrast to the device on the isotopically enriched ^{28}Si epi-layer, the device on ^{nat}Si demonstrates spin-splitting for $B > 3$ T. Both devices are fabricated on the same Si chip; see main text for more information. The relative uncertainty associated with R_{xx} and R_{xy} is typically less than 0.1% and is mostly due to the uncertainty of the measured current.

Near zero magnetic field, both devices demonstrate a peak in the sample resistance; see Fig. 5.3. This increase in resistance near zero magnetic field is known

as weak localization (WL). Weak localization is a quantum mechanical phenomenon that can be observed in two-dimensional (2D) electron systems at low temperatures where the phase coherence length (l_ϕ) is greater than the mean free path (l) [159, 160]. Relative to the zero-field resistance, the weak-localization is larger for the device fabricated on isotopically enriched ^{28}Si.

To further investigate the WL behavior of these devices, we plot the change in conductivity $\Delta\sigma_{xx}$ as a function of magnetic field B applied perpendicular to the 2D electron system (see Fig. 5.4). The change in conductivity due to WL $\Delta\sigma_{xx} = \sigma_{xx}(B) - \sigma_{xx}(B = 0)$, where $\sigma_{xx} = \rho_{xx}/(\rho^2_{xx}+\rho^2_{xy})$. For nonzero B, the change in conductivity due to WL in a 2D electron system can be modeled by the Hikami-Larkin-Nagaoka (HLN) equation [161]:

$$\Delta\sigma_{xx}(\mathrm{B}) = \alpha\left(\frac{e^2}{2\pi^2\hbar}\right)\left[\Psi\left(\frac{1}{2}+\frac{\hbar}{4el_\phi^2 B}\right)-\Psi\left(\frac{1}{2}+\frac{\hbar}{2el^2 B}\right)-ln\left(\frac{l}{2l_\phi}\right)\right] \qquad (5.1)$$

where Ψ is the digamma function, l is the mean free path, l_Φ is the phase coherence length that determines the magnitude of the effect, and α is a constant close to unity, which comes from the scattering symmetry of the system [162]. In Fig. 5.4, the solid lines are the fits to experimental data (symbols) using the HLN equation. For these fits, we use the calculated values of l using the relation $l = \sqrt{2D\tau}$. Here, D is the diffusion coefficient defined as $D = v^2_F\tau/2$, where the Fermi velocity $v_F = \hbar k_F/m^*$ and τ is the elastic scattering time, also known as the transport lifetime, defined as $\tau = \mu m^*/e$. The effective mass m^* is defined as $m^*/m_0 = 0.19$, where m_0 is the rest mass of an electron [163, 164]. The Fermi wavevector k_F can be calculated for a 2D electron system in Si as $k_F = (4\pi n_{2D}/g_s g_v)^{1/2}$, where n_{2D}, g_s and g_v are the charge carrier density, spin degeneracy and valley degeneracy,

respectively. We leave α and l_ϕ as the free fitting parameters, constraining the value of α to be close to unity. From the fit-extracted values of l_ϕ, we calculate $1/\tau_\phi$, where inelastic scattering time $\tau_\phi = l^2\phi/D$. The fit derived values of $1/\tau_\phi$ as a function of T are plotted in the inset of Fig. 5.4 for devices fabricated on isotopically enriched ^{28}Si and natural abundance Si, respectively. The solid lines in the inset of Fig. 5.4 are the least-squares-fit to the data using the equation:

$$\frac{1}{\tau_\phi} = a + bT + cT^2 \tag{5.2}$$

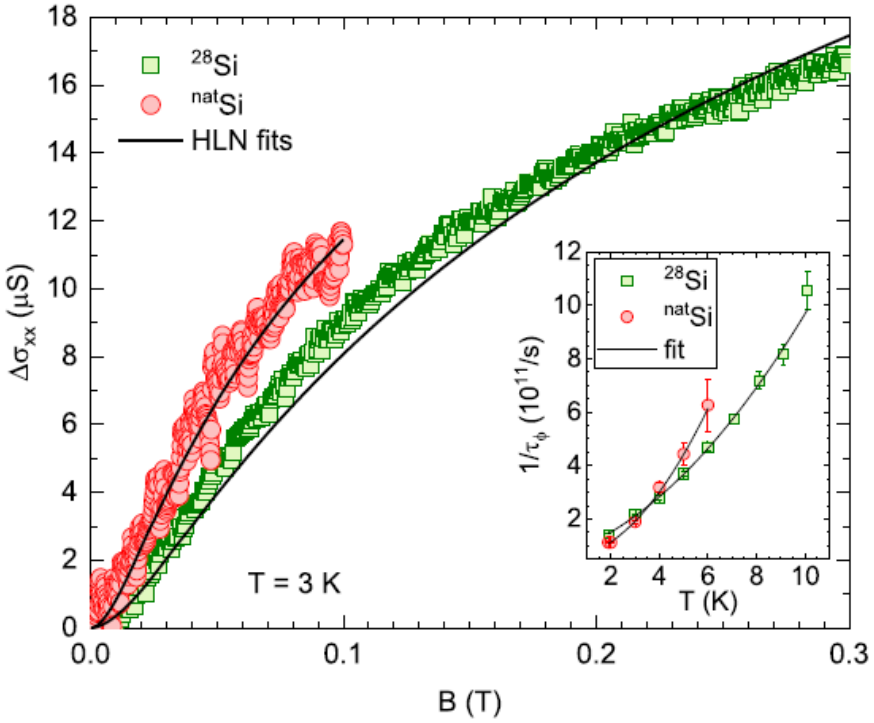

Figure 5.4: The change in conductivity ($\Delta\sigma_{xx}$) vs external magnetic field (B) for devices fabricated on ^{28}Si (□) and ^{nat}Si (○) measured at 3 K. Solid lines are the least-squares-fits to the HLN equation [Eq. (1)]. Estimated uncertainty for $\Delta\sigma_{xx}$ is < 0.3 %. Inset: The inelastic scattering rates ($1/\tau_\phi$) for ^{28}Si and ^{nat}Si vs the measurement temperature are shown. Here, the solid lines are the least-squares-fit to a quadratic equation; see main text for details. Error bars in the inset represent the fit uncertainty associated with the values extracted for $1/\tau_\phi$ at each temperature.

The linear in the T term captures the scattering from impurities, and the quadratic in the T term is related to the electron-electron scattering [165]. Table VII. shows the parameters extracted from the least-squares-fit to the data, the fit uncertainties for both devices, and the adjusted R-square. For the natural abundance Si, the best fit is achieved when the linear term is set to zero, i.e., $b = 0$. Consequently, for natural abundance Si, the dominant scattering mechanism appears to be the electron-electron (long-range) scattering. In contrast, for isotopically enriched ^{28}Si, the best fit is

Table VII. Parameters extracted from the least-squares-fits of Eq. (2) to the data in the inset of Fig. 5.4.

Device	a (10^{10} s^{-1})	b (10^{10} K^{-1} s^{-1})	c (10^{10} K^{-2} s^{-1})	Adjusted R-square
^{28}Si	6.6 ± 2	3.1 ± 0.7	0.60 ± 0.08	0.997
^{nat}Si	5.1 ± 0.4	. . .	1.5 ± 0.1	0.989

achieved with a significant linear in the T term. This large linear term implies that impurity (short-range) scattering is a significant contribution in ^{28}Si. The temperature independent parameter a is similar (within the uncertainties) for both the devices indicating that the processes (e.g., interface roughness) contributing to a are likely the same.

Line shape analysis of the SdH oscillations as a function of temperature is also used to investigate the underlying scattering mechanisms in 2D electron systems. The amplitude of the SdH oscillations can be written as $A_{SdH} = X(T)R_0 \exp(-\pi/\omega_c\tau_q)$ [166, 167], where R_0 is the zero field resistance, $X(T) = (2\pi^2 k_B T/\hbar\omega_c)/\sinh(2\pi^2 k_B T/\hbar\omega_c)$ is the temperature damping factor, and $\omega_c = eB/m^*$ is the cyclotron frequency.

Here, k_B is Boltzmann's constant and τ_q is the single particle (quantum) lifetime [166-168]. To extract the amplitude of SdH oscillations, we first subtract a slow varying background (external disturbance, background dopant conductivity, measurement conditions, etc.) from R_{xx} [169] to isolate the oscillatory part of R_{xx}. The R_{xx} after background subtraction (ΔR_{xx}) is plotted against $1/B$ in Fig. 5.5 (a). Then, we extract the amplitude A_{SdH} as schematically defined in Fig. 5.5 (a) at each minimum of ΔR_{xx} and calculate $\ln(A_{SdH}/X(T))$. Fig. 5.5 (b) is a plot of $\ln(A_{SdH}/X(T))$ vs $1/B$, also known as the "Dingle plot" [166, 167] for the device fabricated on ^{28}Si measured at $T = 3$ K. The approximately linear dependence of $\ln(A_{SdH}/X(T))$ on $1/B$ [see Fig. 5.5 (b)] indicates a magnetic field independent quantum lifetime, τ_q. In Fig. 5.5 (c), we plot the quantum lifetimes, τ_q, for devices fabricated on ^{28}Si and ^{nat}Si extracted from a linear least-squares-fit to Dingle plots at each temperature. The calculated values of the transport lifetimes, where $\tau = \mu m^*/e$, using the magnetotransport measurement at low magnetic fields for both devices, are also plotted in Fig. 5.5 (c).

For the device fabricated on ^{28}Si, the ratio of $\tau/\tau_q \approx 1$, and for the device on ^{nat}Si, the ratio of $\tau/\tau_q \approx 1.4$. The transport lifetime τ is primarily affected by the large angle scattering events that cause a large momentum change, whereas τ_q is affected by all the scattering events [170]. It can either be dominated by the background impurities, where the scattering ratio τ/τ_q is less than or equal to 10, or dominated by short-range isotropic scattering [170], where the ratio ≈ 1 when the scattering is, e.g., surface roughness scattering [171]. However, the thickness of the gate oxide for the devices reported here is ≈ 60 nm, which is too thick for a surface scattering effect. We therefore neglect the scattering due to remote interface roughness (i.e., the interface

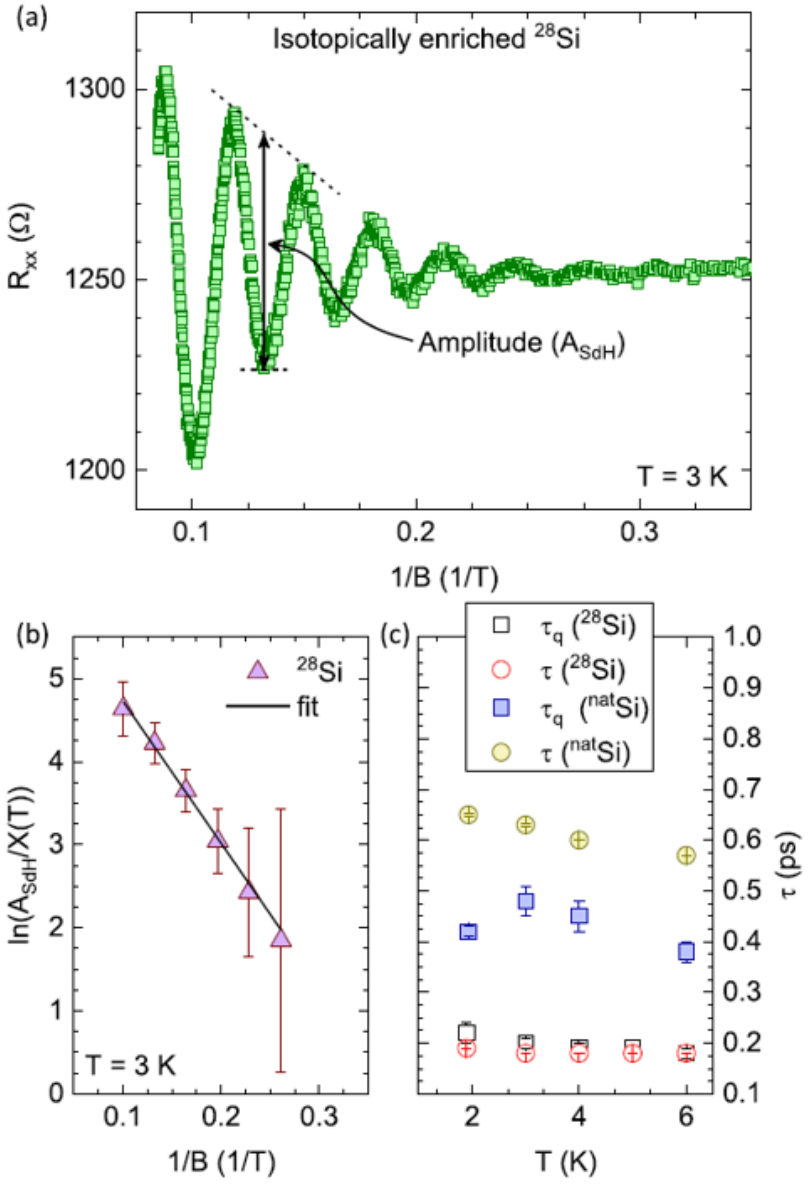

Figure 5.5: Quantum and transport lifetime extracted from the magnetotransport. (a) The background subtracted (see text) R_{xx}, i.e., ΔR_{xx}, vs the inverse of the external magnetic field ($1/B$) for the ^{28}Si device is shown. (b) A "Dingle plot" of $\ln(A_{SdH}/X(T))$ vs $1/B$. Error bars represent the uncertainty associated with extracting A_{SdH} from the ΔR_{xx} vs $1/B$ plot. (c) The single particle lifetimes, τ_q, extracted from the Dingle plots and transport lifetimes, τ, at different temperatures for devices on ^{28}Si and ^{nat}Si. Error bars represent the uncertainty associated with calculating the values of τ_q (τ) using the Dingle plots (charge carrier mobilities) at each temperature.

between the gate oxide and the gate metal) as a dominant scattering mechanism for these devices [172]. Therefore, the ratio τ/τ_q implies that the charge carrier mobility is limited by the background impurity scattering.

The analysis of the weak-localization, SdH oscillations, and low-field magnetotransport data indicates the shortest scattering length scale to be the elastic (transport) scattering length l calculated as ≈ 33 nm and ≈ 71 nm for ^{28}Si and ^{nat}Si, respectively. Capacitance voltage (CV) measurements of MOS capacitors fabricated on natural abundance silicon (data not shown) with gate oxides grown using similar conditions to the devices reported here reveal a fixed charge density of approximately 3×10^{10} cm^{-2} corresponding to the nearest neighbor distance of ≈ 58 nm. This nearest neighbor distance is in close agreement with the transport scattering length l.

5.4 Conclusion

In conclusion, we have reported on the first low temperature electrical measurements of MBE grown isotopically enriched ^{28}Si. For this report, we fabricated and characterized the low temperature magnetotransport of gated Hall bar devices fabricated on highly enriched ^{28}Si. In comparison to control devices fabricated on float-zone grown, intrinsic, natural abundance Si on the same substrate, the charge carrier mobility on isotopically enriched ^{28}Si is approximately a factor of 3 lower. Nevertheless, the magnetotransport measurements of devices fabricated on isotopically enriched ^{28}Si demonstrate strong manifestations of quantum effects. Based on the analysis of temperature dependence of the weak localization and SdH oscillations, we believe that the dominant scattering mechanism is short-range

scattering (impurity scattering). We believe that adventitious chemical impurities detected in the ^{28}Si epilayers act as the impurity scatters in the devices fabricated on ^{28}Si. However, higher levels of adventitious chemical impurities detected in the ^{28}Si epilayers are too high to be considered as isolated scattering centers since the nearest neighbor distance is considerably shorter than the scattering lengths extracted from the transport data. Furthermore, for these impurity levels, the dipolar interactions between randomly distributed electron spins associated with impurities and the central spin of a potential qubit are considered to be the dominant decoherence mechanism at high enrichment [147]. For the worst-case analysis, if all the N and O chemical impurities are considered as randomly distributed single electron spins, the influence of these dipolar interactions on the central spin could result in qubit coherence times poorer than high purity natural abundance Si. However, we are confident that the recent and planned improvements, as well as techniques for depleting impurities near the surfaces, will allow us to move forward and study the tension between chemical impurities and enrichment on quantum coherence.

Next, we plan to fabricate quantum dot devices on control (natural abundance) and isotopically enriched ^{28}Si to more rigorously assess the impact of purity and enrichment, e.g., charge offset drift, as the chemical purity of these MBE grown ^{28}Si films is improved. Therefore, macroscopic transport and material characteristics of the devices reported here will serve as a benchmark for finding the correlations between macroscopic properties and the performance of future nanoscale devices,

e.g., quantum dots, and lead to identifying qualifying metrics for “quantum grade” silicon.

This chapter is reproduced from Ref. [173] with permissions from all the co-authors. The authors acknowledge stimulating discussions with Michael Stewart, Neil Zimmerman, Roy Murray, Ryan Stein, Binhui Hu, and Peihao Huang. For the contribution of this work, I was responsible for the material preparation and growth of the ^{28}Si thin films, SIMS data analysis and part of other analysis processes. The devices were fabricated, measured, and analyzed mostly by Dr. Aruna Ramanayaka and Dr. Joe Hagmann.

Chapter 6: Al Delta-doping on Si(100): Solving the Puzzle of Max 2D Density

The previous chapters discussed isotopically enriched ^{28}Si, one of the two core materials that we are interested in when pursuing hybrid quantum computing. In the following chapters, we will be focusing on the second core material: Al delta layers. Unlike other delta-doped material systems that have been extensively studied, such as boron (B) and phosphorus (P) [77, 83, 174, 175], Al delta-doping in Si is a new material system where its material properties are largely unknown. To pursue a superconducting Al delta-doped Si, understanding the maximum number of atoms in the smallest possible distance (one atomic layer) is critical for maximizing the 3D density of this dopant. In this chapter, we will first introduce the previously studied results of Al atomic layer growth on Si(100). Then we will demonstrate our approach to study the absolute number density of one atomic layer of Al on Si(100) before cluster formation, using different techniques such as STM, SIMS and APT. The 2D density will be extracted and compared and the uncertainties associated with each of those techniques will be discussed.

6.1 Introduction

Si(100) surfaces have been studied extensively in the past decades because of their importance in semiconductor technology. The surface is reconstructed with basic 2 × 1 dimer rows from the surface atoms. At low temperature (< 350 °C for Al), the structure and growth of the metal layers depends strongly on this reconstructed surface [176]. Previous studies [177-180] using low energy electron diffraction (LEED) have demonstrated the formation of well-ordered structures of Al on Si(100) surface that is also coverage dependent. Several phases of Al have been found on the Si surface. Those studies indicated that the most common phases of Al as the coverage increases up to a full coverage or one atomic layer (or equivalently, 0.5 ML as commonly used in the literature) are: 2 × 1, 2 × 3 and 2 × 2. Note that for Si(100), 1 monolayer (ML) corresponds to a surface density of 6.8×10^{14} cm^{-2}. Therefore, it is suggested that Al are adatoms that form dimers on top of the Si(100) surface without disruption of the Si dimers. An orthogonal-dimer model has been proposed by Ide *et al.* [177] where the Al dimers are located between and oriented orthogonally to the Si dimers. Initially as Al atoms reach the Si(100) substrate, they adsorb onto the surface and form chains perpendicular to the Si dimer rows. As the coverage increases (from 0 to 1 atomic layer), Al dimer rows run perpendicularly to the Si dimer rows and an intermediate phase of 2 × 3 is formed when those dimer rows are 2*a* or 3*a* apart (*a* = 3.84 Å). At full coverage (one atomic layer) of Al, a closely packed 2 × 2 structure is formed by saturating all the dangling bonds on the Si surface [181].

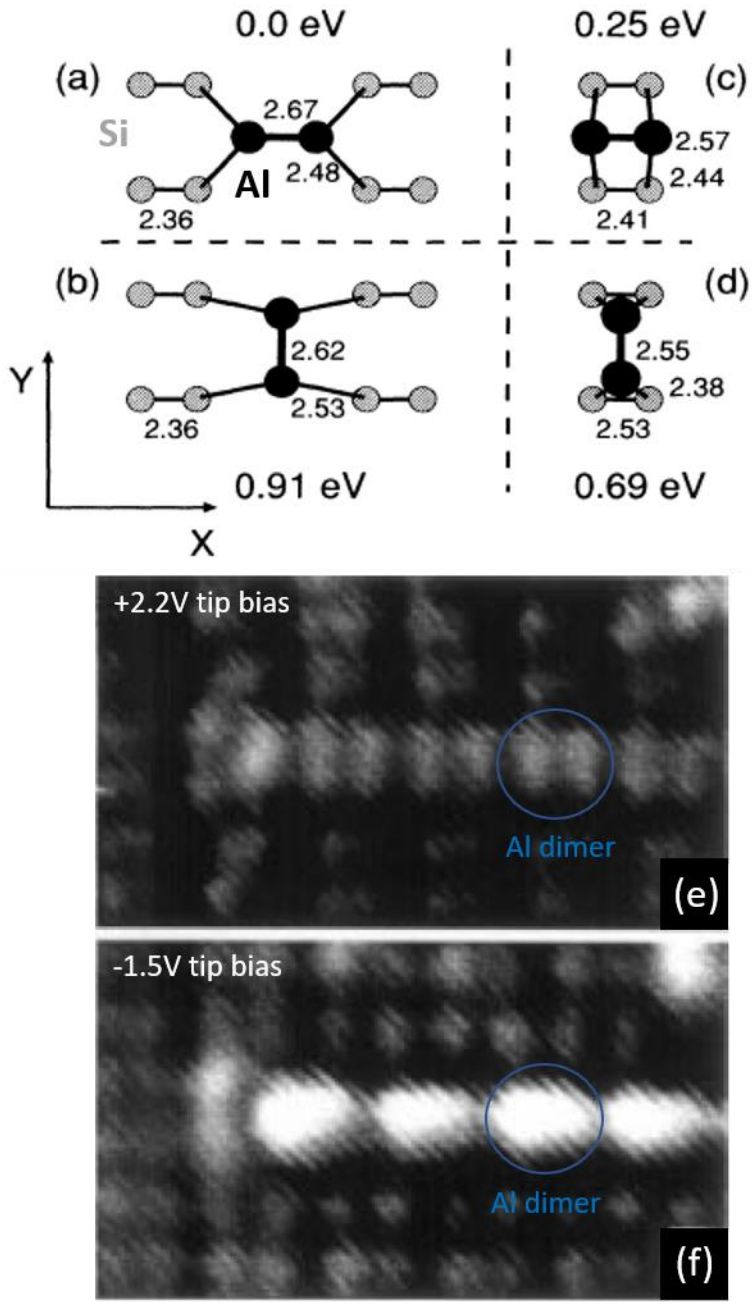

Figure 6.1: Al adatoms on Si(100) surface.
(a) – (e) possible structures of Al dimers on Si(100) surface using *ab initio* calculation. The bond length of the Al-Al, Al-Si and Si-Si are given in small numbers in Å. (e) and (f) show the STM images of the Al adsorbed Si(100) surface, taken at dual-bias condition. Al atoms are observed as two bean-shaped protrusions in negative bias and single bright protrusions in positive bias. (Panel a – d are modified from [182]; panel e and f are modified from [181] with permissions)

The proposed structures were firstly studied by Nogami *et al.* using STM [183], which provided direct observations of the Al dimer chains and the transitions into 2 × 3 and 2 × 2 phases. However, in contrast to the orthogonal-dimer model, Nogami *et al.* described a parallel-dimer model, where the Al dimers are parallel to the Si dimers. Follow on studies [176, 182, 184] based on total energy calculations revealed that the parallel-dimer model is more energetically favorable. Fig. 6.1 (a) to (d) show the schematic drawing of possible structures of an Al ad-dimer on the Si(100) surface. The black circles represent the Al atoms and the gray circles represent the Si atoms from the substrate. The total energies of the structures are given on the top with respect to the minimum, where the Al-dimer is parallel to the Si substrate dimers, as shown in structure (a) [182]. This model is further supported by other experimental techniques, such as a tensor LEED study [185] and an ion-scattering spectroscopy study [186]. However, the absence of atomically resolved STM makes it difficult to distinguish between those two models. Since then, higher resolution STM have been demonstrated and the details of the atomic structure have been studied with dual tip biases (filled state and empty state) [181, 187]. Ref. [181] described the STM topography of the Al structures on Si surface, as shown in Fig. 6.1 (e) and (f). In a positive sample (or equivalently, negative tip) bias condition (panel f), electrons tunnel from the tip into the empty state of the sample surface, double maxima of each Si dimer that reflect the symmetric properties of the antibonding state π^* [188] and Al dimers as bright oblong protrusions between the Si dimers can be seen (marked in blue circle). In a negative sample (or equivalently positive tip) bias condition (panel e), electrons tunnel out of the filled state of the sample surface to the tip, each

protrusion observed in the positive bias is replaced with two bean-shaped protrusions located on the Si dimers (marked in blue circle) [181]. The reasons for the changes in the Al features were also described. For positive sample bias, the bright protrusions represent the local density of states (LOD) that consist mostly of the dangling bond states of Al dimers. The protrusion between the Si dimers are the Al-Al dimer bonds. For negative sample bias, the two bean-shaped protrusions represent the local density of occupied states around Al dimers, showing the location of the Al-Si backbond states [181].

The growth mechanism of the Al atoms on Si(100) surface with coverage above one full atomic layer (0.5 ML) is more complicated compared to the coverage below. Different results have been shown with somewhat contradictory conclusions. For example, one study showed that the 2 × 2 structure persists at a coverage higher than one atomic layer [179] while the other showed that the 2 × 2 surface is not simply covered by the clusters, but is disrupted due to embedment of the clusters (brighter objects shown in Fig. 6.3a) [181]. Despite the differences in the detailed surface structure, it is generally true that as the coverage exceeds one atomic layer, all the Si dangling bonds are saturated, and some clusters start to form on top of the Al 2 × 2 structures. In this work, we are focusing on the 2D delta layer growth, mostly with a coverage of ≈ one atomic layer.

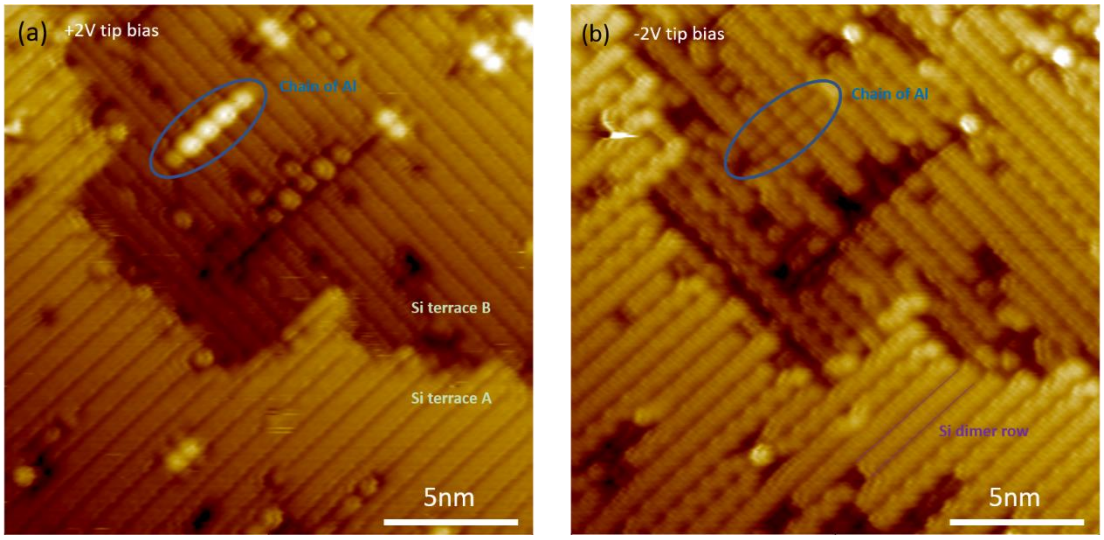

Figure 6.2: STM images of Al deposited on Si(100) surface with low coverage. The images are taken simultaneously under dual-bias. Si dimer rows can be seen clearly, with Si terraces perpendicular to each other. (a) Filled state image (+2 V, 100 pA): an Al dimer chain is marked with blue circle, 5 bright protrusions are observed. (b) Empty state image (-2 V, 100 pA): the same area of the Al chain is marked. 5 dim protrusions are observed. The bean-shaped protrusions described in the literatures are not seen. (This image is taken from Dr. Hyun-soo Kim with permission)

Since our objective is to obtain a superconducting Al delta layer in Si, understanding the maximum 2D density of Al that we can put on Si(100) in order to reach the critical 3D density of the dopant is important. The strategy here is to: 1) reach a saturation density of Al dopant and 2) confine the dopant as good as possible by depositing a Si overgrowth layer on top of the delta layer. However, there are a few discrepancies between our observation and the previous studies. For instance, the literature studies seem to suggest that there are roughly 2 Al atoms on top of 4 Si, indicating a maximum 2D Al density of 3.4×10^{14} cm^{-2}, our STM did not reveal the same structure. Fig. 6.2 shows a set of STM images with Al deposited on Si(100) at very low coverage. The two images are taken simultaneously under dual-bias tip condition with a dimension of 20 nm × 20 nm. The Si substrate was prepared in UHV

with high temperature flashing, described earlier in Chapter 2. Si dimer rows can be seen clearly, with terraces perpendicular to each other. Panel (a) shows the filled state image (+2 V tip voltage, 100 pA). An Al dimer chain is marked with blue circle, where 5 bright protrusions are observed. This structure seen is similar to what was reported in the previous literature results. Panel (b) shows the empty state image (-2 V tip voltage, 100 pA). The same area of the Al chain is marked as a comparison, where 5 dimmed protrusions are observed. The two bean-shaped protrusions described from the literatures are not seen. Instead, we are seeing single circular protrusions under both bias conditions. The reason that we saw a different feature could be due to potential different structures of Al on Si or from the tip effect. Since STM is a convolution of the LDOS of both the tip and the sample, atoms can be picked up by the tip and that might cause difference in resolution between the two bias conditions [189]. In addition, the Al protrusions seem to be located on top of the Si dimer rows instead of between the Si dimer rows, different compared to the configuration shown in Fig. 6.1. More interestingly, the first electrical measurement of this delta layer type showed that the carrier densities of the Al samples with similar doses are measured to be $\approx 1.4 \times 10^{14}$ cm^{-2} to 1.7×10^{14} cm^{-2}, very close to the density of single protrusions measured in STM. The discrepancies mentioned above either indicate that there is a different Al surface configuration on Si(100) or the dopant activation of our delta layer is limited.

Given the differences between our STM, electrical measurements and the STM shown in previous studies, the question really simplifies to whether there are two Al atoms/protrusion or there is only one Al atom/protrusion. In the next section, we are

going to study the maximum 2D number density of Al (for one atomic layer) that can be deposited on the Si(100) surface. Different technical approaches are demonstrated, which include STM, SIMS and APT. Since each sample has a small variation in dosing, the 2D density extracted from those techniques will be compared to the STM number density obtained at positive tip bias (filled states) for better consistency.

6.2 Measuring 2D Protrusion Density of Al on Si(100) using STM

Here, we investigate the Al surface saturation density using STM, with one atomic layer of Al on Si(100) surface before second layer formation. The details of the material growth processes for Al delta layer are introduced in Chapter 7, a brief summary is given here. We started with a high temperature flashing of the Si substrate in UHV condition as described in Chapter 2. The sample was ramped down from 800 °C to 300 °C and slowly cooled down to RT. After 15 mins waiting time, the sample was moved to the STM chamber for initial characterization. At this point, the sample would be at RT and it was then transferred to the Al source (Radak) for deposition.

To estimate the 2D density of the Al atoms on Si under full coverage, we use a filled state image and count the number of bright protrusions in that area. An example of the counting procedure is shown in Fig. 6.3. Panel (a) shows a surface close to one atomic layer (full coverage) of Al deposited on Si(100) at room temperature (RT). The deposition rate is close to 1/3 ML per min. 2 × 2 structures of Al are shown as the bright circular protrusions. Note that apart from the Al

protrusions, there are two more important features in this image: vacancies (dark) and Al-Al clusters (larger white areas). When counting the total number of Al protrusions accurately, contributions from the vacancies and clusters must be taken into account.

ImageJ with Image-based Tool for Counting Nuclei (ITCN) plugin was used to set the threshold and count the total number of Al features in the image. ITCN is a plugin developed by Thomas Kuo and Jiyun Byun at UC Santa Barbara [190]. The algorithm assumes blob-like nuclei with roughly convex local intensity distributions where the iso-level contour is approximately ellipsoidal and the nuclei are fitted by an inverted Laplacian of Gaussian filter [190, 191]. In the case of our images, ITCN works pretty well for features that are close together and yields better results when identifying Al features compared to the build-in functions of thresholding and watershed processing.

The standard procedure of the protrusion counting is described here. The image from panel (a) was converted to 8-bit greyscale before using ITCN. The protrusion detection was performed with the following parameters: width of protrusions is selected between 7 - 10 pixels and minimum distance between 3.5 - 5 pixels, depending on the quality of the final detection. This agrees with the pixel size based on the area density taken from 4 Si atoms (assuming one Al protrusion takes the same area of 4 Si atoms). For all samples analyzed here, a constant image scale of 50 nm × 50 nm (566 × 566 pixels) was used for consistency. An example of the image after detection is shown in Fig. 6.3 (b), where each of the red dot represents one Al protrusion. A total number of 3153 protrusions was detected in panel (b). Note that this number includes the counting from the larger clusters that appeared as brighter

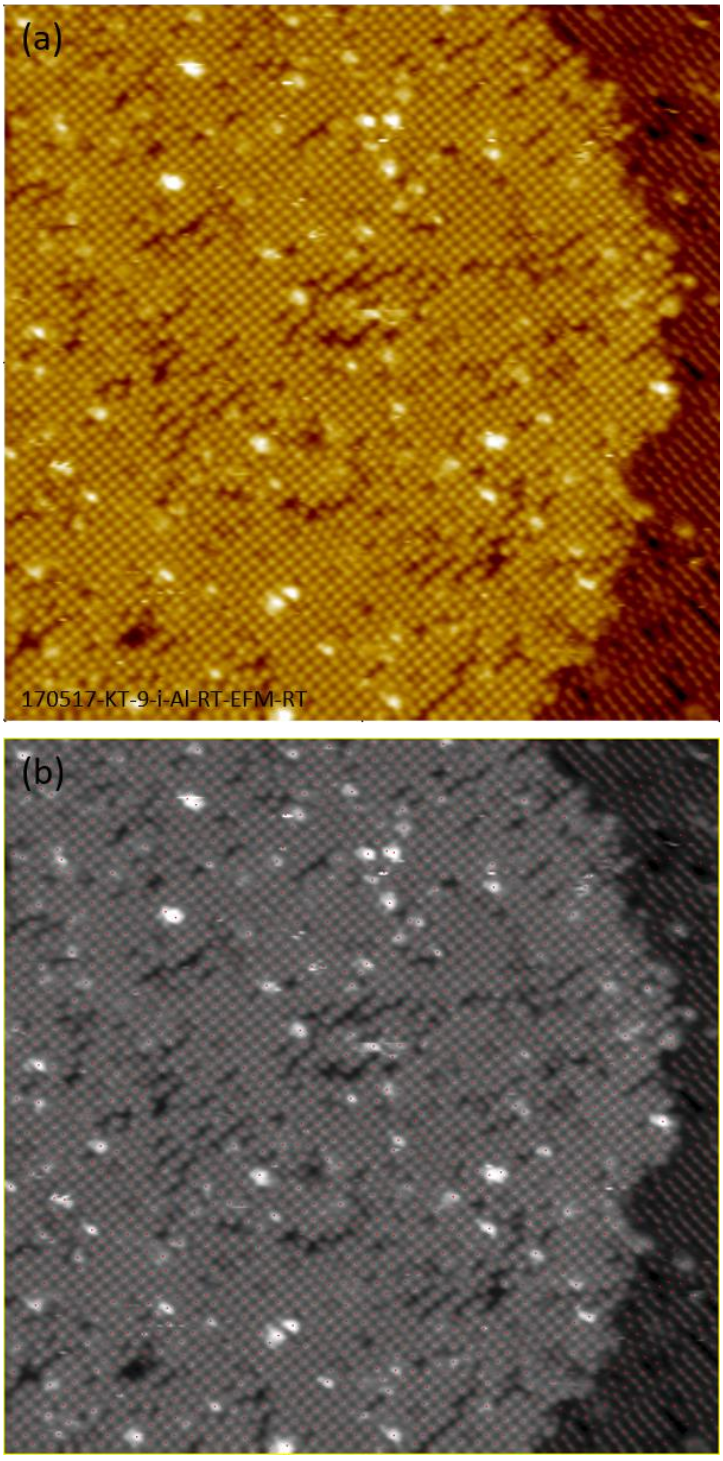

Figure 6.3: Counting Al 2D density using STM and ImageJ.
(a) is a filled state image of the surface of Al deposited on Si(100) at RT, close to full coverage. (b) shows the auto-counting of the Al protrusions using ImageJ. There are 3153 protrusions in this image. Note that the total number of protrusions excluded the contribution from the vacancies but included the clusters.

white areas. Each cluster feature was counted as either one or two protrusions depending on the size. However, this is still an underestimate of the number of Al atoms been deposited on the Si surface since there are clearly more than one or two Al atoms in each of the clusters.

To address this problem, an estimation for the number of Al atoms in these clusters is needed. By using the fill down function of the ImageJ, we can mark the cluster areas with larger height values and calculate the percentage of these areas compared to the total area of the image. For example, in Fig. 6.3 (a), 1.51 % of the total area corresponds to the larger cluster features. This is 37.75 nm^2 in the 50 nm × 50 nm image scale. Here we assume that the Al-Al clusters have a bulk Al crystal structure (FCC). The lattice constant of Al is 0.405 nm, the bulk density is 2.7 g/cm^3 and the molar mass is 26.98 g/mol. In 2D following the (100) direction, the density of Al atoms in these clusters is therefore 1.22×10^{15} cm^{-2}. For a 1.51 % cluster area, which is equivalent to an area of 37.75 nm^2, it corresponds to 460 Al atoms. This is the estimated number of Al atoms from clusters, which should be added to the total number of protrusions as shown in Fig. 6.3 (b). Now, since we are not sure if each Al protrusion shown in the STM represents one or two Al atoms, we will use 460 Al atoms as the first try and compare that to SIMS extracted density (in next section). The total number of protrusions including the clusters is therefore 3153 + 460 = 3613 in this 50 nm × 50 nm region. This corresponds to a 2D protrusion number density of 1.45×10^{14} cm^{-2}. If the final ratio of SIMS/STM is closer to 1, which represents there are 1 Al atom per STM protrusion, then 460 Al atoms coming from the clusters is valid. The 2D density of Al atoms should be 1.45×10^{14} cm^{-2}. However, if the

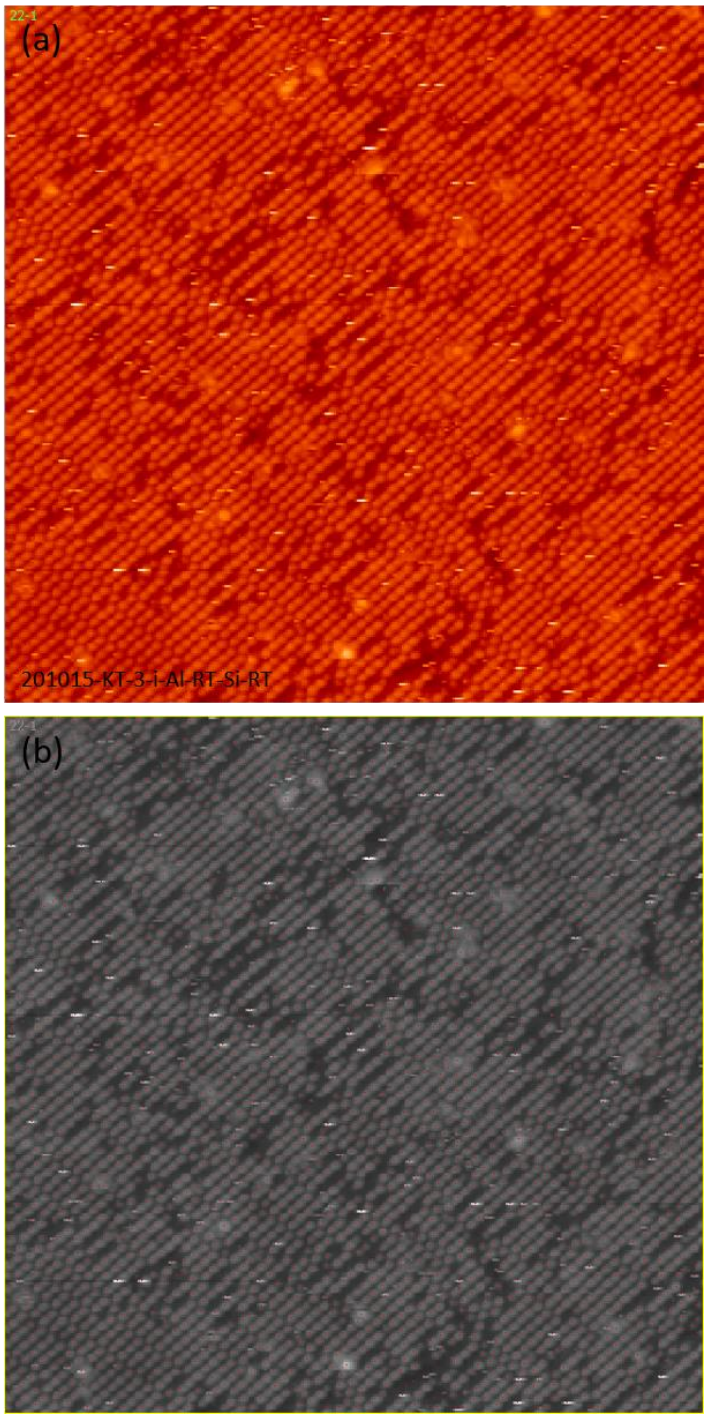

Figure 6.4: Al 2D density counting with larger area of vacancies and fewer clusters. (a) is a filled state image of the surface of Al deposited on Si(100) at RT, close to full coverage. (b) shows the auto-counting of the Al protrusions using ImageJ. There are 3415 protrusions in this image. More vacancies are shown in this sample, this counting method is able to exclude the vacancies accurately.

SIMS/STM ratio is closer to 2, which represents 2 Al atoms per protrusion, then we need to re-calibrate by adding only 230 (half of 460) Al protrusions from the clusters to the total density. And the corrected number of protrusions will be 3153 + 230 = 3383. This corresponds to a 2D protrusion number density of 1.35×10^{14} cm^{-2}. That means, the 2D density of Al atoms will be 2.66×10^{14} cm^{-2}. Another Al sample that has a higher areal density of vacancies but fewer clusters was scanned and counted using the same method, as shown in Fig. 6.4. The area percentage of vacancies in this image is ≈ 6.63 %. Using this ITCN method, the vacancy areas were accurately avoided and not included in the final number of protrusions. The image in Fig. 6.4 has a total number of protrusions of 3415, which corresponds to a 2D protrusion density of 1.46×10^{14} cm^{-2} and 1.41×10^{14} cm^{-2}, respectively. A total of 10 samples have been analyzed, a summary of the STM counted protrusion density and the corresponding uncertainties is shown in Table. VIII.

The uncertainty of this method falls in two parts. First is the miss counted Al protrusions that the software did not pick up due to the relatively weaker contrast and the miss counted vacancies. However, the estimated number of miss counts due to these two uncertainties in Fig. 6.3 is small, with a value of < 10 (< 0.3 %), which is negligible. The second type of uncertainty is from the STM scale bar. We can calibrate the scale bar by comparing it to the known Si dimer row width, which is measured to be 0.76 nm from the literature. Although this calibration depends largely on the image quality during substrate scanning (before Al deposition), the average uncertainty is estimated to be ≈ 7 % (5 % in each direction, corresponds to ≈ 7 % in two-dimension).

Table VIII. A summary of the STM protrusion density count. The cluster area percentage, STM protrusion density including the contribution from surface clusters under two different assumptions are shown. The estimated uncertainty is approximately 7 %.

Cluster area percentage	Protrusion density assuming 1 protrusion = 1 atom (cm^{-2})	Protrusion density assuming 1 protrusion = 2 atoms (cm^{-2})
2.59 %	1.51×10^{14}	1.35×10^{14}
1.60 %	1.38×10^{14}	1.28×10^{14}
1.51 %	1.45×10^{14}	1.35×10^{14}
0.79 %	1.45×10^{14}	1.40×10^{14}
0.88 %	1.47×10^{14}	1.42×10^{14}
0.17 %	1.52×10^{14}	1.50×10^{14}
0.82 %	1.37×10^{14}	1.32×10^{14}
0.38 %	1.37×10^{14}	1.33×10^{14}
0.89 %	1.45×10^{14}	1.40×10^{14}
0.80 %	1.46×10^{14}	1.41×10^{14}

6.3 Measuring 2D Atom Density of Al using SIMS

One method of measuring the 2D density of Al delta layer in Si is using SIMS. SIMS is a powerful tool that can be used to access the profile of the delta-doped layers accurately. The 3D peak density can be extracted, with relatively good sensitivity down to < 5 nm/decade and the 2D density can be calculated by integrating the area of the delta layer peak. Although extensive studies have been done with boron (B) and phosphorus (P) delta layers using SIMS [83, 192], none has been done with Al delta layers. To obtain the optimum measurement conditions (that could result in a sharpest delta layer peak) for Al delta layers, the SIMS parameters in terms of the ion beam energy and sputter beam angle are studied. This is because the choice

of primary ion beam energy will affect the depth resolution, secondary ion yield and the sputter rate of the measurement. For example, depth resolution degrades as the ion energy increases and

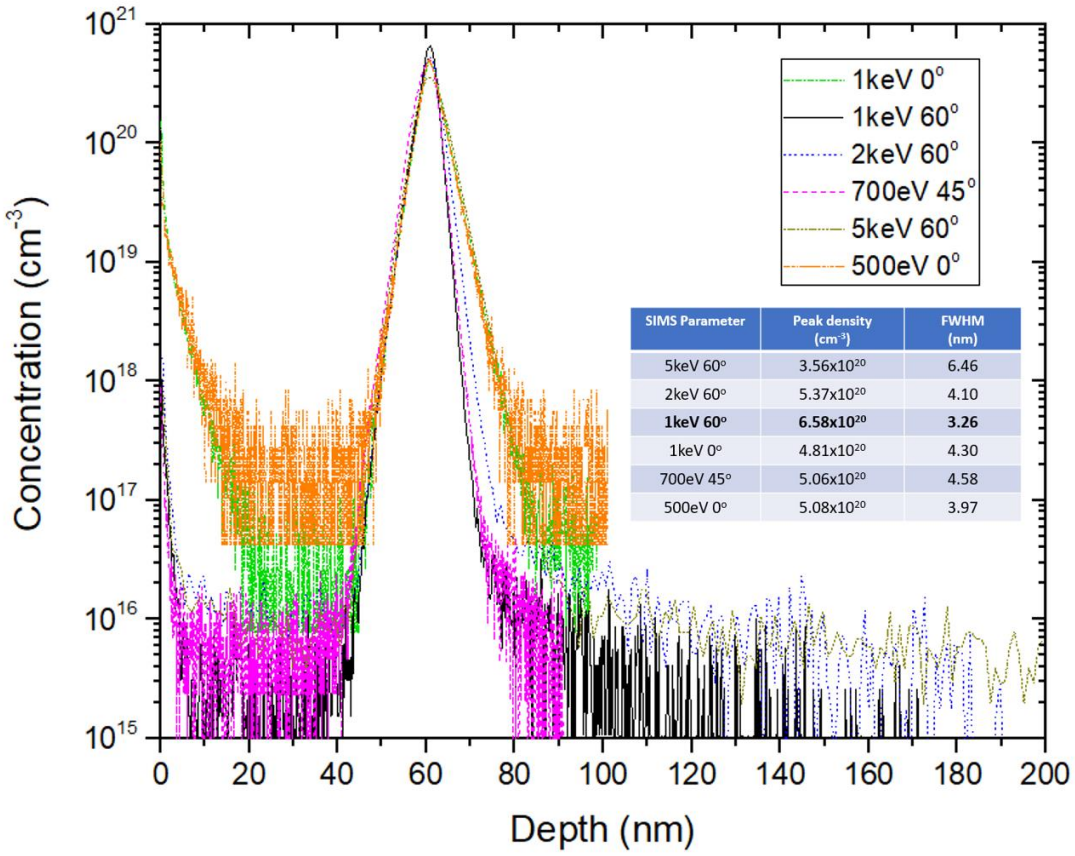

SIMS Parameter	Peak density (cm^{-3})	FWHM (nm)
5keV 60°	3.56×10^{20}	6.46
2keV 60°	5.37×10^{20}	4.10
1keV 60°	**6.58×10^{20}**	**3.26**
1keV 0°	4.81×10^{20}	4.30
700eV 45°	5.06×10^{20}	4.58
500eV 0°	5.08×10^{20}	3.97

Figure 6.5: SIMS depth profiles with different ion energies and sputter angles. A range of primary ion energies are studied from 500 eV to 5000 eV and bombardment angles are chosen from 0 ° to 90 ° relative to the surface normal. The optimum condition in terms of peak height and FWHM is 1keV with 60 ° angle, shown in solid black line. A peak density of 6.58×10^{20} cm^{-3} and a FWHM of 3.26 nm is obtained. There is more Al tailing toward the surface (3.5 nm/decades) than toward the substrate (2.3 nm/decades). The precision of this measurement (repeatability and reproducibility) is dependent on the impurity matrix combination and the analysis tool.

sputtering yield increase (then saturates) as the ion energy increases. To extract the highest peak density and sharpest delta layer width, a range of primary ion energies are studied from 500 eV to 5000 eV and bombardment angles are chosen from 0 ° to

90 ° relative to the surface normal. The sample measured was a delta layer sample with one atomic layer of Al sandwiched between the Si substrate and an electron-beam evaporated Si capping layer deposited at RT. Unlike other delta layer samples with different thermal anneals, no thermal treatment has been done on this sample after substrate flashing, this is to minimize the Al movement. A summary of the depth profiles of this Al delta layer is shown in Fig. 6.5 (a) using O_2 bombardment. The y-axis is the Al concentration and x-axis is the depth from the surface. The insert shows the extracted delta layer peak density and full width half maximum (FWHM) for each parameter set, using the Origin built in integration function. This integration tool performs numerical integration on the data plot using the trapezoidal rule, where the area under the curve is evaluated by dividing the total area into small trapezoids. As a result, 1 keV ion energy with 60 ° sputter angle (black solid line) gives the highest 3D density and lowest FWHM. The Al delta layer is located at 60 nm from the surface, with a peak 3D density of 6.58×10^{20} cm^{-3} and a FWHM of 3.26 nm. Note that the FWHM extracted here is larger than the real delta layer thickness, as it is a mixing of both delta layer roughness and instrumental effects. The integrated 2D density is 2.64×10^{14} cm^{-2}. The STM counting of this sample has a protrusion density of 1.46×10^{14} cm^{-2}. This results in a SIMS/STM ratio of 1.81, indicating that there is ≈ 2 Al atoms in each protrusion seen in the STM. Since the atom number is discretized (either an integer of 1 or 2), the extracted ratio of 1.81 means that the probability of having 2 atoms/protrusion is much higher compared to the probability of having only 1 atom/protrusion. A more detailed comparison is described later. The data point density of this measurement is 5 nm^{-1}. One thing to note is that the SIMS profile

shows more Al tailing toward the surface (3.5 nm/decades) than toward the substrate (2.3 nm/decades). This indicates that although there is no thermal anneal, the Al still migrated a little toward the surface since we generally expect more SIMS depth resolution artifact on the substrate side than the surface side. The reason for this is due to the forward recoil of the sputtered ions (or recoil mixing) which is a forward momentum component of the sputtering and will push some atoms deeper into the sample. Or it is possible that Al-Al clusters are formed at the interface and is causing a broadening in the peak toward the Si capping layer.

With the optimum SIMS, i.e. condition that generates the sharpest peak, now we look at our Al delta layer devices. An example of the SIMS depth profile of an Al delta layer device at full coverage (one atomic layer) is presented in Fig. 6.6. The insert in (c) is a schematic of the sample structure. Mesa-etched Hall bar devices are fabricated on top of the sample, as shown in (d). Panel (a) is the SIMS data from the device without background subtraction, where the Al delta layer peak (located at 60 nm from the surface) can be seen. As shown in the figure, there appears to be a high concentration region closer to the surface (0 – 40 nm). For the moment, we are going to assume that the tail is not dominated by the segregation of the Al delta layer (although there must be some contribution) and that is coming predominantly from the surface contamination during the transport out of the UHV environment (from vacuum chamber to EAG) and from the Al metal contact of the Hall bar device that is fabricated on top of the delta layer sample (Al metal dust on the sample surface). To obtain a better estimation of the delta layer peak, the surface tail is fitted to an

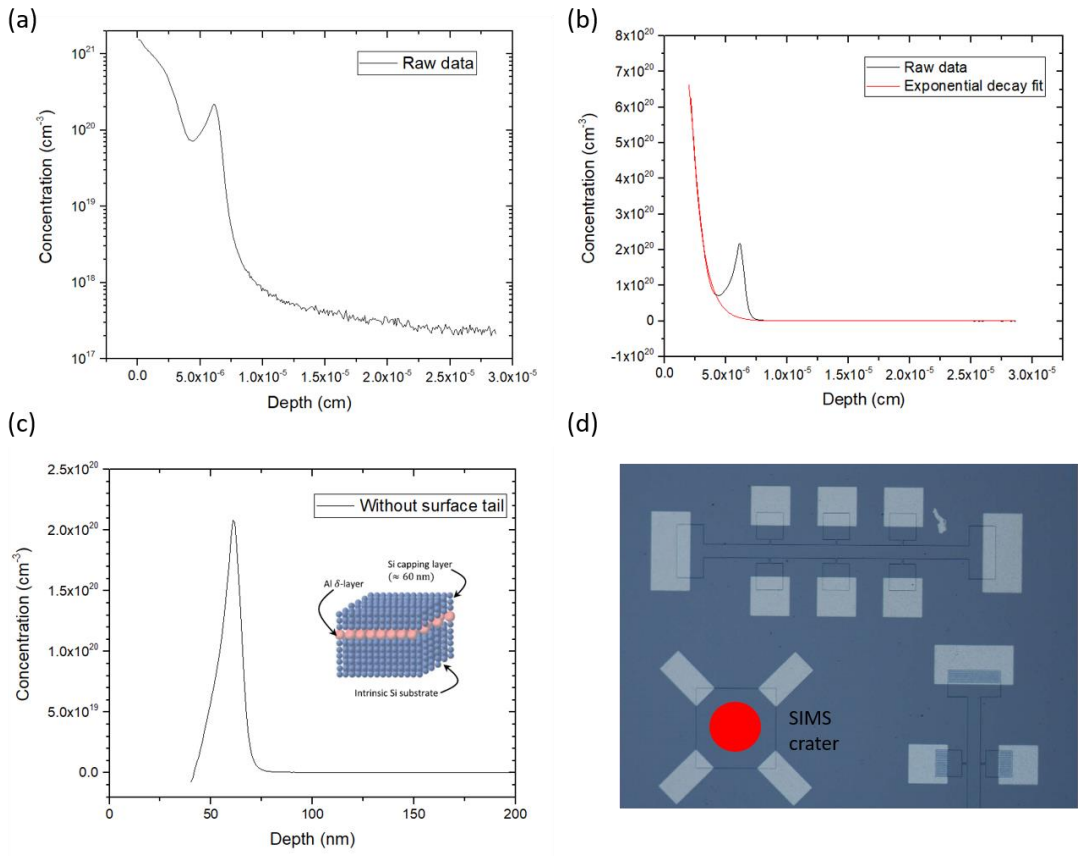

Figure 6.6: SIMS depth profile of an Al delta-doped sample with 100% Al dosing at 1 keV.

The SIMS measurement is performed on this sample after mesa-etched Hall bar device fabrication. (a) shows the raw data, where a delta layer peak is located at about 60 nm from the surface. A high concentration surface tail is observed, from the surface to ≈ 40 nm down. This is mostly from the surface contamination during transport and the Al metal contact on the surface during device fabrication. (b) an exponential decay fit to the surface tail. The background noise level is also included. (c) The delta layer peak after subtracting the surface tail effect and background noise (subtracting a constant average). A peak density of 2.10×10^{20} cm^{-3} and a FWHM of 10.1 nm is extracted. The integrated 2D density is 2.62×10^{14} cm^{-2}. (d) Optical microscope image of an Al delta layer Hall bar device, the SIMS crater is focused on one of the Van der paw (VDP) device, marked in red.

exponential decay function and subtracted from the raw data, as shown in panel (b). The Al delta layer peak without surface tail is shown in panel (c). A 3D peak density of 2.10×10^{20} cm^{-3} is extracted, with a FWHM of 10.1 nm. The integrated 2D density of this delta layer peak is 2.62×10^{14} cm^{-2}. The uncertainty in the 2D density before

and after the surface tail subtraction for this sample is 20.2 %, which is the largest among all samples we characterized by SIMS. However, this sample is a special case, where the same analysis has been done on multiple samples, and the uncertainty for 9 other samples only range from 0.04 % to 2.5 %.

It is observed that the delta layer peak is broadened compared to the sample shown in Fig. 6.5, and it is not symmetric, with left side of the peak shape flatter than the right side. By comparing to the profile from the sample without any thermal treatment, it seems likely that there is some thermal redistribution of the Al atoms and more Al atoms have been migrated toward the surface of the Si capping layer than into the Si substrate. This is not surprising because multiple thermal processes have been done to this sample, including the incorporation anneal at 550 °C for 1 min and the final solid phase epitaxial (SPE) anneal at 550 °C for 10 mins. Al can diffuse along the grain boundaries much faster than through the gains. As a result, under the same SIMS measurement conditions, the peak density of the thermally annealed sample (2.10×10^{20} cm^{-3}) is approximately 1/3 of that for the sample without thermal anneal (6.58×10^{20} cm^{-3}). Another reason for peak broadening is due to the SIMS measurement, where forward recoil of the sputtered ions is inevitable, especially for delta layer samples with FWHM < 10 nm. Note that the direction of this effect is towards the substrate side, which is opposite to the segregation process (toward the surface). Both effects will reduce the 3D peak density and increase the FWHM of the delta layer peak. Furthermore, since most of the area on this sample was etched away during device fabrication, the remaining areas of the Hall bar devices are usually too

small compared to the diameter of the primary beam, results in a reduction in detection sensitivity.

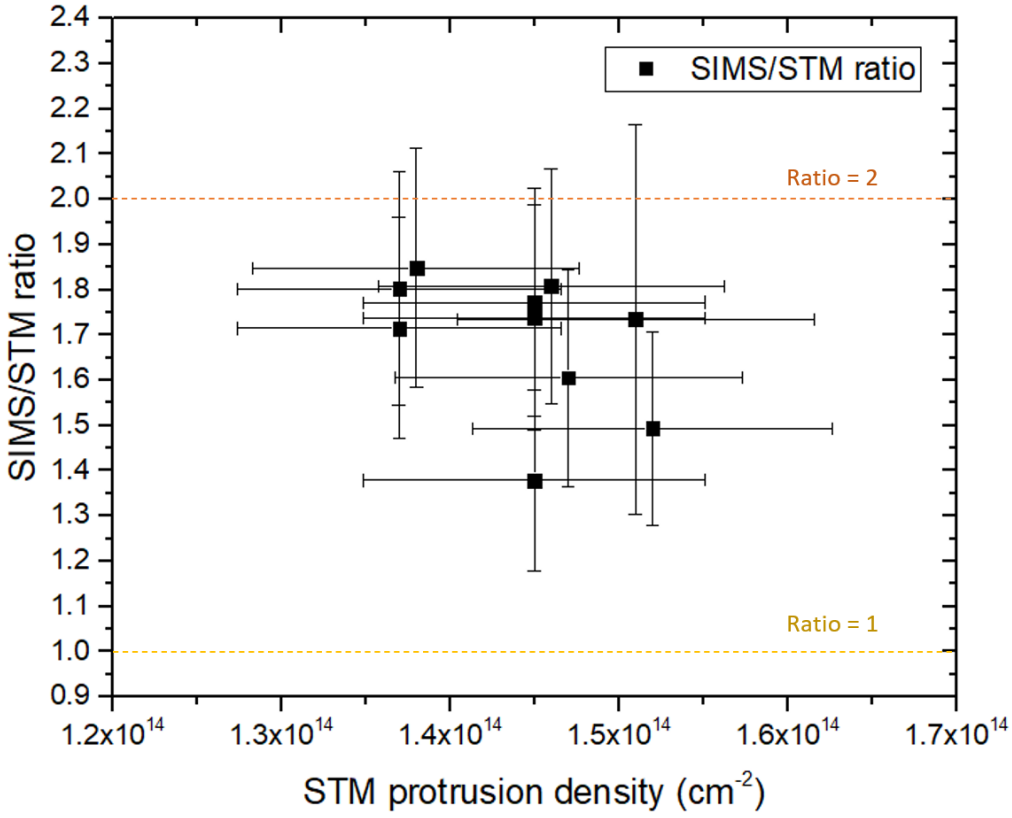

Figure 6.7: 1st iteration of SIMS to STM number density ratio. 10 Samples with slightly different Al doses are measured using SIMS. Error bars for both SIMS measurements and STM counts are shown. The average SIMS/STM density ratio is 1.69 ± 0.96, closest to an integer of 2. This indicates that it is most likely to have 2 atoms per protrusion at positive tip bias.

One important note here is that there is a discrepancy between the 2D density number extracted here and the actual Al dosing on the sample. This is because we are assuming no Al segregated onto the surface. However, this is not always the case, especially for the samples that went through multiple thermal treatments. Some Al migration to the surface has been observed, as will be introduced in Chapter 7. Therefore, the SIMS extracted density is an underestimated value of the actual Al

atoms that have been deposited on the surface and is expected to be smaller than the actual maximum 2D density of one atomic layer of Al on Si(100).

A set of 10 samples has been measured using SIMS, and the 2D densities are extracted using the method described above. Since the estimated Al doses may vary slightly from sample to sample and from STM tip to STM tip, the number density is compared by taking the ratio between the two techniques. For example, a SIMS/STM ratio of 2 means that there are two Al atoms (most likely dimers due to energy calculation) in each of the circular protrusion observed in the positive bias STM image. In another word, there are 2 Al atoms sitting on top of 4 Si atoms and the max surface density of this dopant is therefore 50 % of the Si(100) surface density. As introduced in the last section, since we are not sure about the exact number of atoms in one protrusion yet (there should be either one or two atoms/protrusion), we are going to treat the contribution calculated from surface clusters in an one to one ratio first and add that to the total protrusion count (see Table. VIII middle column). Fig. 6.7 shows a summary plot of the SIMS/STM number density ratio versus STM density under this assumption and we this is the 1^{st} iteration of SIMS/STM ratio. On average, a density ratio of 1.69 ± 0.96 is obtained. This means that for each bright protrusion shown at positive tip bias condition (filled state), there are roughly 1.7 Al atoms. Since the atom number is always an integer, the probability of having 2 Al atoms in each protrusion is much bigger than 1, indicating the max 2D density of Al on Si(100) is 3.4×10^{14} cm^{-2}.

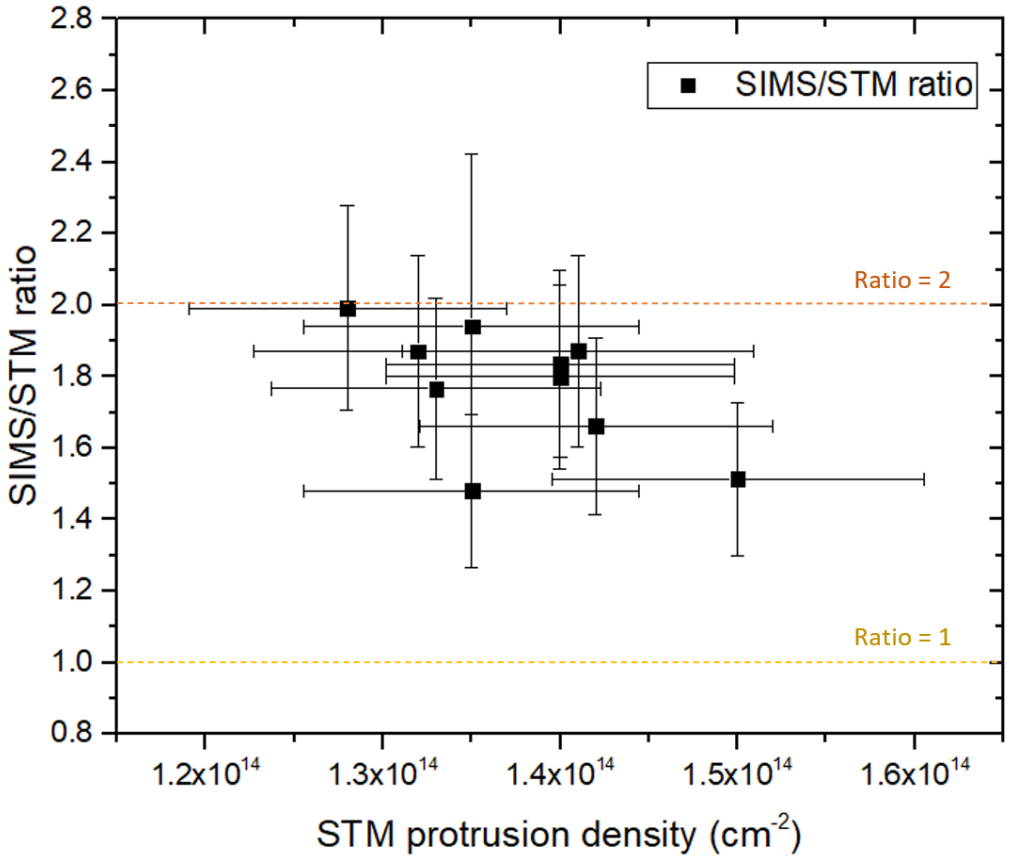

Figure 6.8: 2nd iteration of SIMS to STM number density ratio. The contribution of clusters on protrusion density is corrected by assuming 1 protrusion = 2 Al atoms. The average SIMS/STM density ratio is 1.77 ± 0.88, closest to an integer of 2. This verifies that there are 2 atoms per protrusion at positive tip bias.

From Fig. 6.7, we know that it is more likely to have 2 Al atoms per protrusions, therefore we need to correct the assumption made in the 1st iteration that each of the estimated cluster atoms on the surface contributes to 1 protrusion. Instead, the number of protrusions from the clusters should be divided by two. For example, a 1 % cluster area contributes to 305 Al atoms (calculated in the last section), which is equivalent to 153 protrusions. As seen in the third column of Table. VIII, the corrected STM density is smaller than in the 1st iteration, this will give a slightly higher ratio of

SIMS/STM. A corrected version of the SIMS/STM ratio plot is shown in Fig. 6.8, this is the 2nd iteration. On average, a density ratio of 1.77 ± 0.88 is obtained. This verifies that for each bright protrusion shown at positive tip bias condition (filled state), there are 2 Al atoms. This again indicates that the max 2D density of Al on Si(100) is 3.4×10^{14} cm^{-2}.

The error bars are estimated for both SIMS measurements and for STM density counts. For SIMS, two uncertainties are taken into account: tool calibration and surface tail. As will be introduced in the next paragraph, the tool calibration error from EAG (a commercial lab that did SIMS measurements for our Al samples) is in the range of 10 – 15 %, an average value of 12.5 % is used in the analysis. The uncertainties for the surface tail subtraction is summarized in Table IX. The total uncertainty is a quadrature sum of the two.

Table IX. A summary of the SIMS density count and uncertainties. The SIMS density value shown here is after surface tail subtraction. The total uncertainty is the quadrature sum of the tool calibration and surface tail.

SIMS density (cm^{-2})	Uncertainty in surface tail	Total uncertainty
2.62×10^{14}	20.2 %	23.8%
2.55×10^{14}	0.4 %	12.5%
2.00×10^{14}	2.5 %	12.7%
2.52×10^{14}	0.4 %	12.5%
2.43×10^{14}	2.9 %	12.8%
2.24×10^{14}	1.3 %	12.6%
2.47×10^{14}	0.3 %	12.5%
2.34×10^{14}	0.5 %	12.5%
2.56×10^{14}	0.4 %	12.5%
2.64×10^{14}	0.0 %	12.5%

The reasons for a non-integer number of the density ratio can be complicated. One of the possibilities is that there are some systematic errors present in the SIMS measurements that lower the total number of counts. An ultimate weak link for SIMS is the calibration of the measurements. The calibration relies primarily on NIST Standard Reference Materials - As, B and P in the case of our measurements done by EAG. Outside this small subset of elements, the calibration is relying on ion implanter dosimetry. Al as a dopant is not well studied and as a result, the calibration error for Al is much more significant compared to other dopants (the standard error for B is 3.5 %, P is 1.65 % and As is 0.4 %). This is because instead of using a known reference material, the integrated signal under the measured implant distribution is set equal to the dose of the implanter. However, the ion implanters have relatively large uncertainties. In general, the uncertainty in sensitivity calibration using Al as a dopant can be as large as 30 %. By comparing several ion-implanted standards of Al in Si and average the results, a "consensus" sensitivity with lower uncertainty can be obtained, but still in the range of 10 – 15 %. Another possible reason is the subsurface Al atoms that are not seen during the STM scan. It is also likely that some Al atoms migrated towards the surface due to the thermal treatments and were subtracted from the surface tail during analysis, as we described before.

In conclusion, the obtained SIMS/STM ratio of 1.77 ± 0.88 indicates that it is most likely to have 2 Al atoms adsorbed on top of 4 Si atoms in the form of 2×2 dimer structures, in accord with the literature predictions that were described in section 6.1. The most likely maximum 2D density of Al on Si(100) at one atomic layer coverage is therefore 3.4×10^{14} cm^{-2}, neglecting the presence of dimer

vacancies on the Si(100) surface. In the next section, we will further explore this density using another powerful technique: the atom probe tomography.

6.4 Measuring 2D Atom Density of Al using Atom Probe Tomography (APT)

The APT data presented in this section is acquired in collaboration with Dr. Karen A. DeRocher and Dr. F. Meisenkothen.

APT is a powerful microscopy technique that can be used to identify and quantify individual chemical species in a fast and accurate way. The high spatial resolution and three-dimensional characterization capabilities make it a good complement to other microscopy techniques such as SIMS and tunneling electron microscopy (TEM). The mechanism for APT is briefly described here. The APT uses a time-of-flight mass spectrometer with a point projection microscope that is capable of atomic scale imaging [193]. When combined with the position sensing, a full three-dimensional reconstruction of the sample species can be obtained. The sample is usually prepared in advance with focused ion beam (FIB) into needle-shaped tips that are nanometer in size. By applying a high voltage between the specimen and the local electrode, a high electric field of ~10^{10} V/m is applied to the apex of the specimen tip, usually at cryogenic temperatures. The atoms will be evaporated from the apex as ions and accelerated toward the imaging camera. When laser or high voltage pulses are used during evaporation, atoms are evaporated from the surface by field effect and project onto a Position Sensitive Detector (PSD). The flight time of each ion can be measured, and the corresponding mass-to-charge ratio can be calculated. The position

at which the ions hit the detector is used to determine the original position on the specimen apex and the sequence of evaporation events is used to provide depth information [194]. The combination of those collected data allows 3D imaging of the element distribution with atomic resolution.

In our case, an Al delta layer sample that has no thermal treatment was studied, this is the same sample used in Fig. 6.5. Prior to the FIB milling, a thin capping layer of cobalt (Co) with a thickness of 75 nm was deposited. In the FIB, a protective Pt film was deposited on a 30 μm × 2 μm region of the sample surface to protect it from Ga beam damage. The sample was then tilted to 22 degrees relative to the ion beam and an angled cut was made on one side of the protective Pt. The sample was rotated 180 degrees in azimuth so the same kind of cut could be made on the opposite side. By repeating this cutting step until these angled cuts have met below the sample and what is left is a bridge with a triangular cross section. The sample is then un-tilted so that it is now perpendicular to the electron beam, and one side of the sample is cut free from the bulk. A tungsten needle inside the FIB chamber was then welded with Pt to the side that was already cut free. The other side of the sample was then cut free from the bulk and the entire 30 μm × 2 μm sample was lifted out of the bulk on the W needle and transferred over to a microtip array. The free end of the sample was positioned on top of the first Si post of the microtip array, welded on with Pt, and cut from the remainder of the sample. Each tip was then sharpened using the Ga ion beam and annular mill patterns with progressively smaller outer and inner diameters until the tip radius was around 50 nm. Finally, a low kV ion bombardment step was

performed to remove Ga ions implanted during tip sharpening, and the entire microtip array was moved into the atom probe [195].

The APT was measured at a 30 K specimen temperature with a pulse frequency of 333 to 500 kHz and laser energy of 15 pJ. Fig. 6.9 (a) shows the collected atom probe data of the delta layer using tip 1 (R37_03481). The cone represents the apex of the tip and the distribution of the chemical species (Si, Al, Co and Si_xO_y) are shown in four different colors. The atom probe reconstruction of the Al delta layer is constrained using the SIMS depth profile, where the delta layer is located at ≈ 60 nm from the surface. The left cone shows the distribution of the Al delta layer in Si and the right cone shows the distribution of the Co. It seems some Co has penetrated into the Si layer. Fig. 6.9 (b) is the reconstructed concentration profiles of each chemical species as a function of depth. In addition to the Co (red) and O (green), an Al delta layer peak is observed (blue). Each concentration profile is obtained by choosing a cylindrical region at the middle area of Fig. 6.9 (a) and counting the number of atoms of each element in 1 nm slices (in z-direction) of the cylinder.

(a)

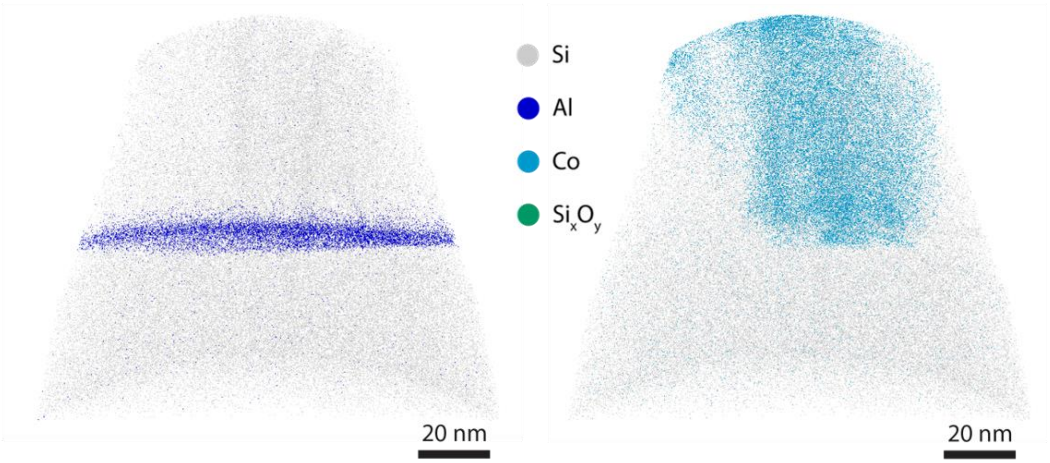

(b)

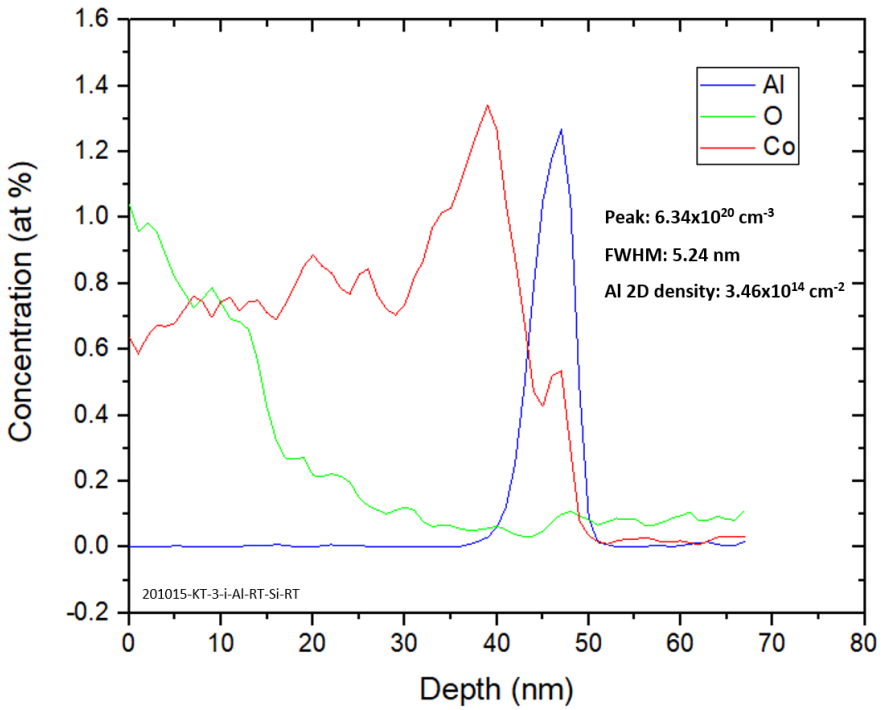

Figure 6.9: APT of the Al delta layer without thermal treatment.
(a) The cone represents the apex of the tip and the distribution of the chemical species (Si, Al, Co and Si_xO_y) are shown. Co is penetrated into the capping layer and some Si has been oxidized during the evaporation. (b) the concentration profile of each species. A 3D density of 6.34×10^{20} cm^{-3} and a 2D density of 3.46×10^{14} cm^{-2} is obtained for Al.

From Fig. 6.9 (b), the peak density of this Al delta layer is 6.34×10^{20} cm^{-3} with a FWHM of 5.24 nm. The integrated 2D density is calculated to be $(3.46 \pm 0.69) \times 10^{14}$ cm^{-2}. The STM density count for this sample after Al deposition is 1.46×10^{14} cm^{-2}, which gives an APT/STM density ratio of 2.37 ± 0.50. Since we are counting the Al protrusions in STM assuming a 2D layer, there might be Al atoms in the lower (Al atoms going in the substrate) or higher (Al atoms further up in the clusters) plane that are not taken into account. That means the ratio extracted here might be an over-estimation. However, since we do not have a good way to evaluate the quantitative contribution of this effect, it would not be included in the uncertainty calculation. The uncertainty of this measurement is approximately 20 %, mainly comes from the reconstruction of the Al delta layer thickness from the atom probe. The extracted value means that each of the protrusion that we see in the STM filled state image represents 2.37 Al atoms. Of course, the atom number of each protrusion is an integer, indicating that most likely there are 2 Al atoms in each protrusion or the max 2D density of Al on Si(100) is 3.4×10^{14} cm^{-2}, in accord with the density measured by SIMS. Similarly, the APT extracted 2D density is also a non-integer number that is close but not exactly equal to 2. This difference might be due to the reconstruction of the Al profile in APT. The reconstruction of the concentration profile was done by selecting an analysis region along the long axis of the tip with a cylinder that is ≈ 20 nm in diameter. In fact, Fig. 6.9 (a) showed an Al delta layer that is uneven in thickness, where the middle blue area is thicker compared to the edges of the tip. This uneven thickness of the delta layer is either an artifact or a consequence of solid migration caused by laser heating of this specimen. It could also be the strain effect

from the excess Co diffused into the Si. Since the data was collected by an analysis region located closer to the middle of the tip, an overestimate of the 2D density is possible.

6.5 Conclusions

In this chapter, we have reviewed the previous results on growing atomic layers of Al on Si(100) surface and studied the max 2D number density of Al dopant that can be grown on this surface, using various techniques. STM was used to determine the dosing of our Al atomic layer until full coverage or one atomic layer. Number densities were counted under positive tip condition. SIMS and APT were used to measure the total number of Al dopant atoms remained in the delta layer sample. The extracted 2D densities are then compared to the STM protrusion densities to minimize the variation in Al doses. As a result, an average SIMS/STM density ratio of 1.77 ± 0.88 and APT/STM ratio of 2.37 ± 0.50 is obtained, respectively. The mean ratio from the two measurements is therefore 2.07 ± 1.11. This indicates that for each protrusion observed in the filled state STM image, there are 2 Al atoms. This extracted density ratio confirmed the literature results that Al dimers are formed on Si(100) surface at low temperature. The maximum 2D density of Al that can be reached on Si(100) surface for one atomic layer is therefore 3.4×10^{14} cm^{-2}, half of the Si(100) surface density. We believe this fills the gap for the missing information that is needed to confirm the Al atomic layer structure on Si(100) and provides help on reaching the critical density needed for superconducting transition using Al as a

dopant. In the next chapter, we will compare this 2D density value to our magnetotransport measurements using Hall bar devices and explore the relation between Al doses, dopant activation and delta layer conduction.

Chapter 7: Al Delta-doping on Si(100): Material Growth and Characterization

7.1 Introduction

As stated in Chapter 1, the main goal of this project is to develop a superconducting Al delta layer in ^{28}Si. From the last chapter, we verified that the maximum achievable 2D density of Al on Si is 3.4×10^{14} cm^{-2} and the highest 3D density of our delta layer film is $\approx 6 \times 10^{20}$ cm^{-3} (1.2 at. %), which is still lower than the predicted critical density needed for superconducting transition (> 2 at. %). In order to reach this high enough 3D density, the 3D confinement of this dopant material needs to be improved. In this chapter, we will perform studies on three major process steps during material synthesis and explore the possibility of superconductivity using this Al delta-doped layer in Si.

In our previous work [86], we have successfully demonstrated the ability to grow a Si-Al-Si heterostructure that is electrically conducting at low temperature. Here's a summary of the previous results. The growth method for this first-generation Al delta layer is summarized in Fig. 7.1. As a starting point, intrinsic, float-zone Si(100) substrate was flash annealed at high temperature under UHV condition in the deposition chamber, as described in Chapter 2, under sample preparation. After flashing, the sample was ramped down from 800 °C to 300 °C then slowly cooled down to RT. The sample is then transferred to the STM chamber after 15 mins

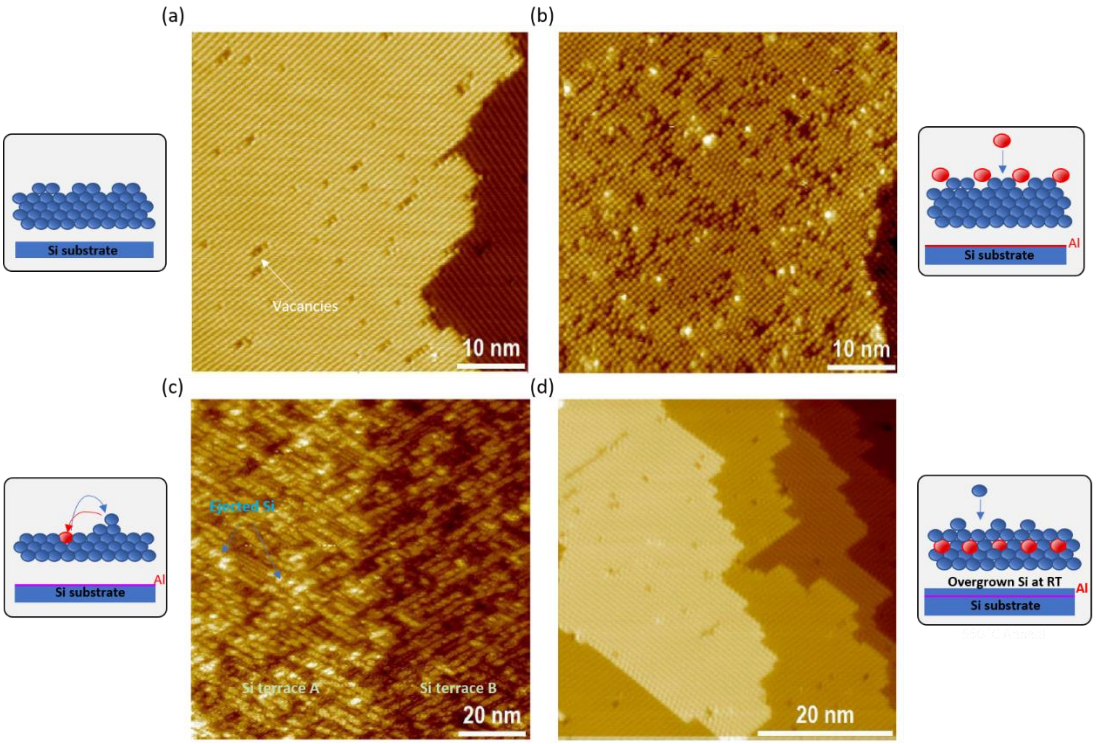

Figure 7.1: STM images of the surface after each growth step of the first-generation Al delta layer.
The schematics for each of the growth steps are included. (a) STM image showing the prepared surface of Si(100) after high temperature flashing in UHV. (b) After full coverage (100% dose) of Al deposited on top of Si substrate. Some vacancies and brighter Al clusters can be seen. The estimated Al protrusion density is (1.5 ± 0.2) × 10^{14} cm^{-2}. (c) surface after incorporation anneal at 550 °C for 1 min. Some ejected Si island (as brighter streaks) can be seen. (d) After 60 nm of Si overgrowth at room temperature and 550 °C anneal for 10 min for re-crystallization. (Those images are modified from Ref. [76] with permission)

interval and scanned. Fig. 7.1 (a) shows a typical surface after sample preparation, where 2 × 1 reconstructed dimer rows and Si terraces perpendicular to each other can be seen. The defect density is very small (< 5 %). After scanning, the sample is transferred back to the Al deposition source (Radak) in deposition chamber and Al is deposited without substrate heating. Although there is no sample heating, there might be some radiation heat from the Radak source that is placed below the sample, but we don't have an accurate measurement of the temperature at this moment. A constant

deposition rate of Al (1/3 ML/min) is used on most samples to reduce deviation from this radiation heat.

Fig. 7.1 (b) shows the surface after close to full coverage of Al onto the Si(100) surface. We refer to this as one atomic layer of Al or 100 % dose since it covers the whole Si substrate. The estimated Al protrusion density from STM is approximately $(1.5 \pm 0.2) \times 10^{14}$ cm^{-2}, under positive tip bias condition. This corresponds to a 2D dosing density of $\approx 3.0 \times 10^{14}$ cm^{-2}. After that, the sample will be heated up to 550 °C for 1 min. This is known as an incorporation anneal, which allows the Al atoms to substitute into the Si lattice site and eject Si atoms that form islands at the surface [196, 197]. Fig. 7.1 (c) shows those elongated Si islands and dark lines that represent incorporated Al, with the Si terraces still visible. The final step is the Si overgrowth, where a 60 nm Si capping layer is grown on top of the Al delta layer. The silicon is grown at room temperature using an electron-beam evaporation source. The Si capping layer is then annealed at 550 °C for 10 mins, which served as re-crystallization and dopant activation steps. As a result, a reconstructed Si surface with similar quality to the starting substrate is formed, as shown in Fig. 7.1 (d).

The sample is then transported out of the UHV chamber and used for device fabrication. Mesa-etched Hall bar devices are fabricated on top of it. The details of the device fabrication process and the principle of Hall measurement are described in Chapter 2. Fig. 7.2 (a) is a schematic of the mesa-etched Hall bar device. The light blue areas are the metal contact pads. A DC current I_{SD} is applied from the top to the bottom electrode and the magnetoresistance R_{xx} is measured along the current direction with V_{xx}. The Hall voltage V_{xy} is measured between the two electrodes

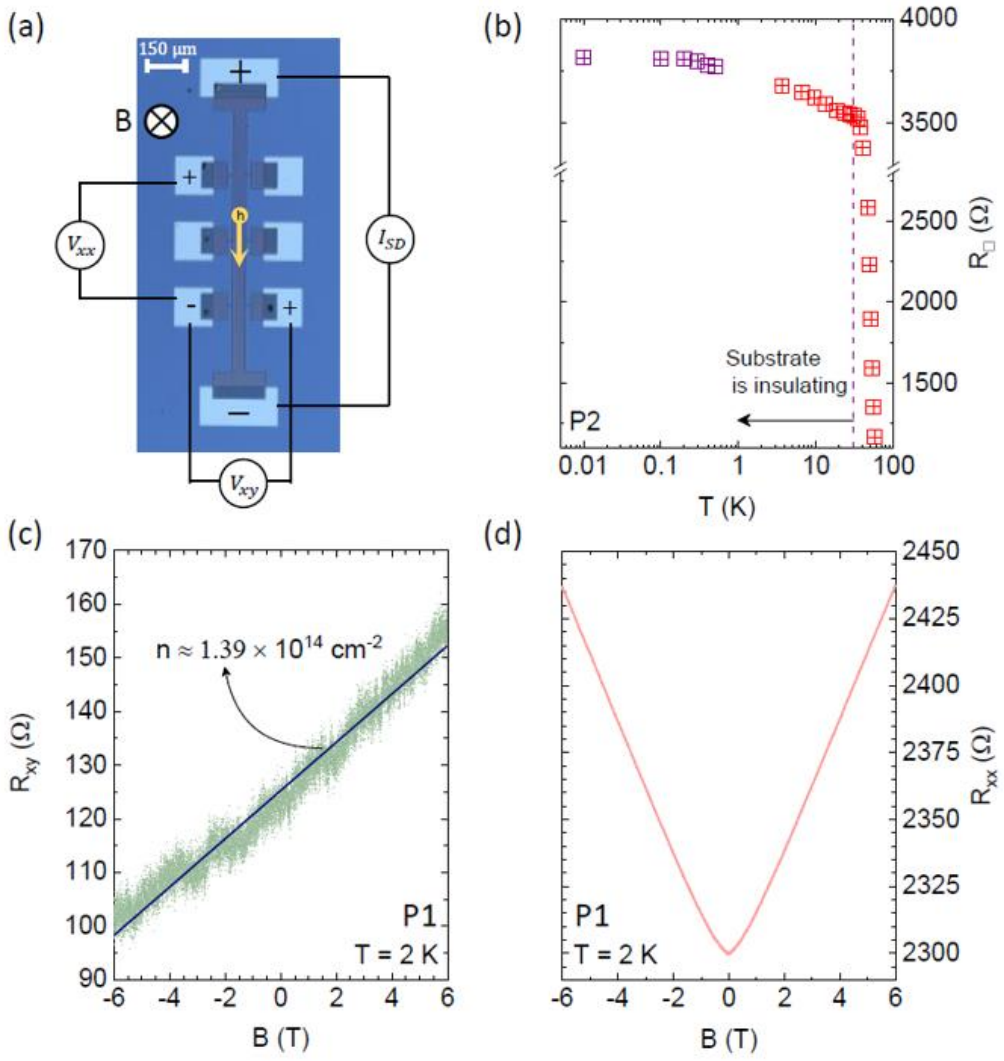

Figure 7.2: Electrical properties of our previously reported Al delta layer devices. (a) A schematic of the Hall bar device and measurement circuit. (b) The sheet resistance per square ($R_{\square}$) as a function of temperature. (c) Hall resistance (R_{xy}) vs external magnetic field B at 2 K. From the slope, a 2D carrier density of 1.39×10^{14} cm^{-2} and a mobility of 20 $cm^2/V{\cdot}s$ are extracted. (d) Magnetoresistance R_{xx} as a function of B field. Anti-weak localization behavior has been observed. (This is taken from Ref. [86] with permission)

perpendicularly. An external magnetic field is applied out of the plane, normal to the Hall bar. Fig. 7.2 (b) shows the resistance per square ($R_{\square}$) as a function of temperature, where $R_{\square}$ is defined as the sheet resistance divided by the number of squares between the two electrodes measured (V_{xx}). The data points plotted in red (T

> 3 K) were measured in a closed cycle refrigerator, while the data points plotted in purple (< 1K) were measured in a dilution refrigerator with base temperature down to 10 mK. As shown in (b), $R_{\square}$ increases rapidly when T decreases to around 30 K, then slowly levels off at lower temperature. This is mostly due to the freeze out of the substrate carriers and delta layer is dominating the conduction at T < 30 K. No superconductivity is observed in this sample. Fig. 7.2 (c) shows the Hall resistance R_{xy} as a function of external field B. The positive slope of this curve indicates that the majority charge carriers are holes. From the slope, a 2D carrier density of 1.39×10^{14} cm^{-2} and a mobility of 20 $cm^2/V{\cdot}s$ is extracted. The mobility value of this Al delta layer is comparable to other hole-doped systems at similar density, like B [198]. Note that the mobility values for the delta layer samples are usually lower compared to the Si MOSFET. In a delta layer system, the mobilities are typically in the range of 10 – 200 $cm^2/V{\cdot}s$ [199]. However, in Si-MOS devices, peak mobilities in the range of thousands [200-202] or even > 10^4 $cm^2/V{\cdot}s$ [153] are measured. The main reason is because the confinement potentials are defined differently in two systems. The delta layer is confined by the delta function potential well while the Si-MOS is defined by the sinusoidal function of the Si Bloch states. Furthermore, at low temperature range, since the delta layer carriers are confined to a dopant plane by strong confining electric fields, the mobility is limited by the charged Coulomb scattering from the ionized dopants. For Si-MOS devices, the surface roughness scattering is usually the dominating factor [203]. Fig. 7.2 (d) is the magnetoresistance vs magnetic field, where at low B field, it demonstrates parabolic behavior of the 2D conducting

channel [204]. At higher B field, R_{xx} deviates from parabolic to linear and this linear behavior can be due to the polycrystallinity or topological effects [205-207].

Let us now compare the measured 2D carrier density to the 2D dosing density of Al on Si(100). From the last chapter using different techniques, we know that the max 2D density for a full coverage of Al delta layer on Si(100) is most likely to be 3.4×10^{14} cm^{-2}. However, this value is 2.4 times larger compared to the carrier density measured by Hall, which indicates that the dopant activation of this Al delta layer is only 41 %. Or equivalently, only 41 % of the dopants were contributing to the electrical conduction. This is quite an interesting phenomenon because in other delta layer systems such as B and P, a dopant activation efficiency close to 100 % is achievable [80, 83]. Possible reasons for a limited dopant activation could be due to electrically inactive cluster formation, excess dopants forming dopant-pair defects, some Al carriers fall below metal-insulator-transition (MIT) due to dopant diffusion or segregation, or even opposite polarity charge carriers from contamination during growth. Although there is no direct evidence connecting the 2D density to the superconducting transition observed in silicon, it is generally believed that increasing the active 2D carrier density would be beneficial [192] and a better 2D conduction of the delta layer would facilitate other device applications.

7.2 Effects of Different Growth Methods

To pursue superconductivity and understand the material properties of this new Al delta layer system, we will be focusing on the following parts: 1) study the correlation

between each growth methods to carrier density and dopant activation and 2) explore the possibilities to improve 3D confinement of this dopant. In the following sections, we will modify and explore our material growth methods in 4 different ways to study the effect of each growth steps. This includes: 1) incorporation anneal; 2) solid phase epitaxy (SPE) or molecular beam epitaxy (MBE) for Si capping layer; 3) locking layer (LL) and 4) different Al doses. For each growth method, STM will be used to characterize the surface properties and magnetotransport measurements will be performed using Hall bar devices to characterize the electrical properties of this material.

7.2.1 Effects of the Incorporation Anneal

In other dopant systems, such as B, Sb and P delta-doped Si, incorporation anneal is a critical step for dopant activation [208-210]. The annealing process provides enough energy for the dopant species to substitute into the silicon lattice sites and become electrically conductive. In this section, we will explore the effects of incorporation anneal on surface topography and dopant activation in our Al delta layer samples.

The first two steps for delta layer growth are the same as introduced in the beginning of this chapter: prepare the substrate by UHV flash anneal and deposit thermally evaporated Al onto the Si(100) surface. For 100 % dose (full coverage or one atomic layer), three different heat treatments were studied: no anneal, as well as 1 minute and 10 minutes incorporation anneal times at 550 °C. The no anneal and 10 minutes anneal treatments were repeated for 200 % Al dose. Fig. 7.3 shows the STM

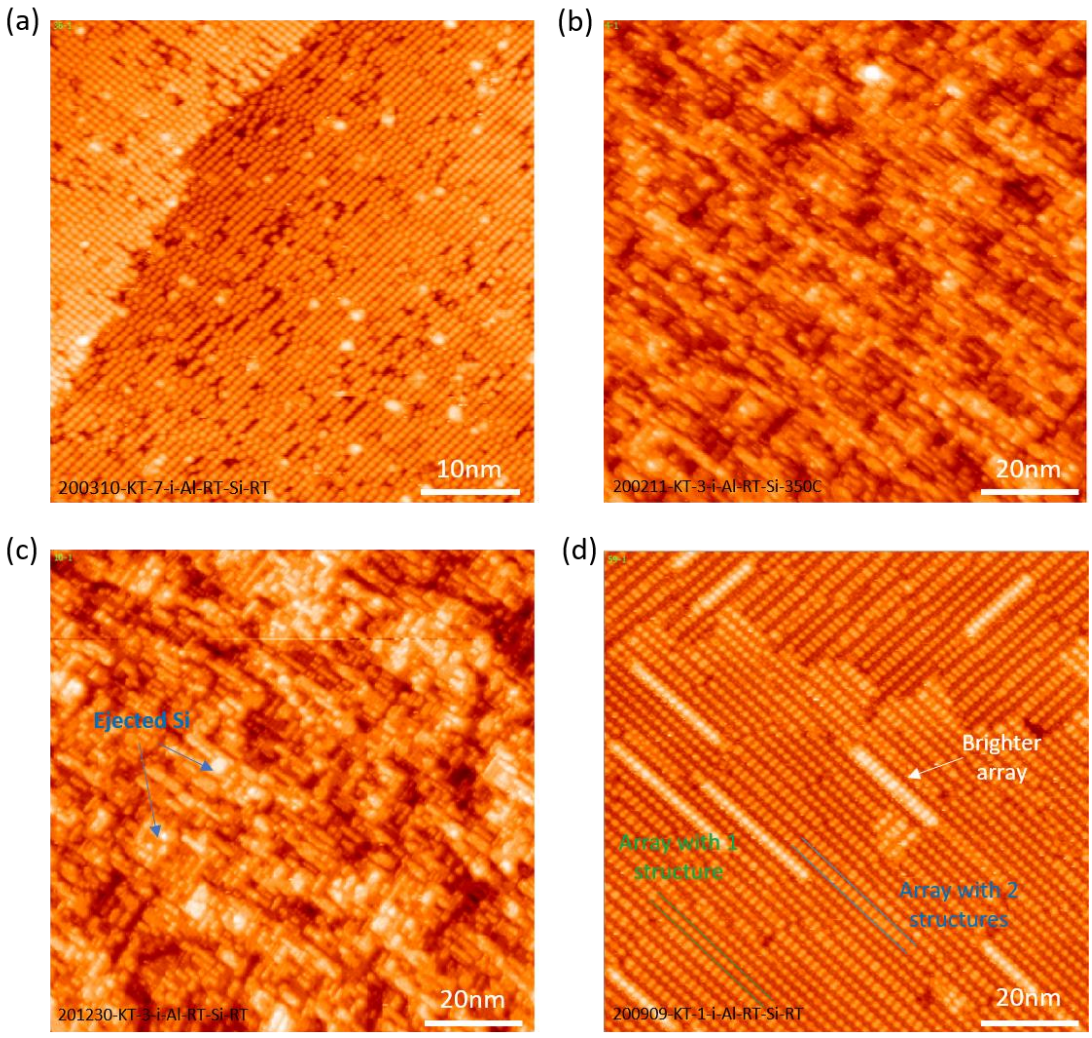

Figure 7.3: STM images of the surface with different incorporation annealing times. The images are taken at the same tip bias conditions: +2 V, 110 pA demanded. (a) No anneal with 100 % of Al dose (one atomic layer) on Si (100) substrate. Circular bright protrusions of Al (dimer) can be seen. (b) After 1 minute anneal with 100 % of Al dose. Dark lines (possibly incorporated Al) and brighter elongated streaks are observed. Those streaks are most likely the ejected Si from the lattice that formed islands on the surface. (c) After 10 minutes anneal with 100 % of Al dose. Similar features and structural sizes are observed compared to (b). This indicates that 1 minute anneal is having the same effect compared to 10 minutes anneal. (d) After 10 minutes anneal with 200 % Al dose. The structure is very different compared to (b) and (c). Closely packed, periodic arrays with two widths are seen. Further arrays are deposited in parallel on top of the gap between two underneath arrays.

images of the surface after different incorporation anneal times with the two doses described above. Fig. 7.3 (a) is a Si(100) surface after 100 % Al dose with no (0 min)

incorporation anneal, scanned using a +2 V tip bias and 110 pA demanded current. This is similar to Fig. 7.1 (b) where Al 2 × 2 structures are covering the Si terraces. Fig. 7.3 (b) and (c) are the surfaces with the same dose (100 %) after incorporation anneal for 1 minute and 10 minutes, respectively. Elongated streaks of silicon islands formed from ejected Si atoms and dark lines of incorporated Al can be seen in both figures. The feature sizes are also very similar. Considering the difference in contrast and tip conditions, we can say that Al with 10 mins anneal displays comparable surface topography compared to 1 minute anneal. And any further anneal at the same temperature does not change the surface structures. However, if the Al dose is increased to 200 %, the surface structure changes dramatically after annealing, as shown in Fig. 7.3 (d). Panel (d) shows the incorporated Al surface after 10 minutes anneal, using the same tip bias and current setpoint. Unlike (b) and (c), closely packed, periodic arrays are seen in (d). This is quite surprising because based on the Al-Si phase diagram, Al solubility limit in Si is very low. We would expect Al to form clusters on top of Si surface instead of these well-organized arrays following the underlying Si dimer row and terrace structures. There appears to be two array types, one with single circular protrusions and one with double protrusions binding together. The measured width of these arrays under STM are ≈ 1.0 nm (marked with green lines) and 2.0 nm (marked with blue lines), respectively. Some arrays with brighter color (marked with white arrow) are also seen, with growing direction parallel to the underneath arrays. Those arrays seem to follow the direction of the Si terraces.

Next, let us compare the effects on the electrical properties from different Al incorporation anneal processes. Fig. 7.4 shows the magnetotransport measurements of

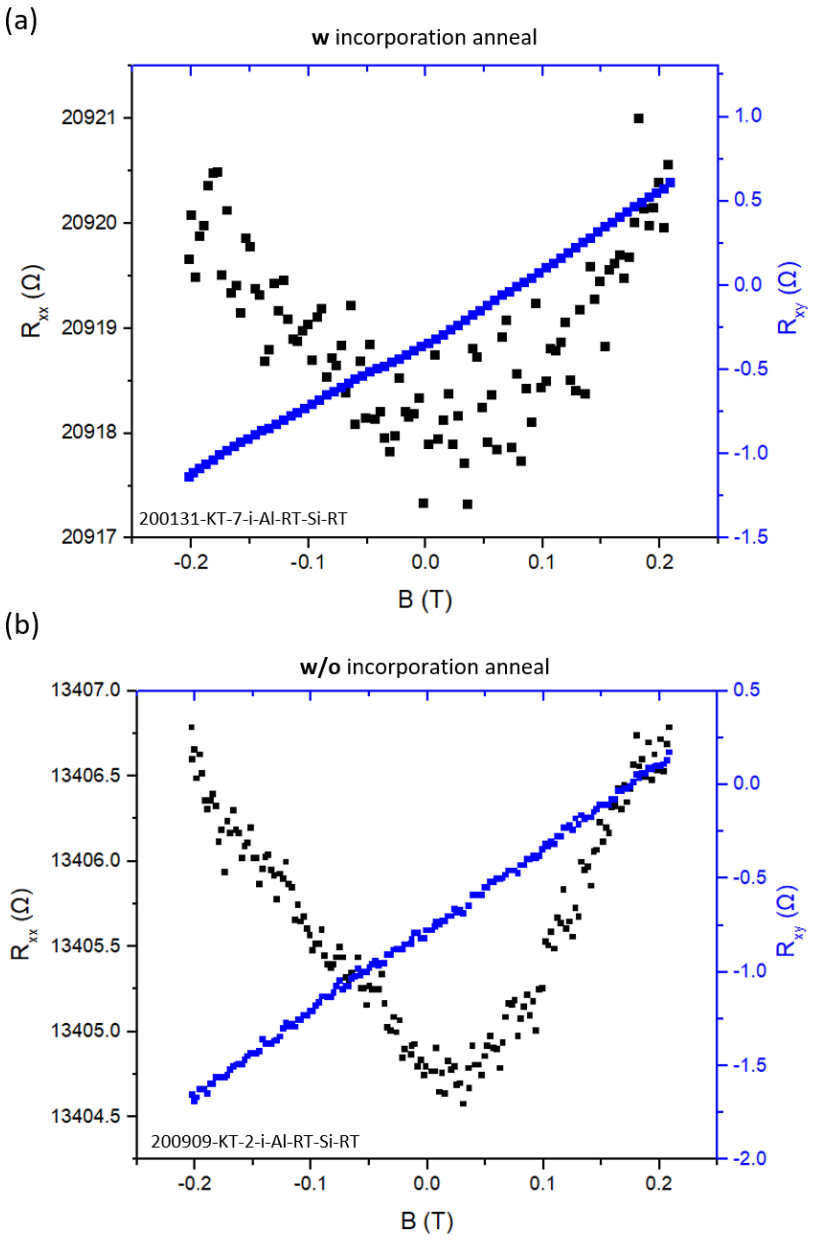

Figure 7.4: Electrical measurements of the Al delta layer samples with and without 550 °C 1 min incorporation anneal.
The measurements were taken at 4 K. Same substrate and device fabrication steps were used. (a) shows the Hall measurement with incorporation anneal. A carrier density ≈ 1.50×10^{14} cm^{-2} and a mobility of 10 $cm^2/V{\cdot}s$ is extracted. (b) shows the Hall measurement without incorporation anneal, with a carrier density ≈ 1.41×10^{14} cm^{-2} and a mobility of 16.5 $cm^2/V{\cdot}s$. Repeat samples and measurements have been done, all showed similar results, indicating that incorporation anneal (at least as a separate step) is not necessary for dopant activation.

two samples, one with 1 min incorporation anneal and one without. Other processing conditions such as the substrate type, dosing (100%), annealing time and temperature and Si overgrowth (SPE) are kept being the same. Both samples were measured in a closed cycle refrigerator with base temperature of about 4.5 K. Fig. 7.4 (a) shows the Hall measurement with 550 °C incorporation anneal. A carrier density $\approx 1.50 \times 10^{14}$ cm^{-2} and a mobility of 10 $cm^2/V{\cdot}s$ is extracted. Fig. 7.4 (b) shows the Hall measurement without 550 °C incorporation anneal, with a carrier density $\approx 1.41 \times 10^{14}$ cm^{-2} and a mobility of 16.5 $cm^2/V{\cdot}s$. Multiple samples with the same growth methods were measured, all showed similar carrier density, i.e. approximately 1.4×10^{14} cm^{-2} to 1.5×10^{14} cm^{-2}. Considering possible slight differences in sample substrate, Al dosing and wire bonds, we can conclude that there is essentially no difference in carrier density with and without incorporation anneal. However, the R_{sq} values of the two samples are different, resulting in different mobility values. This might indicate that there are other differences in the processing steps or with/without this incorporation step is having different effects on scattering of the carriers. In general, the incorporation anneal, as a separate step, does not seem to change Al dopant activation efficiency. It is likely that other growth processes, such as the final SPE anneal, served as the dopant activation of this Al delta layer. Since our focus is to reach a high enough 3D density, with or without this incorporation step can go in both directions. This is because although thermal budget is reduced when ignoring the incorporation, an incorporation step might be able to lock down the dopants into Si lattice positions and prevents further diffusion or segregation.

7.2.2 Solid Phase Epitaxy (SPE) or Molecular Beam Epitaxy (MBE)

In the previous section, we have found that with a SPE grown Si capping layer, an incorporation anneal does not affect the carrier density of the Al sample and the incorporation step seems be included in the final SPE overgrowth. In this section, we will discuss and compare the two methods of Si overgrowth: SPE and MBE as an effort to improve the 3D confinement of the Al delta layer by suppressing the segregation process and reduce the thermal budget.

SPE is an important processing step in the semiconductor community [211]. It is a crystallization process that allows atoms to rearrange their bonding configurations and transfer from a metastable amorphous phase to a crystalline phase [212]. When an amorphous material is heated, atoms in amorphous phase will reorder at the crystalline-amorphous (c-a) interface, using the starting substrate as a template. It can aid the dopant activation above the solid solubility limit and recover from damage after processes such as ion implantation, with a relatively low thermal budget.

MBE is another important process for growing thin films with epitaxial quality. In this process, beams of atoms in UHV are incident on a heated substrate (for most of the case) and the arriving atoms form a crystalline layer in registry with the substrate [213]. The beams are usually produced by evaporation or sublimation using an ultra-pure crucible. Since our goal is to maximize the carrier density while minimizing the dopant movement, MBE growth of the capping layer is expected to have several advantages over SPE growth. One of the advantages of MBE is the very low thermal budget, where epitaxial Si can be grown at temperatures from 300 – 350 °C with a deposition rate of ≈ 0.4 nm/min [78]. Another expected advantage of MBE over SPE

is that the diffusion mechanism is greatly suppressed in crystalline Si than in amorphous Si, where the diffusion is mediated by the dangling-bonds [214]. The reduction in defect density with MBE growth also decreases the chance of defect-enhanced diffusion processes [77, 215]. As a result, B delta layers with extremely high 3D density has been achieved using low-temperature MBE, with $n_s = 1 \times 10^{22}$ cm^{-3} or 20 at. % [83, 216], even higher than the delta-doped layer using gas immersion laser doping ($n_s = 2.8 \times 10^{21}$ cm^{-3}) [71].

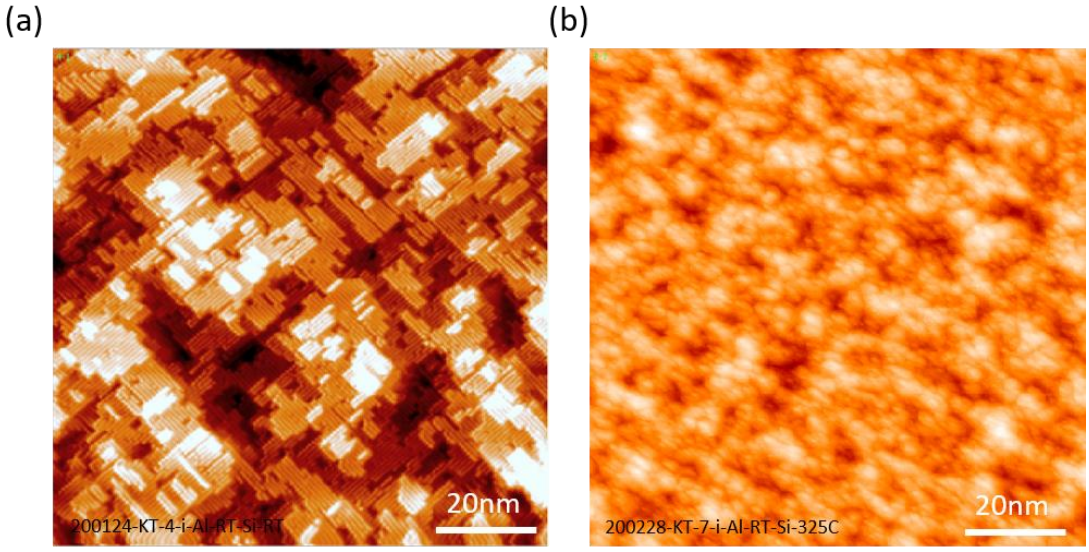

Figure 7.5: STM images of the deposited Si capping layer on different starting surfaces.
(a) a test sample using the e-gun Si source deposited at 350 °C. 4 nm of Si has been deposited on Si substrate with a deposition rate of 0.2 nm/min. 3D epitaxial island growth with Si dimer rows and terraces can be seen. (b) 20 nm of Si using the same Si source, deposited on top of a Al delta layer at 325 °C, with a rate of 0.12 nm/min. Polycrystalline Si instead of monocrystalline has been observed.

The SPE overgrowth on our Al delta layer sample has been introduced in section 7.1: a polycrystalline Si layer is grown at room temperature, followed by a 550 °C anneal for 10 mins. The Si surface after annealing usually has similar epitaxial quality (in terms of defect density and terrace size) compared to the starting substrate. For

MBE overgrowth, the same e-gun Si source was used. The substrate was heated up to 350 °C. A test sample with 4 nm of Si overgrowth layer was deposited on a Si substrate and is shown in Fig. 7.5 (a). The deposition rate was 0.2 nm/min. 3D islands with clear Si dimer rows were seen, indicating the epitaxial quality of the grown layer using our Si source. However, when trying to grow MBE Si over an Al delta layer with the same parameters, the deposited surfaces were always polycrystalline. For example, in Fig. 7.5 (b), a 20 nm thick Si capping layer was grown on top of a Al layer at 325 °C with a rate of 0.12 nm/min, well below the threshold of epitaxial thickness and growth rate (< 0.4 – 0.6 nm/min) at this temperature [82, 119, 217]. One possible reason for a polycrystalline Si overgrowth may be due to the fact that epitaxial growth requires a starting surface (as a template) that is monocrystalline. The Al-Si structure formed after incorporation anneal is likely in a meta-stable state with cluster-like structure instead of crystalline structures, deviating from the required crystalline template. Interdiffusion between the heteroepitaxial Al-Si interface might be another possible explanation, where interdiffusion has been reported for Al and Si at the temperature range of 400 – 500 °C despite the small solubility of Si into Al (0.4 % at 400 °C) and the non-existing solubility of Al into Si below the eutectic temperature of 577 °C [218].

Additional efforts have been carried out to pursue MBE growth: for example, grow the Si capping layer at 350 °C with an additional thermal anneal at 550 °C for 10 mins at the end to help for recrystallization. Fig. 7.6 (a) shows the deposited surface after final annealing. Although Si dimer rows and terraces can be seen, indicating the epitaxial quality of the deposited Si layer, high density of Al chains and

clusters are also present on the surface. Fig. 7.6 (c) is a SIMS depth profile of the same sample, where two Al peaks can be observed. One is the original delta layer peak, buried at a depth of 30 nm from the surface. A higher density peak is

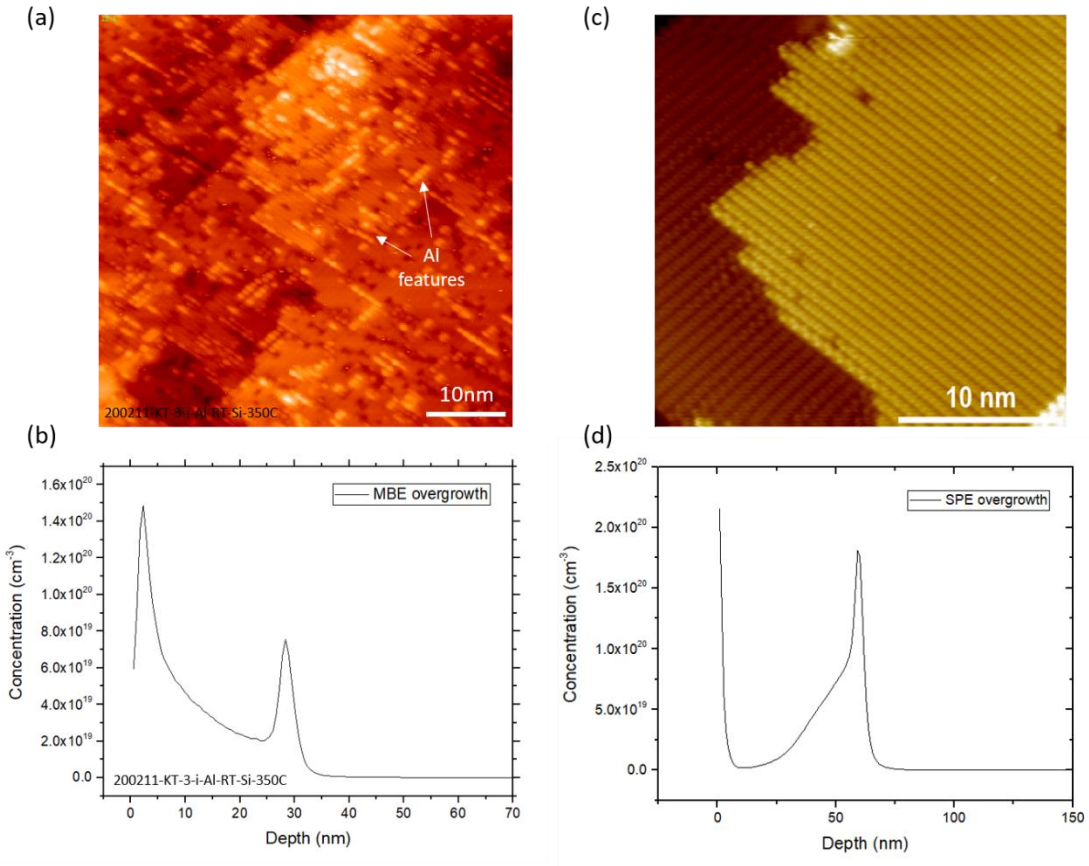

Figure 7.6: Comparison between MBE and SPE grown Al delta layer samples. (a) shows the STM images after Si overgrowth at 350 °C and thermal anneal at 550 °C for 10 mins. The Si layer is epitaxial with visible Si dimer rows and terraces, but excess Al chains and clusters are also observed on the surface. (b) shows a SIMS depth profile of the same sample. A high-density surface peak along with the delta layer peak is observed, most likely due to the combination of surface segregation and Al contamination from the Hall device. (c) shows the STM image after SPE overgrowth with 550 °C anneal. (d) shows a SIMS depth profile of the SPE grown sample, only surface tail but no surface peak observed.

observed at < 5 nm, closer to the Si surface. Since this is the sample with Hall bar devices on top, the peak at the surface might be a combination of both the surface contamination from the metal contact and the migrated Al observed from the STM images. Fig. 7.6 (c) and (d) are measured from a SPE overgrown sample, as a comparison to the MBE overgrowth. This sample has the exact same processing steps compared to the MBE case (also has surface tail). Panel (c) shows an epitaxial surface of Si after SPE overgrowth and (d) shows the SIMS profile of this SPE grown sample. The Al delta layer can be observed at ≈ 50 nm with a surface tail, but no surface peak of Al is seen. This indicates that during MBE overgrowth with 550 °C final anneal, some Al migrated to the surface, results in a worse dopant confinement compared to the SPE overgrowth method.

From the results described above, we can conclude that for Al delta layers at full coverage, SPE growth method is preferred over MBE method. This is due to: 1) the MBE growth method results in polycrystalline Si overgrowth instead of epitaxial overgrowth, probably due to the lack of crystalline template to start with; 2) evidence showed that there are more Al atoms migrated to the surface (Fig. 7.6 a, c) compared to the SPE growth method, indicating a worse dopant confinement. We believe this is largely due to the formation of an Al-Si meta-stable state whose coexistence has a lower free energy compared to the Si crystalline phase alone. And this broken symmetry allows the Al to segregate up to the surface during MBE growth process, probably through the defects and interstitial sites that are created during the epitaxial growth.

7.2.3 Effects of the Locking Layers

In B and P delta-doped systems, a locking layer (LL), a thin (monolayers thick) room temperature grown silicon layer, is helpful for suppressing dopant segregation and diffusion into the Si capping layer, resulting in a higher 3D dopant confinement and electrical activation [79, 192, 219, 220]. A locking layer might be helpful for achieving better dopant confinement. In this section, we will explore the effects of a locking layer on the Al delta layer samples.

Fig. 7.7 (a) shows a STM image after 1.6 nm of LL growth on Al delta layer at full coverage. The LL was deposited at room temperature, with a deposition rate of 0.138 nm/min. The deposited LL surface looks very similar to the ones reported in the P delta layer system [79, 220], where grains of polycrystalline Si can be observed. The LL was then annealed at 550 °C for 1 min to recrystallize the surface. However, unlike what was reported in P delta layer system [220], where the locking layer recrystallized and formed epitaxial Si dimers and terraces, the LL on Al delta layer surface showed clear evidence of Al migration (bright Al chains and circular protrusions that look like Al clusters) on top of the reconstructed Si dimers and terraces, as shown in Fig. 7.7 (b). Note that the samples shown in Fig. 7.7 (a) and (b) had the same processing steps. This might be an indication of the Al segregation towards the growth front of the Si.

LL combined with Si overgrowth with elevated temperature was also investigated. Fig. 7.7 (c) shows the surface of a Si capping layer grown at 325 °C on top of the LL after the process of Fig. 7.7 (a). Evidence for polycrystalline Si is observed, which is not surprising since the starting surface was not monocrystalline.

The topography of the surface of this poly-Si after thermal annealing at 550 °C for 10 mins is also shown in Fig. 7.7 (d). The resulting surface topography is very similar to what was presented in Fig. 7.6, where excess Al were seen on top of the epitaxial Si surface.

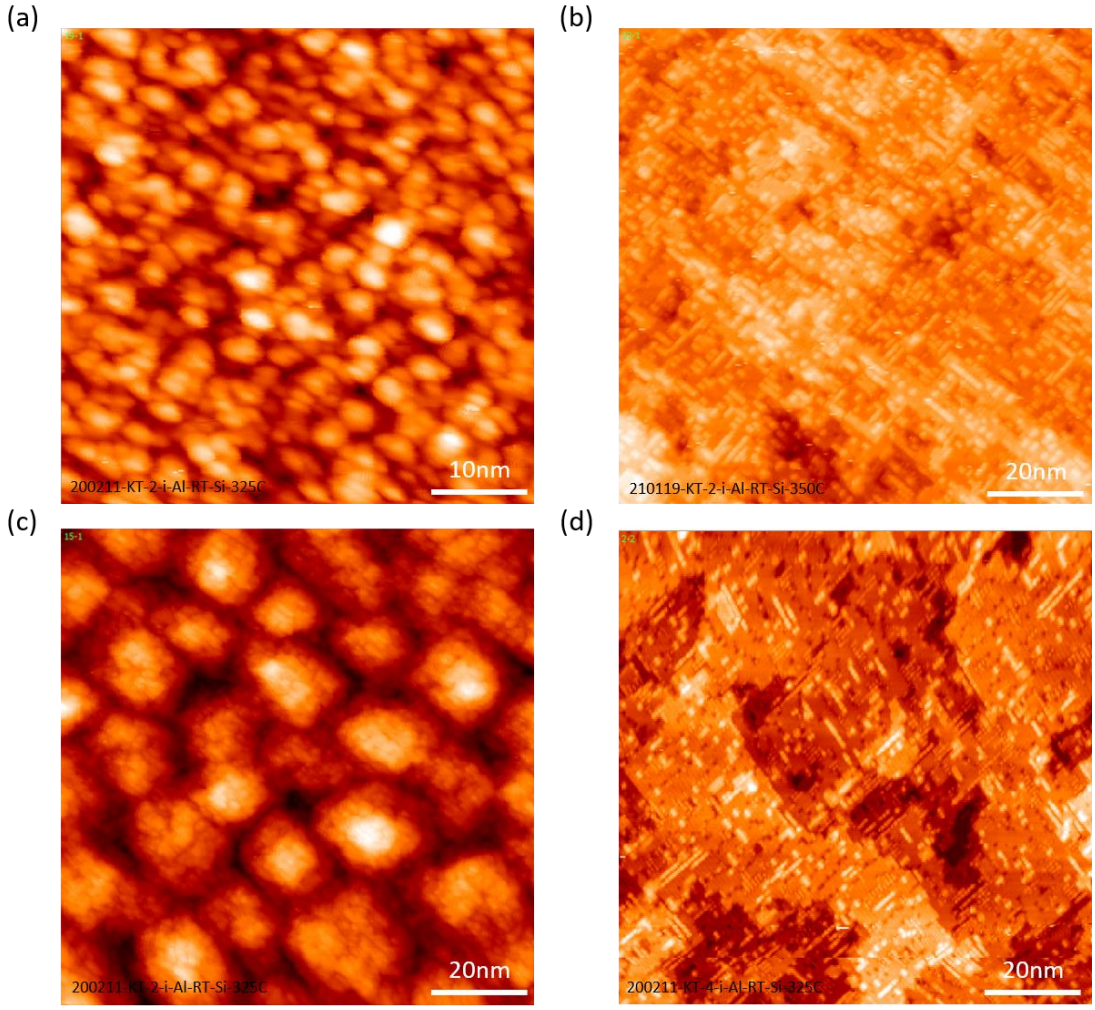

Figure 7.7: STM images of the deposited Si surfaces with LL.
(a) 1.6 nm of LL grown at RT with a rate of 0.138 nm/min. Polycrystalline surface is seen with a similar quality compared to other LL growth methods. (b) LL after 550 °C 1 min to recrystallize the surface. Epitaxial Si is observed, but with high density of Al chains and clusters on the top. (c) Si overgrowth on top of the LL at 325 °C, however, poly-Si is seen instead of epitaxial Si. (d) The overgrown Si followed by a final 550 °C 10 mins anneal. Reconstructed Si is observed, but with excess Al on the surface.

In summary, there are three outcomes: 1) Epitaxial Si overgrowth layer was not grown successfully using MBE method due to a lack of epitaxial starting surface. In B and P systems, the LL was usually annealed and recrystallized for a good starting surface for capping layer. However, Fig.7.7 (b) showed that an epitaxial LL surface after annealing is not possible due to Al migration. 2) directly grow Si at elevated temperature on RT LL, but it showed poly-Si (Fig.7.7 c). 3) grow a RT LL with MBE Si then anneal at 550C, but excess Al were shown on the surface (Fig.7.7 d). As a result, the LL method on Al delta layer was not successful. Chains and clusters of excess Al are observed on the surface of this LL after thermal annealing (which is a typically step to recrystallize the LL). However, without this thermal annealing step, the surface of the MBE overgrown Si becomes polycrystalline, due to the absence of an epitaxial surface to start with. A final SPE anneal after MBE overgrowth also experiences Al segregation toward the surface. Further efforts (e.g. higher Si deposition rate and lower annealing T) are needed to develop a better LL growth on Al samples.

7.2.4 Effects of Al Doses on Dopant Activation

In Chapter 6, we studied the atom density of Al on Si(100) surface using various techniques. The results showed that the 2D density at full coverage is most likely 3.4 $\times 10^{14}$ cm^{-2}. However, when compared to our Hall measurements, the extracted carrier densities of Al samples are approximately 1.5×10^{14} cm^{-2}, which corresponds

to a dopant activation of only ≈ 44 %. In this section, we will explore and discuss the factors that might affect dopant activation of the Al delta layer.

The first obvious factor is the incorporation anneal. However, as we have discussed in the previous section, the incorporation anneal does not change the carrier density of our delta layer sample (but changes the mobility. The second factor that might improve the dopant activation is the use of a locking layer (LL) as it suppresses dopant segregation and preserved the 3D confinement. However, in Al case, the LL process that we tried does not prevent the dopant from segregating onto the Si surface. A better approach is yet to be developed.

In this section, we will study the correlation between different Al doses (amount of Al that we put down) and dopant activation. 8 Al delta layer samples with 3 different doses were prepared and fabricated into Hall bar devices: 50 % dose (half atomic layer), 100 % dose (one atomic layer) and 200 % dose (two atomic layer). The 100 % dose was determined by topographical imaging of the result in STM after Al deposition, while the other two doses were calibrated based on the deposition rate used for 100 % dose. All samples were deposited using the SPE method, while some of them employed an incorporation anneal step and some of them did not. The STM images of the surface after Al deposition at 50 % and 200 % doses are shown in Fig. 7.8 (a) and (b), respectively. For the 50 % dose, both the Al chains and the underlying Si dimer rows can be seen. For the 200 % dose, the Si surface is completely covered with 2 × 2 Al dimer structures before forming clusters. After that, some clusters are formed on top of the adsorbed Al atoms. These Al adatoms tend to wet the Si

substrate first before forming larger Al-Al clusters. Thee clusters appear as larger bright islands in the image.

Transport measurements have been done in a closed cycle refrigerator at temperatures from 4 – 10 K. A summary plot of the Al carrier density measured at low temperature vs Al dosing is shown in Fig. 7.8 (c). Samples with incorporation anneal are marked as blue triangles and samples without incorporation anneal are marked in black circles. As seen in Fig. 7.8, the carrier density increases non-linearly against dosing. The carrier density increases rapidly from 50 % dose to 100 % dose, then slowly saturates at 200 % dose. A logarithmic function (red solid line) has been used to fit this data. The dopant activation efficiency as a function of Al doses is plotted in Fig. 7.8 (d). As the carrier density was doubled from 100 % to 200 % dose, the carrier density was only increased by 30 %, resulting in a decrease in activation efficiency from ≈ 48 % to 26 %. The maximum activation is at 100 % dose, ranging from 41 % to 48 %.

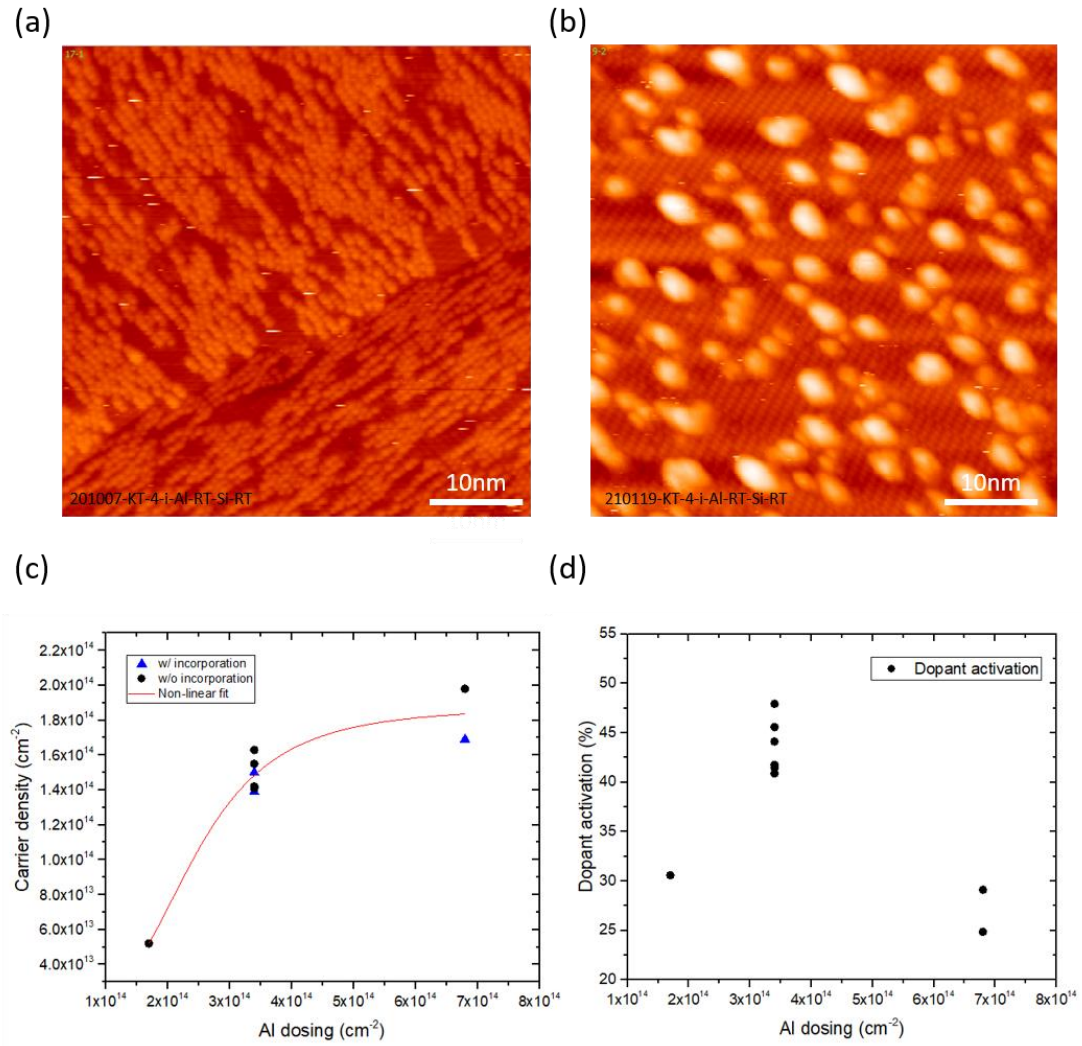

Figure 7.8: Effects of different Al doses on surface topography and dopant activation. (a) 50 % Al dose (half coverage of Al on Si surface). Al chains can be seen on top of the Si dimers and terraces. (b) 200 % Al dose. Si substrate is completely covered with Al 2 × 2 dimer structures, with the formation of some Al clusters on top (shown as bright islands). (c) A summary plot of the carrier density vs Al dose. A non-linear increase in carrier density is observed, with a saturation at about 1.8×10^{14} cm^{-2}. (d) Dopant activation vs Al doses. The activation efficiency is having a maximum value of 48 % at 100 % dose.

We can conclude that under the current growth methods, there seems to be a cap in Al dopant activation efficiency at < 50 %. One possible reason for the cap in activation efficiency of this Al delta layer might be that a meta-stable state of Al-Si

has been formed during the thermal annealing of this dopant. For example, as shown in Fig. 7.3 (d), Al tends to form closely packed periodic arrays that are most likely Al-Si clusters, containing multiple Al atoms and Si atoms. It is possible that only part of the Al atoms has been substituted into the Si lattice and contributed to electrical conduction, while part of the Al atoms was bonded in those cluster forms that is electrically inactive. Another reason might be due to the incomplete confinement of the delta layer in the z-direction. Diffusion along the grain boundary (which is expected to be faster than through the grain) or segregation of the dopants during thermal activation either at the incorporation anneal or the SPE anneal stage can be significant. For higher doses, such as 200 % dose, it is also possible that the excess Al atoms form Al-Al dopant pairs (since there are more Al dopants in the nearest-neighbor lattice sites) that can act as de-activation precipitates, like in the case of B and P delta layers [80, 192, 221].

7.2.5 Conclusions and Future Expectations

In this chapter so far, we discussed the effects of different material growth methods on electrical conduction (carrier density and dopant activation) and explored the possibility of improving the dopant confinement in the Si-Al-Si heterostructure. A summary plot is shown in Fig. 7.9 for the variations in growth methods for Al delta layer samples studied in this work. We start with a clean Si substrate processed in

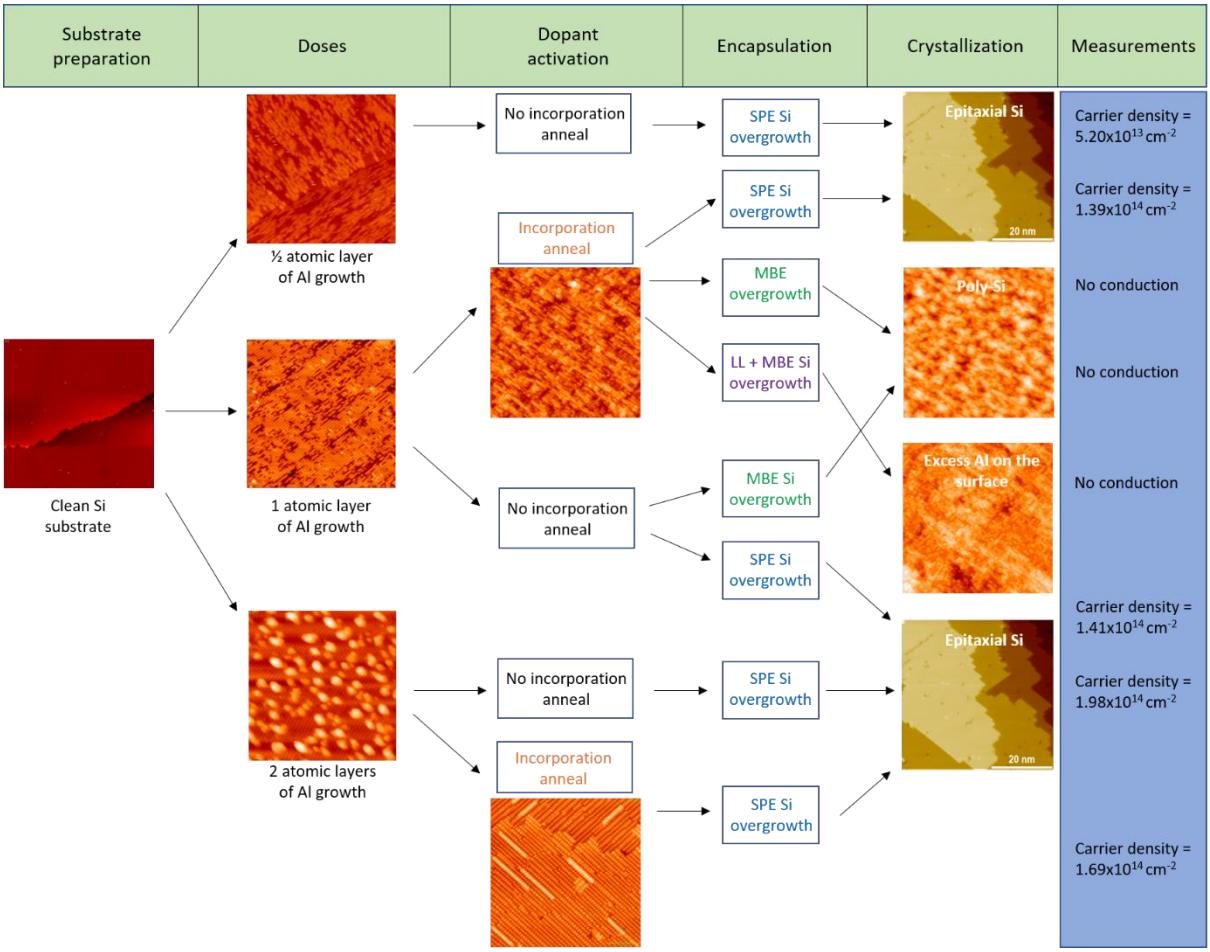

Figure 7.9: Summary of the variations in growth methods for Al delta layer synthesis. Three different major processing steps were studied: Al doses, dopant activation and Si (capping layer) encapsulation. The Si-Al-Si heterostructures were turned into Hall bar devices and characterized at low temperature.

UHV condition. Three different major processing steps during delta layer growth were studied: Al doses, dopant activation and Si (capping layer) encapsulation. The delta layer samples were then turned into Hall bar devices and characterized in low temperature cryostat. The summary of the electrical measurements is shown in the last column. The conclusion is that: the incorporation anneal does not affect the carrier density of this delta layer (although it changes mobility); SPE overgrowth is preferred over MBE; the LL growth was not successful on this delta layer and did not

seem to suppress Al segregation. Finally, the Al carrier density does not increase linearly with dosing, a cap in the dopant activation is found be ≈ 50 %. A detailed summary of the processing steps and characterization results of the Al delta layer samples is included in the Appendix, Table. A1.

Based on the information that we have learned so far, we will discuss the factors that still need to be improved for achieving superconducting transition (SC) and the future expectations of this Al delta-doped material system. One of the most important factors that needs to be considered when pursuing superconductivity in this Si-Al-Si heterostructure is the critical 3D atom density. From the previous SIMS and APT data, the highest Al delta layer peak density that we have is 6.58×10^{20} cm^{-3} and 6.34×10^{20} cm^{-3}, respectively. These correspond to an atomic percentage of ≈ 1.3 at. %. Assume that the same condition for B:Si applies for Al:Si, where a standard electron-phonon mediated BCS mechanism is accounted for the observed SC [75]. The obtained value of ≈ 1.3 at. % is lower than the critical value needed (≈ 2 at. %) for superconducting transition [222]. However, we believe the numbers that are extracted from SIMS and APT may be at the lower bound of the actual density value, since peak broadening effects have been expected from both measurements. For example, the forward recoil of the sputtered ions in SIMS is usually limiting the depth resolution at this delta layer thickness and laser heating during APT measurement may cause the migration of the Al atoms in Si. Therefore, we think that reaching a 2 at. % (this is assuming 100 % dopant activation) of the Al dopant concentration in Si using delta doping method is still possible. However, considering the fact that Al behaves quite differently in many ways compared to other dopant systems, the

simplified theoretical prediction that Al will experience a standard phonon-mediated BCS-type mechanism based on B case for the occurrence of superconductivity [75] might not be correct. Further theoretical studies will be needed to provide more insights into this material system.

From the experimental standpoint, the 3D atom density described above is from the Al sample without post-anneal, and a larger gap exists between the density of our Al delta layer devices and the critical density needed for SC. A typical 3D carrier density of our Al delta layer device that is conducting at low temperature is $\approx 1.1 \times 10^{20}$ cm^{-3} or 0.2 at. % (half of 2.1×10^{20} cm^{-3} based on 50 % activation). Some diffusion toward the Si substrate and segregation towards the Si capping layer surface were observed after thermal annealing steps, which degraded the dopant confinement. Unfortunately, unlike B and P delta layers in Si, the standard MBE growth and locking layer methods that can be used to suppress dopant segregation in other systems do not help in the Al case. In addition, the meta-stable cluster-like features observed in Fig. 7.3 that might be the origin of a limited dopant activation efficiency of $\approx$ 50 % makes it even more challenging. This is because the 2 at. % critical density is assuming that all dopants are fully activated, a 50 % dopant activation means only half of the dopants are contributing to electrical conduction and the other half remains inactive.

Despite the difficulties described above (the gap between a critical density of 2 at. % and 0.2 at. % conducting Al carriers), we think that there are still opportunities to make this new material system superconduct. Al segregation seems to be the biggest limiting factor for reaching high enough 3D dopant density. A method will need to be

developed in the future to suppress this segregation during the growth process better. With this limit to the material structure, it is very hard to achieve the critical density needed for SC, especially for a single delta layer. However, it is possible to deposit superlattices of multiple Al delta layers, which might still exhibit 2D conduction properties after thermal processes but would result in a much higher 3D density and 2D carrier density. A more detailed study on thicker spacer layers or locking layers between those Al delta layers may also be beneficial.

7.3 Temperature Dependent Carrier Densities and Mobilities

The Al delta layer is a new system where the conduction at low T has not been studied before. In this section, the electrical transport properties of the 2D Al delta doped layers at low temperature are investigated. The temperature dependence of the Hall 2D carrier density and mobility of the Al delta layer samples with 100 % Al dose and SPE growth methods have been studied, over a temperature range of 4 K to 80 K.

Transport through Al delta layer samples, with variable temperature, has been measured using Hall devices. Instead of using a fixed magnetic field and rotate the sample direction 180^{o} as in the standard Van der Pauw measurement, we are sweeping the magnetic field ranging from – 0.2 T to + 0.2 T while keeping the sample position unchanged. Unlike other delta doped layers in silicon that display a metallic conduction and characterized by constant values of carrier density and mobility, a two-regime conduction behavior is observed in Al delta layer samples. As shown in Fig. 7.10 (a), in the temperature range of 4 K < T < 20 K, a metallic conduction with

a nearly constant carrier density (≈ 10 % variation) of 1.5×10^{14} cm^{-2} is obtained. As T > 20 K, a sharp transition occurs and the carrier density decreases to a minimum value of 4.4×10^{14} cm^{-2}, then levels off. The mobility vs T is shown in (b), where the mobility increases from 14.3 $cm^2/V{\cdot}s$ at 4 K to a maximum value of 1917.5 $cm^2/V{\cdot}s$ and then gradually decreases when T > 50K. Similar behavior has been observed for multiple Al samples, both with and without incorporation anneal.

To interpret this temperature dependence carrier density and mobility, we use a delta layer conduction model that considers carriers with different densities and mobilities, inspired by similar studies of B delta-doped structures in diamond [223, 224]. This model describes a two-level system where one level can be thermally promoted to the other. For example, holes can be thermally activated from the delta-doped layer into bulk states [225] or from the ground state subband of the delta function potential well into higher energy subbands in the valence band with higher mobilities [226].

A multi-carrier conduction mechanism is assumed, and the Hall mobility of a multi-carrier model is described by [227]:

$$\mu_H = \sum_{i=1}^{N} p_{si}\mu_i^2 \Big/ \sum_{i=1}^{N} p_{si}\mu_i \qquad (7.1)$$

For the simplest case of two-carrier conduction, the Hall mobility becomes:

$$\mu_H = (p_{s1}\mu_1^2 + p_{s2}\mu_2^2)/(p_{s1}\mu_1 + p_{s2}\mu_2) \qquad (7.2)$$

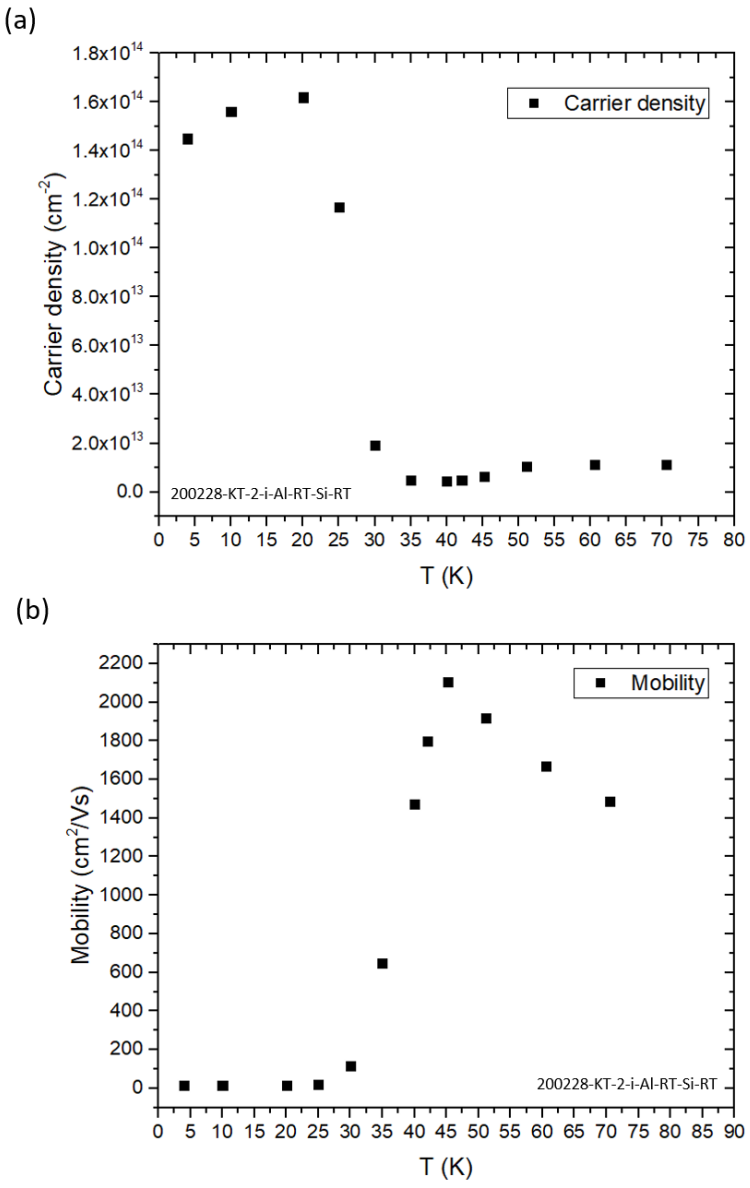

Figure 7.10: Temperature dependent sheet density and mobility.
The sample is measured in a closed cycle refrigerator with an external magnetic field of ± 0.2 T. Sharp transitions have been observed in both carrier density and mobility. The carrier density decreases from ≈ 1.5×10^{14} cm^{-2} to ≈ 1.0×10^{13} cm^{-2} and mobility increases to a max value of 1917.5 $cm^2/V{\cdot}s$ and then gradually decreases.

, where p_{s1} and p_{s2} are the carrier densities, μ_1 and μ_2 are the mobilities for each carrier type (or subband), respectively. The apparent carrier density can be expressed as [227]:

$$p_{s,app} = (p_{s1}\mu_1 + p_{s2}\mu_2)/(p_{s1}\mu_1^2 + p_{s2}\mu_2^2) \quad (7.3)$$

We take the holes in the lowest energy state to have a carrier density of p_{s1} (here assuming a constant p_{s1} at base T) and mobility of μ_1. At a higher temperature, when the holes are thermally excited into either a bulk state or higher energy subbands, the carrier density and mobility are expressed as p_{s2} and μ_2. p_{s2} can be then calculated from the Fermi-Dirac probability distribution [223]:

$$p_{s2} \sim T^{3/2} \exp[(E_F - E_V)/k_B T] \quad (7.4)$$

In a doped semiconductor system, the $T^{3/2}$ dependence usually corresponds to an impurity scattering mechanism. However, previously reported studies showed that predicting the mobility in heavily doped systems are non-trivial [223, 228]. The most frequently used mobility expression is an empirical function with a $T^{2/3}$ dependence:

$$\mu_1(T) = \mu_{1,0}(T/300)^{2/3} \quad (7.5)$$

, where $\mu_{1,0}$ is the single channel mobility extracted at base temperature.

For the second carrier type which has a high mobility and low density at higher temperature, we assume it is dominated by the acoustic and optical phonon-type scatterings (proportional to $T^{-3/2}$). The total density of the two carriers is conserved and the mobility of the second carrier type is expressed by an empirical function with a $T^{-3/2}$ dependence:

$$\mu_2(T) = \mu_{2,0}(T/300)^{-3/2} \quad (7.6)$$

The two equations described in (7.2) and (7.3) are used to fit the experimental Hall data. The constraint is that the total carrier density is conserved, and $p_{s2} = 0$ at T = 0. The activation energy, $\mu_{2,0}$ and a constant in p_{s2} are the free fitting parameters. The fitted curves are shown in Fig. 7.11. In general, the fitted curves are in good

agreement with the experimental data. The transitions observed in both carrier density and mobility are reproduced successfully. At low temperature, the delta layer is at ground state with a triangular potential well. The conduction mechanism is dominated by metallic conduction from carrier type 1 and carrier type 2 freezes out. Note that the carrier density does show a weak temperature dependence at this temperature range ($T < 20$ K); this suggests that the transport is also occurring by a mechanism such as hopping [229], either from the impurity band or the disorder induced band tail state [230]. As the temperature increases, the additional type of carrier that has very high mobility gets into this a triangular potential well. The apparent carrier density begins to drop because some carriers have been thermally re-distributed to the other carrier type 2, while the total number of carriers remain constant. Our results indicate that this second type of carrier has a much smaller population compared to carrier type 1. According to equation (7.2), since the Hall mobility that we measured depends on the quadratic sum of the two carriers, even a small population (< 1 %, for example) of the type 2 carrier with a high mobility will dominate the total Hall mobility, resulting in a mobility value much higher than the type 1 carrier at the base temperature regime. For this type 2 carrier, an activation energy of -38 meV is extracted, meaning that the Fermi level lies 38 meV below the top of the valence band maximum. At $T > 40$ K, the apparent carrier density gradually levels off, with a small increase at higher temperature. We believe this weak temperature dependence is either coming from the substrate, since we are using intrinsic Si substrate with resistivity > 10 kΩ, or the conduction from the bulk Si capping layer.

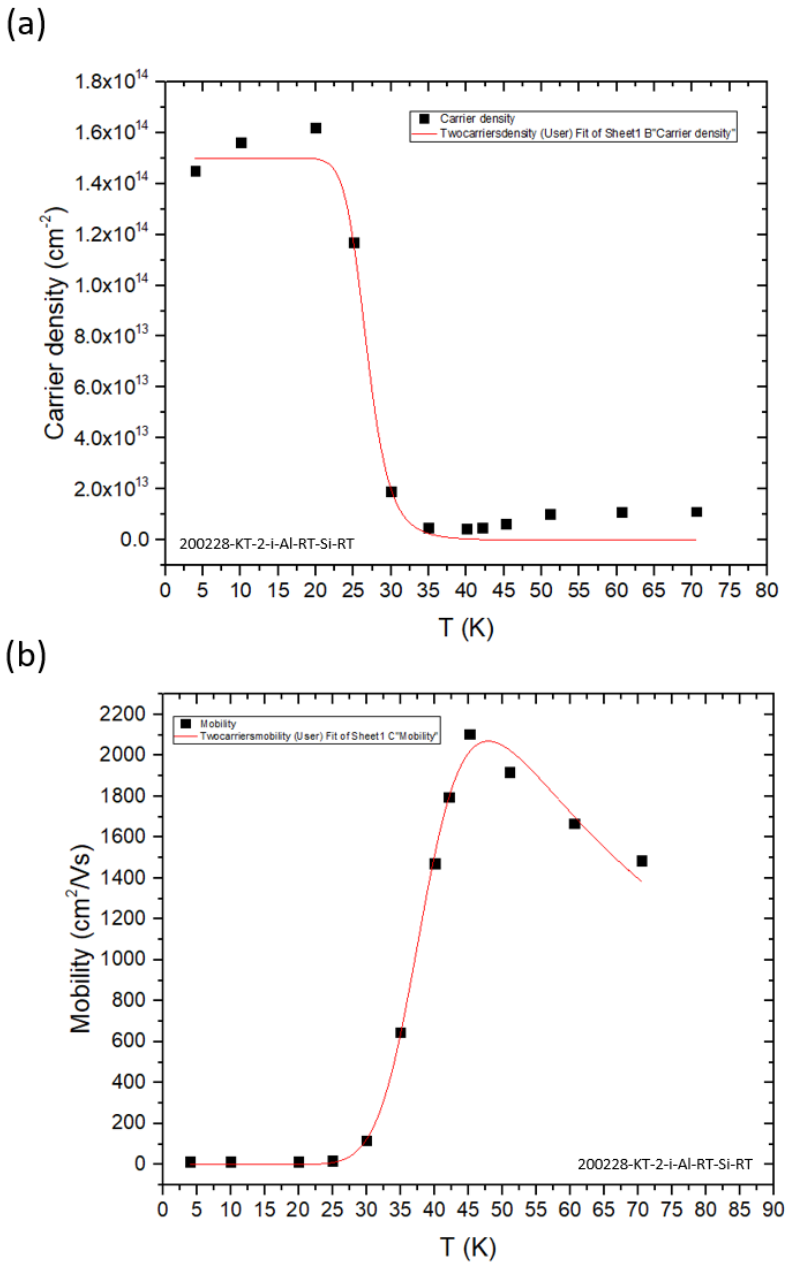

Figure 7.11: Two-carrier model fit to the temperature dependent sheet density and mobility.
The fitted curves are shown in red solid lines. The theoretical model is in good agreement with the experimental data. The transitions observed in both carrier density and mobility are reproduced successfully.

In conclusion, the temperature dependent Hall carrier density and mobility of this Al delta layer in Si can be explained by the two-carrier type model, based on

activation of the localized donor states in the delta layer region to higher energy states in the bulk of the Si. Most of the carriers are remained in the metallic conduction region where ionized impurity scattering is dominating, results in a low mobility value. At higher temperatures, a small portion of the carriers are thermally activated to higher energy subbands, resulting in a much higher Hall mobility because the Hall mobility is a quadratic sum of the two carrier types.

Chapter 8: Summary of Results and Future Experiments

8.1 Summary of Results

In this thesis, two materials: isotopically enriched ^{28}Si (chapter 3 to 5) and Al delta-doped layers (chapter 6 and 7) were synthesized and studied as an effort to develop new approach toward superconducting semiconductor qubits.

High quality ^{28}Si material within the quantum computing community is scarce and limited. In chapter 3, a new UHV version of the hyperthermal Penning ion source was designed and built to improve the chemical purity of our ^{28}Si thin film. The discharge properties based on arc voltage, source magnetic field and flow rate have been studied and optimized for ^{28}Si. The base pressure has been reduced by a factor of ≈ 100 and the total chemical purity of the deposited ^{28}Si film has been improved from 98.47 % to 99.97 %. The isotopic enrichment capability of this new ion source is also investigated. No degradation in enrichment has been found, and a typical isotope fraction of ^{28}Si using this UHV ion source is 99.999987 % (8.32×10^{-7} mol/mol ^{29}Si). Further improvements in chemical purity is still needed. Future efforts including implementation of the ion beam sweeper and UHV gas line with purifier. Improvements in chemical purity of the film with C, O and N contents < 10^{17} – 10^{18} cm^{-3} might be possible. The results described here serve as an important step forward to produce high quality ^{28}Si material that is suitable for quantum information studies.

In chapter 4, the material variety of ^{28}Si at different levels in the quantum information community is broadened by demonstrating the ability to grow isotopically enriched ^{28}Si epitaxial films with precisely controlled (≈ 90 % accuracy) enrichment levels, ranging from natural abundance to < 1 ppm ^{29}Si.. This targeted enrichment of ^{28}Si is achieved by periodically switching the mass analyzer magnetic field to modulate the isotope being deposited. Precise control of the ^{29}Si concentration, with an average accuracy of ≈ 90 % between the targeted and measured value is achieved. This method also enables measurement studies such as the coherence time T_2 vs ^{29}Si concentration over a wide range.

In chapter 5, to better assess the quality of our ^{28}Si material, we have successfully fabricated and characterized ^{28}Si MOSFET devices, and compared to those from natural abundance Si on the same substrate. The charge carrier mobility on isotopically enriched ^{28}Si is found to be approximately a factor of 3 lower. Nevertheless, the magnetotransport measurements of devices fabricated on isotopically enriched ^{28} Si has demonstrated strong manifestations of quantum effects. Based on the analysis of temperature dependence of the weak localization and SdH oscillations, we believe that the dominant scattering mechanism is short-range scattering (impurity scattering). The macroscopic transport and material characteristics of the devices reported here will serve as a benchmark for finding correlations between macroscopic properties and the performance of future nanoscale devices. will lead to identifying qualifying metrics for “quantum grade” silicon.

The impact of this work so far is that we have made substantial improvements on the chemical purity while keeping the ^{29}Si isotope fraction far less than other ^{28}Si

sources. We have broadened the material supply of ^{28}Si with different enrichment levels to allow further studies and provided insights on setting qualifying metrics for "quantum grade" silicon. The demonstration of this cheap, flexible source of high quality ^{28}Si is a crucial step forward to make ^{28}Si as an ideal host material for both semiconductor spin qubits and the proposed hybrid semi-superconductor qubit structure.

Al delta-doping in Si is a brand-new material system with a lot of opportunities. In Chapter 6, we performed studies on Al delta doped layers on Si for reaching localized superconductivity. To pursue a superconducting Al delta-doped Si, a way to reach the critical 3D density is needed. The first step is to understand the maximum number of atoms in the smallest possible distance (one atomic layer) so that a maximized the 3D density can be realized. We used a combination of different characterization tools: STM, SIMS and APT. For one atomic layer of Al dopant on Si(100) surface, the extracted average density ratio between SIMS/STM and APT/STM is 1.77 and 2.37, respectively. This indicates that for each protrusion observed in the filled state STM image, there are 2.07 ± 1.11 Al atoms. This extracted density ratio confirmed the literature results that Al dimers are formed on Si(100) surface at low temperature. The maximum 2D atom density of Al that can be reached on Si(100) surface for one atomic layer is therefore 3.4×10^{14} cm^{-2}, half of the Si(100) surface atom density. We believe this fills the gap for the missing information that is needed to determine the Al atomic layer structure on Si(100) and provides help in reaching the critical density needed for superconducting transition using Al as a dopant. The 3D density of an Al delta-doped layer is also extracted from SIMS and

APT: 6.58×10^{20} cm^{-3} and 6.34×10^{20} cm^{-3}, which is approximately 1.2 at. %, still lower than the critical density needed for superconducting (2 at. %).

In Chapter 7, we studied the effects of different material growth methods on electrical conduction (carrier density and dopant activation) and explored the possibility of improving the dopant confinement in the Si-Al-Si heterostructure. We found a number of aspects of Al delta doping in Si which are different compared to other dopants: the incorporation anneal does not affect the carrier density of this delta layer (although it changes mobility); standard MBE and LL growth methods were not successful on this delta layer and do not seem to suppress Al segregation. Finally, the Al dopant activation is capped at < 50 %, most likely due to the meta-stable state developed during thermal anneals. The conduction mechanism of this delta layer at low temperature is also studied and explained using a temperature dependent two-carrier type model. The possibility of reaching superconducting transition using Al delta layer as a dopant in Si is also discussed. We believe this is possible but will require further studies both experimentally and theoretically on suppressing the Al segregation for a high enough 3D dopant density. A summary table showing the processing steps and characterization results is included in Appendix A.

A summary of the accomplishments of this work is included in Table. X. So far, we have discussed the advancements in ^{28}Si material and provided initial studies on this new super-saturated Al delta layer in Si. The exploration of the phase space of this delta layer growth and the low temperature electrical measurements provided valuable insights on further pursuing superconductivity using this dopant. The results of this work serve as a pioneer and building block to fabricate new, nuclear spin-free

and interface-free monocrystalline material system that is beneficial for combining the strengths of superconducting and semiconducting QIP.

Table X. A summary of the accomplishments of this work.

System	Major Accomplishment	Note
^{28}Si material	Best isotopic enrichment 99.99987 % (with ^{29}Si < 1 ppm)	Best reported enrichment elsewhere: 99.9985 % [231]
^{28}Si material	Targeted enrichment with 90 % accuracy over 10^4 ppm range	1st demonstrated
UHV ion source	Improved vacuum of Penning type ion source to 2×10^{-10} Torr (by 100 ×)	1st Penning type ion source with UHV capability
Al delta layer	Demonstrated high density conducting Al delta layer	1st conducting Al delta layer in Si structure
Al delta layer	Measured and modelled T-dependent carrier density and mobility at low T	1st measured T-dependent conduction of Al delta layer in Si

8.2 Future Experiments

With the improvements in chemical purity of our ^{28}Si and ability to produce targeted enrichment of the deposited films, a natural next step is to measure the coherence time T_2 of the spins within this material and study the correlation between ^{29}Si concentration and T_2. This would provide direct experimental evidences for the theoretical studies done by Witzel *et al.* and match the phase space of T_2 vs ^{29}Si concentration, especially in the < 800 ppm region. Since the ^{28}Si material produced in this work is a flexible, lab scale production with relatively small quantity (nanometer

scale). The traditional ESR measurement which is an ensemble measurement that require large number of spins, thus large volume of ^{28}Si is not suitable. Fortunately, smaller ESR probe can be fabricated onto the ^{28}Si thin film with ^{31}P implantation that have enough sensitivity down to a few tens of spins [232]. A Josephson parametric microwave amplifier combined with high-quality-factor superconducting microresonators at millikelvin temperature [233] can also be used as a high sensitivity tool to measure T_2 of our ^{28}Si.

Another approach for studying the spin properties of the ^{28}Si is through the magnetotransport measurements with the presence of microwave excitation. This proposed idea is based on the electrically detected magnetic resonance (EDMR) method and the work from [234], where a strong microwave-induced resonance in the resistance results in the resistive detection of spin resonance [234]. It can be used to provide measurements of the g-factor, spin relaxation time and valley splitting in graphene. The gated Hall bar devices fabricated on ^{28}Si samples will be mounted at the end of a microwave waveguide and cooled down to low temperature in an applied magnetic field. The longitudinal resistance R_{xx} will then be measured as a function of applied magnetic field under microwave irradiation over the frequency range 10 – 50 GHz and power range of 0.1 – 10 mW. With the microwave excitation, we expect to see microwave-induced resonance in R_{xx}. By plotting the ΔR_{xx} (the difference in R_{xx} value with and without microwave) as a function of magnetic field strength (B), we can extract both the low B-field resonance and the high B-field resonance, which correspond to intra-valley spin resonance and inter-valley spin resonance, respectively. From the linewidth of these resonances, we can calculate the relaxation

times [234]. Although the resonance linewidth might be affected by various of factors, including background donor concentration, defects, local nuclear spin contributions from ^{29}Si, etc., we can potentially improve it by reducing the dimension of the MOSFET devices. As the size of the devices approach nanometer scale, we will be able to reduce the components that contribute to the inhomogeneities that serve to broaden the linewidth and be able to extract the dominating factor that limits the quantum coherence. We can then extend the measurements to devices with different enrichment levels of ^{28}Si while keeping the other parameters optimized and the relationship between the coherence time and the ^{29}Si concentration will be studied. Furthermore, if we change the microwave frequency *f*, we expect to see the shift of the resonances to higher B with increasing *f* and we can calculate the electron g-factor from the *f* vs B plot. Valley splitting can also be detected using this method. In the measurement with graphene [234], a fourfold degeneracy is lifted in the absence of magnetic field and produced a pair of spin degenerate levels separated by $E/h = f_0$, where E is the energy between two valleys and f_0 is the corresponding frequency. Zeeman splitting then lifts the spin degeneracy of the two valleys and microwave excitation induced spin-flip transitions can be seen [234].

For the Al delta doped layers in Si, we have measured the Al delta layer peak density and studied the effects of different growth methods. To achieve a superconducting transition in this Al delta doped Si, several possible future steps can be made. The first is to better tune the recipe for the locking layer (LL) and the epitaxial MBE growth of the Si capping layer on top of the Al delta layer. We have tried several standard growth methods for growing LL and MBE Si, none of them

succeeded in the limited time frame of this project. However, there might be other possible ways to combine LL with MBE Si overgrowth, e.g., using a lower annealing temperature and a lower deposition rate. I still believe that a suppression in Al segregation can be made possible. Another possible way to achieve superconducting transition is by increasing the 3D density and dopant activation. This can be done by introducing a superlattice structure of the Al delta layers with spacer layers. It has been demonstrated in P that superlattices of delta layers can increase the active carrier density from 1.9×10^{14} cm^{-2} to 4.5×10^{14} cm^{-2} and remained 2D conduction [192]. Another possibility might be to reduce the thermal budget of the growth process to suppress segregation process. This might be possible by fine-tuning the deposition and annealing temperatures and further explore the phase space of the delta layer growth methods.

Appendix A: Al Delta Layers Catalog

The details of the Al delta layer sample processing steps introduced in Chapter 7 are shown in Table. A1. This table is a summary of the synthesis processes (including doses, anneals, overgrowth), electrical characterization at low temperature, STM counts and SIMS density measurements.

Table A1: Processing steps and characterizations results of Al delta layer samples studied in Chapter 7.

Sample name	Overgrowth	Doses	Incorporation anneal	Final anneal	STM after overgrowth	2D carrier density at 4K (cm^{-2})	STM protrusion density and no. (cm^{-2})	SIMS 2D density (cm^{-2})
200310-KT-7-i-Al-RT-Si-RT	56nm SPE	100%	N/A	575C 4mins	Epitaxial, can see terraces	1.63E14	1.42E14 3524	2.36E14
200901-KT-2-i-Al-RT-Si-RT	57nm SPE	100%	N/A	625C 1min	Epitaxial, can see terraces	1.55E14	1.50E14 3762	2.27E14
200909-KT-2-i-Al-RT-Si-RT	54nm SPE	100%	N/A	550C 10mins	Epitaxial, can see terraces	1.41E14	1.32E14 3294	2.47E14
201007-KT-7-i-Al-RT-Si-RT	60nm SPE	100%	N/A	650C 11s	Epitaxial, can see terraces	1.42E14	1.33E14 3324	2.35E14
201007-KT-2-i-Al-RT-Si-RT	60nm SPE	100%	N/A	500C, 150mins	Epitaxial, can see terraces	No Hall	1.40E14 3494	2.57E14
201015-KT-3-i-Al-RT-Si-RT	60nm RT	100%	N/A	N/A	Poly Si	N/A	1.41E14 3537	2.64E14 (1kV)
200228-KT-2-i-Al-RT-Si-RT	66nm SPE	100%	N/A	600 C 10mins	Epitaxial, can see terraces	1.45E14	N/A	N/A
161026-HK-9-i-Al-EFM-RT	60nm SPE	100%	550C 1min	550C 10mins (ex situ)	Poly Si	6.6E13	1.35E14 3370	2.62E14
170517-KT-2-i-Al-RT-EFM-RT-P1	60nm SPE	100%	550C 1min	250C 10mins, 400C 10mins, 550C 10mins, 600C 10mins (ex situ)	Poly Si	2.1E12 (400C) 1.2E14 (550C), 9.5E13 (600C)	1.28E14 3207	2.55E14
170517-KT-9-i-Al-RT-EFM-RT-P1	60nm SPE	100%	550C 1min	550C 10mins, 650C 10mins (ex situ)	Poly Si	1.6E14 (550C), 2.7E13 (650C)	1.35E14 3383	2.0E14
170705-HK-9-i-Al-RT-EFM-RT-P2	60nm SPE	100%	550C 1min	550C 10mins + 550C 10mins (ex situ)	Epitaxial, can see terraces	1.1E14	1.40E14 3510	2.52E14
200131-KT-7-i-Al-RT-Si-RT	50nm SPE	100%	550C 1min	550C 10mins	Epitaxial, can see terraces	1.39E14	1.05E14 2626	1.58E14
200211-KT-3-i-Al-RT-Si-350C	50nm 350C	100%	550C 1min	550C 10mins	Epitaxial, Al chains and atoms visible on surface	No Hall	1.33E14 3335	1.51E14
200211-KT-2-i-Al-RT-Si-325C	1.6nm RT LL + 50nm 325C	100%	550C 1min	N/A	Poly Si growth with big grain size	No Hall	1.45E14 3623	1.51E14
200211-KT-4-i-Al-RT-Si-325C	1.6nm RT LL + 50nm 325C	100%	550C 1min	550C 10mins	Epitaxial, Al chains and atoms visible on surface	No Hall	1.52E14 3801	N/A
200228-KT-3-i-Al-RT-Si-350C	30nm 350C	100%	550C 10min	N/A	Poly Si, cannot see dimers; no Al on surface	No Hall	1.65E14 4119	5.4E13
200228-KT-7-i-Al-RT-Si-325C	20nm 325C	100%	550C 1min	550C 10mins	Poly Si, cannot see dimers; no Al on surface	No Hall	Bad STM	N/A
201007-KT-4-i-Al-RT-Si-RT	68nm SPE	50%	N/A	550C 10mins	Epitaxial, can see terraces	No Hall	N/A	N/A
210119-KT-4-i-Al-RT-Si-RT	50nm SPE	200%	550C 10mins	550C 10mins	Epitaxial, Al chains and atoms visible on surface	1.69E14	N/A	N/A
201230-KT-4-i-Al-RT-Si-RT	56nm SPE	200%	N/A	550C 10mins	Epitaxial, can see terraces	1.98E14	N/A	N/A

Bibliography

1. Zhang, S. *Review of Modern Field Effect Transistor Technologies for Scaling*. in *Journal of Physics: Conference Series*. 2020. IOP Publishing.
2. Shalf, J.M. and R. Leland, *Computing beyond moore's law.* Computer, 2015. **48**(12): p. 14-23.
3. Shor, P.W., *Polynomial-time algorithms for prime factorization and discrete logarithms on a quantum computer.* SIAM review, 1999. **41**(2): p. 303-332.
4. Wiebe, N., D. Braun, and S. Lloyd, *Quantum algorithm for data fitting.* Physical review letters, 2012. **109**(5): p. 050505.
5. Biamonte, J., P. Wittek, N. Pancotti, P. Rebentrost, N. Wiebe, and S. Lloyd, *Quantum machine learning.* Nature, 2017. **549**(7671): p. 195-202.
6. Moll, N., P. Barkoutsos, L.S. Bishop, J.M. Chow, A. Cross, D.J. Egger, S. Filipp, A. Fuhrer, J.M. Gambetta, and M. Ganzhorn, *Quantum optimization using variational algorithms on near-term quantum devices.* Quantum Science and Technology, 2018. **3**(3): p. 030503.
7. Grover, L.K. *A fast quantum mechanical algorithm for database search*. in *Proceedings of the twenty-eighth annual ACM symposium on Theory of computing*. 1996.
8. Yao, A.C.-C. *Quantum circuit complexity*. in *Proceedings of 1993 IEEE 34th Annual Foundations of Computer Science*. 1993. IEEE.
9. Nielsen, M.A. and I. Chuang, *Quantum computation and quantum information*. 2002, American Association of Physics Teachers.
10. Zhang, X., H.-O. Li, G. Cao, M. Xiao, G.-C. Guo, and G.-P. Guo, *Semiconductor quantum computation.* National Science Review, 2019. **6**(1): p. 32-54.
11. Vandersypen, L.M. and I.L. Chuang, *NMR techniques for quantum control and computation.* Reviews of modern physics, 2005. **76**(4): p. 1037.
12. Medford, J., C. Barthel, C. Marcus, M. Hanson, and A. Gossard, *Scaling of dynamical decoupling for spin qubits.* Physical review letters, 2012. **108**(8): p. 086802.
13. Häffner, H., C.F. Roos, and R. Blatt, *Quantum computing with trapped ions.* Physics reports, 2008. **469**(4): p. 155-203.
14. Monroe, C. and J. Kim, *Scaling the ion trap quantum processor.* Science, 2013. **339**(6124): p. 1164-1169.
15. Devoret, M.H. and R.J. Schoelkopf, *Superconducting circuits for quantum information: an outlook.* Science, 2013. **339**(6124): p. 1169-1174.
16. Wendin, G., *Quantum information processing with superconducting circuits: a review.* Reports on Progress in Physics, 2017. **80**(10): p. 106001.
17. Awschalom, D.D., L.C. Bassett, A.S. Dzurak, E.L. Hu, and J.R. Petta, *Quantum spintronics: engineering and manipulating atom-like spins in semiconductors.* Science, 2013. **339**(6124): p. 1174-1179.
18. Zhang, X., H.-O. Li, K. Wang, G. Cao, M. Xiao, and G.-P. Guo, *Qubits based on semiconductor quantum dots.* Chinese Physics B, 2018. **27**(2): p. 020305.
19. Childress, L. and R. Hanson, *Diamond NV centers for quantum computing and quantum networks.* MRS bulletin, 2013. **38**(2): p. 134-138.

20. Weber, J., W. Koehl, J. Varley, A. Janotti, B. Buckley, C. Van de Walle, and D.D. Awschalom, *Quantum computing with defects.* Proceedings of the National Academy of Sciences, 2010. **107**(19): p. 8513-8518.
21. Loss, D. and D.P. DiVincenzo, *Quantum computation with quantum dots.* Physical Review A, 1998. **57**(1): p. 120.
22. Hanson, R., L.P. Kouwenhoven, J.R. Petta, S. Tarucha, and L.M. Vandersypen, *Spins in few-electron quantum dots.* Reviews of modern physics, 2007. **79**(4): p. 1217.
23. Zwanenburg, F.A., A.S. Dzurak, A. Morello, M.Y. Simmons, L.C. Hollenberg, G. Klimeck, S. Rogge, S.N. Coppersmith, and M.A. Eriksson, *Silicon quantum electronics.* Reviews of modern physics, 2013. **85**(3): p. 961.
24. Nadj-Perge, S., S. Frolov, E. Bakkers, and L.P. Kouwenhoven, *Spin–orbit qubit in a semiconductor nanowire.* Nature, 2010. **468**(7327): p. 1084-1087.
25. Wei, D., H.-O. Li, G. Cao, G. Luo, Z.-X. Zheng, T. Tu, M. Xiao, G.-C. Guo, H.-W. Jiang, and G.-P. Guo, *Tuning inter-dot tunnel coupling of an etched graphene double quantum dot by adjacent metal gates.* Scientific reports, 2013. **3**(1): p. 1-6.
26. Klein, D.L., P.L. McEuen, J.E.B. Katari, R. Roth, and A.P. Alivisatos, *An approach to electrical studies of single nanocrystals.* Applied Physics Letters, 1996. **68**(18): p. 2574-2576.
27. Kane, B.E., *A silicon-based nuclear spin quantum computer.* nature, 1998. **393**(6681): p. 133-137.
28. Hile, S.J., L. Fricke, M.G. House, E. Peretz, C.Y. Chen, Y. Wang, M. Broome, S.K. Gorman, J.G. Keizer, and R. Rahman, *Addressable electron spin resonance using donors and donor molecules in silicon.* Science advances, 2018. **4**(7): p. eaaq1459.
29. Muhonen, J.T., J.P. Dehollain, A. Laucht, F.E. Hudson, R. Kalra, T. Sekiguchi, K.M. Itoh, D.N. Jamieson, J.C. McCallum, A.S. Dzurak, et al., *Storing quantum information for 30 seconds in a nanoelectronic device.* Nature Nanotechnology, 2014. **9**(12): p. 986 DOI: 10.1038/Nnano.2014.211.
30. Saeedi, K., S. Simmons, J.Z. Salvail, P. Dluhy, H. Riemann, N.V. Abrosimov, P. Becker, H.J. Pohl, J.J.L. Morton, and M.L.W. Thewalt, *Room-Temperature Quantum Bit Storage Exceeding 39 Minutes Using Ionized Donors in Silicon-28.* Science, 2013. **342**(6160): p. 830-833 DOI: 10.1126/science.1239584.
31. Tyryshkin, A.M., S. Tojo, J.J.L. Morton, H. Riemann, N.V. Abrosimov, P. Becker, H.J. Pohl, T. Schenkel, M.L.W. Thewalt, K.M. Itoh, et al., *Electron spin coherence exceeding seconds in high-purity silicon.* Nature Materials, 2012. **11**(2): p. 143 DOI: 10.1038/Nmat3182.
32. Abe, E., A.M. Tyryshkin, S. Tojo, J.J.L. Morton, W.M. Witzel, A. Fujimoto, J.W. Ager, E.E. Haller, J. Isoya, S.A. Lyon, et al., *Electron spin coherence of phosphorus donors in silicon: Effect of environmental nuclei.* Physical Review B, 2010. **82**(12) DOI: ARTN 121201
10.1103/PhysRevB.82.121201.
33. Witzel, W.M., M.S. Carroll, L. Cywinski, and S. Das Sarma, *Quantum decoherence of the central spin in a sparse system of dipolar coupled spins.* Physical Review B, 2012. **86**(3) DOI: ARTN 035452

10.1103/PhysRevB.86.035452.
34. Steger, M., K. Saeedi, M.L.W. Thewalt, J.J.L. Morton, H. Riemann, N.V. Abrosimov, P. Becker, and H.J. Pohl, *Quantum Information Storage for over 180 s Using Donor Spins in a Si-28 "Semiconductor Vacuum".* Science, 2012. **336**(6086): p. 1280-1283 DOI: 10.1126/science.1217635.
35. Muhonen, J.T., J.P. Dehollain, A. Laucht, F.E. Hudson, R. Kalra, T. Sekiguchi, K.M. Itoh, D.N. Jamieson, J.C. McCallum, A.S. Dzurak, et al., *Storing quantum information for 30 seconds in a nanoelectronic device.* Nature Nanotechnology, 2014. **9**(12): p. 986-991 DOI: 10.1038/Nnano.2014.211.
36. Ito, T., T. Otsuka, T. Nakajima, M.R. Delbecq, S. Amaha, J. Yoneda, K. Takeda, A. Noiri, G. Allison, and A. Ludwig, *Four single-spin Rabi oscillations in a quadruple quantum dot.* Applied Physics Letters, 2018. **113**(9): p. 093102.
37. Yang, C., A. Rossi, R. Ruskov, N. Lai, F. Mohiyaddin, S. Lee, C. Tahan, G. Klimeck, A. Morello, and A. Dzurak, *Spin-valley lifetimes in a silicon quantum dot with tunable valley splitting.* Nature communications, 2013. **4**(1): p. 1-8.
38. Ruskov, R., M. Veldhorst, A.S. Dzurak, and C. Tahan, *Electron g-factor of valley states in realistic silicon quantum dots.* Physical Review B, 2018. **98**(24): p. 245424.
39. Kawakami, E., P. Scarlino, D.R. Ward, F. Braakman, D. Savage, M. Lagally, M. Friesen, S.N. Coppersmith, M.A. Eriksson, and L. Vandersypen, *Electrical control of a long-lived spin qubit in a Si/SiGe quantum dot.* Nature nanotechnology, 2014. **9**(9): p. 666-670.
40. Becker, P., H.J. Pohl, H. Riemann, and N. Abrosimov, *Enrichment of silicon for a better kilogram.* Physica Status Solidi a-Applications and Materials Science, 2010. **207**(1): p. 49-66 DOI: 10.1002/pssa.200925148.
41. Abrosimov, N.V., D.G. Aref'ev, P. Becker, H. Bettin, A.D. Bulanov, M.F. Churbanov, S.V. Filimonov, V.A. Gavva, O.N. Godisov, A.V. Gusev, et al., *A new generation of 99.999% enriched (2)8(S)i single crystals for the determination of Avogadro's constant.* Metrologia, 2017. **54**(4): p. 599-609 DOI: 10.1088/1681-7575/aa7a62.
42. Mazzocchi, V., P.G. Sennikov, A.D. Bulanov, M.F. Churbanov, B. Bertrand, L. Hutin, J.P. Barnes, M.N. Drozdov, J.M. Hartmann, and M. Sanquer, *99.992% ^{28}Si CVD-grown epilayer on 300 mm substrates for large scale integration of silicon spin qubits.* Journal of Crystal Growth, 2019. **509**: p. 1-7 DOI: 10.1016/j.jcrysgro.2018.12.010.
43. Itoh, K.M. and H. Watanabe, *Isotope engineering of silicon and diamond for quantum computing and sensing applications.* Mrs Communications, 2014. **4**(4): p. 143-157 DOI: 10.1557/mrc.2014.32.
44. Takyu, K., K.M. Itoh, K. Oka, N. Saito, and V.I. Ozhogin, *Growth and characterization of the isotopically enriched Si-28 bulk single crystal.* Japanese Journal of Applied Physics, 1999. **38**(12b): p. L1493 DOI: Doi 10.1143/Jjap.38.L1493.

45. Li, J.Y., C.T. Huang, L.P. Rokhinson, and J.C. Sturm, *Extremely high electron mobility in isotopically-enriched Si-28 two-dimensional electron gases grown by chemical vapor deposition.* Applied Physics Letters, 2013. **103**(16): p. 162105 DOI: Artn 162105 10.1063/1.4824729.
46. Sailer, J., V. Lang, G. Abstreiter, G. Tsuchiya, K.M. Itoh, J.W. Ager, E.E. Haller, D. Kupidura, D. Harbusch, S. Ludwig, et al., *A Schottky top-gated two-dimensional electron system in a nuclear spin free Si/SiGe heterostructure.* Physica Status Solidi-Rapid Research Letters, 2009. **3**(2-3): p. 61-63 DOI: 10.1002/pssr.200802275.
47. Fiedler, H., P. Gupta, J. Kennedy, and A. Markwitz, *$^{28}Si^{+}$ ion beams from Penning ion source based implanter systems for near-surface isotopic purification of silicon.* Review of Scientific Instruments, 2018. **89**(12): p. 123305 DOI: Artn 123305 10.1063/1.5048949.
48. Nakamura, Y., Y.A. Pashkin, and J.S. Tsai, *Coherent control of macroscopic quantum states in a single-Cooper-pair box.* nature, 1999. **398**(6730): p. 786-788.
49. Barends, R., J. Kelly, A. Megrant, A. Veitia, D. Sank, E. Jeffrey, T.C. White, J. Mutus, A.G. Fowler, and B. Campbell, *Superconducting quantum circuits at the surface code threshold for fault tolerance.* Nature, 2014. **508**(7497): p. 500-503.
50. Fowler, A.G., M. Mariantoni, J.M. Martinis, and A.N. Cleland, *Surface codes: Towards practical large-scale quantum computation.* Physical Review A, 2012. **86**(3): p. 032324.
51. Huang, H.-L., D. Wu, D. Fan, and X. Zhu, *Superconducting quantum computing: a review.* Science China Information Sciences, 2020. **63**(8): p. 1-32.
52. Bouchiat, V., D. Vion, P. Joyez, D. Esteve, and M. Devoret, *Quantum coherence with a single Cooper pair.* Physica Scripta, 1998. **1998**(T76): p. 165.
53. Martinis, J.M., *Superconducting phase qubits.* Quantum Information Processing, 2009. **8**(2): p. 81-103.
54. Mooij, J., T. Orlando, L. Levitov, L. Tian, C.H. Van der Wal, and S. Lloyd, *Josephson persistent-current qubit.* Science, 1999. **285**(5430): p. 1036-1039.
55. Friedman, J.R., V. Patel, W. Chen, S. Tolpygo, and J.E. Lukens, *Quantum superposition of distinct macroscopic states.* nature, 2000. **406**(6791): p. 43-46.
56. Koch, J., M.Y. Terri, J. Gambetta, A.A. Houck, D.I. Schuster, J. Majer, A. Blais, M.H. Devoret, S.M. Girvin, and R.J. Schoelkopf, *Charge-insensitive qubit design derived from the Cooper pair box.* Physical Review A, 2007. **76**(4): p. 042319.
57. Yang, C.-P., S.-I. Chu, and S. Han, *Possible realization of entanglement, logical gates, and quantum-information transfer with superconducting-quantum-interference-device qubits in cavity QED.* Physical Review A, 2003. **67**(4): p. 042311.

58. You, J. and F. Nori, *Quantum information processing with superconducting qubits in a microwave field.* Physical Review B, 2003. **68**(6): p. 064509.
59. Blais, A., R.-S. Huang, A. Wallraff, S.M. Girvin, and R.J. Schoelkopf, *Cavity quantum electrodynamics for superconducting electrical circuits: An architecture for quantum computation.* Physical Review A, 2004. **69**(6): p. 062320.
60. Paik, H., D. Schuster, L.S. Bishop, G. Kirchmair, G. Catelani, A. Sears, B. Johnson, M. Reagor, L. Frunzio, and L. Glazman, *Observation of high coherence in Josephson junction qubits measured in a three-dimensional circuit QED architecture.* Physical Review Letters, 2011. **107**(24): p. 240501.
61. Shim, Y.-P. and C. Tahan, *Bottom-up superconducting and Josephson junction devices inside a group-IV semiconductor.* Nature communications, 2014. **5**(1): p. 1-8.
62. Takano, Y., T. Takenouchi, S. Ishii, S. Ueda, T. Okutsu, I. Sakaguchi, H. Umezawa, H. Kawarada, and M. Tachiki, *Superconducting properties of homoepitaxial CVD diamond.* Diamond and related materials, 2007. **16**(4-7): p. 911-914.
63. Lasbley, A., R. Granger, and S. Rolland, *High temperature superconducting behaviour in PbTe□ Pb system.* Solid State Communications, 1973. **13**(8): p. 1045-1048.
64. Zhang, Y., R. Zhao, and W. Yang, *Surface superstructures of the Pb/Ge (001) system.* Surface Science Letters, 1993. **293**(1-2): p. L821-L825.
65. Schooley, J., W. Hosler, E. Ambler, J. Becker, M.L. Cohen, and C. Koonce, *Dependence of the superconducting transition temperature on carrier concentration in semiconducting srti o 3.* Physical Review Letters, 1965. **14**(9): p. 305.
66. Makise, K., N. Kokubo, S. Takada, T. Yamaguti, S. Ogura, K. Yamada, B. Shinozaki, K. Yano, K. Inoue, and H. Nakamura, *Superconductivity in transparent zinc-doped In2O3 films having low carrier density.* Science and technology of advanced materials, 2009. **9**(4): p. 044208.
67. Koonce, C. and M.L. Cohen, *Theory of superconducting semiconductors and semimetals.* Physical Review, 1969. **177**(2): p. 707.
68. Fiedler, J., V. Heera, R. Hübner, M. Voelskow, S. Germer, B. Schmidt, and W. Skorupa, *High-fluence Ga-implanted silicon—The effect of annealing and cover layers.* Journal of Applied Physics, 2014. **116**(2): p. 024502.
69. Seeger, A. and K. Chik, *Diffusion Mechanisms and Point Defects in Silicon and Germanium.* Phys. Status Solidi, 29: 455-542 (Oct. 1, 1968). 1968.
70. Fiedler, J., V. Heera, R. Skrotzki, T. Herrmannsdörfer, M. Voelskow, A. Mücklich, S. Oswald, B. Schmidt, W. Skorupa, and G. Gobsch, *Superconducting films fabricated by high-fluence Ga implantation in Si.* Physical Review B, 2011. **83**(21): p. 214504.
71. Bustarret, E., C. Marcenat, P. Achatz, J. Kačmarčik, F. Lévy, A. Huxley, L. Ortéga, E. Bourgeois, X. Blase, and D. Débarre, *Superconductivity in doped cubic silicon.* Nature, 2006. **444**(7118): p. 465-468.
72. Ekimov, E., V. Sidorov, E. Bauer, N. Mel'Nik, N. Curro, J. Thompson, and S. Stishov, *Superconductivity in diamond.* nature, 2004. **428**(6982): p. 542-545.

73. Takano, Y., *Superconductivity in CVD diamond films.* Journal of Physics: Condensed Matter, 2009. **21**(25): p. 253201.
74. Prucnal, S., V. Heera, R. Hübner, M. Wang, G.P. Mazur, M.J. Grzybowski, X. Qin, Y. Yuan, M. Voelskow, and W. Skorupa, *Superconductivity in single-crystalline aluminum-and gallium-hyperdoped germanium.* Physical Review Materials, 2019. **3**(5): p. 054802.
75. Bourgeois, E. and X. Blase, *Superconductivity in doped cubic silicon: An ab initio study.* Applied physics letters, 2007. **90**(14): p. 142511.
76. Kim, H.S., *Monocrystalline Supersaturated Aluminum Layers Buried in Epitaxial Silicon*. 2019, University of Maryland, College Park.
77. Gossmann, H.-J. and E. Schubert, *Delta doping in silicon.* Critical Reviews in Solid State and Material Sciences, 1993. **18**(1): p. 1-67.
78. Jewell, A.D., M.E. Hoenk, A.G. Carver, and S. Nikzad, *Low-temperature homoepitaxial growth of two-dimensional antimony superlattices in silicon.* Journal of Vacuum Science & Technology A: Vacuum, Surfaces, and Films, 2018. **36**(6): p. 061513.
79. Wang, X., J.A. Hagmann, P. Namboodiri, J. Wyrick, K. Li, R.E. Murray, A. Myers, F. Misenkosen, M.D. Stewart, and C.A. Richter, *Quantifying atom-scale dopant movement and electrical activation in Si: P monolayers.* Nanoscale, 2018. **10**(9): p. 4488-4499.
80. McKibbin, S., C. Polley, G. Scappucci, J. Keizer, and M. Simmons, *Low resistivity, super-saturation phosphorus-in-silicon monolayer doping.* Applied Physics Letters, 2014. **104**(12): p. 123502.
81. Thomsen, E., O. Hansen, K. Harrekilde-Petersen, J.L. Hansen, S.Y. Shiryaev, and A. Nylandsted Larsen, *Thermal stability of highly Sb-doped molecular beam epitaxy silicon grown at low temperatures: Structural and electrical characterization.* Journal of Vacuum Science & Technology B: Microelectronics and Nanometer Structures Processing, Measurement, and Phenomena, 1994. **12**(5): p. 3016-3022.
82. Gossmann, H.J., E. Schubert, D. Eaglesham, and M. Cerullo, *Low-temperature Si molecular beam epitaxy: Solution to the doping problem.* Applied physics letters, 1990. **57**(23): p. 2440-2442.
83. Weir, B., L. Feldman, D. Monroe, H.J. Grossmann, R. Headrick, and T. Hart, *Electrical characterization of an ultrahigh concentration boron delta-doping layer.* Applied physics letters, 1994. **65**(6): p. 737-739.
84. Salfi, J., M. Tong, S. Rogge, and D. Culcer, *Quantum computing with acceptor spins in silicon.* Nanotechnology, 2016. **27**(24): p. 244001.
85. van der Heijden, J., T. Kobayashi, M.G. House, J. Salfi, S. Barraud, R. Laviéville, M.Y. Simmons, and S. Rogge, *Readout and control of the spin-orbit states of two coupled acceptor atoms in a silicon transistor.* Science advances, 2018. **4**(12): p. eaat9199.
86. Ramanayaka, A.N., H.-S. Kim, J.A. Hagmann, R.E. Murray, K. Tang, F. Meisenkothen, H. Zhang, L. Bendersky, A. Davydov, and N.M. Zimmerman, *Towards superconductivity in p-type delta-doped Si/Al/Si heterostructures.* AIP Advances, 2018. **8**(7): p. 075329.

87. Dwyer, K.J., *In Situ Enrichment and Epitaxial Growth of 28 Si Films via Ion Beam Deposition*. 2017, University of Maryland, College Park.
88. Swartzentruber, B.S., Y.W. Mo, M. Webb, and M. Lagally, *Scanning tunneling microscopy studies of structural disorder and steps on Si surfaces.* Journal of Vacuum Science & Technology A: Vacuum, Surfaces, and Films, 1989. **7**(4): p. 2901-2905.
89. Poppendieck, T.D., T.C. Ngoc, and M.B. Webb, *An electron diffraction study of the structure of silicon (100).* Surface Science, 1978. **75**(2): p. 287-315.
90. Nulman, J., S. Antonio, and W. Blonigan, *Observation of Silicon-Wafer Emissivity in Rapid Thermal-Processing Chambers for Pyrometric Temperature Monitoring.* Applied Physics Letters, 1990. **56**(25): p. 2513-2515 DOI: Doi 10.1063/1.102874.
91. Rudakov, V.I., V.V. Ovcharov, and V.P. Prigara, *Influence of optical properties of the SOI structure on the wafer temperature during rapid thermal annealing.* Russian Microelectronics, 2012. **41**(1): p. 15-24 DOI: 10.1134/s1063739712010106.
92. Vander Voort, G.F. and J. Asensio-Lozano, *The Al-Si Phase Diagram.* Microscopy and Microanalysis, 2009. **15**: p. 60-61 DOI: 10.1017/S1431927609092642.
93. Gerlach, G. and W. Dötzel, *Introduction to microsystem technology : a guide for students*. Wiley microsystem and nanotechnology series. 2008, Chichester, England ; Hoboken, NJ: J. Wiley & Sons. xxiii, 351 p.
94. Sato, T., *Spectral Emissivity of Silicon.* Japanese Journal of Applied Physics, 1967. **6**(3): p. 339-& DOI: Doi 10.1143/Jjap.6.339.
95. Phillips, C.E.S., *"The action of magnetised electrodes upon electrical discharge phenomena in rarefied gases."*. Proceedings of the Royal Society of London, 1901. **68**(444): p. 147-149 DOI: DOI 10.1098/rspl.1901.0030.
96. Baumann, H. and K. Bethge, *Pig Ion-Source with End Extraction for Multiply Charged Ions.* Nuclear Instruments & Methods, 1974. **122**(3): p. 517-525 DOI: Doi 10.1016/0029-554x(74)90521-7.
97. Baumann, H. and K. Bethge, *The Frankfurt Pig Ion-Source*. Nuclear Instruments & Methods in Physics Research, 1981. **189**(1): p. 107-110 DOI: Doi 10.1016/0029-554x(81)90131-2.
98. Rohwer, P., H. Baumann, K. Bethge, and W. Schutze, *Ion Energy Analysis of a Penning Ion-Source Using a High-Resolution Mass-Spectrometer.* Nuclear Instruments & Methods in Physics Research, 1982. **204**(1): p. 245-248 DOI: Doi 10.1016/0167-5087(82)90103-X.
99. Rohwer, P., H. Baumann, W. Schutze, and K. Bethge, *Studies of the Center Potential in a Penning Discharge.* Nuclear Instruments & Methods in Physics Research, 1983. **211**(2-3): p. 543-546 DOI: Doi 10.1016/0167-5087(83)90285-5.
100. Pierce, J.R., *Theory and design of electron beams*. 2nd ed. The Bell Telephone Laboratories series. 1954, New York,: Van Nostrand.
101. Pomeroy, J.M., A.J. Couture, M.V.R. Murty, E.N. Butler, and B.H. Cooper, *Hyperthermal ion beam system optimized for studying the effects of kinetic*

energy on thin-film growth. Review of Scientific Instruments, 2002. **73**(11): p. 3846-3852 DOI: 10.1063/1.1512337.
102. Dwyer, K.J., J.M. Pomeroy, D.S. Simons, K.L. Steffens, and J.W. Lau, *Enriching Si-28 beyond 99.9998% for semiconductor quantum computing.* Journal of Physics D-Applied Physics, 2014. **47**(34): p. 345105 DOI: Artn 345105
10.1088/0022-3727/47/34/345105.
103. Dwyer, K.J., J.M. Pomeroy, D.S. Simons, K.L. Steffens, and J.W. Lau, *Enriching Si-28 beyond 99.9998% for semiconductor quantum computing.* Journal of Physics D-Applied Physics, 2014. **47**(34) DOI: Artn 345105
10.1088/0022-3727/47/34/345105.
104. Kanaya, K. and S. Ono, *Secondary electron emission from solid surfaces by bombardment with charged particles.* Japanese Journal of Applied Physics, 1974. **13**(6): p. 944.
105. Bai, C., *Scanning tunneling microscopy and its application*. Vol. 32. 2000: Springer Science & Business Media.
106. Chen, C.J., *Introduction to scanning tunneling microscopy*. Vol. 4. 1993: Oxford University Press on Demand.
107. Wikipedia, *Scanning Tunneling Microscope* https://en.wikipedia.org/w/index.php?title=Scanning_tunneling_microscope&oldid=1010053950, 2021.
108. Hall, E.H., *On a new action of the magnet on electric currents.* American Journal of Mathematics, 1879. **2**(3): p. 287-292.
109. Veldhorst, M., J.C.C. Hwang, C.H. Yang, A.W. Leenstra, B. de Ronde, J.P. Dehollain, J.T. Muhonen, F.E. Hudson, K.M. Itoh, A. Morello, et al., *An addressable quantum dot qubit with fault-tolerant control-fidelity.* Nature Nanotechnology, 2014. **9**(12): p. 981 DOI: 10.1038/Nnano.2014.216.
110. Yoneda, J., K. Takeda, T. Otsuka, T. Nakajima, M.R. Delbecq, G. Allison, T. Honda, T. Kodera, S. Oda, Y. Hoshi, et al., *A quantum-dot spin qubit with coherence limited by charge noise and fidelity higher than 99.9%.* Nature Nanotechnology, 2018. **13**(2): p. 102-+ DOI: 10.1038/s41565-017-0014-x.
111. Veldhorst, M., C.H. Yang, J.C.C. Hwang, W. Huang, J.P. Dehollain, J.T. Muhonen, S. Simmons, A. Laucht, F.E. Hudson, K.M. Itoh, et al., *A two-qubit logic gate in silicon.* Nature, 2015. **526**(7573): p. 410 DOI: 10.1038/nature15263.
112. Dwyer, K.J., H.S. Kim, D.S. Simons, and J.M. Pomeroy, *Temperature-dependent Si-29 incorporation during deposition of highly enriched Si-28 films.* Physical Review Materials, 2017. **1**(6): p. 064603 DOI: ARTN 064603
10.1103/PhysRevMaterials.1.064603.
113. Tyryshkin, A.M., J.J.L. Morton, S.C. Benjamin, A. Ardavan, G.A.D. Briggs, J.W. Ager, and S.A. Lyon, *Coherence of spin qubits in silicon.* Journal of Physics-Condensed Matter, 2006. **18**(21): p. S783 DOI: 10.1088/0953-8984/18/21/S06.
114. Culcer, D. and N.M. Zimmerman, *Dephasing of Si singlet-triplet qubits due to charge and spin defects.* Applied Physics Letters, 2013. **102**(23): p. 232108 DOI: Artn 232108

10.1063/1.4810911.
115. Penning, F.M., *A new manometer for low gas pressures especially between 10(-3) and 10(-5) mm.* Physica, 1937. **4**: p. 71-5 DOI: Doi 10.1016/S0031-8914(37)80123-8.
116. Ota, Y., *Silicon molecular beam epitaxy.* Thin Solid Films, 1983. **106**(1-2): p. 1-136.
117. Eaglesham, D., H.-J. Gossmann, and M. Cerullo, *Limiting thickness h epi for epitaxial growth and room-temperature Si growth on Si (100).* Physical review letters, 1990. **65**(10): p. 1227.
118. Eaglesham, D., *Semiconductor molecular-beam epitaxy at low temperatures.* Journal of applied physics, 1995. **77**(8): p. 3597-3617.
119. Nerding, M., L. Oberbeck, T. Wagner, R. Bergmann, and H. Strunk, *Single to polycrystalline transition in silicon growth by ion-assisted deposition at low temperatures.* Journal of applied physics, 2003. **93**(5): p. 2570-2574.
120. Lee, N.E., G. Xue, and J. Greene, *Epitaxial Si (001) grown at 80–750 C by ion-beam sputter deposition: Crystal growth, doping, and electronic properties.* Journal of applied physics, 1996. **80**(2): p. 769-780.
121. Murty, M.R., H.A. Atwater, A. Kellock, and J. Baglin, *Very low temperature (< 400° C) silicon molecular beam epitaxy: The role of low energy ion irradiation.* Applied physics letters, 1993. **62**(20): p. 2566-2568.
122. Murty, M.R. and H.A. Atwater, *Crystal-state–amorphous-state transition in low-temperature silicon homoepitaxy.* Physical Review B, 1994. **49**(12): p. 8483.
123. Thiesen, J., H.M. Branz, and R.S. Crandall, *Explanation of the limiting thickness observed in low-temperature silicon epitaxy.* Applied Physics Letters, 2000. **77**(22): p. 3589-3591.
124. Jorke, H., H.-J. Herzog, and H. Kibbel, *Kinetics of ordered growth of Si on Si (100) at low temperatures.* Physical Review B, 1989. **40**(3): p. 2005.
125. Eaglesham, D., H.-J. Gossmann, M. Cerullo, L. Pfeiffer, and K. West, *Limited thickness epitaxy of semiconductors and Si MBE down to room temperature.* Journal of crystal growth, 1991. **111**(1-4): p. 833-837.
126. Lee, N.E., G. Tomasch, and J. Greene, *Low-temperature Si (001) epitaxy using low-energy (< E> ≈ 18 eV) Si atoms.* Applied physics letters, 1994. **65**(25): p. 3236-3238.
127. Chason, E., P. Bedrossian, K. Horn, J. Tsao, and S. Picraux, *Ion beam enhanced epitaxial growth of Ge (001).* Applied physics letters, 1990. **57**(17): p. 1793-1795.
128. Choi, C.-H., R. Ai, and S. Barnett, *Suppression of three-dimensional island nucleation during GaAs growth on Si (100).* Physical review letters, 1991. **67**(20): p. 2826.
129. Orrman-Rossiter, K.G., D. Mitchell, S. Donnelly, C. Rossouw, S. Glanvill, P. Miller, A.H. Al-Bayati, J. Van Den Berg, and D. Armour, *Evidence for competing growth phases in ion-beam-deposited epitaxial silicon films.* Philosophical Magazine Letters, 1990. **61**(6): p. 311-318.

130. Tsubouchi, N., A. Chayahara, Y. Mokuno, A. Kinomura, and Y. Horino, *Epitaxial Growth of Pure 28Si Thin Films Using Isotopically Purified Ion Beams.* Japanese Journal of Applied Physics, 2001. **40**(12A): p. L1283.
131. Rabalais, J., A. Al-Bayati, K. Boyd, D. Marton, J. Kulik, Z. Zhang, and W. Chu, *Ion-energy effects in silicon ion-beam epitaxy.* Physical Review B, 1996. **53**(16): p. 10781.
132. Kitabatake, M., P. Fons, and J. Greene, *Molecular dynamics and quasidynamics simulations of low-energy ion/surface interactions leading to decreased epitaxial temperatures and increased dopant incorporation probabilities during Si MBE.* Journal of crystal growth, 1991. **111**(1-4): p. 870-875.
133. Dwyer, K.J., H.S. Kim, D.S. Simons, and J.M. Pomeroy, *Temperature-dependent Si-29 incorporation during deposition of highly enriched Si-28 films.* Physical Review Materials, 2017. **1**(6) DOI: ARTN 064603 10.1103/PhysRevMaterials.1.064603.
134. Tang, K., H. Kim, A. Ramanayaka, D. Simons, and J. Pomeroy, *A compact, ultra-high vacuum ion source for isotopically enriching and depositing 28Si thin films.* Review of Scientific Instruments, 2019. **90**(8): p. 083308.
135. Gordon, J.P. and K.D. Bowers, *Microwave Spin Echoes from Donor Electrons in Silicon.* Physical Review Letters, 1958. **1**(10): p. 368-370 DOI: DOI 10.1103/PhysRevLett.1.368.
136. Morton, J.J.L., D.R. McCamey, M.A. Eriksson, and S.A. Lyon, *Embracing the quantum limit in silicon computing.* Nature, 2011. **479**(7373): p. 345-353 DOI: 10.1038/nature10681.
137. Witzel, W.M. and S. Das Sarma, *Quantum theory for electron spin decoherence induced by nuclear spin dynamics in semiconductor quantum computer architectures: Spectral diffusion of localized electron spins in the nuclear solid-state environment.* Physical Review B, 2006. **74**(3) DOI: ARTN 035322 10.1103/PhysRevB.74.035322.
138. Tyryshkin, A.M., S. Tojo, J.J.L. Morton, H. Riemann, N.V. Abrosimov, P. Becker, H.J. Pohl, T. Schenkel, M.L.W. Thewalt, K.M. Itoh, et al., *Electron spin coherence exceeding seconds in high-purity silicon.* Nature Materials, 2012. **11**(2): p. 143-147 DOI: 10.1038/Nmat3182.
139. Tracy, L.A., D.R. Luhman, S.M. Carr, N.C. Bishop, G.A. Ten Eyck, T. Pluym, J.R. Wendt, M.P. Lilly, and M.S. Carroll, *Single shot spin readout using a cryogenic high-electron-mobility transistor amplifier at sub-Kelvin temperatures.* Applied Physics Letters, 2016. **108**(6): p. 063101 DOI: Artn 063101 10.1063/1.4941421.
140. Abrosimov, N.V., D.G. Aref'ev, P. Becker, H. Bettin, A.D. Bulanov, M.F. Churbanov, S.V. Filimonov, V.A. Gavva, O.N. Godisov, A.V. Gusev, et al., *A new generation of 99.999% enriched ^{28}Si single crystals for the determination of Avogadro's constant.* Metrologia, 2017. **54**(4): p. 599 DOI: 10.1088/1681-7575/aa7a62.

141. Mazzocchi, V., P.G. Sennikov, A.D. Bulanov, M.F. Churbanov, B. Bertrand, L. Hutin, J.P. Barnes, M.N. Drozdov, J.M. Hartmann, and M. Sanquer, *99.992% Si-28 CVD-grown epilayer on 300 mm substrates for large scale integration of silicon spin qubits.* Journal of Crystal Growth, 2019. **509**: p. 1-7 DOI: 10.1016/j.jcrysgro.2018.12.010.
142. Reshchikov, M., M. Vorobiov, O. Andrieiev, K. Ding, N. Izyumskaya, V. Avrutin, A. Usikov, H. Helava, and Y. Makarov, *Determination of the concentration of impurities in GaN from photoluminescence and secondary-ion mass spectrometry.* Scientific reports, 2020. **10**(1): p. 1-7.
143. Tang, K., H.S. Kim, A.N. Ramanayaka, D.S. Simons, and J.M. Pomeroy, *Targeted enrichment of 28Si thin films for quantum computing.* Journal of physics communications, 2020. **4**(3): p. 035006.
144. Petta, J.R., A.C. Johnson, J.M. Taylor, E.A. Laird, A. Yacoby, M.D. Lukin, C.M. Marcus, M.P. Hanson, and A.C. Gossard, *Coherent manipulation of coupled electron spins in semiconductor quantum dots.* Science, 2005. **309**(5744): p. 2180-2184.
145. Reilly, D., J. Taylor, J. Petta, C. Marcus, M. Hanson, and A. Gossard, *Suppressing spin qubit dephasing by nuclear state preparation.* Science, 2008. **321**(5890): p. 817-821.
146. de Leon, N.P., K.M. Itoh, D. Kim, K.K. Mehta, T.E. Northup, H. Paik, B. Palmer, N. Samarth, S. Sangtawesin, and D. Steuerman, *Materials challenges and opportunities for quantum computing hardware.* Science, 2021. **372**(6539).
147. Witzel, W.M., M.S. Carroll, A. Morello, L. Cywinski, and S. Das Sarma, *Electron Spin Decoherence in Isotope-Enriched Silicon.* Physical Review Letters, 2010. **105**(18): p. 187602 DOI: ARTN 187602 10.1103/PhysRevLett.105.187602.
148. Itoh, K.M., J. Kato, M. Uemura, A.K. Kaliteevskii, O.N. Godisov, G.G. Devyatych, A.D. Bulanov, A.V. Gusev, I.D. Kovalev, and P.G. Sennikov, *High purity isotopically enriched 29Si and 30Si single crystals: isotope separation, purification, and growth.* Japanese journal of applied physics, 2003. **42**(10R): p. 6248.
149. Petit, L., J. Boter, H. Eenink, G. Droulers, M. Tagliaferri, R. Li, D. Franke, K. Singh, J. Clarke, and R. Schouten, *Spin lifetime and charge noise in hot silicon quantum dot qubits.* Physical review letters, 2018. **121**(7): p. 076801.
150. Mazzocchi, V., P. Sennikov, A. Bulanov, M. Churbanov, B. Bertrand, L. Hutin, J. Barnes, M. Drozdov, J. Hartmann, and M. Sanquer, *99.992% 28Si CVD-grown epilayer on 300 mm substrates for large scale integration of silicon spin qubits.* Journal of Crystal Growth, 2019. **509**: p. 1-7.
151. Koch, M., J.G. Keizer, P. Pakkiam, D. Keith, M.G. House, E. Peretz, and M.Y. Simmons, *Spin read-out in atomic qubits in an all-epitaxial three-dimensional transistor.* Nature nanotechnology, 2019. **14**(2): p. 137-140.
152. Pillarisetty, R., N. Thomas, H. George, K. Singh, J. Roberts, L. Lampert, P. Amin, T. Watson, G. Zheng, and J. Torres. *Qubit device integration using advanced semiconductor manufacturing process technology*. in *2018 IEEE International Electron Devices Meeting (IEDM)*. 2018. IEEE.

153. Kravchenko, S. and M. Sarachik, *Metal–insulator transition in two-dimensional electron systems.* Reports on Progress in Physics, 2003. **67**(1): p. 1.
154. Swartz, R., G. Chin, A. Voshchenkov, P. Ko, B. Wooley, S. Finegan, and R. Bosworth, *Digital NMOS test circuits fabricated in silicon MBE.* IEEE electron device letters, 1984. **5**(2): p. 29-31.
155. Leadbeater, M., C. Foden, J. Burroughes, M. Pepper, T. Burke, L. Wang, M. Grimshaw, and D. Ritchie, *Magnetotransport in a nonplanar two-dimensional electron gas.* Physical Review B, 1995. **52**(12): p. R8629.
156. Vorob'ev, A., K.-J. Friedland, H. Kostial, R. Hey, U. Jahn, E. Wiebicke, J.S. Yukecheva, and V.Y. Prinz, *Giant asymmetry of the longitudinal magnetoresistance in high-mobility two-dimensional electron gas on a cylindrical surface.* Physical Review B, 2007. **75**(20): p. 205309.
157. Komiyama, S. and H. Hirai, *Theory of contacts in a two-dimensional electron gas at high magnetic fields.* Physical Review B, 1989. **40**(11): p. 7767.
158. Van Degrift, C., K. Yoshihiro, E. Palm, J. Wakabayashi, and S. Kawaji, *Re-examination of quantum Hall plateaus.* IEEE transactions on instrumentation and measurement, 1993. **42**(2): p. 562-567.
159. Lee, P.A. and T. Ramakrishnan, *Disordered electronic systems.* Reviews of Modern Physics, 1985. **57**(2): p. 287.
160. Hagmann, J.A., X. Wang, P. Namboodiri, J. Wyrick, R. Murray, M. Stewart Jr, R.M. Silver, and C.A. Richter, *High resolution thickness measurements of ultrathin Si: P monolayers using weak localization.* Applied Physics Letters, 2018. **112**(4): p. 043102.
161. Hikami, S., A.I. Larkin, and Y. Nagaoka, *Spin-orbit interaction and magnetoresistance in the two dimensional random system.* Progress of Theoretical Physics, 1980. **63**(2): p. 707-710.
162. Hagmann, J.A., *Magnetotransport investigation of bismuth chalcogenide topological insulators*. 2013: University of Notre Dame.
163. Ando, T., A.B. Fowler, and F. Stern, *Electronic properties of two-dimensional systems.* Reviews of Modern Physics, 1982. **54**(2): p. 437.
164. Sze, S.M., Y. Li, and K.K. Ng, *Physics of semiconductor devices*. 2021: John wiley & sons.
165. Davies, R. and M. Pepper, *Electron-electron scattering in silicon inversion layers.* Journal of Physics C: Solid State Physics, 1983. **16**(12): p. L353.
166. Padmanabhan, M., T. Gokmen, N. Bishop, and M. Shayegan, *Effective mass suppression in dilute, spin-polarized two-dimensional electron systems.* Physical review letters, 2008. **101**(2): p. 026402.
167. Mi, X., T. Hazard, C. Payette, K. Wang, D. Zajac, J. Cady, and J.R. Petta, *Magnetotransport studies of mobility limiting mechanisms in undoped Si/SiGe heterostructures.* Physical Review B, 2015. **92**(3): p. 035304.
168. Mani, R., W. Johnson, V. Umansky, V. Narayanamurti, and K. Ploog, *Phase study of oscillatory resistances in microwave-irradiated-and dark-GaAs/AlGaAs devices: Indications of an unfamiliar class of the integral quantum Hall effect.* Physical Review B, 2009. **79**(20): p. 205320.

169. Coleridge, P., *Inter-subband scattering in a 2D electron gas.* Semiconductor science and technology, 1990. **5**(9): p. 961.
170. MacLeod, S., K. Chan, T. Martin, A. Hamilton, A. See, A. Micolich, M. Aagesen, and P. Lindelof, *Role of background impurities in the single-particle relaxation lifetime of a two-dimensional electron gas.* Physical Review B, 2009. **80**(3): p. 035310.
171. Gold, A., *Scattering time and single-particle relaxation time in a disordered two-dimensional electron gas.* Physical Review B, 1988. **38**(15): p. 10798.
172. Li, J. and T.P. Ma, *Scattering of silicon inversion layer electrons by metal/oxide interface roughness.* Journal of applied physics, 1987. **62**(10): p. 4212-4215.
173. Ramanayaka, A.N., K. Tang, J.A. Hagmann, H.-S. Kim, D.S. Simons, C.A. Richter, and J.M. Pomeroy, *Use of quantum effects as potential qualifying metrics for "quantum grade silicon".* AIP Advances, 2019. **9**(12): p. 125153.
174. Carter, D.J., O. Warschkow, N.A. Marks, and D.R. McKenzie, *Electronic structure models of phosphorus δ-doped silicon.* Physical Review B, 2009. **79**(3): p. 033204.
175. Goh, K.E., L. Oberbeck, M. Simmons, and R. Clark, *Electrical activation of phosphorus in silicon.* 2003.
176. Brocks, G., P. Kelly, and R. Car, *Aluminum on Si (100): Growth and structure of the first layer.* Journal of Vacuum Science & Technology B: Microelectronics and Nanometer Structures Processing, Measurement, and Phenomena, 1994. **12**(4): p. 2705-2708.
177. Ide, T., T. Nishimori, and T. Ichinokawa, *Surface structures of Si (100)-Al phases.* Surface Science, 1989. **209**(3): p. 335-344.
178. Murakami, K.-i., K. Nishikata, M. Yoshimura, and A. Kawazu, *Structural studies of Al/Si (100) by LEED.* Applied surface science, 1992. **60**: p. 146-151.
179. Yeom, H., T. Abukawa, M. Nakamura, S. Suzuki, S. Sato, K. Sakamoto, T. Sakamoto, and S. Kono, *Initial stage growth of In and A1 on a single-domain Si (001) 2× 1 surface.* Surface science, 1995. **341**(3): p. 328-334.
180. Lander, J. and J. Morrison, *Surface reactions of silicon with aluminum and with indium.* Surface Science, 1964. **2**: p. 553-565.
181. Zhu, C., S. Misawa, S. Tsukahara, A. Kawazu, and S. Pang, *Adsorption and growth of Al on Si (100) in the initial stage.* Applied Physics A: Materials Science & Processing, 1999. **68**(2).
182. Brocks, G., P. Kelly, and R. Car, *Adsorption of Al on Si (100): A surface polymerization reaction.* Physical review letters, 1993. **70**(18): p. 2786.
183. Nogami, J., A. Baski, and C. Quate, *Aluminum on the Si (100) surface: Growth of the first monolayer.* Physical Review B, 1991. **44**(3): p. 1415.
184. Northrup, J.E., M. Schabel, C. Karlsson, and R. Uhrberg, *Structure of low-coverage phases of Al, Ga, and In on Si (100).* Physical Review B, 1991. **44**(24): p. 13799.
185. Sakama, H., K.-i. Murakami, K. Nishikata, and A. Kawazu, *Structural determination of Si (100) 2× 2-Al by tensor LEED.* Physical Review B, 1993. **48**(8): p. 5278.

186. Steele, B., L. Li, J. Stevens, and I. Tsong, *Structure of the Si (100)-(2× 2) In surface.* Physical Review B, 1993. **47**(15): p. 9925.
187. Kucera, M., F. Rozboril, P. Sobotik, and I. Ostadal, *Aluminium on the Si (100)-2× 1—Growth, Morphology, and Different Modifications of Aluminium Dimers Studied by STM.*
188. Appelbaum, J.A., G. Baraff, and D. Hamann, *The si (100) surface. iii. surface reconstruction.* Physical Review B, 1976. **14**(2): p. 588.
189. Tromp, R., E. Van Loenen, J. Demuth, and N. Lang, *Tip electronic structure in scanning tunneling microscopy.* Physical Review B, 1988. **37**(15): p. 9042.
190. Byun, J., M.R. Verardo, B. Sumengen, G.P. Lewis, B. Manjunath, and S.K. Fisher, *Automated tool for the detection of cell nuclei in digital microscopic images: application to retinal images.* Mol Vis, 2006. **12**(105-07): p. 949-60.
191. Drey, L.L., M.C. Graber, and J. Bieschke, *Counting unstained, confluent cells by modified bright-field microscopy.* Biotechniques, 2013. **55**(1): p. 28-33.
192. Keizer, J.G., S.R. McKibbin, and M.Y. Simmons, *The impact of dopant segregation on the maximum carrier density in Si: P multilayers.* ACS nano, 2015. **9**(7): p. 7080-7084.
193. Müller, E.W., J.A. Panitz, and S.B. McLane, *The atom-probe field ion microscope.* Review of Scientific Instruments, 1968. **39**(1): p. 83-86.
194. Cerezo, A., P.H. Clifton, M.J. Galtrey, C.J. Humphreys, T.F. Kelly, D.J. Larson, S. Lozano-Perez, E.A. Marquis, R.A. Oliver, and G. Sha, *Atom probe tomography today.* Materials Today, 2007. **10**(12): p. 36-42.
195. Barroo, C., A.J. Akey, and D.C. Bell, *Atom probe tomography for catalysis applications: a review.* Applied Sciences, 2019. **9**(13): p. 2721.
196. Schofield, S., N. Curson, M. Simmons, F. Rueß, T. Hallam, L. Oberbeck, and R. Clark, *Atomically precise placement of single dopants in Si.* Physical review letters, 2003. **91**(13): p. 136104.
197. Hallam, T., T. Reusch, L. Oberbeck, N. Curson, and M. Simmons, *Scanning tunneling microscope based fabrication of nano-and atomic scale dopant devices in silicon: The crucial step of hydrogen removal.* Journal of applied physics, 2007. **101**(3): p. 034305.
198. Gossmann, H.-J. and F. Unterwald, *Dopant electrical activity and majority-carrier mobility in B-and Sb-δ-doped Si thin films.* Physical Review B, 1993. **47**(19): p. 12618.
199. Murakami, M., *Critical Reviews in Solid State and Materials.* Science, 1998. **23**: p. 1.
200. Tsui, D. and G. Kaminsky, *Observation of Higher Sub-band in n-Type (100) Si Inversion Layers.* Physical Review Letters, 1975. **35**(21): p. 1468.
201. Cham, K. and R. Wheeler, *Temperature-dependent resistivities in silicon inversion layers at low temperatures.* Physical Review Letters, 1980. **44**(22): p. 1472.
202. Zieve, R., D. Prober, and R. Wheeler, *Low-temperature electron-phonon interaction in Si MOSFETs.* Physical Review B, 1998. **57**(4): p. 2443.
203. Hwang, E. and S.D. Sarma, *Electronic transport in two-dimensional Si: P δ-doped layers.* Physical Review B, 2013. **87**(12): p. 125411.

204. Sommerfeld, A. and N.H. Frank, *The Statistical theory of thermoelectric, galvano-and thermomagnetic phenomena in metals.* Reviews of Modern Physics, 1931. **3**(1): p. 1.
205. Kapitza, P., *The study of the specific resistance of bismuth crystals and its change in strong magnetic fields and some allied problems.* Proceedings of the Royal Society of London. Series A, Containing Papers of a Mathematical and Physical Character, 1928. **119**(782): p. 358-443.
206. Novak, M., S. Sasaki, K. Segawa, and Y. Ando, *Large linear magnetoresistance in the Dirac semimetal TlBiSSe.* Physical Review B, 2015. **91**(4): p. 041203.
207. Abrikosov, A., *Quantum linear magnetoresistance; solution of an old mystery.* Journal of Physics A: Mathematical and General, 2003. **36**(35): p. 9119.
208. Goh, K., L. Oberbeck, and M. Simmons, *Relevance of phosphorus incorporation and hydrogen removal for Si: P δ-doped layers fabricated using phosphine.* physica status solidi (a), 2005. **202**(6): p. 1002-1005.
209. Reusch, T., N. Curson, S. Schofield, T. Hallam, and M. Simmons, *Phosphorus and hydrogen atoms on the (0 0 1) surface of silicon: A comparative scanning tunnelling microscopy study of surface species with a single dangling bond.* Surface science, 2006. **600**(2): p. 318-324.
210. Warschkow, O., H.F. Wilson, N.A. Marks, S. Schofield, N. Curson, P. Smith, M. Radny, D. McKenzie, and M. Simmons, *Phosphine adsorption and dissociation on the Si (001) surface: An ab initio survey of structures.* Physical Review B, 2005. **72**(12): p. 125328.
211. Bottoms, B. *The International Roadmap for Semiconductors 2007*. in *2007 8th International Conference on Electronic Packaging Technology*. 2007. IEEE.
212. Johnson, B.C., J.C. McCallum, and M.J. Aziz, *Solid-phase epitaxy*, in *Handbook of Crystal Growth*. 2015, Elsevier. p. 317-363.
213. Arthur, J.R., *Molecular beam epitaxy.* Surface science, 2002. **500**(1-3): p. 189-217.
214. Mirabella, S., D. De Salvador, E. Bruno, E. Napolitani, E.F. Pecora, S. Boninelli, and F. Priolo, *Mechanism of boron diffusion in amorphous silicon.* Physical review letters, 2008. **100**(15): p. 155901.
215. Krause, O., H. Ryssel, and P. Pichler, *Determination of aluminum diffusion parameters in silicon.* Journal of Applied Physics, 2002. **91**(9): p. 5645-5649.
216. Weir, B., D. Eaglesham, L. Feldman, H. Luftman, and R. Headrick, *Electron microscopy of the ordered boron 2× 1 structure buried in crystalline silicon.* Applied surface science, 1995. **84**(4): p. 413-418.
217. Nishida, S., T. Shiimoto, A. Yamada, S. Karasawa, M. Konagai, and K. Takahashi, *Epitaxial growth of silicon by photochemical vapor deposition at a very low temperature of 200° C.* Applied physics letters, 1986. **49**(2): p. 79-81.
218. Brillson, L., M. Slade, A. Katnani, M. Kelly, and G. Margaritondo, *Reduction of silicon-aluminum interdiffusion by improved semiconductor surface ordering.* Applied physics letters, 1984. **44**(1): p. 110-112.

219. Yamada, M., K. Sawano, M. Uematsu, and K.M. Itoh, *Suppression of surface segregation of the phosphorous δ-doping layer by insertion of an ultra-thin silicon layer for ultra-shallow Ohmic contacts on n-type germanium.* Applied Physics Letters, 2015. **107**(13): p. 132101.
220. Keizer, J.G., S. Koelling, P.M. Koenraad, and M.Y. Simmons, *Suppressing segregation in highly phosphorus doped silicon monolayers.* ACS nano, 2015. **9**(12): p. 12537-12541.
221. Moon, C.-Y., W.-J. Lee, and K.-J. Chang, *Formation of dopant-pair defects and doping efficiency in B-and P-doped silicon nanowires.* Nano letters, 2008. **8**(10): p. 3086-3091.
222. Marcenat, C., J. Kačmarčík, R. Piquerel, P. Achatz, G. Prudon, C. Dubois, B. Gautier, J. Dupuy, E. Bustarret, and L. Ortega, *Low-temperature transition to a superconducting phase in boron-doped silicon films grown on (001)-oriented silicon wafers.* Physical Review B, 2010. **81**(2): p. 020501.
223. Balmer, R.S., I. Friel, S. Hepplestone, J. Isberg, M.J. Uren, M.L. Markham, N.L. Palmer, J. Pilkington, P. Huggett, and S. Majdi, *Transport behavior of holes in boron delta-doped diamond structures.* Journal of Applied Physics, 2013. **113**(3): p. 033702.
224. Chicot, G., T. Tran Thi, A. Fiori, F. Jomard, E. Gheeraert, E. Bustarret, and J. Pernot, *Hole transport in boron delta-doped diamond structures.* Applied Physics Letters, 2012. **101**(16): p. 162101.
225. Sussmann, R.S., *CVD diamond for electronic devices and sensors*. Vol. 26. 2009: John Wiley & Sons.
226. Davies, J.H., *The physics of low-dimensional semiconductors: an introduction*. 1998: Cambridge university press.
227. Schroder, D.K., *Semiconductor material and device characterization*. 2015: John Wiley & Sons.
228. Aono, M., O. Maida, and T. Ito, *Hall data analysis of heavily boron-doped CVD diamond films using a model considering an impurity band well separated from valence bands.* Diamond and related materials, 2011. **20**(10): p. 1357-1362.
229. Borst, T. and O. Weis, *Boron-Doped Homoepitaxial Diamond Layers: Fabrication, Characterization, and Electronic Applications.* physica status solidi (a), 1996. **154**(1): p. 423-444.
230. Mott, N., *Metal-insulator transitions*. 2004: CRC Press.
231. Bartl, G., P. Becker, B. Beckhoff, H. Bettin, E. Beyer, M. Borys, I. Busch, L. Cibik, G. D'Agostino, and E. Darlatt, *A new 28Si single crystal: counting the atoms for the new kilogram definition.* Metrologia, 2017. **54**(5): p. 693.
232. Artzi, Y., Y. Twig, and A. Blank, *Induction-detection electron spin resonance with spin sensitivity of a few tens of spins.* Applied Physics Letters, 2015. **106**(8): p. 084104.
233. Bienfait, A., J. Pla, Y. Kubo, M. Stern, X. Zhou, C. Lo, C. Weis, T. Schenkel, M. Thewalt, and D. Vion, *Reaching the quantum limit of sensitivity in electron spin resonance.* Nature nanotechnology, 2016. **11**(3): p. 253.

234. Mani, R.G., J. Hankinson, C. Berger, and W.A. De Heer, *Observation of resistively detected hole spin resonance and zero-field pseudo-spin splitting in epitaxial graphene.* Nature communications, 2012. **3**(1): p. 1-6.